UNIVERSITY OF NAIROBI

FACULTY OF ENGINEERING

Development of a super resolution imaging technique based on ultrasonic guided waves for non-destructive testing

John Kiprotich Birir

S95/51107/2016

BSc Mechanical Engineering and MSc Nuclear Science

University of Nairobi

A thesis submitted in fulfillment of the requirements for the degree of Doctor of Philosophy in Nuclear Science and Technology in the Department of Electrical and Information Engineering in the University of Nairobi.

@2023

DECLARATION

This thesis has not been submitted for a degree in any other university and the contents are my original work.

Name: John Kiprotich Birir Reg. No: S95/51107/2016

Sign .... Date 15/11/2023

APPROVAL

This thesis has been submitted for examination with our knowledge as university supervisors.

1) Prof. Michael J. Gatari,
Department of Electrical & Information Engineering, University of Nairobi.

Sign .... Date 15 November 2023

2) Prof. Prabhu Rajagopal,
Mechanical Engineering Department, Indian Institute of Technology – Madras, Chennai, India.

Sign .... Date 15/11/2023

DEDICATION

This research work is dedicated to all my family members who gave me their overwhelming support, understanding and encouragement during the research period.

ACKNOWLEDGEMENTS

I would like to express my sincere appreciation and gratitude to: my supervisors Prof. Michael Gatari and Prof. Prabhu Rajagopal, for their encouragements, guidance, support, advice and criticism; the staff and colleagues of the Institute of Nuclear Science and Technology for the support they gave me during the research period; staff and colleagues of the Indian Institute of Technology Madras for granting me access to their lectures, trainings, research equipment and for support during my trips to India.

I wish to acknowledge the support I received from: the National Research Fund (NRF) for financing part of this work through a research grant No. NRF/PhD/02/150; the International Atomic Energy Agency for their infrastructure support in NDT at the institute and for facilitating my trainings through fellowship trainings to NDT Level 3 at CNESTEN; the International Science Programme based in Uppsala University, Sweden, for facilitating my travel to attend several conferences including the 46th Annual Review of Progress in Quantitative Nondestructive Evaluation conference, which was held in Oregon, USA, in July 2019 and for financing my numerous trips to India to perform experiments and to consult with my supervisor, Prof. Prabhu Rajagopal. The financial, intellectual, social and moral support from all the above and others not mentioned ensured successful completion of this research.

Finally, I am grateful to God for the gift of life, good health, wisdom and protection which enabled me to carry out research without much disruptions despite the outbreak of the corona virus pandemic when I was in the middle of my work.

TABLE OF CONTENTS

LIST OF FIGURES

ACRONYMS AND ABBREVIATIONS

1D:	One Dimensional
2D:	Two Dimensional
3D:	Three Dimensional
CNDE:	Centre for Non-Destructive Evaluation
CNESTEN:	Centre National de l’Energie des Sciences et des Techniques Nucleaires
FEM:	Finite Element Method
GUWs:	Guided Ultrasonic Waves
GWT:	Guided Wave Testing
GWUT:	Guided Waves Ultrasonic Testing
IAEA:	International Atomic Energy Agency
IITM:	Indian Institute of Technology, Madras
INST:	Institute of Nuclear Science and Technology
ISP:	International Science Program
LHM:	Left-Handed Materials
LRUT:	Long Range Ultrasonic Testing
NACOSTI:	National Council for Science, Technology and Innovation
NDT:	Non-Destructive Testing
NRF:	National Research Fund
ODE:	Ordinary Differential Equation
PDE:	Partial Differential Equation
SDH:	Side Drilled Holes
UGW:	Ultrasonic Guided Waves

SYMBOLS

A: Anti-symmetric Lamb wave
C: Damping coefficient
c_g: Group velocity
c_{ij}: Stiffness elastic constants
c_L: Longitudinal wave velocity
c_p: Phase velocity
c_T: Transverse wave velocity
E: Modulus of elasticity
ε_{ij}: Strains
F: Internal force
G: Shear modulus
h: Plate half-thickness
k: Wavenumber
K: Stiffness coefficient
L: Longitudinal wave
λ: Wavelength
M: Mass
P: External force
υ: Poisson's ratio
ρ: Density
S: Symmetric Lamb wave
σ_{ij}: Stress
t: Time
U: Displacement
ω: Circular wave frequency

ABSTRACT

Guided ultrasonic waves testing is a well-established inspection technique for structures such as plates, pipes, and rail tracks. The method is very useful for inspecting buried or otherwise inaccessible sections of a structure from a remote location. Guided ultrasonic wave, like any other wave, is diffraction limited in that features smaller than half of the working wavelength cannot be resolved under normal circumstances. Defects lying within half a wavelength of design features such as welds and supports may go undetected. Due to the low frequencies used in guided wave testing the resolution capability is relatively poor. Therefore, it is used for screening purposes to inspect and identify areas of concern in a structure. A secondary more sensitive method, such as bulk ultrasonic waves testing, is then deployed to explore in detail the identified areas of concern. Not all areas of structures are easily accessible for purposes of secondary close contact, high-resolution inspection. It was therefore of practical interest to develop a method for detection and characterization of defects beyond the half-wavelength limitation from a remote location. The approach proposed in this research utilized fabricated metamaterials to capture and amplify evanescent waves which are generated at defect boundaries. Both simulations and experiments were carried out in this research. Simulations were done using commercial finite element analysis software, *Abaqus*, to determine the viability of the method and to optimize the dimensions of the metamaterials. Some of the variables investigated included metamaterial parameters, defect types, size and spacing. Crack-like linear defects and corrosion-like rounded defects in a plate were considered. Subwavelength resolution was achieved in both categories of defects with $\lambda/72$ resolution attained for rounded defects and $\lambda/6$ for linear defects. The method developed in this research improved the resolution of guided ultrasonic wave inspection to the same sensitivity level as that of bulk ultrasonics while retaining its application over a long range. The results of this research have much promise for remote nondestructive inspection in hazardous environments such as radiation contamination zones as well as petrochemical industry, utilities, pipelines, railways and in biomedicine. In the design of the metamaterials used in this wok it is recommended that the channel holes should be reduced to smaller than a tenth of the probing wavelength and the channel lengths to remain integer multiples of half a wavelength.

CHAPTER 1: INTRODUCTION

1.1 Introduction

Pipelines are extensively used for the transportation of many products in Kenya and across the world. These products include water, steam, chemicals, and fuel. For instance, petrol, diesel and kerosene from Mombasa is normally pumped through pipelines to towns inland such as Nairobi, Nakuru, Eldoret and Kisumu. Some pipes are used to transport water in a distribution network from dams and treatment plants to consumers. As an example, residents of Nairobi consume water that has been piped all the way from dams located in the neighborhoods of Thika town. Leakage of water leads to loss of product, and scarcity of water which affects the quality of life and can promote spread of diseases such as cholera and corona virus due to poor hygiene. A leakage from pipelines could also be fatal as a direct result from the product being transported. Many accidents have been well documented in Kenya and across the world involving petroleum products. Leakage of petroleum products leads to loss of product, fires, and ecological pollutions both inland and at sea lives (Huho et al.,2016; Chen et al., 2016). The products can be in hazardous form such as high-pressure super-heated steam, highly corrosive chemicals, and highly inflammable petroleum products. In the geothermal industry pipelines transport steam from wells to the power generation plants such as in Naivasha and Nakuru geothermal power plants. If these steam leaks, the harmful chemicals from underground will be discharged to the environment and this can lead to diseases and loss of life.

From the time of commissioning the pipes degrade continuously. Erosion and corrosion are the main mechanisms of degradation and occur due to effects of the product transported inside the pipe as well as the environmental conditions under which the pipeline is exposed to. The pipelines are usually buried underground. Leakages from such pipes can go undetected for a long duration resulting in product loss, environmental pollution, as well as property damage and loss of human lives.

It is therefore necessary that pipes and other structures are checked on a regular interval so as to detect flaws hence minimize chances of failure. Any areas requiring repairs or other corrective measures can then be addressed in good time. This ensures the safety of the products they transport and the safety of the environment and the people around where these structures are located. Some of the methods used to inspect these utilities include guided ultrasonic waves, bulk ultrasonic waves, magnetic flux leakage, magnetic particle testing, dye penetrant testing, eddy current testing, leakage testing, among many other non-destructive techniques. The work presented in this thesis and the associated published papers (Birir and Kairu, et al., 2019; Birir et al., 2020) which abstracts are in Appendix A and B, and conference proceedings (Birir et al., 2019) with abstract in Appendix C addresses the development of a method for super resolution imaging of guided ultrasonic waves. Another paper has been submitted to NDT & E International, an Elsevier journal, titled “Material enhanced subwavelength of inaccessible defects in guided ultrasonic wave inspection”.

1.2 Background

Guided ultrasonic waves (GUWs) are of great interest for nondestructive testing, medical imaging and structural health monitoring due to their long-range capabilities. They are generated in structures such as plates, rods and pipes when the wavelength of propagating ultrasonic wave is larger than the structure thickness. This leads to the wave bouncing between the boundaries of the structure with minimum loss of energy. As a result, the GUWs are guided by the structure boundaries and can travel tens of metres in the up-stream and down-stream directions from the location of the sensor. In the absence of boundaries, the waves will generally spread and attenuate in accordance to the inverse square law. Thus, GUWs find applications in inspection of structures such as pipes (Nahil-Mahal et al., 2019), rail tracks (Xing et al., 2019), cables (Zhang et al., 2019), plates (Fan et al., 2018), bars (Zhang et al., 2018), composites (Wronkowicz et al., 2018), aircraft wings (Zhao and Rose, 2016), and in biomedical diagnostics (Okumura et al., 2018).

Traditionally, integrity of structures such as a pipeline is evaluated through visual inspection and bulk ultrasonic thickness measurements and flaw detection. These tests are localized to the accessible areas and thus require that any buried sections are entirely excavated before full inspection can be achieved. The size of most commercial sensors for ultrasonic testing is in the order of 5 mm to 20 mm diameter. Every single reading in a bulk ultrasonic testing is usually limited to the zone covered by the sensor. To cover 100% of the area of interest would require moving the sensor millions of times. This assumes that the buried sections have been excavated to expose the entire structure surface area. Obviously, this is not feasible from the perspective of both time constraints and cost implications. Therefore, in real life it is not practicable to carry out 100% bulk ultrasonic test. Instead, points are sampled at specified grid intervals of the structure.

Guided ultrasonic waves was developed as an aid to conventional bulk ultrasonic testing. When the wavelength of a probing ultrasonic wave is larger than the thickness of the structure the wave is bounced back and forth by the wall boundaries and thus the wave is guided along the thickness over a large distance. To conduct this test, a small section is excavated to expose the buried section. Low frequency (hence large wavelength) ultrasonic sensors are mounted at the excavated location of the structure. From this setup it is possible to scan tens of metres on both the upstream and the downstream of the structure from the single sensor location. Thus, there is no need for excavating entire structure. Instead, the excavation is only done at selected intervals which is determined by the effective range of the wave and the coverage desired. The area needing excavation is small and just sufficient to mount the sensor system. The guided waves signal transmitted is such that the entire length, wall thickness volume and circumference is inspected simultaneously. This technique is fast and cheaper as it enables the inspection of large areas from one remote sensor location and requires few excavation points. The frequency of operation is low to ensure that the wavelengths are larger than the thickness to be inspected. Low frequency result in limited attenuation hence long range of propagation. These frequencies are typically between 20 kHz and 200 kHz (Cawley, 2003) for common structural thicknesses. This is in contrast with conventional bulk ultrasonic waves which operate at high frequencies typically from 1 MHz to 20 MHz. A challenge that arises with operating at low frequencies is that the resolution is low. There is a direct relationship between frequency and resolution such that resolution is increased by increasing the frequency of operation.

The minimum resolution attainable for a given wave is given by $\lambda/2$ where λ is the working wavelength. This is known as the Abbe diffraction limit (Anzan-Uz-Zaman et al., 2020) and it presents a challenge in application of GUWs (Shen et al., 2019). This is made worse in the absolute sense by the fact that the wavelengths used in GUWs are large (tens of centimetres) due to low frequencies required to ensure long distance propagation. A shorter wavelength (higher frequency) wave could be used as an alternative but then attenuation will set in and the long-range advantages of GUWs testing will be lost. Therefore, GUWs are generally used for screening purposes to identify areas of concern (Spytek et al., 2020). Once such an area is identified, a secondary more high-resolution technique (such as conventional high frequency bulk ultrasonic wave) is employed to quantify the discontinuity identified. Since GUWs reflects a signal from natural design features such as welds, elbows, supports and bends, these signals from design features are usually identified and ignored (Nakhli-Mahal et al., 2019). As a result, any defect occurring near these design features (within half of wavelength of probing wave) will easily go undetected. This distance is in the order of several centimetres for the GUWs frequencies generally used for inspection.

Conventional materials are diffraction limited. One way in which resolution can be improved is by use of unconventional materials. One such example of unconventional materials is what is known as metamaterials. These are specially engineered materials that attain exotic properties that can be manipulated as desired (Kaina et al., 2015; Kuchibhatla and Rajagopal, 2019; Pendry, 2000; Shelby et al., 2001; Zhu et al., 2011). These special properties are as a result of design shapes rather than by elemental composition. The purpose of this delicate engineering manipulation is to provide special material properties that would otherwise not be attainable with ordinary materials. Metamaterials find applications in many fields for specifically targeted outcomes. Some areas where metamaterials have been applied include in: optics (Haxha et al., 2018; Huszka and Gijs, 2019; Ou et al.,, 2018; Repänet al., 2015), medical (Kim and Rho, 2015; Waterman et al., 2015), mechanical (Bertoldi et al., 2017; Kelkar et al., 2020; Surjadi et al., 2019; Yu et al., 2018), acoustics (Ma and Sheng, 2016a; Tang et al., 2017; Zangeneh-Nejad and Fleury, 2019), and ultrasonics (Yang et al., 2020; Zhao et al., 2020; Zhu and Semperlotti, 2014). A research group at Indian Institute of Technology Madras, India (IITM) has recently developed metamaterials for various ultrasonic applications including mode filtering (Sikundalapuram Ramesh et al., 2020) and super resolution imaging (Amireddy, Balasubramaniam and Rajagopal, 2016, 2017, 2018; Syed Akbar Ali et al., 2019). The experimental research presented in this thesis was conducted at IITM and complements investigations by others in this research group that aims at exploring wider applications of novel metamaterials. There has been a global increase in research in many disciplines to find new exotic applications of metamaterials. The idea of metamaterials gained popularity mainly from the many developments in the field of electromagnetic waves with attainments of negative permeability and negative permittivity.

The metamaterials developed in this research work on the principle of Fabry-Perot resonance. When waves interact with the defect, evanescent waves are generated. These are non-propagating as they usually decay within a wavelength from the regions of formation. The metamaterials developed were used to capture these evanescent waves, amplify them and then transmit to a remote location for imaging. The advantage of capturing the high frequency evanescent waves is that they carry detailed information about the defect as compared to information carried by the normal low frequency propagating waves. The capture and imaging of evanescent waves enable resolution at the subwavelength level. The developed technology can be of great interest in ensuring critical structures such as pipelines and nuclear power plants are operated safely. This technology aims at reducing the cost of inspection and the time taken to complete inspection work compared to existing technologies. The technology can be adopted for use in micro, small, medium, and large enterprises to enhance the quality and safety of products produced by the sectors. This can also increase on reliability of products made in Kenya which then has potential for increasing exports to existing markets as well as opening new markets. This developed technology will go a long way in contributing towards the improvement of safety of nuclear power plants and its supporting infrastructure.

Rail tracks are used primary for transportation of goods and people. As the country develops, pipelines and railway lines will continue to increase in number. Recent additions to the existing infrastructure include the petroleum pipelines from Mombasa all the way to western Kenya and the standard gauge railway lines. Utilities suffer deterioration with age. Erosion and corrosion are some of the deterioration mechanisms that occur due to the effects of product, high temperatures, pressure and the environmental conditions. Additional defects such as cracks are likely to develop and grow during operation. If defects are not detected in good time this can lead to catastrophe depending on the hazardous nature of the products. Due to such risks, it is essential to carry out effective and timely inspection to prevent disasters. There are many inspection techniques developed and used over the years to ensure integrity of these utilities. Long range guided ultrasonic wave is a non-destructive testing method useful in the inspection of utilities. Pipes and rail tracks are just two examples of structures, among many other structures, capable of inspection by this technique. Guided ultrasonic waves inspection is fast and economical compared to competing technologies primarily due to the long-range capability and entire volume coverage.

This thesis presents work done to develop a high resolution guided ultrasonic wave inspection technique. Different methods for achieving high resolution have been considered in literature. However, none of these methods overcame the diffraction limit. In this work the aim was to overcome the diffraction limit. This was achieved by developing materials, referred to as metamaterials, that give novel properties not found in regular materials. The design of metamaterial dimensions with respect to interrogating wave wavelength leads to a state of Fabry-Perot resonance that amplify evanescent waves to aid in imaging finer details of the defects.

Defects were fabricated into plate samples. In non-destructive testing defects are generally grouped as either rounded or linear. A defect is considered rounded if the major dimensions are less than or equal to three times the minor dimensions of the defect (Kadarno et al., 2019) and for a linear defect, the major dimension is greater. Both linear and rounded defects were considered and the sizes and separation distances between them were varied. Resolution tests were then done. Cases were compared for when a metamaterial was used and when it was not used. Numerical simulation as well as experimental validation were done and both results agreed. It was found that indeed use of metamaterial led to improved resolution. Sub-wavelength resolution was therefore achieved in the investigated rounded and linear defects.

1.3 Problem statement

Guided ultrasonic wave testing is the only method currently available with long range capability. The method is however limited in resolution capability due to the long wavelength (λ) waves required to achieve the long ranges desired. Defects located near design features like welds can go undetected due to inability to discriminate signals from the flaw and from the weld. Due to diffraction limits, the maximum achievable resolution is λ/2. Selection of short wavelength waves would improve resolution but then would also reduce the range of the guided waves due to increased attenuation. At present guided waves are used for screening to identify areas of questionable integrity. It achieves this faster than any other method since it covers 100% of the structure's volume. When an area of questionable integrity is identified, a higher resolution method such as bulk ultrasonics is then used to focus on those areas. This usually is time consuming and costly as it needs close contact. Some sections are extremely difficult to access for example areas buried under concrete while others can be in high radiation zones for the case of nuclear power plants. Based on the problem stated, the purpose of this research was to explore the possibility of improving resolution capability of guided ultrasonic wave testing to levels smaller than the λ/2 diffraction limit in a single-step process, without the need for additional secondary high sensitivity methods.

1.4 Objectives

1.4.1 Main objective

The main objective of this research was to improve defect resolution capability beyond the diffraction limits for guided ultrasonic waves inspection.

1.4.2 Specific objectives

The following were the specific objectives:

i) To determine optimum excitation parameters such as modes and frequency
ii) To design and develop appropriate metamaterials
iii) To determine optimum metamaterial lens parameters such as channel size and periodicity
iv) To determine resolution limits for corrosion-like rounded defects with the aid of developed metamaterial lens
v) To determine resolution limits for crack-like linear defects with the aid of developed metamaterial lens

1.5 Justification and significance of the research

Guided ultrasonic wave testing has capability to inspect tens of metres of structures from just one access point. For the case of a buried structures, excavation can be carried out at longer intervals compared with bulk ultrasonic waves which would require excavation of entire structures. The traditional method of corrosion monitoring using ultrasonic thickness measurements require taking readings at regular interval, say two metres, which is not practical for example for pipeline running thousands of kilometres. In addition, the readings obtained by ultrasonic thickness measurements represent a local reading that is not a true representation of the entire pipe condition. Critical defects located at areas not sampled can go undetected when using conventional bulk ultrasonic waves. On the other hand, guided ultrasonic wave testing has full thickness volume coverage for example of the pipe and gives a true representation of the entire stretch inspected. It is also cheap and fast as it covers large stretches from a single sensor location. The improvement on resolution can therefore make guided ultrasonic waves a final method of choice for the inspection of critical structures. This can be particularly useful on areas that are not readily accessible such as those buried underground, in concrete, under roads, or otherwise insulated. This method can also be of great benefit for inspection of structures located in high radiation zones such as in nuclear power plants.

1.6 Scope of work

The scope of this work was chosen based on the capabilities of available research facility. Metamaterial sensors were chosen as the tool to achieve the super resolution. The work involved both numerical simulation and experimental work. Simulations were used to determine optimum dimensions and to investigate the resolution capabilities of the proposed metamaterials. Experiments were carried out for validation of the models developed. Parameters of interest included frequency, velocity, mode, defect type, defect size, unit cell size, pattern and spacing. These parameters were selected appropriately during the theoretical and the experimental stages of the research. The defects considered were holes and slits in a plate. The design was limited to a configuration that could be fabricated from the materials and with the available tools.

CHAPTER 2: LITERATURE REVIEW

2.1 Introduction

In this chapter the literature covering topics relevant to this research including theoretical background, non-destructive testing, guided waves, and metamaterials are presented. Before introducing the method used in this work, potential avenues for improvements to resolution are addressed. Since most principles were developed in the field of optical microscopy there will be an occasional reference to electromagnetic waves even though the bulk of materials and main focus of this thesis is on mechanical waves and more specifically on ultrasonic guided waves in an elastic media.

2.2 Theoretical background

2.2.1 The wave equation

It is important to investigate how mechanical disturbances propagate through an elastic media for purposes of applications in ultrasonic testing. In this section the basic concepts are presented for mechanical wave propagation. When a mechanical disturbance occurs at a given point, the disturbance will travel through a media and will then be detected at a distant location after some time has elapsed (Kolsky, 1964). This elapsed time is dependent upon the velocity of propagation. Examples of mechanical disturbance propagations include earthquakes, underground explosions, and sound. Mechanical wave motion begins when an object at rest is given a small forced displacement. The forcefully disturbed particle then transmits that displacement to an adjacent particle without itself migrating. The next particle transfers the displacement to another adjacent particle and the same process continues. The material offers some level of resistance to this displacement. At every point of particle to particle transfer some energy is lost through friction and eventually there will be no energy left to transfer hence the wave will die off after such a time has elapsed. All natural materials are deformable hence able to transfer the disturbance from particle to particle. Real materials are usually modelled as a network of mass-spring matrix whereby the masses represent the particles and the springs connects these particles in an elastic manner. The springs allow local elastic deformations to happen without any permanent damage. Thus, each particle vibrates within a given location and the spring transmits the vibration to the next particles and so forth.

Consider an infinite solid body subjected to a disturbance $f(t)$ with the disturbance propagation speed of c (Cagniard et al., 1963). For mechanical waves this disturbance can be stress, displacement, velocity, acceleration, or rotation. After a time t_1 the wave will have traveled a distance ct_1. After a time t_2 the wave will have travelled a distance ct_2. Mathematically, a travelling wave in one-dimension is given by $f=f(x-ct)$. This function represents a mechanical disturbance propagating in the x-axis at a velocity c. When the source of the mechanical disturbance is removed, the object will eventually return to rest.

The propagation of a wave can be described mathematically by means of appropriate partial differential equations, initial time conditions and boundary spatial conditions (Lewis et al., 2022). Solution of the differential equations then yields desired variable values generally in terms of the conditions at a given distance and time. To achieve this several theories come into play and includes theory of elasticity, continuum mechanics, stress, motion, deformation, mass conservation, momentum conservation, energy conservation and constitutive relations. These are important topics that are well covered in classical textbooks (Achenbach, 1999) and due to limited scope of this thesis they will not be covered in detail.

2.2.2 Notation and mathematical preliminaries

Tensors are mathematical objects widely used in mathematics, physics and engineering to describe relationships between vectors and scalars (Milton and Cherkaev, 1995). It is a generalization of vectors and matrices, with both magnitude and direction. It can be used to describe many complex physical quantities, laws, systems and phenomena including the flow of fluids, deformations of solid objects, behaviour of electromagnetic fields and the propagation of waves. Tensor notation is a mathematical notation used to represent tensors. In tensor notation, a tensor is represented using a symbol with multiple indices. The number of indices corresponds to the number of dimensions of the tensor. The rules for manipulating tensors are expressed using index notation, which involves the use of indices and the summation convention. Index notation can be used to express tensor equations in a simple compact way. Different tensor notations are used in this thesis and in literature. The choice of a notation to use is dependent upon the particular quantity being described for clarity, convenience and simplicity. Hence it is important to highlight some of these notations in this section since different notations are used interchangeably in this work and in literature. The notations presented here are those used in the area of elasticity and include indicial notations and vector operators. In this section bold letters are used to indicate vectors as opposed to scalar quantities. Vectors have both magnitude and direction whereas scalars have only magnitude with no particular direction.

For a rectangular cartesian coordinate system the coordinates can be represented as x_i or x_1, x_2, x_3 or x, y, z. The unit vectors in the x, y, z directions are given by $\boldsymbol{e}_j$ or $\boldsymbol{e}_1$, $\boldsymbol{e}_2$, $\boldsymbol{e}_3$ or $\boldsymbol{e}_x$, $\boldsymbol{e}_y$, $\boldsymbol{e}_z$. In both cases i and j takes the values 1, 2, 3. Base vectors are given by the following,

$$\boldsymbol{e}_x = \boldsymbol{e}_1 = \begin{Bmatrix} 1 \\ 0 \\ 0 \end{Bmatrix} \tag{2.1}$$

$$\boldsymbol{e}_y = \boldsymbol{e}_2 = \begin{Bmatrix} 0 \\ 1 \\ 0 \end{Bmatrix} \tag{2.2}$$

$$\boldsymbol{e}_z = \boldsymbol{e}_3 = \begin{Bmatrix} 0 \\ 0 \\ 1 \end{Bmatrix} \tag{2.3}$$

As an example, a position vector $\boldsymbol{x}$ can be represented by any of the ways below,

$$\boldsymbol{x} = \begin{Bmatrix} x \\ y \\ z \end{Bmatrix} = x\,\boldsymbol{e}_x + y\,\boldsymbol{e}_y + z\,\boldsymbol{e}_z \tag{2.4}$$

or

$$\boldsymbol{x} = \begin{Bmatrix} x_1 \\ x_2 \\ x_3 \end{Bmatrix} = x_1\,\boldsymbol{e}_1 + x_2\,\boldsymbol{e}_2 + x_3\,\boldsymbol{e}_3 \tag{2.5}$$

Using the summation convention, the above vector $\boldsymbol{x}$ can also be represented in the following way.

$$\boldsymbol{x} = \begin{Bmatrix} x_1 \\ x_2 \\ x_3 \end{Bmatrix} = \sum_{i=1}^{3}(x_i\, \boldsymbol{e}_i) = x_i\, \boldsymbol{e}_i \tag{2.6}$$

The last term $x_i\, \boldsymbol{e}_i$ is the indicial or index notation of the vector $\boldsymbol{x}$.

Another notation used is the Kronecker delta (Graham, 1981) and is given as follows.

$$\delta_{ij} = \begin{cases} 1 \ \ if\ i = j \\ 0\ if\ i \neq j \end{cases} \tag{2.7}$$

As an example, the Kronecker delta is useful when multiplying vectors and yields the following results.

$$\boldsymbol{e}_i . \boldsymbol{e}_j = \delta_{ij}$$

which yields

$$\boldsymbol{e}_i . \boldsymbol{e}_j = 0 \text{ when } i \neq j$$

and

$$\boldsymbol{e}_i . \boldsymbol{e}_j = 1 \text{ when } i = j$$

Another notation is the alternating tensor (Milton and Cherkaev, 1995) or permutation symbol ε_{ijk} and is given below.

$$\varepsilon_{ijk} = \begin{cases} +1 \ \ \text{if i, j, k are even permutations of 1, 2, 3} \\ \ \ 0 \qquad \text{if any two of the i, j, k are equal} \\ -1 \ \ \ \text{if i j k are odd permutations of 1, 2, 3} \end{cases} \tag{2.8}$$

Using the above, the scalar and vector products of two vectors can be evaluated and additional notations developed. The dot product between vectors $\boldsymbol{u}$ and $\boldsymbol{v}$ is given by,

$$a = \boldsymbol{u} . \boldsymbol{v} = (u_i \boldsymbol{e}_i).(v_j \boldsymbol{e}_j) = u_i v_j\, \boldsymbol{e}_i . \boldsymbol{e}_j = u_i v_j\, \delta_{ij} = u_1 v_1 + u_2 v_2 + u_3 v_3 = u_i v_j$$

thus,

$$a = \boldsymbol{u} . \boldsymbol{v} = u_i v_j \tag{2.9}$$

The cross product between vectors $\boldsymbol{u}$ and $\boldsymbol{v}$ is given by,

$$\boldsymbol{u} = u_1\, \boldsymbol{i} + u_2\, \boldsymbol{j} + u_3\, \boldsymbol{k}$$

$$\boldsymbol{v} = v_1\, \boldsymbol{i} + v_2\, \boldsymbol{j} + v_3\, \boldsymbol{k}$$

$$\boldsymbol{h} = \boldsymbol{u}\, x\, \boldsymbol{v} = \begin{Bmatrix} u_1 \\ u_2 \\ u_3 \end{Bmatrix} x \begin{Bmatrix} v_1 \\ v_2 \\ v_3 \end{Bmatrix}$$

$$= \{u_1\, \boldsymbol{e}_1 + u_2\, \boldsymbol{e}_2 + u_3\, \boldsymbol{e}_3\}\, x\, \{v_1\, \boldsymbol{e}_1 + v_2\, \boldsymbol{e}_2 + v_3\, \boldsymbol{e}_3\}$$

$$= \{u_1\, \boldsymbol{e}_1 + u_2\, \boldsymbol{e}_2 + u_3\, \boldsymbol{e}_3\}\, \boldsymbol{x}\, \{v_1\, \boldsymbol{e}_1 + v_2\, \boldsymbol{e}_2 + v_3\, \boldsymbol{e}_3\}$$

$$= u_1v_1(\boldsymbol{e}_1\boldsymbol{x}\boldsymbol{e}_1) + u_1v_2(\boldsymbol{e}_1\boldsymbol{x}\boldsymbol{e}_2) + u_1v_3(\boldsymbol{e}_1\boldsymbol{x}\boldsymbol{e}_3) + u_2v_1(\boldsymbol{e}_2\boldsymbol{x}\boldsymbol{e}_1) + u_2v_2(\boldsymbol{e}_2\boldsymbol{x}\boldsymbol{e}_2)$$
$$+ u_2v_3(\boldsymbol{e}_2\boldsymbol{x}\boldsymbol{e}_3) + u_3v_1(\boldsymbol{e}_3\boldsymbol{x}\boldsymbol{e}_1) + u_3v_2(\boldsymbol{e}_3\boldsymbol{x}\boldsymbol{e}_2) + u_3v_3(\boldsymbol{e}_3\boldsymbol{x}\boldsymbol{e}_3)$$

$$= \boldsymbol{e}_i\varepsilon_{ijk}u_jv_k$$

$$= u_1v_1(\boldsymbol{0}) + u_1v_2(\boldsymbol{e}_3) + u_1v_3(-\boldsymbol{e}_2) + u_2v_1(-\boldsymbol{e}_3) + u_2v_2(\boldsymbol{0}) + u_2v_3(\boldsymbol{e}_1)$$
$$+ u_3v_1(\boldsymbol{e}_2) + u_3v_2(-\boldsymbol{e}_1) + u_3v_3(\boldsymbol{0})$$

$$= u_2v_3(\boldsymbol{e}_1) + u_3v_2(-\boldsymbol{e}_1) + u_3v_1(\boldsymbol{e}_2) + u_1v_3(-\boldsymbol{e}_2) + u_1v_2(\boldsymbol{e}_3) + u_2v_1(-\boldsymbol{e}_3)$$

$$= (u_2v_3 - u_3v_2)\boldsymbol{e}_1 + (u_3v_1 - u_1v_3)\boldsymbol{e}_2 + (u_1v_2 - u_2v_1)\boldsymbol{e}_3$$

$$\boldsymbol{h} = (u_2v_3 - u_3v_2)\boldsymbol{e}_1 + (u_3v_1 - u_1v_3)\boldsymbol{e}_2 + (u_1v_2 - u_2v_1)\boldsymbol{e}_3$$

$$\boldsymbol{h} = \boldsymbol{u}\, x\, \boldsymbol{v} = \begin{Bmatrix} u_1 \\ u_2 \\ u_3 \end{Bmatrix} x \begin{Bmatrix} v_1 \\ v_2 \\ v_3 \end{Bmatrix} = \begin{Bmatrix} u_2v_3 - u_3v_2 \\ u_3v_1 - u_1v_3 \\ u_1v_2 - u_2v_1 \end{Bmatrix} \begin{Bmatrix} \boldsymbol{e}_1 \\ \boldsymbol{e}_2 \\ \boldsymbol{e}_3 \end{Bmatrix} = \boldsymbol{e}_i\varepsilon_{ijk}u_jv_k$$

thus,

$$\boldsymbol{h} = \boldsymbol{u}\, x\, \boldsymbol{v} = h_i = \boldsymbol{e}_i\varepsilon_{ijk}u_jv_k \qquad (2.10)$$

from which the components of h_i are given by the following.

$$h_1 = u_2\, v_3 - u_3\, v_2$$

$$h_2 = u_3\, v_1 - u_1\, v_3$$

$$h_3 = u_1\, v_2 - u_2\, v_1$$

An important expression that relates the Kronecker delta and the alternating tensor is given below.

$$\varepsilon_{ijk}\varepsilon_{klm} = \delta_{il}\delta_{jm} - \delta_{im}\delta_{jl} \tag{2.11}$$

The del operator ∇ is given by the following.

$$\nabla = \boldsymbol{e}_1 \frac{\partial}{\partial x_1} + \boldsymbol{e}_2 \frac{\partial}{\partial x_2} + \boldsymbol{e}_3 \frac{\partial}{\partial x_3} \tag{2.12}$$

A gradient is given by the following.

$$grad\, f = \nabla f = \boldsymbol{e}_1 \frac{\partial f}{\partial x_1} + \boldsymbol{e}_2 \frac{\partial f}{\partial x_2} + \boldsymbol{e}_3 \frac{\partial f}{\partial x_3} \tag{2.13}$$

The above partial differentiation can also be expressed indicial notation as follows.

$$grad\, f = \nabla f = \boldsymbol{e}_i\, f_{,i} \tag{2.14}$$

As indicated above a comma in the subscript is used to indicate differentiation. As an example for a vector $\boldsymbol{u(x)}$ with components $u_i(x_1,x_2,x_3)$ the derivative can be presented in the following ways.

$$\frac{\partial u_i}{\partial x_j}(x_1, x_2, x_3) = u_{i,j} \tag{2.15}$$

The divergence of vector $\boldsymbol{u}$ is given,

$$div\, \boldsymbol{u} = \nabla.\boldsymbol{u} = u_{i,j} \tag{2.16}$$

The curl of vector $\boldsymbol{u}$ is given by,

$$curl\, \boldsymbol{u} = \nabla * \boldsymbol{u} = e_{ijk}\, u_{k,j} \tag{2.17}$$

The Laplace ∇^2 of a scalar field is given by the following.

$$div\, grad\, f = \nabla.\nabla f = \nabla^2 f = f_{,ii} \tag{2.18}$$

The Laplace of a vector field (Razdan and Ravichandran, 2022) is given by the following.

$$\nabla^2 \boldsymbol{u} = u_{i,jj}\, \boldsymbol{e}_i \tag{2.19}$$

Where,

$$u_{i,jj} = \frac{\partial^2 u_i}{\partial {x_j}^2} \qquad (for\ i,j = 1,2,3)$$

The following notations are used in elasticity,

x_i: coordinates of position vector $\boldsymbol{x}$

u_i: components of displacement vector $\boldsymbol{u}$

ε_{ij}: components of strain tensor $\boldsymbol{\varepsilon}$

τ_{ij}: components of stress tensor $\boldsymbol{\tau}$

The notations described above in this section are quite important as they are used extensively and interchangeably in this thesis.

2.2.3 1D wave in a taut string

Consider a string of length *L* that is subjected to deflection. The string deflection is a function of two variables namely time and distance. Let the deflection in the y-axis be given by *u(x,t)*. The wave equation that governs this vibration is derived by Chen et al. (2009). Consider a small element *PQ* of this string. *P* is at coordinates *P=P(x)* and *Q* is at coordinates *Q=Q(x+Δx)* in the x-axis (Figure 2.1.).

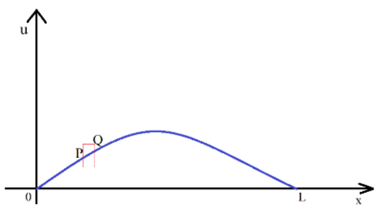

Figure 2. 1. Waves in a taut string subjected to tensile forces

Let the string be homogenous with linear density ρ (kg/m), perfectly elastic, does not resist bending, gravity on element is negligible, displacement in the x-axis is negligible compared to y-axis displacement. The vertical deflection in the $\boldsymbol{u}$ direction is small at all times hence slope θ of string is also small. The string is subjected to a tension T_1 at location P and T_2 at location Q. T_1 is inclined at angle α. T_2 is inclined at angle β (Figure 2.2.).

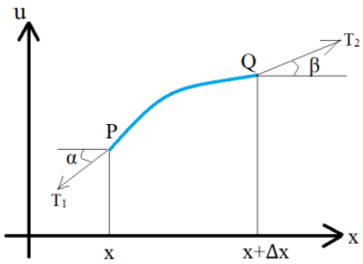

Figure 2. 2. An element PQ in a taut string subjected to tension forces

Balancing horizontal forces of the element. Sum of horizontal forces is zero,

$$T_1 \cos \alpha - T_2 \cos \beta = 0$$

$$T_1 \cos \alpha = T_2 \cos \beta \qquad (2.20)$$

For small angles,

$$\cos \alpha \approx \cos \beta \approx 1 \qquad (2.21)$$

hence,

$$T_1 \approx T_2 \approx T \qquad (2.22)$$

Balancing vertical forces of the element. Sum of vertical forces is zero,

$$T2 \sin \beta - T1 \sin \alpha - \rho \Delta x \frac{\partial^2 u}{\partial t^2} = 0$$

$$T2 \sin \beta - T1 \sin \alpha = \rho \Delta x \frac{\partial^2 u}{\partial t^2} \qquad (2.23)$$

Dividing through by T,

$$\frac{T2}{T} \sin \beta - \frac{T1}{T} \sin \alpha = \frac{\rho \Delta x}{T} \frac{\partial^2 u}{\partial t^2}$$

$$\frac{T2 \sin \beta}{T2 \cos \beta} - \frac{T1 \sin \alpha}{T1 \cos \alpha} = \frac{\rho \Delta x}{T} \frac{\partial^2 u}{\partial t^2}$$

$$\tan \beta - \tan \alpha = \frac{\rho \Delta x}{T} \frac{\partial^2 u}{\partial t^2} \qquad (2.24)$$

$$tan\,\beta \;=\left(\frac{\partial u}{\partial x}\right)_{x+\Delta x}$$

$$tan\,\alpha \;=\left(\frac{\partial u}{\partial x}\right)_{x}$$

$$\left(\frac{\partial u}{\partial x}\right)_{x+\Delta x}-\;\left(\frac{\partial u}{\partial x}\right)_{x}\;=\frac{\rho\Delta x}{T}\frac{\partial^2 u}{\partial t^2} \tag{2.25}$$

dividing through by Δx,

$$\frac{1}{\Delta x}\left(\frac{\partial u}{\partial x}\right)_{x+\Delta x}-\;\frac{1}{\Delta x}\left(\frac{\partial u}{\partial x}\right)_{x}\;=\frac{\rho}{T}\frac{\partial^2 u}{\partial t^2} \tag{2.26}$$

In the limit as Δx tends to zero,

$$\frac{\partial^2 u}{\partial x^2}\;=\frac{\rho}{T}\frac{\partial^2 u}{\partial t^2} \tag{2.27}$$

Or,

$$\frac{\partial^2 u}{\partial t^2}\;=\;\frac{T}{\rho}\;\frac{\partial^2 u}{\partial x^2}$$

Let,

$$\frac{T}{\rho}=\;c^2=\text{constant} \tag{2.28}$$

Finally, the wave equation in one-dimensional by Beranek and Mellow (2012) is obtained as,

$$\frac{\partial^2 u}{\partial x^2}\;=\frac{1}{c^2}\frac{\partial^2 u}{\partial t^2} \tag{2.29}$$

Or,

$$\frac{\partial^2 u}{\partial t^2}\;=\;c^2\;\frac{\partial^2 u}{\partial x^2} \tag{2.30}$$

This is a linear homogeneous second order partial differential equation.

Solving the One-dimensional Wave Equation

Consider an elastic string of density ρ (kg/m), length L (m), subjected to tension T (N). The interest here is to solve for the string vertical deflection u (in metres) which is a function of distance x (metres) from one end and time t (seconds) i.e. $u = u(x, t)$. Deflection in the y-axis is represented by the one-dimensional wave equation which is given by,

$$\frac{\partial^2 u}{\partial t^2} = c^2 \frac{\partial^2 u}{\partial x^2}$$

Where,

$$c = \sqrt{\frac{T}{\rho}}$$

Assume that the string is pin-jointed at the ends. Thus, the deflection is zero at both ends of the string. This yields the two boundary conditions (BCs) below,

At $x=0$,

$$u(x=0, t) = 0 \tag{2.31}$$

At $x=L$,

$$u(x=L, t) = 0 \tag{2.32}$$

The initial conditions (ICs) are also defined when time equals zero. Let the initial vertical position $\boldsymbol{u}$ at any given point x be some random function $f(x)$ at time $t=0$. A random function for the initial velocity in the vertical direction du/dt at time $t=0$ can be assigned as $g(x)$. Thus, the following two ICs are obtained,

$$u(x, t = 0) = f(x) \tag{2.33}$$

$$\frac{\partial}{\partial t} u(x, \ t = 0) = g(x) \tag{2.34}$$

The BCs and ICs can now be applied to solve the equation. There are different ways this can be achieved. One way is by separation of variables to yield ordinary differential equations (ODE) from the partial differential equation (PDE). BCs are used to solve the ODEs. The initial PDE problem is then solved using Fourier series analysis of the ODEs and the initial conditions.

Separation of variable assumes that displacement function $u(x,t)$ is a product of two separate functions namely distance function $F(x)$ and time function $G(t)$. Thus, the following relation is obtained,

$$u(x,t) = F(x) \ G(t) \tag{2.35}$$

The wave equation can be modified by replacing $u(x,t)$ with $F(x)$ and $G(t)$ in the original PDE equation. Here, F is a function of distance only whereas G is a function of time only. Differentiate *u(x,t)* twice with respect to time keeping distance constant to obtain the following equation,

$$\frac{\partial^2 u}{\partial t^2} = F(x)\ \frac{\partial^2 G(t)}{\partial t^2} = F(x)\ \ddot{G}(t) = F\ \ \ddot{G} \tag{2.36}$$

Differentiate *u(x,t)* twice with respect to distance keeping time constant to obtain the following equation,

$$\frac{\partial^2 u}{\partial x^2} = G(t)\ \ \frac{\partial^2 F(x)}{\partial x^2} = G(t)\ \ F''(x) = G\ \ F'' \tag{2.37}$$

These equations are then replaced in the original wave equation which was given by,

$$\frac{\partial^2 u}{\partial t^2} = \ c^2\ \frac{\partial^2 u}{\partial x^2}$$

And the wave equation transforms to,

$$F\ \ \ddot{G} = \ c^2\ G\ \ F'' \tag{2.38}$$

Separate time functions on one side and distance functions on the other. The wave equation transforms further to,

$$\frac{\ddot{G}}{G} = \ c^2\ \ \frac{F''}{F}$$

$$\frac{1}{c^2}\ \frac{\ddot{G}(t)}{G(t)} = \ \frac{F''(x)}{F(x)} \tag{2.39}$$

Thus, the variables have been separated so that one side is only a function of time whereas the other side is only a function of distance. Time and distance are independent of each other. The above equation equals to some constant value say *k*. Thus,

$$\frac{1}{c^2}\ \frac{\ddot{G}(t)}{G(t)} = \ \frac{F''(x)}{F(x)} = k$$

Thus,

$$\frac{1}{c^2}\ \frac{\ddot{G}(t)}{G(t)} = k \tag{2.40}$$

$$\frac{F''(x)}{F(x)} = k \tag{2.41}$$

Where *k* is the separation constant. The above can be rewritten as,

$$F''(x) - \ k\ F(x) = 0 \tag{2.42}$$

$$\ddot{G}(t) - \ k\ c^2\ G(t)\ = 0 \tag{2.43}$$

These are linear second order ODEs. Thus, two linear second order ODEs have been obtained from the one PDE. Now the boundary conditions can be applied to solve the two ODEs above. Recall the boundary conditions,

At $x=0$,

$$u(x=0, t) = 0$$

$$u(x,t) = F(x)\ G(t)$$

$$u(0,t) = F(0)\ G(t) = 0 \tag{2.44}$$

At $x=L$,

$$u(x=L, t) = 0$$

$$u(x,t) = F(x)\ G(t)$$

$$u(L,t) = F(L)\ G(t) = 0 \tag{2.45}$$

Thus, there are two equations to solve here,

$$F(0)\ G(t) = 0$$

$$F(L)\ G(t) = 0$$

For non-trivial solutions, $G(t)$ cannot be zero. Therefore,

$$F(0) = 0$$

$$F(L) = 0$$

Applying these conditions to the space ODE,

$$F''(x) - k\ F(x) = 0$$

From the theory of solving ordinary differential equations, for a non-trivial solution of the above ODE, then the constant k has to be negative. Let's say,

$$k=-p^2 \tag{2.46}$$

where p is an arbitrary constant as well. Thus, above equation becomes,

$$F''(x) + p^2\ F(x) = 0 \tag{2.47}$$

This type of ODE has solution of the form,

$$F(x) = A \cos(px) + B \sin(px) \tag{2.48}$$

Now the BCs are applied to find A and B.

At $x=0$,

$$F\,(x=0) = 0$$

$$F(x) = A\cos(px) + B\sin(px)$$

$$F(0) = A\cos(p.\,0) + B\sin(p.\,0) = 0$$

$$A=0 \tag{2.49}$$

At $x=L$,

$$F\,(x=L) = 0$$

$$F(x) = A\cos(px) + B\sin(px)$$

$$F(L) = 0\cos(pL) + B\sin(pL) = 0$$

$$B\sin(pL) = 0 \tag{2.50}$$

For non-trivial solution B cannot be zero. Thus,

$$\sin(pL) = 0 \tag{2.51}$$

$$pL = \pi,\ 2\pi,\ 3\pi,\ \ldots$$

$$pL = n\pi$$

$$p = \frac{n\pi}{L} \tag{2.52}$$

For $n=1, 2, 3, \ldots$

Replacing A and p in the equation,

$$F(x) = A\cos(px) + B\sin(px)$$

$$F(x) = 0\cos([n\pi/L]x) + B\sin([n\pi/L]x)$$

$$F(x) = B\sin\left(\frac{n\pi}{L}\right)x \tag{2.53}$$

Thus, the ODE

$$F''(x) + p^2\,F(x) = 0$$

Has solutions given by,

$$F_n(x) = B_n\sin\left(\frac{n\pi}{L}\right)x \tag{2.54}$$

For $n=1, 2, 3, \ldots$

Now to the second ODE which is a function of time.

$$\ddot{G}(t) - k\,c^2\,G(t) = 0$$

With initial conditions,

$$u(x, t = 0) = f(x)$$

$$\frac{\partial}{\partial t} u(x,\ t = 0) = g(x)$$

Also recall,

$$k = -p^2$$

$$p = \frac{n\pi}{L}$$

Thus,

$$\ddot{G}(t) - k\,c^2\,G(t) = 0$$

$$\ddot{G}(t) + \left(\frac{cn\pi}{L}\right)^2 G(t) = 0$$

Let,

$$\lambda_n = \frac{cn\pi}{L} \tag{2.55}$$

Thus,

$$\ddot{G}(t) + {\lambda_n}^2\,G(t) = 0 \tag{2.56}$$

Again, this is an ODE with solution of the form,

$$G(t) = A\cos(\lambda t) + D\sin(\lambda t)$$

$$G_n(t) = A_n \cos(\lambda_n t) + D_n \sin(\lambda_n t) \tag{2.57}$$

For $n=1, 2, 3, \ldots$

Now recall the separation of variables expression to solve the PDE,

$$u_n(x,t) = F_n(x)\ G_n(t)$$

After obtaining $F(x)$ and $G(t)$, the above can be replaced,

$$F_n(x) = B_n \sin\left(\frac{n\pi}{L}\right) x$$

$$G_n(t) = A_n \cos(\lambda_n t) + D_n \sin(\lambda_n t)$$

$$u_n(x,t) = F_n(x)\, G_n(t) = [\, B_n \sin\left(\frac{n\pi}{L}\right) x\,]\ [\, A_n \cos(\lambda_n t) + D_n \sin(\lambda_n t)\,]$$

$$u_n(x,t) = A_n B_n \sin\left(\frac{n\pi}{L}\right) x \cos(\lambda_n t) + B_n D_n \sin\left(\frac{n\pi}{L}\right) x \sin(\lambda_n t)$$

Where *A*, *B*, *D* are arbitrary constants. The above can be written as,

$$u_n(x,t) = A_n \sin\left(\frac{n\pi}{L}\right) x \cos(\lambda_n t) + B_n \sin\left(\frac{n\pi}{L}\right) x \sin(\lambda_n t)$$

Or,

$$u_n(x,t) = [A_n \cos(\lambda_n t) + B_n \sin(\lambda_n t)] \sin\left(\frac{n\pi}{L}\right) x \qquad (2.58)$$

With,

$$\lambda_n = \frac{cn\pi}{L} \qquad (2.59)$$

Being eigen values to the eigen functions,

$$u_n(x,t) = \left[A_n \cos\left(\frac{cn\pi}{L}\right) t + B_n \sin\left(\frac{cn\pi}{L}\right) t\right] \sin\left(\frac{n\pi}{L}\right) x$$

For $n=1, 2, 3, \ldots$

The initial conditions can be applied to solve the wave equation and to find *A* and *B* in the eigen function above. The initial conditions are,

$$u(x, t=0) = f(x)$$

$$\frac{\partial}{\partial t} u(x,\ t=0) = g(x)$$

Applying Fourier analysis the total solution can be given by,

$$u(x,t) = \sum_{n=1}^{\infty} u_n(x,t) = \sum_{n=1}^{\infty} \left[A_n \cos\left(\frac{cn\pi}{L}\right) t + B_n \sin\left(\frac{cn\pi}{L}\right) t\right] \sin\left(\frac{n\pi}{L}\right) x$$

Applying initial condition in position,

$$u(x, t=0) = f(x)$$

$$u(x,0) = \sum_{n=1}^{\infty} u_n(x,0) = \sum_{n=1}^{\infty} \left[A_n \cos\left(\frac{cn\pi}{L}\right) 0 + B_n \sin\left(\frac{cn\pi}{L}\right) 0\right] \sin\left(\frac{n\pi}{L}\right) x$$
$$= f(x)$$

$$\sum_{n=1}^{\infty} A_n \sin\left(\frac{n\pi}{L}\right) x = f(x) \qquad (2.60)$$

This is actually a Fourier series for a function of period L which is expanded as follows,

$$f(x) = \sum_{n=1}^{\infty} a_n \, sin\left(\frac{n\pi}{L}\right) x \tag{2.61}$$

where,

$$a_n = \frac{2}{L} \int_0^L f(x) \, sin\left(\frac{n\pi}{L} x\right) \, dx \tag{2.62}$$

n=1, 2, 3, …

Going back to the equation and applying the Fourier series analysis the coefficients A_n are obtained as,

$$\sum_{n=1}^{\infty} A_n \, sin\left(\frac{n\pi}{L}\right) x = f(x)$$

$$A_n = \frac{2}{L} \int_0^L f(x) \, sin\left(\frac{n\pi}{L} x\right) \, dx \tag{2.63}$$

Where *n=1, 2, 3, …*

Applying initial condition in velocity,

$$\frac{\partial}{\partial t} u(x, \;\; t = 0) = g(x)$$

$$u(x,t) = \sum_{n=1}^{\infty} u_n(x,t) = \sum_{n=1}^{\infty} \left[A_n \, cos\left(\frac{cn\pi}{L}\right) t + B_n \;\, sin\left(\frac{cn\pi}{L}\right) t\right] sin\left(\frac{n\pi}{L}\right) x$$

$$\frac{\partial u(x,t)}{\partial t} = \frac{\partial}{\partial t} \sum_{n=1}^{\infty} u_n(x,t)$$

$$= \frac{\partial}{\partial t} \sum_{n=1}^{\infty} \left[A_n \, cos\left(\frac{cn\pi}{L}\right) t + B_n \;\, sin\left(\frac{cn\pi}{L}\right) t\right] sin\left(\frac{n\pi}{L}\right) x = g(x)$$

$$\frac{\partial u(x,t)}{\partial t} = \frac{\partial}{\partial t} \sum_{n=1}^{\infty} u_n(x,t)$$

$$= \sum_{n=1}^{\infty} \left[-A_n \frac{cn\pi}{L} \, sin\left(\frac{cn\pi}{L}\right) t + B_n \frac{cn\pi}{L} \;\, cos\left(\frac{cn\pi}{L}\right) t\right] sin\left(\frac{n\pi}{L}\right) x$$

$$= g(x)$$

At *t=0*

$$\frac{\partial u(x,t)}{\partial t} = \sum_{n=1}^{\infty} \left[-A_n \frac{cn\pi}{L} \, sin\left(\frac{cn\pi}{L}\right)0 + B_n \frac{cn\pi}{L} \; cos\left(\frac{cn\pi}{L}\right)0\right] sin\left(\frac{n\pi}{L}\right)x$$

$$= g(x)$$

$$\frac{\partial u(x,t)}{\partial t} = \sum_{n=1}^{\infty} B_n \frac{cn\pi}{L} \, sin\left(\frac{n\pi}{L}\right)x \;\; = g(x) \qquad (2.64)$$

This again is a Fourier series for a function *g(x)* which when expanded gives us the coefficient B_n values as follows,

$$B_n \frac{cn\pi}{L} = \frac{2}{L} \int_0^L g(x) \, sin\left(\frac{n\pi}{L}x\right) \, dx \qquad (2.65)$$

Or,

$$B_n = \frac{2}{cn\pi} \int_0^L g(x) \, sin\left(\frac{n\pi}{L}x\right) \, dx \qquad (2.66)$$

Where $n=1, 2, 3, \ldots$

Thus, the solution to the wave equation,

$$\frac{\partial^2 u}{\partial t^2} = c^2 \frac{\partial^2 u}{\partial x^2}$$

is given by Beranek and Mellow (2012),

$$u(x,t) = \sum_{n=1}^{\infty} \left[A_n \, cos\left(\frac{cn\pi}{L}\right)t + B_n \; sin\left(\frac{cn\pi}{L}\right)t\right] sin\left(\frac{n\pi}{L}\right)x$$

$$A_n = \frac{2}{L} \int_0^L f(x) \, sin\left(\frac{n\pi}{L}x\right) \, dx$$

$$B_n = \frac{2}{cn\pi} \int_0^L g(x) \, sin\left(\frac{n\pi}{L}x\right) \, dx$$

With *f(x)* as the initial position and *g(x)* the initial velocity.

2.2.4 2D wave in a membrane

Consider a small element in a membrane with uniform density. The membrane is thin and perfectly flexible. A case is considered in which the membrane is fixed around its boundaries, the tension is uniform across the membrane surface, and that out of plane deflections are small (Articolo, 2009) (Figure 2.3.). Consider a small rectangular element of dimensions Δx by Δy subjected to uniform tension of magnitude T (Figure 2.4.).

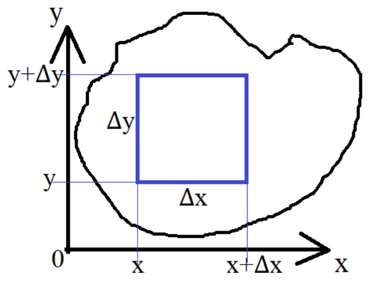

Figure 2. 3. Waves in a taut membrane subjected to tensile forces

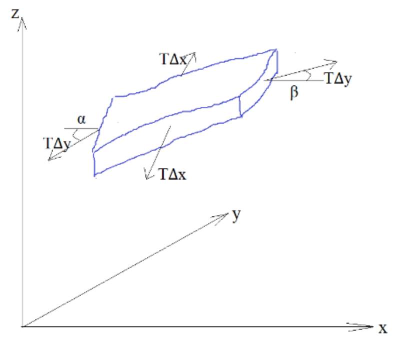

Figure 2. 4. An arbitrary element of a taut membrane subjected to tensile forces

Summing forces in the horizontal direction,

$$\sum F_{horizontal} = T\Delta y \cos\beta - T\Delta y \cos\alpha = 0 \tag{2.67}$$

Since for small angles,

$$\cos\beta \approx \cos\alpha \approx 1$$

Summing up forces in the vertical direction in the left-hand and right-hand side,

$$\sum F_{vertical\ LR} = T\Delta y \sin\beta - T\Delta y \sin\alpha \tag{2.68}$$

For small angles,

$$\sin\alpha \approx \alpha \approx \tan\alpha$$

$$\sin\beta \approx \beta \approx \tan\beta$$

Hence,

$$\sum F_{vertical\,LR} = T\Delta y\,[tan\,\beta - tan\,\alpha] \tag{2.69}$$

$$tan\,\beta = \left(\frac{\partial u}{\partial x}\right)_{\substack{x=x+\Delta x \\ y=y_1,\in[y,\ \ y+\Delta y]}} = u_x(x+\Delta x, y_1) \tag{2.70}$$

$$tan\,\alpha = \left(\frac{\partial u}{\partial x}\right)_{\substack{x=x \\ y=y_2,\in[y,\ \ y+\Delta y]}} = u_x(x, y_2) \tag{2.71}$$

$$\sum F_{vertical\,LR} = T\Delta y\,[u_x(x+\Delta x, y_1) - u_x(x, y_2)] \tag{2.72}$$

Summing up forces in the vertical direction in the front and back side,

$$\sum F_{vertical\,FB} = T\Delta x\,[sin\,\varphi - sin\,\theta]$$

$$\sum F_{vertical\,FB} = T\Delta x\,tan\,\varphi - T\Delta x\,tan\,\theta$$

$$tan\,\varphi = \left(\frac{\partial u}{\partial y}\right)_{\substack{x=x_1,\in[x+\Delta x, y] \\ y=y+\Delta y}} = u_y(x_1, y+\Delta y) \tag{2.73}$$

$$tan\,\theta = \left(\frac{\partial u}{\partial y}\right)_{\substack{x=x_2,\in[x, y] \\ y=y}} = u_y(x_2, y) \tag{2.74}$$

$$\sum F_{vertical\,FB} = T\Delta x\left[u_y(x_1, y+\Delta y) - u_y(x_2, y)\right] \tag{2.75}$$

Summing up total force in the vertical direction,

$$\sum F_{vertical} = \sum F_v = \sum F_{vertical\,LR} + \sum F_{vertical\,FB}$$

$$\sum F_v = T\Delta y\,[u_x(x+\Delta x,\ y_1) - u_x(x, y_2)] + T\Delta x\left[u_y(x_1, y+\Delta y) - u_y(x_2, y)\right] \tag{2.76}$$

Applying newtons second law of motion,

$$\sum F_{vertical} = ma_{vertical}$$

$$\sum F_v = \rho\,\Delta x\,\Delta y\,\frac{\partial^2 u}{\partial t^2} = T\Delta y\,[u_x(x+\Delta x, y_1) - u_x(x, y_2)] + T\Delta x\left[u_y(x_1, y+\Delta y) - u_y(x_2, y)\right] \tag{2.77}$$

$$\rho\,\Delta x\,\Delta y\,\frac{\partial^2 u}{\partial t^2} = T\Delta y\,[u_x(x+\Delta x, y_1) - u_x(x, y_2)] + T\Delta x\left[u_y(x_1, y+\Delta y) - u_y(x_2, y)\right] \tag{2.78}$$

Dividing through by,

$$\rho\, \Delta x\, \Delta y$$

$$\frac{\partial^2 u}{\partial t^2} = \frac{T}{\rho}\left[\frac{[u_x(x+\Delta x, y_1) - u_x(x, y_2)]}{\Delta x} + \frac{\left[u_y(x_1, y+\Delta y) - u_y(x_2, y)\right]}{\Delta y}\right]$$

$$\frac{\partial^2 u}{\partial t^2} = \frac{T}{\rho}\left[\frac{\partial^2 u}{\partial x^2} + \frac{\partial^2 u}{\partial y^2}\right] = \frac{T}{\rho}\left[u_{xx} + u_{yy}\right] = c^2\, \nabla^2 u \qquad (2.79)$$

Thus, the 2D wave equation becomes,

$$\frac{\partial^2 u}{\partial t^2} = c^2\, \nabla^2 u \qquad (2.80)$$

Or,

$$\frac{\partial^2 u}{\partial t^2} = c^2 \left(\frac{\partial^2 u}{\partial x^2} + \frac{\partial^2 u}{\partial y^2}\right) \qquad (2.81)$$

Or,

$$\frac{\partial^2 u}{\partial x^2} + \frac{\partial^2 u}{\partial y^2} = \frac{1}{c^2}\frac{\partial^2 u}{\partial t^2} \qquad (2.82)$$

Where,

$$c^2 = \frac{T}{\rho} \qquad (2.83)$$

$$c = \sqrt{\frac{T}{\rho}} = \text{some constant}$$

Where,

ρ = area density (kg/m^2)

Solving the two-dimensional wave equation

The goal here is to find the solution to the 2D wave equation given the boundary and initial conditions. The 2D wave equation is given by,

$$\frac{\partial^2 u}{\partial t^2} = c^2\, \nabla^2 u$$

or

$$\frac{\partial^2 u}{\partial t^2} = c^2 \left[\frac{\partial^2 u}{\partial x^2} + \frac{\partial^2 u}{\partial y^2}\right]$$

Imposing the boundary condition that displacement is zero at the boundaries for all *x* and *y*,

$$u(x,y,t) = 0$$

Imposing initial conditions at time *t=0*, the displacement is some function *f(x,y)* whereas the velocity is some function *g(x,y)*.

Thus,

Displacement:

$$u(x,y,t=0)=f(x,y)$$

Velocity:

$$u_t(x,y,t=0)=g(x,y)$$

Consider a small rectangular area of the membrane with dimensions *a* by *b* (Figure 2.5.).

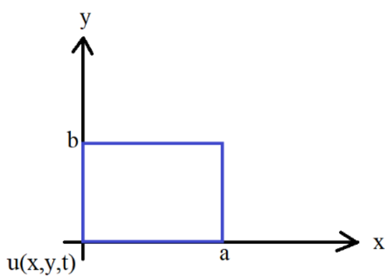

Figure 2. 5. A rectangular element of a taut membrane subjected to tensile forces

The equation is solved by separation of variables method. In this case there are three variables namely *x, y* and *t*. Thus, the variables have to be separated twice. Next, the eigenfunctions u_{mn} that satisfy the stated boundary conditions have to be obtained. Finally, the total solution of the 2D wave equation is obtained by application of Fourier analysis and the stated initial conditions. First, the space variables *(x,y)* is separated from the time variable *(t)*,

$$u(x,y,t) = F(x,y)\,G(t) \tag{2.84}$$

$$\frac{d^2u}{dt^2} = F\,\frac{d^2G}{dt^2} = F\ddot{G} \tag{2.85}$$

$$\frac{d^2u}{dx^2} = G\,\frac{d^2F}{dx^2} = GF_{xx} \tag{2.86}$$

$$\frac{d^2u}{dy^2} = G\ \frac{d^2F}{dy^2} = GF_{yy} \tag{2.87}$$

Second, the *x* variable is separated from the *y* variables,

$$F(x,y) = H(x)\ Q(y) \tag{2.88}$$

Substituting the first separation of variables into the 2D wave equation gives,

$$\frac{1}{c^2}\frac{\partial^2 u}{\partial t^2} = \left[\frac{\partial^2 u}{\partial x^2} + \frac{\partial^2 u}{\partial y^2}\right] = \left[u_{xx} + u_{yy}\right]$$

$$\frac{1}{c^2}F\ddot{G} = \left[GF_{xx} + GF_{yy}\right]$$

$$\frac{1}{c^2}\frac{\ddot{G}}{G} = \frac{1}{F}\left(F_{xx} + F_{yy}\right) \tag{2.89}$$

The left-hand side is a function of time only while the right-hand side is a function of space only. This must equal some constant value since time and space are independent of each other. Let the constant be some random value say $-\mu^2$. Thus,

$$\frac{\ddot{G}}{c^2G} = \frac{1}{F}\left(F_{xx} + F_{yy}\right) = -\mu^2$$

Considering the time side of the equation,

$$\frac{\ddot{G}}{c^2G} = -\mu^2 \tag{2.90}$$

$$\ddot{G} + \mu^2c^2G = 0$$

Let,

$$\lambda=\mu c \tag{2.91}$$

this yields,

$$\ddot{G} + \lambda^2G = 0 \tag{2.92}$$

This is a second order linear ordinary differential equation.

Considering the space side of the equation,

$$\frac{1}{F}\left(F_{xx} + F_{yy}\right) = -\mu^2$$

$$F_{xx} + F_{yy} + \mu^2\ F = 0 \tag{2.93}$$

This is the two-dimensional partial differential equation (Helmholtz equation).

Next step is to separate the variables a second time on the Helmholtz equation,

$$F(x,y) = H(x)\,Q(y)$$

$$\frac{d^2F}{dx^2} = Q\,\frac{d^2H}{dx^2}$$

$$\frac{d^2F}{dy^2} = H\,\frac{d^2Q}{dy^2} \tag{2.94}$$

Substituting above in the Helmholtz equation yields,

$$F_{xx} + F_{yy} + \mu^2 F = 0$$

$$Q\,\frac{d^2H}{dx^2} + H\,\frac{d^2Q}{dy^2} + \mu^2 HQ = 0$$

$$\frac{1}{H}\,\frac{d^2H}{dx^2} + \frac{1}{Q}\,\frac{d^2Q}{dy^2} + \mu^2 = 0$$

$$\frac{1}{H}\,\frac{d^2H}{dx^2} = -\left(\frac{1}{Q}\,\frac{d^2Q}{dy^2} + \mu^2\right) = -\frac{1}{Q}\left(\frac{d^2Q}{dy^2} + \mu^2 Q\right) \tag{2.95}$$

One side is a function of *x* only while the other is a function of *y* only. *x* and *y* are independent of each. This equation must equal some constant value say $-k^2$.

$$\frac{1}{H}\,\frac{d^2H}{dx^2} = -\,\frac{1}{Q}\left(\frac{d^2Q}{dy^2} + \mu^2 Q\right) = -k^2 \tag{2.96}$$

Considering the *x* variable equation,

$$\frac{1}{H}\,\frac{d^2H}{dx^2} = -k^2$$

$$\frac{d^2H}{dx^2} + k^2 H = 0 \tag{2.97}$$

Considering the *y* variable equation,

$$-\,\frac{1}{Q}\left(\frac{d^2Q}{dy^2} + \mu^2 Q\right) = -k^2$$

$$\frac{d^2Q}{dy^2} + \mu^2 Q - k^2 Q = 0$$

$$\frac{d^2Q}{dy^2} + (\mu^2 - k^2)Q = 0$$

$$\frac{d^2Q}{dy^2} + p^2 Q = 0 \tag{2.98}$$

Where,

$$p^2 = \mu^2 - k^2 \tag{2.99}$$

Thus, the PDE,

$$\frac{\partial^2 u}{\partial t^2} = c^2 \left[\frac{\partial^2 u}{\partial x^2} + \frac{\partial^2 u}{\partial y^2}\right] \tag{2.100}$$

Has been reduced to three ODEs,

$$\ddot{G} + \lambda^2 G = 0$$

$$\frac{d^2 H}{dx^2} + k^2 H = 0$$

$$\frac{d^2 Q}{dy^2} + p^2 Q = 0 \tag{2.101}$$

Where,

$$c^2 = \frac{T}{\rho}$$

$$\lambda^2 = \mu^2 c^2$$

$$p^2 = \mu^2 - k^2 \tag{2.102}$$

Applying boundary conditions,

u(x,y,t) = 0 for all *x* and *y* at the boundaries.

u(x,y,t) = F(x,y) G(t) = 0

For non-trivial solution *G(t)* cannot be zero thus,

$$F(x,y) = 0$$

For variable *x* equation,

$$\frac{d^2 H(x)}{dx^2} + k^2 H(x) = 0$$

$$H(x) = A \cos kx + B \sin kx \tag{2.103}$$

For variable *y* equation,

$$\frac{d^2 Q(y)}{dy^2} + p^2 Q(y) = 0$$

$$Q(y) = C \cos py + D \sin py \tag{2.104}$$

Now at all boundaries,

$$F(x,y) = H(x)\, Q(y) = 0 \tag{2.105}$$

At the left-hand side,

$$F(x=0,y) = H(x=0)\, Q(y) = 0 \tag{2.106}$$

For non-trivial solution $Q(y)$ cannot be zero at this point hence,

$$H(0) = 0 \tag{2.107}$$

At the right-hand side,

$$F(x{=}a,y) = H(x{=}a)\, Q(y) = 0 \tag{2.108}$$

Again, here for $Q(y)$ cannot be zero for non-trivial solution hence,

$$H(a) = 0 \tag{2.109}$$

Bottom,

$$F(x,y{=}0) = H(x)\, Q(y{=}0) = 0$$

$$Q(0) = 0 \tag{2.110}$$

Top,

$$F(x,y{=}b) = H(x)\, Q(y{=}b) = 0$$

$$Q(b) = 0 \tag{2.111}$$

These four boundary conditions are applied to evaluate the variables in the two solutions,

$$H(x) = A \cos kx + B \sin kx$$

$$Q(y) = C \cos py + D \sin py$$

$$H(0) = 0$$

$$H(a) = 0$$

$$Q(0) = 0$$

$$Q(b) = 0$$

$$H(0) = A \cos k(0) + B \sin k(0) = 0$$

$$A = 0$$

$$H(x) = B \sin k(x)$$

$$H(a) = B \sin k(a) = 0 \tag{2.112}$$

B cannot be zero hence,

$$\sin ka = 0$$

$$ka = m\pi,$$

$$k = \frac{m\pi}{a}$$

$$H_m(x) = B_m \sin\frac{m\pi}{a}x \tag{2.113}$$

Where $m=1,2,3,\ldots$

$$Q(0) = C\cos p(0) + D\sin p(0) = 0$$

$$C = 0$$

$$Q(y) = D\sin py$$

$$Q(b) = D\sin pb$$

$$\sin pb = 0$$

$$pb = n\pi,$$

$$p = \frac{n\pi}{b}$$

$$Q_n(y) = D_n \sin\frac{n\pi}{b}\,y \tag{2.114}$$

Where $n=1,2,3,\ldots$

Now going back to the equation,

$$F_{mn}(x,y) = H(x)\,Q(y) = \left(B_m \sin\frac{m\pi}{a}x\right)\left(D_n \sin\frac{n\pi}{b}y\right)$$

Since B and D are arbitrary constants,

Let $\Gamma=BD$

$$F_{mn}(x,y) = \Gamma\left(\sin\frac{m\pi}{a}x\right)\left(\sin\frac{n\pi}{b}y\right) \tag{2.115}$$

Where $m,n=1,2,3,\ldots$

Going back to the Helmholtz equation,

$$F_{xx} + F_{yy} + \mu^2 F = 0$$

$$\frac{\partial^2}{\partial x^2}\left[\Gamma \sin\left(\frac{m\pi}{a}x\right)\sin\left(\frac{n\pi}{b}y\right)\right] + \frac{\partial^2}{\partial y^2}\left[\Gamma \sin\left(\frac{m\pi}{a}x\right)\sin\left(\frac{n\pi}{b}y\right)\right]$$
$$+ \mu^2\left[\Gamma \sin\left(\frac{m\pi}{a}x\right)\sin\left(\frac{n\pi}{b}y\right)\right] = 0$$

$$-\left(\frac{m\pi}{a}\right)^2\left[\Gamma\,sin\,\left(\frac{m\pi}{a}x\right)sin\,\left(\frac{n\pi}{b}y\right)\right]-\left(\frac{n\pi}{b}\right)^2\left[\Gamma\,sin\left(\frac{m\pi}{a}x\right)sin\,\left(\frac{n\pi}{b}y\right)\right]$$
$$+\ \mu^2\left[\Gamma\,sin\left(\frac{m\pi}{a}x\right)sin\,\left(\frac{n\pi}{b}y\right)\right]=\ 0$$

$$\left[\Gamma\,sin\,\left(\frac{m\pi}{a}x\right)sin\,\left(\frac{n\pi}{b}y\right)\right]\left[-\left(\frac{m\pi}{a}\right)^2-\left(\frac{n\pi}{b}\right)^2+\ \mu^2\right]=0 \qquad (2.116)$$

For non-trivial solution the first part of the equation cannot be zero thus,

$$-\left(\frac{m\pi}{a}\right)^2-\left(\frac{n\pi}{b}\right)^2+\ \mu^2=0$$

$$\mu^2=\left(\frac{m\pi}{a}\right)^2+\left(\frac{n\pi}{b}\right)^2 \qquad (2.117)$$

Going back to the final ODE which was a function of time,

$$\ddot{G}(t)+\ \lambda^2 G(t)=0$$

$$\lambda^2\ =\ \mu^2 c^2$$

$$\lambda\ =\ \mu c$$

$$p^2=\ \mu^2-\ k^2$$

$$\mu^2=\ k^2+p^2$$

$$\mu=\ \sqrt{k^2+p^2} \qquad (2.118)$$

The solutions for *k* and *p* are given by,

$$k\ =\frac{m\pi}{a}$$

$$p\ =\frac{n\pi}{b}$$

$$\mu=\ \sqrt{\left(\frac{m\pi}{a}\right)^2+\left(\frac{n\pi}{b}\right)^2}$$

$$\lambda\ =\ \mu c=c\pi\left[\sqrt{\left(\frac{m}{a}\right)^2+\left(\frac{n}{b}\right)^2}\right]$$

$$\lambda_{mn}\ =c\pi\left[\sqrt{\left(\frac{m}{a}\right)^2+\left(\frac{n}{b}\right)^2}\right] \qquad (2.119)$$

Where *m,n = 1,2,3*, …

now the equation,

$$\ddot{G}(t) + \lambda^2 G(t) = 0 \tag{2.120}$$

Has solution of the form,

$$G(t) = A\cos(\lambda t) + D\sin(\lambda t)$$

$$G_{mn}(t) = A_{mn}\cos(\lambda_{mn}t) + D_{mn}\sin(\lambda_{mn}t) \tag{2.121}$$

With,

$$\lambda_{mn} = c\pi\left[\sqrt{\left(\frac{m}{a}\right)^2 + \left(\frac{n}{b}\right)^2}\right] \tag{2.122}$$

m,n=1,2,3, …

these are eigenvalues.

Going back to the original 2D PDE,

$$\frac{\partial^2 u}{\partial t^2} = c^2\left[\frac{\partial^2 u}{\partial x^2} + \frac{\partial^2 u}{\partial y^2}\right]$$

$$c = \sqrt{\frac{T}{\rho}}$$

$$u(x,y,t) = F(x,y)\,G(t)$$

$$u_{mn}(x,y,t) = F_{mn}(x,y)G_{mn}(t)$$

$$F_{mn}(x,y) = \Gamma\sin\left(\frac{m\pi}{a}x\right)\sin\left(\frac{n\pi}{b}y\right)$$

$$G_{mn}(t) = A_{mn}\cos(\lambda_{mn}t) + D_{mn}\sin(\lambda_{mn}t)$$

$$u_{mn}(x,y,t) = \left[\Gamma\sin\left(\frac{m\pi}{a}x\right)\sin\left(\frac{n\pi}{b}y\right)\right][A_{mn}\cos(\lambda_{mn}t) + D_{mn}\sin(\lambda_{mn}t)]$$

$$u_{mn}(x,y,t) = \left[\sin\left(\frac{m\pi}{a}x\right)\sin\left(\frac{n\pi}{b}y\right)\right][A_{mn}\Gamma\cos(\lambda_{mn}t) + D_{mn}\Gamma\sin(\lambda_{mn}t)] \tag{2.123}$$

Since *A*, *D* and *Γ* are arbitrary constants so any product is just another constant hence,

$$u_{mn}(x,y,t) = [A_{mn}\cos(\lambda_{mn}t) + D_{mn}\sin(\lambda_{mn}t)]\left[\sin\left(\frac{m\pi}{a}x\right)\sin\left(\frac{n\pi}{b}y\right)\right] \tag{2.124}$$

This is an eigenfunction.

The final solution for 2D wave equation is composed,

$$\frac{\partial^2 u}{\partial t^2} = c^2 \left[\frac{\partial^2 u}{\partial x^2} + \frac{\partial^2 u}{\partial y^2}\right] \tag{2.125}$$

Applying Fourier analysis,

$$u_{mn}(x,y,t) = F_{mn}(x,y)G_{mn}(t)$$

$$u(x,y,t) = \sum_{m=1}^{\infty}\sum_{n=1}^{\infty} u_{mn}(x,y,t)$$

$$u(x,y,t) = \sum_{m=1}^{\infty}\sum_{n=1}^{\infty}\begin{bmatrix} A_{mn}\cos(\lambda_{mn}t) \\ + D_{mn}\, sin\,(\lambda_{mn}t)\end{bmatrix}\left[\, sin\left(\frac{m\pi}{a}x\right)\, sin\left(\frac{n\pi}{b}y\right)\right] \tag{2.126}$$

With initial conditions:

Initial displacement is given by,

$$u(x,y,t=0)=f(x,y) \tag{2.127}$$

Initial velocity is given by,

$$u_t(x,y,t=0)=g(x,y) \tag{2.128}$$

Applying initial position condition,

$$u(x,y,t=0)=f(x,y)$$

$$u(x,y,0) = f(x,y)$$
$$= \sum_{m=1}^{\infty}\sum_{n=1}^{\infty}[A_{mn}\, cos\,(\lambda_{mn}0)$$
$$+\ D\, sin\,(\lambda_{mn}0)]\left[\, sin\left(\frac{m\pi}{a}x\right)\, sin\left(\frac{n\pi}{b}y\right)\right]$$

$$f(x,y) = \sum_{m=1}^{\infty}\sum_{n=1}^{\infty} A_{mn}\ sin\left(\frac{m\pi}{a}x\right)\ sin\left(\frac{n\pi}{b}y\right) \tag{2.129}$$

This is a double infinite series.

Let

$$K_m(y) = \sum_{n=1}^{\infty} A_{mn}\ sin\left(\frac{n\pi}{b}y\right) \tag{2.130}$$

This is a Fourier series with coefficients A_{mn},

$$A_{mn} = \frac{2}{b}\int_0^b K_m(y)\, sin\left(\frac{n\pi}{b}y\right)\, dy \tag{2.131}$$

$$f(x,y) = \sum_{m=1}^{\infty} K_m(y)\, sin\left(\frac{m\pi}{a}x\right) \tag{2.132}$$

This is a Fourier series with coefficients $K_m(y)$,

$$K_m(y) = \frac{2}{a}\int_0^a f(x,y)\, \sin\left(\frac{m\pi}{a}x\right) dx \tag{2.133}$$

Substituting $K_m(y)$ in A_{mn},

$$A_{mn} = \frac{2}{b}\int_0^b \left(\frac{2}{a}\int_0^a f(x,y)\, sin\left(\frac{m\pi}{a}x\right) dx\right) sin\left(\frac{n\pi}{b}y\right) dy$$

$$A_{mn} = \frac{4}{ab}\int_0^b \int_0^a f(x,y)\, sin\left(\frac{m\pi}{a}x\right)\, sin\left(\frac{n\pi}{b}y\right) dxdy \tag{2.134}$$

m,n=1,2,3, …

applying initial velocity condition,

$$u_t(x,y,t=0)=g(x,y)$$

$$u_{mn}(x,y,t) = [A_{mn}\, cos\,(\lambda_{mn}t) + D_{mn}\, sin\,(\lambda_{mn}t)]\left[sin\left(\frac{m\pi}{a}x\right)\, sin\left(\frac{n\pi}{b}y\right)\right]$$

$$\frac{\partial}{\partial t}\{u_{mn}(x,y,t)\} = \frac{\partial}{\partial t}\, [A_{mn}\, cos\,(\lambda_{mn}t) + D_{mn}\, sin\,(\lambda_{mn}t)]\left[sin\left(\frac{m\pi}{a}x\right)\, sin\left(\frac{n\pi}{b}y\right)\right]$$

$$\frac{\partial}{\partial t}\{u_{mn}(x,y,t)\} = [-\lambda_{mn}A_{mn}\, sin\,(\lambda_{mn}t) + \lambda_{mn}D_{mn}\, cos\,(\lambda_{mn}t)]\left[sin\left(\frac{m\pi}{a}x\right)\, sin\left(\frac{n\pi}{b}y\right)\right]$$

$$\frac{\partial}{\partial t}\{u_{mn}(x,y,t)\} = [D_{mn}\, cos\,(\lambda_{mn}t) - A_{mn}\, sin\,(\lambda_{mn}t)]\left[\lambda_{mn}\, sin\left(\frac{m\pi}{a}x\right)\, sin\left(\frac{n\pi}{b}y\right)\right]$$

At $t=0$,

$$u(x,y,0) = g(x,y)$$

$$g(x,y) = \left\{\sum_{m=1}^{\infty}\sum_{n=1}^{\infty}[D_{mn}\, cos\,(\lambda_{mn}0) - A_{mn}\, sin\,(\lambda_{mn}0)]\left[\lambda_{mn}\, sin\left(\frac{m\pi}{a}x\right)\, sin\left(\frac{n\pi}{b}y\right)\right]\right\}$$

$$g(x,y) = \sum_{m=1}^{\infty}\sum_{n=1}^{\infty} \lambda_{mn} D_{mn}\ sin\left(\frac{m\pi}{a}x\right)\ sin\left(\frac{n\pi}{b}y\right) \qquad (2.135)$$

This is same expression as previously with exception that

A_{mn}

Is replaced by

$\lambda_{mn} D_{mn}$

Thus, the coefficients D_{mn} is given by,

$$D_{mn} = \frac{4}{ab\lambda_{mn}} \int_0^b \int_0^a g(x,y)\ sin\left(\frac{m\pi}{a}x\right)\ sin\left(\frac{n\pi}{b}y\right)\ dxdy \qquad (2.136)$$

m,n=1,2,3, …

Thus, for a rectangle membrane fixed at the boundaries with dimensions $x=a$ and $y=b$, the solution to the 2D wave equation,

$$\frac{\partial^2 u}{\partial t^2} = c^2\ \left[\frac{\partial^2 u}{\partial x^2} + \frac{\partial^2 u}{\partial y^2}\right]$$

is given by (Beranek & Mellow, 2012),

$$u(x,y,t) = \sum_{m=1}^{\infty}\sum_{n=1}^{\infty}[A_{mn}\ cos\ (\lambda_{mn}t) + D_{mn}\ sin\ (\lambda_{mn}t)]\left[\ sin\left(\frac{m\pi}{a}x\right)\ sin\left(\frac{n\pi}{b}y\right)\right] \qquad (2.137)$$

With coefficients,

$$A_{mn} = \frac{4}{ab} \int_0^b \int_0^a f(x,y)\ sin\left(\frac{m\pi}{a}x\right)\ sin\left(\frac{n\pi}{b}y\right)\ dxdy \qquad (2.138)$$

And,

$$D_{mn} = \frac{4}{ab\lambda_{mn}} \int_0^b \int_0^a g(x,y)\ sin\left(\frac{m\pi}{a}x\right)\ sin\left(\frac{n\pi}{b}y\right)\ dxdy \qquad (2.139)$$

Where,

m,n=1,2,3, …

2.2.5 3D wave in an elastic solid

Consider a cube subjected to the loads f_x, f_y, and f_z in the x, y and z axes respectively (Miklowitz, 1984). The resulting stresses on the faces of the cube are shown in Figure 2.6.

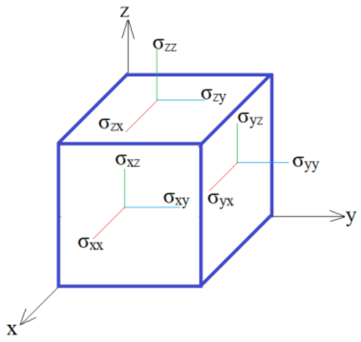

Figure 2. 6. A cube element subjected to stresses at the faces

Application of Newton's second law summing forces in the faces of the 3D element yields the equations of motion given by,

$$\sigma_{ij,j} + \rho f_i = \rho \ddot{u}_i \tag{2.140}$$

or

$$\frac{\partial \sigma_{ij}}{\partial x_j} + \rho f_i = \rho \frac{\partial^2 u_i}{\partial t^2} \tag{2.141}$$

Where,

i=1,2,3

For linear elastic material,

$$\sigma_{ij} = E_{ijkl}\varepsilon_{kl} \tag{2.142}$$

Strain displacement equations are given by,

$$\varepsilon_{ij} = \frac{1}{2}\left(u_{i,j} + u_{j,i}\right) \tag{2.143}$$

Or

$$\varepsilon_{ij} = \frac{1}{2}\left(\frac{\partial u_i}{\partial x_j} + \frac{\partial u_j}{\partial x_i}\right) \tag{2.144}$$

Constitutive equations for isotropic material are given by,

$$\sigma_{ij} = \lambda\varepsilon_{kk}\delta_{ij} + 2\mu\varepsilon_{ij} \tag{2.145}$$

Where,

$$\varepsilon_{kk} = \frac{\partial u_k}{\partial x_k} = \text{dilatation}$$

$$\delta_{ij} = \begin{cases} 1 & \text{for } i = j \\ 0 & \text{for } i \neq j \end{cases} = \text{Kronecker delta} \tag{2.146}$$

Replacing above to eliminate stress and strain yields the elastic dynamic equations in a homogeneous isotropic medium,

$$\rho\frac{\partial^2 u_i}{\partial t^2} = \partial_j\left[\lambda\delta_{ij}\partial_k u_k + \mu\left(\partial_i u_j + \partial_j u_i\right)\right] + \rho\, f_i$$

$$\rho\frac{\partial^2 u_i}{\partial t^2} = \partial_i\lambda\partial_k u_k + \lambda\partial_i\partial_k u_k + \partial_j\mu\left(\partial_i u_j + \partial_j u_i\right) + \mu\partial_j\partial_i u_j + \mu\partial_j\partial_j u_i\ + \rho\, f_i$$

$$\rho\frac{\partial^2 u_i}{\partial t^2} = \partial_i\lambda\partial_k u_k + \partial_j\mu\left(\partial_i u_j + \partial_j u_i\right) + \lambda\partial_i\partial_k u_k + \mu\partial_i\partial_j u_j + \mu\partial_j\partial_j u_i\ + \rho\, f_i$$

$$\rho\ddot{\boldsymbol{u}} = \nabla\lambda(\nabla.\mathbf{u}) + \nabla\mu.\left[\nabla\mathbf{u} + (\nabla\mathbf{u})^T\right] + (\lambda+\mu)\nabla\nabla.\mathbf{u} + \mu\nabla^2\mathbf{u}\ \ + \rho\, f_i \tag{2.147}$$

Using the identity,

$$\nabla\times\nabla\times\mathbf{u} = \nabla\nabla.\mathbf{u} - \nabla^2\mathbf{u}$$

$$\nabla^2\mathbf{u}\ = \nabla\nabla.\mathbf{u} - \nabla\times\nabla\times\mathbf{u} \tag{2.148}$$

Substituting in the equation,

$$\rho\ddot{\boldsymbol{u}} = \nabla\lambda(\nabla.\mathbf{u}) + \nabla\mu.\left[\nabla\mathbf{u} + (\nabla\mathbf{u})^T\right] + (\lambda+2\mu)\nabla\nabla.\mathbf{u} - \mu\nabla\times\nabla\times\mathbf{u}\ + \rho\, f_i \tag{2.149}$$

Ignoring gradient terms,

$$\rho\ddot{\boldsymbol{u}} = (\lambda+2\mu)\nabla\nabla.\mathbf{u} - \mu\nabla\times\nabla\times\mathbf{u}\ + \rho\, f_i \tag{2.150}$$

Or

$$\rho\ddot{\boldsymbol{u}} = (\lambda+\mu)\nabla\nabla.\mathbf{u} + \mu\nabla^2\mathbf{u}\ + \rho\, f_i$$

$$\rho\frac{\partial^2 u_i}{\partial t^2} = (\lambda+\mu)\frac{\partial^2 u_j}{\partial x_i\partial x_j} + \mu\frac{\partial^2 u_i}{\partial x_j\partial x_j}\ + \rho\, f_i \tag{2.151}$$

Which can be re-arranged as,

$$\mu \frac{\partial^2 u_i}{\partial x_j \partial x_j} + (\lambda + \mu) \frac{\partial^2 u_j}{\partial x_i \partial x_j} + \rho f_i = \rho \frac{\partial^2 u_i}{\partial t^2}$$

Or

$$\mu u_{i,jj} + (\lambda + \mu) u_{j,ji} + \rho f_i = \rho \ddot{u}_i \qquad (2.152)$$

Where,

$i=1,2,3$

$$\mu = \frac{E}{2(1+\upsilon)} = G = \text{shear modulus} \qquad (2.153)$$

$$\lambda = \frac{E\upsilon}{(1+\upsilon)(1-2\upsilon)} = \frac{2\mu\upsilon}{1-2\upsilon} = \text{Lame constant} \qquad (2.154)$$

E = Young's modulus

υ = Poisson's ratio

u_i = displacement in direction x_i,

f_i = body forces in direction x_i,

ρ = density

υ = Poisson's ratio

The above compressed equation represents the following three equations.

$$\mu \nabla^2 u_1 + (\lambda + \mu) \frac{\partial}{\partial x_1}\left(\frac{\partial u_1}{\partial x_1} + \frac{\partial u_2}{\partial x_2} + \frac{\partial u_3}{\partial x_3}\right) + \rho f_x = \rho \frac{\partial^2 u_1}{\partial t^2}$$

$$\mu \nabla^2 u_2 + (\lambda + \mu) \frac{\partial}{\partial x_2}\left(\frac{\partial u_1}{\partial x_1} + \frac{\partial u_2}{\partial x_2} + \frac{\partial u_3}{\partial x_3}\right) + \rho f_y = \rho \frac{\partial^2 u_2}{\partial t^2}$$

$$\mu \nabla^2 u_3 + (\lambda + \mu) \frac{\partial}{\partial x_3}\left(\frac{\partial u_1}{\partial x_1} + \frac{\partial u_2}{\partial x_2} + \frac{\partial u_3}{\partial x_3}\right) + \rho f_z = \rho \frac{\partial^2 u_3}{\partial t^2} \qquad (2.155)$$

Where,

$$\nabla^2 = \frac{\partial^2}{\partial {x_1}^2} + \frac{\partial^2}{\partial {x_2}^2} + \frac{\partial^2}{\partial {x_3}^2} \qquad (2.156)$$

In the case where $f_i=0$, i.e. no body forces,

$$\mu u_{i,jj} + (\lambda + \mu) u_{j,ji} = \rho \ddot{u}_i \qquad (2.157)$$

Or

$$\mu \nabla^2 u_1 + (\lambda+\mu) \frac{\partial}{\partial x_1}\left(\frac{\partial u_1}{\partial x_1} + \frac{\partial u_2}{\partial x_2} + \frac{\partial u_3}{\partial x_3}\right) = \rho \frac{\partial^2 u_1}{\partial t^2}$$

$$\mu \nabla^2 u_2 + (\lambda+\mu) \frac{\partial}{\partial x_2}\left(\frac{\partial u_1}{\partial x_1} + \frac{\partial u_2}{\partial x_2} + \frac{\partial u_3}{\partial x_3}\right) = \rho \frac{\partial^2 u_2}{\partial t^2}$$

$$\mu \nabla^2 u_3 + (\lambda+\mu) \frac{\partial}{\partial x_3}\left(\frac{\partial u_1}{\partial x_1} + \frac{\partial u_2}{\partial x_2} + \frac{\partial u_3}{\partial x_3}\right) = \rho \frac{\partial^2 u_3}{\partial t^2} \tag{2.158}$$

These equations can be expressed alternatively as follows as well,

$$\mu \nabla^2 u + (\lambda+\mu)\nabla\nabla.u = \rho \frac{\partial^2 u}{\partial t^2} \tag{2.159}$$

Where,

$$\nabla = i_1 \frac{\partial}{\partial x_1} + i_2 \frac{\partial}{\partial x_2} + i_3 \frac{\partial}{\partial x_3} \tag{2.160}$$

$$u = (u_1, u_2, u_3) \tag{2.161}$$

The same equation can be expressed alternatively as,

$$(\lambda + 2\mu)\nabla\nabla.u - \mu\nabla \times \nabla \times u = \rho \frac{\partial^2 u}{\partial t^2} \tag{2.162}$$

Where,

$$\nabla\nabla.u = \nabla \times \nabla \times u + \nabla^2 u \tag{2.163}$$

Where,

$$\nabla \times u = \begin{vmatrix} i_1 & i_2 & i_3 \\ \frac{\partial}{\partial x_1} & \frac{\partial}{\partial x_2} & \frac{\partial}{\partial x_3} \\ u_1 & u_2 & u_3 \end{vmatrix} \tag{2.164}$$

Dividing through by density gives the equation in terms of wave velocities (Achenbach, 1999) as,

$$\frac{(\lambda+2\mu)}{\rho}\nabla\nabla.u - \frac{\mu}{\rho}\nabla \times \nabla \times u = \frac{\partial^2 u}{\partial t^2}$$

$$\alpha^2 \nabla\nabla.\mathbf{u} - \beta^2 \nabla \times \nabla \times \mathbf{u} = \ddot{\boldsymbol{u}} \tag{2.165}$$

Where,

$$\alpha^2 = \frac{\lambda+2\mu}{\rho} = {C_L}^2 \tag{2.166}$$

$$\beta^2 = \frac{\mu}{\rho} = {C_T}^2 \tag{2.167}$$

α=C_L = longitudinal wave velocity

β=C_T = shear wave velocity

The equation can also be expressed as follows,

$$(\lambda + \mu)\nabla\nabla . u + \ \mu \, \nabla^2 \, u = \ \rho \, \frac{\partial^2 u}{\partial t^2}$$

$$(\lambda + \mu)\nabla\nabla . (\nabla\phi + \nabla x\psi) + \mu\nabla^2(\nabla\phi + \nabla x\psi) \ = \ \rho\left(\nabla\frac{\partial^2\phi}{\partial t^2} + \ \nabla x\frac{\partial^2\psi}{\partial t^2}\right) \tag{2.168}$$

Where,

$$u = \ \nabla\phi + \nabla x\psi \tag{2.169}$$

$$\nabla . \psi = 0 \tag{2.170}$$

ϕ is scalar potential. ψ is vector potential.

Another way of writing the wave motion equation in terms of scalar and vector components is as follows,

$$\left[(\lambda + 2\mu)\nabla\nabla . (\nabla\phi) - \rho \, \nabla\frac{\partial^2\phi}{\partial t^2}\right] - \mu\nabla \times \nabla \times \nabla\phi + (\lambda + \mu)\nabla\nabla . \nabla \times \psi$$

$$+\left[\mu\nabla^2\nabla \times \psi - \rho\nabla \times \frac{\partial^2\psi}{\partial t^2}\right] = 0$$

$$\nabla\left[(\lambda + 2\mu)\nabla^2\phi - \rho \, \frac{\partial^2\phi}{\partial t^2}\right] + \nabla \times \left[\mu\nabla^2\psi - \rho\frac{\partial^2\psi}{\partial t^2}\right] = 0 \tag{2.171}$$

Where,

$$\nabla . \nabla\phi = \nabla^2\phi$$

$$\nabla \times \nabla \times \nabla\phi = 0$$

$$\nabla . \psi = 0 \tag{2.172}$$

This equation is satisfied if each term equals zero. Thus, the following solutions is obtained. The first part give rise to longitudinal/pressure modes,

$$(\lambda + 2\mu)\nabla^2\phi = \rho \, \frac{\partial^2\phi}{\partial t^2}$$

$$\nabla^2\phi = \frac{\rho}{\lambda+2\mu}\frac{\partial^2\phi}{\partial t^2}$$

$$\nabla^2\phi = \frac{1}{{C_L}^2}\frac{\partial^2\phi}{\partial t^2} \tag{2.173}$$

Where,

$${C_L}^2 = \frac{\lambda+2\mu}{\rho}$$

C_L is longitudinal wave propagation velocity.

The second part give rise to transverse/shear modes,

$$\mu\nabla^2\psi = \rho\frac{\partial^2\psi}{\partial t^2}$$

$$\nabla^2\psi = \frac{\rho}{\mu}\frac{\partial^2\psi}{\partial t^2}$$

$$\nabla^2\psi = \frac{1}{{C_T}^2}\frac{\partial^2\psi}{\partial t^2} \tag{2.174}$$

Where,

$${C_T}^2 = \frac{\mu}{\rho}$$

C_T is shear wave propagation velocity.

The solutions of the above equations are given by the following.

$$\nabla^2\phi = \frac{1}{{C_L}^2}\frac{\partial^2\phi}{\partial t^2}$$

$$\phi = [A\sin px + B\cos px]e^{i(kx-wt)} \tag{2.175}$$

where,

$$p^2 = \frac{w^2}{{C_L}^2} - k^2$$

$k = \frac{2\pi}{\lambda} =$ wavenumber

ω = circular frequency

λ = wavelength

$$\nabla^2\psi = \frac{1}{{C_T}^2}\frac{\partial^2\psi}{\partial t^2}$$

$$\psi = [C\sin qx + D\cos qx]e^{i(kx-wt)} \tag{2.176}$$

Where,

$$q^2 = \frac{w^2}{c_T{}^2} - k^2$$

The constants *A, B, C* and *D* are determined from boundary conditions.

Waves in a plate

Consider a plate that is *2h* thick. The applicable boundary conditions here are,

Surface displacement,

$$u(x,t)=u_0(x,t) \tag{2.177}$$

Surface traction,

$$t_i=\sigma_{ji}n_j \tag{2.178}$$

There are various methods that can be used to deal with the problem. One such solution is by the displacement potential method (Achenbach, 1999). For plane strains, displacements in the various directions are given by the following,

$$u_1 = \frac{\partial\phi}{\partial x_1} - \frac{\partial\psi}{\partial x_3}$$

$$u_2 = 0$$

$$u_3 = \frac{\partial\phi}{\partial x_3} + \frac{\partial\psi}{\partial x_1} \tag{2.179}$$

Stress tensors components are given by the following.

$$\sigma_{31} = \mu\left[\frac{\partial u_3}{\partial x_1} + \frac{\partial u_1}{\partial x_3}\right]$$

$$\sigma_{33} = \lambda\left[\frac{\partial u_1}{\partial x_1} + \frac{\partial u_3}{\partial x_3}\right] + 2\mu\frac{\partial u_3}{\partial x_3} \tag{2.180}$$

Replacing u_1 and u_3 in above equations gives,

$$\sigma_{31} = \mu\left[\frac{\partial u_3}{\partial x_1} + \frac{\partial u_1}{\partial x_3}\right]$$

$$\sigma_{33} = \lambda\left[\frac{\partial u_1}{\partial x_1} + \frac{\partial u_3}{\partial x_3}\right] + 2\mu\frac{\partial u_3}{\partial x_3} \tag{2.181}$$

The boundary conditions for plane strain case is given by,

$$u(x,t) = u_0(x,t)$$

$$t_i = \sigma_{ij} n_j$$

$$\sigma_{31} = \sigma_{33} = 0 \text{ for } x_3 = \pm d/2 = \pm h \tag{2.182}$$

Thus, the general lamb wave equation is obtained as follows.

$$\frac{tan(qh)}{tan(ph)} = \frac{-4k^2 pq\mu}{(\lambda k^2 + \lambda p^2 + 2\mu p^2)\,(k^2 - q^2)} \tag{2.183}$$

The above equation can be separated in two to yield symmetric modes and anti-symmetric modes given below (Rose, 2007).

For the symmetric mode the equation is given by,

$$\frac{tan(qh)}{tan(ph)} = \frac{-4k^2 pq}{(k^2 - q^2)^2} \tag{2.184}$$

For the anti-symmetric mode the equation is given by,

$$\frac{tan(qh)}{tan(ph)} = \frac{(k^2 - q^2)^2}{-4k^2 pq} \tag{2.185}$$

Where:

$$p^2 = \frac{\omega^2}{V_L^2} - k^2 \tag{2.186}$$

$$q^2 = \frac{\omega^2}{V_S^2} - k^2 \tag{2.187}$$

The above equations are often solved numerically in practice. Some of the numerical techniques include finite difference method, boundary element method, finite element method, and finite volume method. The procedures, advantages and limitations of the different numerical methods are well covered in literature and are beyond the scope of this thesis. In this research commercial software based on the finite element method was used as by Nobrega et al. (2016); Rajagopal et al. (2012); Zheng et al. (2011).

2.2.6 Interaction of waves with defects

Ultrasonic waves are extensively applied in medical and industrial diagnostics (Kundu, 2014; Lowe and Cawley, 2006; Pavlakovic and Calwley, 1999; Periyannan and

Balasubramaniam, 2016; Ray et al., 2017; Rose, 1995, 2014; Shah et al., 2017; Staszewski et al., 2009). This capability arises as a consequence of the scattering phenomena caused by fluctuations in acoustic impedance within a medium (Beniwal and Ganguli, 2015; Dobson et al., 2017; Michaels et al., 2011; van Pamel et al., 2016). When sound waves come across such a disruption, they undergo partial transmission, reflection, and diffraction (Leinov et al., 2016; Qi et al., 2015). Processed signals from scattered waves are utilized to extract information about obstacle features like dimensions, form, and depth, crucial for nondestructive testing.

In dealing with wave propagation in solids problems, reflections at discontinuities are fundamental. When a propagating wave encounters a discontinuity such as a boundary between two materials, the wave is partially transmitted while a proportion is reflected back (Figure 2.7.). Consider incidence of a longitudinal wave of amplitude I with a plane wavefront approaching an interface between two media having different mechanical properties. The differences in properties result in different wave velocities in the two media.

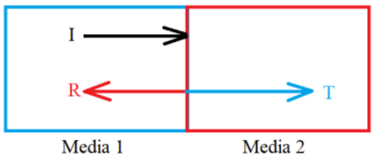

Figure 2. 7. Wave reflection and transmission at an interface between two mediums

Media 1,

$$k_1 = \frac{\omega}{c_{L1}} \tag{2.188}$$

Where, c_L is longitudinal wave velocity.

Media 2,

$$k_2 = \frac{\omega}{c_{L2}} \tag{2.189}$$

$$u^I(x,t) = I\ e^{i(k_1 x + \omega t)}$$

$$u^R(x,t) = R\ e^{i(-k_1 x + \omega t)}$$

$$u^T(x,t) = T\ e^{i(k_2 x + \omega t)} \tag{2.190}$$

It occurs that energy is partially reflected backward, and partially transmitted. The relative properties of the two media determine the amplitude of the reflected and transmitted waves. The relative amplitudes are determined by applying continuity conditions at the interface. In a longitudinal wave with a plane wavefront, the particle displacement is in the parallel direction whereas stresses are generated in the perpendicular direction,

$$\sigma_{xx}(x,t) = (\lambda + 2\mu)\frac{\partial u}{\partial x} = ik(\lambda + 2\mu)\, u(x,t) \tag{2.191}$$

Setting up continuity,

$$I\, e^{i(k_1 x+\omega t)} - R\, e^{i(-k_1 x+\omega t)} = T\, e^{i(k_2 x+\omega t)} \tag{2.192}$$

And equilibrium conditions,

$$ik_1(\lambda_1 + 2\mu_1)Ie^{i(k_1 x+\omega t)} + ik_1(\lambda_1 + 2\mu_1)Re^{i(-k_1 x+\omega t)}$$

$$= ik_2(\lambda_2 + 2\mu_2)Te^{i(k_2 x+\omega t)} \tag{2.193}$$

Recalling that,

$$c = \sqrt{\frac{\lambda+2\mu}{\rho}}$$

Two algebraic equations are obtained as,

$$I+R = T$$

$$\rho_1 c_{1L}\,(I - R) = \rho_2 c_{2L}\, T \tag{2.194}$$

In these equations I is known because it is the incident wave amplitude. The reflected wave amplitude R and transmitted wave amplitude T are determined from the system of equations. R and T can be given in terms of material density and velocity. The solution of the above equations gives the reflected and transmitted wave amplitudes,

$$\frac{R}{I} = \frac{\rho_1 c_{L1} - 2\rho_2 c_{L2}}{\rho_1 c_{L1} + \rho_2 c_{L2}}$$

$$\frac{T}{I} = \frac{2\rho_1 c_{L1}}{\rho_1 c_{L1} + \rho_1 C_{L2}} \tag{2.195}$$

R and T is a function of the ratio r between acoustic impedances ρc, which, in turn, depend on the material properties,

$$r = \frac{\rho_2 c_{L2}}{\rho_1 c_{L1}}$$

$$\frac{R}{I} = \frac{1-r}{1+r}$$

$$\frac{T}{I} = \frac{2}{1+r} \tag{2.196}$$

If the second material has the same properties of the first one *(r=1)*, no reflection occurs and all of the wave is transmitted. If the first material is stiffer and /or heavier than the second *(r<1)*, the wave is partially transmitted and reflected. If the second material is stiffer and or heavier than the first *(r>1)*, the whole wave will be reflected and there is no transmission because *T* tends to zero for *r* going to infinity. The value of *T* can be greater than one *(T>1)*. At the interface between two materials with mechanical properties that differ much from each other, concentrations of stress may occur. This may cause debonding between layers. The calculations fit perfectly if the conservation of energy is checked. Conservation of energy may be evaluated if the rate of work done by internal forces per unit area normal to the directions of propagation is calculated,

$$\sigma^R u^R + \sigma^T u^T = \sigma^I u^I \tag{2.197}$$

A value of one is obtained,

$$\left(\frac{1-r}{1+r}\right)^2 + r\left(\frac{2}{1+r}\right)^2 = 1 \tag{2.198}$$

The presence of defects in a component creates a condition of discontinuity. There is an interface between the defect edges and the parent material leading to a change in acoustic impedance. Numerous investigations have been undertaken by researchers to simulate the interactions between guided waves and irregularities such as cracks, holes, notches, variations in thickness, and bends (Beard, 2002; Dubois et al., 2013; Periyannan et al., 2016). Addressing the scattering problem of guided waves poses challenges due to the presence of numerous mode shapes dependent on both frequency and thickness, along with mode conversions upon interaction with discontinuities. This complexity contrasts with the more straightforward scenario of bulk waves, where only shear and longitudinal wave modes are present. Various approaches are accessible for solving guided elastic wave scattering problems, categorized into exact solutions, approximate analytical methods, or numerical methods.

There are different approaches towards finding exact solutions for guided ultrasonic wave scattering problems (Snieder, 2002). This is summarized here for completeness' sake. In this research solutions were based on approximation methods using finite element method discussed in the next section. The first approach in exact solutions involves the expansion of the wave mode equations into scalar and vector components (Castaings et al., 2002; Grahn, 2003; Lowe et al., 2002). This is similar to separating equations for longitudinal from transverse components for ease of solution. The second alternative approach is to divide the scattering field in two regions. The first region is the near-field closer to the defect while the second region is the far-field some distance away from the defect. The near-field can then be enlarged for finer details whereas the far-field outputs are averaged out (Wang and Ying, 2001; Wang et al., 2000). This saves on computational power in the sense that more resources can be dedicated and focused on regions that necessary. The third option for finding precise answers to the guided waves scattering problem combines the Green's function approach with the reciprocity theorem. Reciprocity theorems establish a connection between displacements, tractions, and body forces in a given medium under two different loading conditions (Auld, 1979; Bai et al., 2001; Tan and Auld, 1980). For instance, the effect of an excitation from an arbitrary point A on another point B can be used to predict other responses e.g. excitation on point B will have similar effect on point A. Consider an incident wave with power *P* striking a defect. Let the resulting displacement fields be given by *u* and stress fields be *T*. The surface parameter formalism produces the scattering coefficients for a mode *I* to be reflected or transmitted into a mode *R* as (Rajagopal and Lowe, 2008) as follows:

$$\delta S_{I,R} = \frac{i\omega}{4P}\int_{S_F}(u_{1R}\,.T_{2I} - u_{2I}\,.\,T_{1R})\,.\,\vec{n}dS \qquad (2.199)$$

For defects such as cracks in which normal tractions vanish the above equation reduces to,

$$\delta S_{I,R} = \frac{i\omega}{4P}\int_{S_C}\Delta u_{2I}\,.T_{1R}\,.\vec{n}dS \qquad (2.200)$$

Where,

Δu = crack opening displacement

Subscript 1 = no defect

Subscript 2 = defect present

The above surface parameter equation can be converted into a volume integral to yield,

$$\delta S_{I,R} = \frac{i\omega}{4P} \int_{V_F} \nabla \,.\, (u_{1R} \,.\, T_{2I} - u_{2I} \,.\, T_{1R}) \; dV$$

$$= \frac{i\omega}{4P} \int_{V_F} (\Delta\rho\omega^2 u_{1R} \,.\, u_{2I} + T_{2I} \colon \Delta s \colon T_{1R}) \; dV \tag{2.201}$$

Due to the challenges presented by the guided wave interactions, there are only a few problems that can be solved using exact methods. As a result, the study of guided wave scattering challenges has heavily relied on approximation analytical techniques (Pao and Mow, 1973). These analytical techniques include Kirchhoff approximation, Born approximation, and quasi-static approximation (Alleyne et al., 2015; Lowe et al., 1998). For majority of the more complicated real-world problems numerical approaches are more applicable. The finite element, finite difference, and boundary element methods are a few possible numerical techniques that may be helpful in solving the guided wave scattering problems (Diligent and Rose, 2002). Each of the aforementioned approaches has its own unique set of problems that have been extensively researched in the literature and solutions created to address them. One drawback of numerical approaches is that they frequently focus more on specific rather than generic outcomes. A semi-analytical-numerical hybrid approach can be utilized in addition to the analytical and numerical methods (Thakare et al., 2017). In this research commercial software based on the finite element method was used.

2.2.7 Finite element method

Finite element method (FEM) is a numerical method used to solve complex mathematical and engineering problems through approximations. FEM is applied in all real-life problems such as wave propagation, structural analysis, heat transfer, fluid flow, mass flow among many others. In FEM, a complex engineering problem is broken down into a simple problem (called finite elements) which are much easier to solve. In this section one-dimensional problems are used to demonstrate the key procedures involved in finite element analysis. Detailed procedures can be obtained from literature by Reddy, (2006).

Finite element analysis of 1D problems

Consider a rod of density ρ, cross-sectional area *A*, length *L*, and elasticity modulus *E*. Let the rod be subjected to motion in the longitudinal direction. This problem can be represented by a one-dimensional (1D) partial differential equation (PDE) given by,

$$-\frac{\partial}{\partial x}\left(EA\frac{\partial u}{\partial x}\right)+\ \rho A\ \frac{\partial^2 u}{\partial t^2}=f(x,t) \tag{2.202}$$

To analyze this problem by finite element method, the rod is broken down into finite elements. Let each element be of length *h*. In Figure 2.8 four finite elements with five nodes are presented. This process is referred to as discretization. The number of elements can be increased as desired. The more the number of elements the smaller the error of approximation. If the bar is subjected to external tensile load *P*, there will be displacements u_i at each of the nodes 1, 2, 3, 4 and 5.

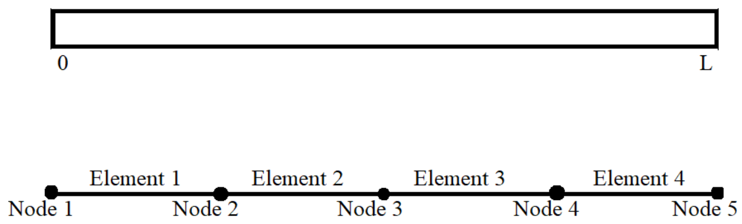

Figure 2. 8. Linear discretization of a rod

Instead of solving the entire rod at once, each of the elements is evaluated separately. The PDE is converted to what is referred to as its 'weak form' by introducing a function *w* on both sides of the equation and then integrating over each element. This is given by,

$$0=\int_{x_A}^{x_B} w\left[-\frac{\partial}{\partial x}\left(EA\frac{\partial u}{\partial x}\right)+\ \rho A\ \frac{\partial^2 u}{\partial t^2}-f\right]dx$$

$$= \int_{x_A}^{x_B} \left[\frac{\partial w}{\partial x} EA \frac{\partial u}{\partial x} + \rho A w \; \frac{\partial^2 u}{\partial t^2} - wf \right] dx + w \left[-EA \frac{\partial u}{\partial x} \right]_{x_A}^{x_B}$$

$$= \int_{x_A}^{x_B} \left(EA \frac{\partial w}{\partial x} \frac{\partial u}{\partial x} + \rho A w \; \frac{\partial^2 u}{\partial t^2} - wf \right) dx - EAw \frac{\partial u}{\partial x} \bigg|_{x_A} - EAw \frac{\partial u}{\partial x} \bigg|_{x_B}$$

(2.203)

Where,

x_A = left-hand node of a given element

x_B = right-hand node of a given element

The solution to above weak form equation can be approximated at any given time by the following (Idesman and Pham, 2014),

$$u(x, t_s) = \sum_{j=1}^{n} \left\{ u_j^e(t_s) \, \psi_j^e(x) \right\} = \sum_{j=1}^{n} \left\{ \left(u_j^s\right)^e \, \psi_j^e(x) \right\} \qquad (2.204)$$

Where,

s=1, 2, …

$\left(u_j^s\right)^e$ = value of $u(x, t)$ at time $t = t_s$ and node element Ω^e

Substitute,

$$w = \psi_j$$

$$\frac{dw}{dx} = \frac{d\psi_j}{dx}$$

$$u = \sum_{j=1}^{n} \left(\psi_j u_j\right)$$

$$\frac{du}{dx} = \sum_{j=1}^{n} \left(\frac{d\psi_j}{dx} u_j \right)$$

$$\frac{du}{dt} = \sum_{j=1}^{n} \left(\frac{du_j}{dt} \psi_j \right)$$

$$\frac{d^2u}{dt^2} = \sum_{j=1}^{n} \left(\frac{d^2 u_j}{dt^2} \psi_j \right) \qquad (2.205)$$

To get,

$$0 = \int_{x_A}^{x_B} \left(EA \frac{\partial \psi_i}{\partial x} \left(\sum_{j=1}^{n} \left(\frac{d\psi_j}{dx} u_j \right) \right) \; + \; \rho A \psi_i \left(\sum_{j=1}^{n} \left(\frac{d^2 u_j}{dt^2} \psi_j \right) \right) - \psi_i f \right) dx$$

$$- \; EA\psi_i \frac{\partial u}{\partial x}\bigg|_{x_A} \; - \; EA\psi_i \frac{\partial u}{\partial x}\bigg|_{x_B}$$

$$= \sum_{j=1}^{n} \left[K_{ij}^1 u_j + M_{ij}^2 \frac{d^2 u_j}{dt^2} \right] - F_i \tag{2.206}$$

In matrix form

$$[K]\{u\} + [M^2]\{\ddot{u}\} = \{F\} \tag{2.207}$$

Where,

$$K_{ij}^1 = \int_{x_A}^{x_B} EA \frac{\partial \psi_i}{\partial x} \frac{d\psi_j}{dx} dx$$

$$M_{ij}^2 = \int_{x_A}^{x_B} \rho A \psi_i \psi_j \, dx$$

$$F_i = \int_{x_A}^{x_B} \psi_i f \, dx \; + \; EA\psi_i \frac{\partial u}{\partial x}\bigg|_{x_A} \; + \; EA\psi_i \frac{\partial u}{\partial x}\bigg|_{x_B} \tag{2.208}$$

This is the semi discrete finite element formulation over an element. In general, the discretization of linear elastic wave problems yields ordinary differential equations in time of the form given below (Idesman and Pham, 2014).

$$[M]\ddot{U} + [C]\dot{U} + [K]U = F \tag{2.209}$$

M = mass

C = damping

K = stiffness

U = displacement

F = internal load

For simplicity the case of no viscosity (no damping) is considered,

$$C = 0$$

Thus, the discretization equation reduces to the same form as the rod example above,

$$[M]\ddot{U} + [K]U = F$$

An approximation method is then used to solve the above ODEs.

Linear approximation

For a linear approximation only the end nodes of each finite element are considered. The solution to the ODE equation is given by,

$$U^e = a + bx \tag{2.210}$$

The solution at each node is given by,

$$\psi_1 = u_1^e = a + bx_1$$

$$\psi_2 = u_2^e = a + bx_2 \tag{2.211}$$

Where subscript 1 refer to left-hand side node and subscript 2 is right-hand side node for a given element. The functions ψ_i are obtained by simply applying the conditions that the function ψ_i has a value of 1 at node *i* and a value of zero at all other nodes for each element. The constants *a* and *b* are solved by applying these boundary conditions. For the case of linear elements there are only two nodes per element.

To obtain ψ_1,

$$1 = a + bx_1$$

$$0 = a + bx_2 \tag{2.212}$$

In local coordinates

$$x_1 = 0$$

$$x_2 = h \tag{2.213}$$

Thus,

$$a = 1$$

$$b = -\frac{1}{h}$$

$$\psi_1 = a + bx = 1 - \frac{x}{h}$$

$$\psi_1 = 1 - \frac{x}{h} \tag{2.214}$$

To obtain ψ_2,

$$0 = a + bx_A$$

$$1 = a + bx_B \tag{2.215}$$

In local coordinates,

$$x_A = 0$$

$$x_B = h \tag{2.216}$$

Thus,

$$a = 0$$

$$b = \frac{1}{h}$$

$$\psi_2 = a + bx = 0 + \frac{x}{h}$$

$$\psi_2 = \frac{x}{h} \tag{2.217}$$

The linear finite element shape functions ψ_i have been obtained from above in local coordinate system as (Zheng et al., 2013),

$$\psi_1 = 1 - \frac{x}{h}$$

$$\psi_2 = \frac{x}{h} \tag{2.218}$$

The linear shape functions are represented schematically in Figure 2.9 below.

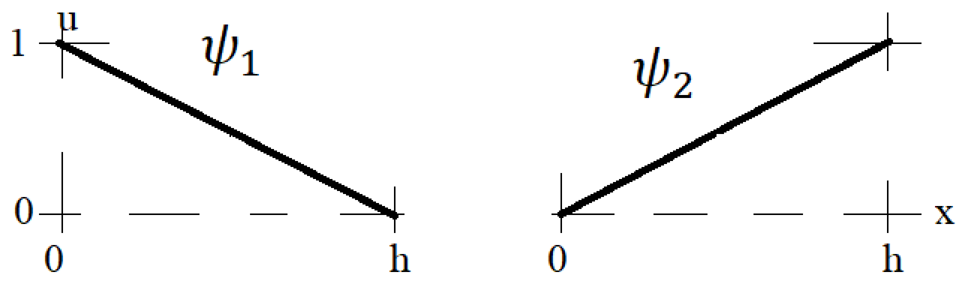

Figure 2. 9. Linear approximation shape functions

Quadratic approximation

The error in an approximation of the weak form solution can be minimized by reducing the element size h_e or by increasing the degree of approximation. The higher the polynomial the better the approximation solution in terms of approaching the exact value. However, higher order polynomials come with a price tag in terms of computational time. A compromise is often necessary with respect to the desired accuracy vis a viz available computational resource. Here we consider a quadratic approximation. For a quadratic approximation the end nodes of each finite element plus an additional point in between are considered. Thus, there are three nodes and the solution of the ODE (Reddy, 2006) is given by,

$$U^e = a + bx + cx^2 \tag{2.219}$$

The solution at each node is given by,

$$\psi_1 = u_1^e = a + bx_1^e + c(x_1^e)^2$$

$$\psi_2 = u_2^e = a + bx_2^e + c(x_2^e)^2$$

$$\psi_3 = u_3^e = a + bx_3^e + c(x_3^e)^2 \tag{2.220}$$

Where subscript 1 refer to left-hand side node, subscript 2 is the centre node and subscript 3 is the right-hand side node for a given element. The functions ψ_i are obtained by simply applying the boundary conditions that the function ψi has a value of 1 at node i and a value of zero at all other nodes for each element. The constants a, b, and c are solved by applying these boundary conditions. For the case of quadratic elements there are three nodes per element.

To obtain ψ_1,

$$1 = a + bx_1 + c{x_1}^2$$

$$0 = a + bx_2 + c{x_2}^2$$

$$0 = a + bx_3 + c{x_3}^2 \tag{2.221}$$

In local coordinates,

$$x_1 = 0$$

$$x_2 = \frac{h}{2}$$

$$x_3 = h \tag{2.222}$$

Thus,

$$a = 1$$

$$b = -\frac{3}{h}$$

$$c = \frac{2}{h^2}$$

$$\psi_1 = a + bx + cx^2 = 1 - \frac{3x}{h} + \frac{2x^2}{h^2}$$

$$\psi_1 = 1 - \frac{3x}{h} + \frac{2x^2}{h^2} = \left(1 - \frac{x}{h}\right)\left(1 - \frac{2x}{h}\right) \tag{2.223}$$

To obtain ψ_2,

$$0 = a + bx_1 + cx_1{}^2$$

$$1 = a + bx_2 + cx_2{}^2$$

$$0 = a + bx_3 + cx_3{}^2 \tag{2.224}$$

Thus,

$$a = 0$$

$$b = \frac{4}{h}$$

$$c = -\frac{4}{h^2}$$

$$\psi_2 = a + bx + cx^2 = 0 + \frac{4x}{h} - \frac{4x^2}{h^2}$$

$$\psi_2 = \frac{4x}{h} - \frac{4x^2}{h^2} = 4\ \frac{x}{h}\left(1 - \frac{x}{h}\right) \tag{2.225}$$

To obtain ψ_3,

$$0 = a + bx_1 + cx_1{}^2$$

$$0 = a + bx_2 + cx_2{}^2$$

$$1 = a + bx_3 + cx_3{}^2 \tag{2.226}$$

Thus,

$$a = 0$$

$$b = -\frac{1}{h}$$

$$c = \frac{2}{h^2}$$

$$\psi_3 = a + bx + cx^2 = 0 - \frac{x}{h} + \frac{2x^2}{h^2}$$

$$\psi_3 = -\frac{x}{h} + \frac{2x^2}{h^2} = -\frac{x}{h}\left(1 - \frac{2x}{h}\right) \tag{2.227}$$

The quadratic finite element shape functions ψ_i have been obtained from above in local coordinate system (Nagaraj and Maiaru, 2023) as follows:

$$\psi_1 = \left(1 - \frac{x}{h}\right)\left(1 - \frac{2x}{h}\right)$$

$$\psi_2 = 4\,\frac{x}{h}\left(1 - \frac{x}{h}\right)$$

$$\psi_3 = -\frac{x}{h}\left(1 - \frac{2x}{h}\right) \tag{2.228}$$

The quadratic shape functions are represented schematically in Figure 2.10 below.

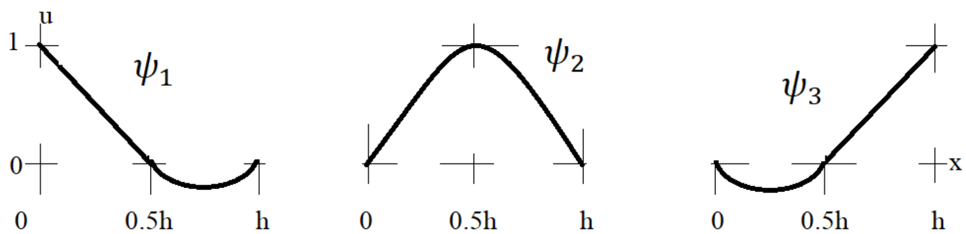

Figure 2. 10. Quadratic approximation shape functions

Lagrange approximation

The ODE can also be approximated by use of Lagrange shape functions (Luo, 2010) which are given by,

$$\psi_1 = \begin{cases} 1 - 2x & 0 \le x \le \frac{1}{2} \\ 0 & \frac{1}{2} \le x \le 1 \end{cases}$$

$$\psi_2 = \begin{cases} 2x & 0 \le x \le \frac{1}{2} \\ 2(1 - x) & \frac{1}{2} \le x \le 1 \end{cases}$$

$$\psi_3 = \begin{cases} 0 & 0 \le x \le \frac{1}{2} \\ 2x - 1 & \frac{1}{2} \le x \le 1 \end{cases} \tag{2.229}$$

The Lagrange shape functions are represented schematically in Figure 2.11 below.

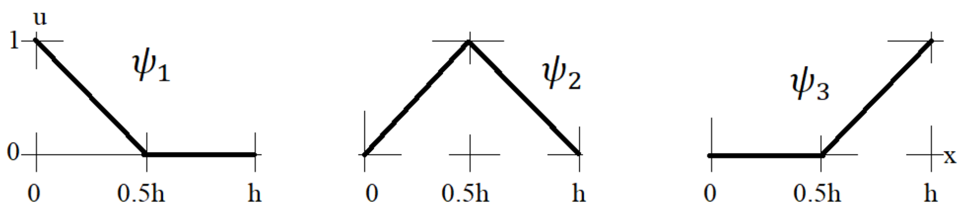

Figure 2. 11. Lagrange approximation shape functions

The shape functions ψ_i obtained above are then used to solve the weak forms of the equations under consideration.

Finite element analysis of 2D problems

The finite element analysis procedure for two dimensional (2D) problems is similar to the one-dimensional cases covered in detail above with slight modifications as indicated next (Drozdz, 2008).

The weak form is obtained by,

$$0 = \int w\,[f(x,y)]\,dx\,dy \tag{2.230}$$

The approximation is given by,

$$u(x,y) \approx U^e(x,y) = \sum_{j=1}^{n} u_j^e \psi_j^e(x,y) \tag{2.231}$$

Where the interpolation function has property,

$$\psi_j^e(x_j, y_j) = \delta_{ij} \tag{2.232}$$

A linear approximation solution can take the form,

$$U^e(x,y) = c_1 + c_2 x + c_3 y + c_4 xy \tag{2.233}$$

A quadratic approximation solution can take the form,

$$U^e(x,y) = c_1 + c_2 x + c_3 y + c_4 xy + c_5 x^2 + c_6 y^2 \tag{2.234}$$

Using the approximation methods presented above, the status of each of the elements in a model is evaluated at a given time. The time is then incremented and the new state is calculated. The finite elements can be analyzed either by explicit or implicit solvers. Each of these solvers have their advantages and limitations. The choice of the solver to use is dependent on the problem at hand. The difference between implicit and explicit solvers arises from the manner in which time is incremented in the respective algorithms.

Implicit analysis is generally used to solve static problems. In static equilibrium the net sum of forces equals zero. To evaluate the new status of the model, the coupled equations have to be solved afresh. The new status cannot be directly evaluated from the current status. Non-linear solutions such as algorithms based on Newton-Raphson iterative solution method are required (Pech et al., 2021). With each time increment, the set of equations have to be solved all over again. Thus, it is more costly in terms of computation time and is slower. Because equations have to be solved in each time increment the method is more accurate. The increment time can be large and varied at each step without any loss in accuracy. Implicit solvers are ideal for linear and slightly non-linear problems with large time increments (steady state problems) (Liu et al., 2020).

Explicit analysis is generally used to solve transient dynamic problems. In a dynamic equilibrium force is given by the product of mass and acceleration. The new status can be directly extrapolated from the current status. The information needed to evaluate the new state is readily available and straight forward from the current status. Thus, it is less costly in terms of computational time and is faster. Because the new status is obtained from a previous status, there is a chance of errors carried forward increasing with each time increment. In addition, since this is an extrapolation process, if the time increment is too large then the result error will be more. The increment time has to be kept small and constant in all steps to minimize on cumulative errors. Explicit solvers are ideal for extreme non-linear problems with small time increments (dynamic problems). Explicit solutions involve analysis of each of the respective nodes (Tian et al., 2020).

Both explicit and implicit time increment procedures calculate the model node acceleration and use the same to evaluate internal element forces. For an element of mass M subjected to an external force P, the internal element forces F and node acceleration d^2u/dt^2 are established. The equilibrium equation (Huang et al., 2019) is given by,

$$M\ddot{u} = P - F \tag{2.235}$$

At each increment Δt at time $t+\Delta t$ the above equilibrium equation should be satisfied. This involves several iterations to arrive at an acceptable value which is typically a chosen tolerance. The displacements are also calculated at each time interval. Implicit analysis involves solving a number of linear equations and the Newton's iterative solution method is used. The simultaneous equations solved at each iteration (Fang et al., 2019) is of the form:

$$K_j c_j = P_j - F_j - M_j \ddot{u}_j \tag{2.236}$$

Where,

K_j = stiffness matrix

c_j = corrections for each displacement increment

Commercial FEM software are used to solve problems in many engineering fields (Liang et al., 2020; Yuan et al., 2021). Some of the physical problems that can be modeled include elasticity, plasticity, ductility, fiber-reinforced composites, elastomers, damping, brittle cracking, viscosity, equations of state, hydrodynamics, conductivity, heat, conductivity, permittivity, permeability, piezoelectricity, acoustics, diffusivity, solubility, permeability, porosity, fluid leakage, among many others. Some of the analysis output that can be visualized include stresses, strain, pressure, beam forces, reactions and moments, mass flow rate, acoustic pressure, density, temperature, tensile, compressive and shear damages, displacements, velocity, acceleration, energy, fracture, volume, thickness, coordinates and energy. The loads and boundary conditions that can be applied include concentrated force, moment, pressure, shell edge load, surface traction, body force line load, gravity, connector force, volume acceleration, symmetry, displacement, rotation, velocity, acceleration, acoustic pressure and Eulerian boundary conditions (Huang et al., 2019). Each of these problems can be represented by an equation which can then be subjected to the finite element analysis procedures discussed in this section.

2.3 Non-destructive testing

Non-destructive testing (NDT) is a broad term that refers to different techniques used to evaluate the properties of materials, components, or systems without causing damage (Drewry and Georgiou, 2007; McCann and Forde, 2001). The primary goal of NDT is to inspect and examine the integrity, properties, and potential defects of materials or structures without altering their future usefulness or functionality. Estimating a component's or structure's remaining service life also uses NDT techniques. Without NDT it may have been impossible to safely operate nuclear power plants, aircrafts, ships, submarines, space crafts, space stations, bridges, pipelines, lifts, wire ropes, and many other engineering mega structures. Common NDT methods include radiography, ultrasonic testing, eddy current testing, dye penetrant testing and magnetic particle testing. In this section the general topic of NDT is presented. The idea is to have a wholistic overview of where guided wave testing comes in and the need for improved resolution. Understanding NDT techniques is important since they are not supplementary but are rather complementary to each other. For effective inspection it is generally important to deploy more than one technique at any given time. Each NDT method has unique strengths and weaknesses and therefore they complement each other and most inspections require more than one method. The NDT is often used in industrial applications where there are large objects which may contain toxic contents such as in nuclear power plants, petroleum industries and chemical industries to inspect tanks, pipelines and other structural components.

An example is the widely used NDT method for pipeline inspection called pigging. A robot that crawls inside the pipe is used. This is usually referred to as ‘pigging’, a term borrowed from the pig-like noise that the robots used to make when the technology was first introduced (Wright et al., 2019). The pigs are usually propelled by the product such as petroleum or it can be powered by a battery. Since the robots travel inside the pipe, the pipes that are buried underground do not need to be excavated. Excavation is done only at areas whereby a problem has been identified and detailed tests need to be carried out. These robots are usually attached with an appropriate technology such as digital cameras, ultrasonic sensors, eddy current probes, or magnetic flux detectors. The robot collects data on the condition of the entire pipe circumference as it moves inside. Thus, they are much safer, cheaper and faster. The challenge with the use of the robots is that they are designed for specific pipe diameters and configurations. Pipes with small diameters or varying cross sections cannot accommodate inspection by a robot. Also, presence of sharp bends, multiple branches, mechanical accessories, connections and other design features prohibits the use of a robot. Thus, a robot cannot inspect majority of pipes due to these design constraints.

The safety of nuclear power reactors depends on NDT. It is extremely cost-effective since it enables thorough and safe testing of crucial nuclear power plant (NPP) components without causing harm or other modifications to the plant. Some of these critical parts in a NPP include piping components, vessels, welds, nozzles, concrete, nuclear fuel elements, nuclear fuel assemblies and valves. The best NDT for NPP is based on online monitoring, non-contact and long range. Some challenges of concern include the detection of leakage, cracking, and wall thinning (Lee, 2016). The difficult operational conditions in an NPP include high temperatures, large pressure, extremely high radiation levels, thermal pressure, corrosion, and chemical interactions between the coolant, the shell, and the fissionable material. For the inspection of particular components, several NDT techniques work best. Ultrasonic techniques are best for evaluating the welded connections of the stopper plugs in the fuel elements, testing the shell of the fuel elements, and diagnosing the machinery used to make the fuel elements. Radiation methods are appropriate in testing welded connections of stopper plugs in fuel elements, equipment used to make fuel elements, reactor fuel elements, examination of fuel cores, measurement of fuel pellets' density and cover thickness (Martínez-Oña, 2021). Eddy current techniques are the best for determining the position of the fuel core and its characteristics for reactor fuel elements, as well as for checking for surface flaws. In nuclear power plants, pipelines that carry super-heated steam from the reactor heat exchangers to the turbines for power generation are usually in a highly radioactive environment. Any leakage from these pipes or failure of critical structures in the power plant may lead to a nuclear accident.

A wave is a disturbance in a medium that carries energy without any net movement of particles. The disturbance propagates in space and time often in a periodic pattern. Mathematically waves are described by partial differential equation (Lewis et al., 2022). The electromagnetic wave and the mechanical wave are two of the most prevalent wave types. Gamma rays, x-rays, visible light, infrared, ultraviolet radiation and radio waves are all examples of electromagnetic waves. Sound waves, seismic waves, gravity waves, surface waves, and string vibrations are all examples of mechanical waves. Sound waves are used for conversation between individuals. Seismic waves are responsible for the transmission of earth tremors from their point of origin to distant places which can range from few to many kilometres away. Mechanical waves require a medium (solid, liquid, or gas) to transmit, but electromagnetic waves can travel through a vacuum. This is one key distinction between the two types of waves. The study and understanding of electromagnetic and mechanical waves are wide and has led to tremendous applications in the modern civilization. An example is waves are utilized in biomedicine for diagnosis and therapy as well as in industry to examine the structural integrity of components. Therefore, development of NDT applications in industry have had a parallel development in biomedicine (Behnamfar et al., 2016). For example, ultrasonic testing is used in industry to check for defects in large volumes whereas the same ultrasonics is used in medicine to check the health status of a fetus in a pregnant mother among other applications. The different types of the waves mentioned above have found applications in NDT in addition to the other traditional applications such as communication.

Mechanical vibrations known as sound waves travel through a solid, liquid, or gaseous media. An acoustic wave with a frequency in the audible range is what can be heard by humans. The range of human hearing frequencies is 20 Hz to 20 kHz (Gerasimov and Bender, 2000). Infrasound and ultrasound are terms used to describe sound waves with frequencies below 20 Hz and above 20 kHz respectively. Acoustic emission testing and ultrasonic testing are the two main NDT methods making use of the sound waves. Acoustic emission testing involves positioning of sensors that only receive and detect sound generated when a defect such as a crack forms and grows. Typical frequency for acoustic emission testing is 100 kHz to 1 MHz (Solodov etal., 2021; Thiyagarajan, 2020). Ultrasonic testing on the other hand involves sending a wave into the material being inspected and analyzing the signals reflected back (pulse-echo mode) or transmitted through (pitch-catch mode), depending on the mode of operation.

Ultrasonic waves find many applications such as imaging of body organs in medicine, navigation for bats, and detection of invisible defects in NDT, among many other uses (Drozdz, 2008). They are used for detection of objects as well as measurement of distance. This is particularly useful in NDT whereby the interest is in detecting an invisible defect and determining the exact position of that defect for purpose of repair.

Ultrasonic waves can be categorized into two general types namely bulk ultrasonic and guided ultrasonic waves. The primary distinction is that guided waves need a structural boundary for propagation, but bulk ultrasonic waves move through an unbounded medium without any effect from boundaries (Hassan and Jones, 2012; Marcantonio et al., 2019; Masserey et al., 2014; Yang et al., 2018). The velocity of bulk waves is constant for a given material irrespective of frequency of operation and inspection is usually conducted at high frequencies of about 2 MHz – 20 MHz for dense, fine grain materials. Examples are metals, plastics and composites whereas less dense, coarse grain materials like wood, concrete and cement are inspected at lower frequencies of about 50 kHz – 500 kHz (Karaiskos et al., 2015; Masserey et al., 2014). Guided ultrasonic waves on the other hand are fundamentally different from bulk ultrasonic waves. They are bounded by boundaries of a wave guide and propagated over longer distances (Dongsheng et al., 2012; Lais et al., 2018). For guided waves the velocity is dispersive meaning that they vary with frequency as well as with material thickness. When compared to bulk waves, guided waves have a more complicated frequency selection process. The desired guided wave mode to be generated and the structure thickness both affect the selection of guided wave frequencies (Chan et al., 2015; Pavlopoulou et al., 2013; Ramdhas et al., 2015; Yu et al., 2019).

2.4 Guided waves

Guided ultrasonic waves testing (GUWs) is today a well-established non-destructive testing method. The technique is also known by different other names such as long-range ultrasonic testing (LRUT), ultrasonic guided waves (UGWs), guided wave testing (GWT) and guided wave ultrasonic testing (GWUT). They are used in many fields such as seismology and structure inspections (Leonard and Hinders, 2003). They enable the inspection of large areas and propagates over long distances from a single sensor location. The GUWs technique is commercially available for long range inspections in areas such as pipelines (Alleyne et al., 2001) and rail tracks (Wilcox et al., 2003).

Ultrasonic guided waves refer to elastic waves that travel within a waveguide, which can be any confined solid structure, such as rods, pipes, plates, and rails (Beard, 2002; Beard et al., 2003; Beniwal and Ganguli, 2015; Chimenti, 1997; Gresil et al., 2017; Hartman et al., 2010; Leinov et al., 2015; Lowe and Cawley, 2006; Park et al., 2007;

Shah et al., 2017; Sharma and Mukherjee, 2011). Guided waves emerge through the repeated reflection of bulk waves (longitudinal and shear waves) between the boundaries of the waveguide, resulting in their superposition.

Understanding guided ultrasonic waves was fundamental in order that the applications, strengths and weaknesses could be identified (Nakhli-Mahal et al., 2019). This was important in this research as it formed the basis of improving its resolution capability. Guided ultrasonic waves travel through materials in specific patterns, interacting with the structure and any defects or irregularities present. Their behavior is influenced by material properties, geometry, and the type of wave mode employed. By comprehending these wave patterns, it becomes possible to optimize various parameters, such as frequency, wave mode, and transducer design, to manipulate and improve resolution. Insight into the behavior of these waves helps in developing advanced signal processing techniques that can distinguish between different types of reflections or attenuations, ultimately leading to better resolution in detecting and characterizing defects within structures or materials.

Historically before the development of GUWs technique, tests used to be conducted using point-by-point techniques. These point-by-point methods include bulk ultrasonic wave thickness measurements and time of flight diffraction (Silk, 1984, 1987). However, with the breakthroughs in guided wave technology it became possible to achieve inspections from remote locations. Pioneering work in development of GUWs technique and subsequent capability improvements was done by the NDT research group at Imperial College London (ICL). Much research work and literature has been generated by the ICL group (Cawley, 2003; Cawley and Alleyne, 1996; Lowe et al., 1998; Wilcox et al., 2003). The method however did not replace the traditional point by point bulk ultrasonic inspection. Instead, GUWs technique is used as a screening tool to locate areas of generally excessive damage. These damaged areas would then be zeroed into by using point by point methods to quantify the damage in greater detail with greater precision than is possible with GUWs technique.

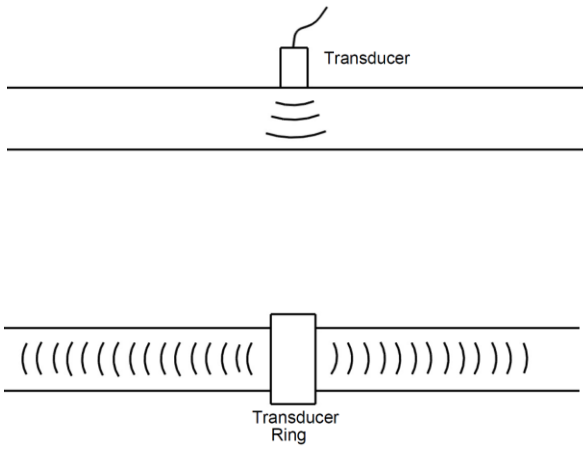

(a)

(b)

Figure 2. 12. Comparison between the size of area inspected when using bulk versus guided ultrasonic waves; (a) bulk ultrasonic waves cover the area just below the transducer, (b) guided ultrasonic waves cover entire thickness and length as indicated by the chevron marks in the images above

The GUWs technique is a long-range technique and is capable of inspecting beyond geometric features such as bends, supports, welds and other joints. Many studies have been conducted to understand interaction of guided waves with features such as edges, thickness changes and bends in both plates and pipes. The main focus is in the detection and location of defects. Studies have been done to investigate the interaction of guided waves with defects such as cracks, notches and drilled holes in both pipes and plates. One area in which GUWs technique find attractive applications is in structures that are coated or insulated. The coatings are generally attenuative and tend to reduce the range of guided wave propagation. As such many researches have been conducted to studying the interaction of guided waves with coatings (Alleyne et al., 2001; Duan et al., 2016; Jarvis et al., 2016).

The GUWs technique is currently used primarily as a screening tool to identify areas of excessive damage. Other secondary point to point contact methods is then deployed to do accurate defect sizing (Wilcox et al., 2003). However, structures are installed in such a manner that some areas cannot be readily accessed for secondary inspection. An example is a pipeline buried under a road or pipeline buried in concrete (Mahal et al., 2019). Under such conditions it may be extremely difficult to access such sections or the cost involved is prohibitive. Another challenge is that signals are always generated at locations of design features such as welds, elbows, supports and other joints. Should there be a defect next to these design features at distances shorter than $\lambda/2$, then the signals from the defects will be hidden inside the signals from the design features. This is where a test method is needed that can be mounted remotely in the accessible area after which a secondary inspection will not be needed.

So far, the GUWs technique is the only inspection method that can be used to inspect structures from a remote location. Its limitation however is in the resolution capability (Velichko and Wilcox, 2008) and therefore improving the current resolution capabilities of guided waves will do away with secondary point by point inspection techniques. Because of their ability to assess structures remotely, spanning distances of several metres, guided ultrasonic waves hold significant relevance for non-invasive imaging and material diagnostics. Guided waves are frequently used in biomedical diagnostics as well as for internal evaluations of composites and concrete, both during curing and during the operational lifetime of concrete buildings. Structure sensors also allow for remote monitoring in harsh environments like high temperatures and radiation, as well as the potential for micro- and nanoscale mediation.

In pipeline inspection, guided wave testing kit includes a probe ring, control instrument, a laptop, and the appropriate software. The probe ring comes in different sizes depending on pipe to be inspected. The ring is clamped onto the surface of pipe after minimal surface preparation. The waves are then sent simultaneously in the two opposite directions from the location where the sensor is mounted. These waves will travel tens of metres in each direction (Leinov et al., 2016). At obstacles, part of the wave energy is reflected back to the probe and the equipment is capable of analyzing the reflected waves from the two directions separately. These reflectors are generally cross-sectional changes such as welds, corrosion and defects. Knowing the velocity of the waves (mode) and the time taken for the wave to be reflected back it is possible to determine the exact location of the reflector. The extent of defect is estimated by the amplitude of the reflected signal. Circumferential dimensions of the reflector are estimated by means of a focusing mechanism. There are three modes of guided waves propagation in pipes namely longitudinal, torsional and flexural modes (Mahal et al., 2019). Figure 2.13 shows a typical guided wave inspection setup. With this setup hundreds of metres can be inspected in both directions from a single sensor location. This enables inspection of areas that are not possible to access.

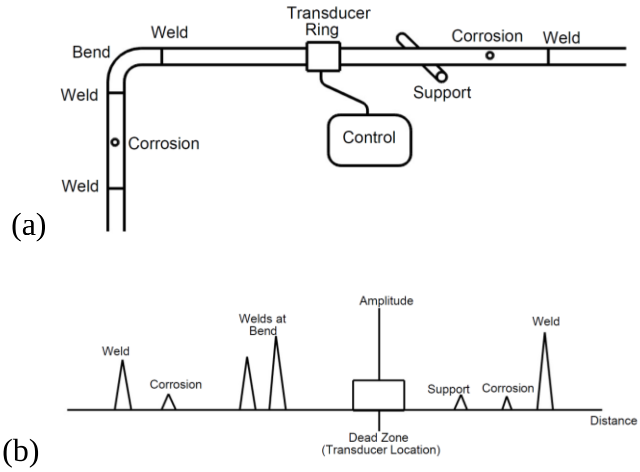

Figure 2. 13. Guided waves in a pipeline; (a) layout with various reflectors, (b) signals received from the different reflectors

The resolution of any system has a fundamental maximum as a result of diffraction. Ernst Abbe demonstrated in 1873 that light with wavelength λ when it travels in a material with refractive index *n* and converges to a point with half angle *θ*, will produce a spot with radius *d* given by (Lauterbach, 2012),

$$d = \frac{\lambda}{2n \sin\theta} \tag{2.237}$$

The Abbe limit is approximately between λ/2 and λ/3 for any kind of wave. Figure 2.14 shows the concept of resolution for two features close to each other. In a well resolved image the two features can be clearly seen separately. When the features are not resolved the image will appear as if there was just one feature.

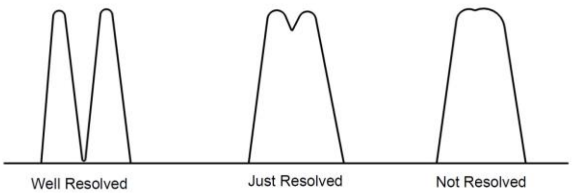

Figure 2. 14. Images for well-resolved, just-resolved and not-resolved features

Resolution of defects by conventional ultrasonic methods is limited by diffraction and the limit is quoted as $\lambda/2$ in most literature. Features separated by less than $\lambda/2$ (where λ is wavelength) cannot be resolved (Zhang and Liu, 2008). This means that two defects close together separated by less than $\lambda/2$ spacing cannot be differentiated and will appear as one flaw. Due to low frequencies used in guided waves, λ is typically in the range of tens to hundreds of millimetres. This means that $\lambda/2$ is large hence resolution of defects is very poor.

Resolution can be improved by increasing the frequency of the interrogating waves as this reduces the wavelength hence the absolute diffraction limit (Li and Chu, 2013). There are challenges associated with operating at high frequencies in GUWs testing. First the range of the waves is significantly reduced and this leads to the loss of long-range advantages of guided waves. Secondly is that guided waves are dispersive meaning that velocity of propagation varies with frequency. Additionally, at high frequencies guided waves theoretically have an infinite number of modes. These many modes create many confusing signals that must be subjected to post-processing form of filtering to make sense of the information. Thus, guided waves are generally operated at low frequencies for long-range propagation and to avoid the many modes present at high frequencies. At low frequencies only two fundamental modes exist. These are referred to as fundamental symmetric (S0) and fundamental asymmetric (A0) modes. Much research work has been done to study the fundamental modes at the low frequency-thickness region. This region has since been established to be ideal for GUWs applications (Ramdhas et al., 2015; Verma et al., 2014) due to among other reasons the fact that there are fewer clear modes as opposed to higher frequency-thickness region whereby many modes are present which are generally confusing and requires extra work to analyze.

Resolution can also be improved by using the focusing technique. The main purpose of focusing is to increase the signal to noise ratio as well as to discriminate between real and false indications. The advantage of focusing technique is that it is carried out at low frequency hence attenuation is kept at minimum level (Brizuela et al., 2019; Zhu et al., 2014). However, focusing requires an array of transducers and complicated algorithms to implement (Velichko and Wilcox, 2008). It does not overcome diffraction limits and it also requires that the defect location is known beforehand. Focusing also requires a separate set of data which then negates the cost and time efficiencies of guided ultrasonic wave testing. Scientists for a long time had been limited to the two options discussed above namely inspection by high frequency waves and the use of focusing techniques to improve resolution. The introduction of the new concept of specially engineered structures called metamaterials two decades ago has presented an opportunity of obtaining properties not found in naturally occurring materials. Among many other novel properties, metamaterial have successfully been constructed that enabled subwavelength resolution in optics and acoustics (Amireddy et al., 2016). This research aimed at exploring the possibility of using metamaterials for subwavelength imaging that overcomes the diffraction limit barrier in the guided ultrasonic waves regime.

2.5 Metamaterials

Metamaterials are artificially engineered materials designed to have properties that are not found in nature (Kumar et al., 2022). These materials are constructed from repeating structures on a scale smaller than the wavelength of the phenomena they influence, giving them unique electromagnetic, acoustic, or mechanical properties. Metamaterials are made of composite materials arranged in some repeating pattern and are obtained by assembling elements from metals or plastics to make up a composite product. The special properties of metamaterials are from the structure attained as opposed to base material chemical composition. The structure parameters include pattern, shape, size, geometry, orientation, and arrangements of unit cells (Ma and Sheng, 2016a). The period of repeating pattern is usually much smaller than the wavelength of the incident wave. At the subwavelength pattern the metamaterial can be considered to behave as a homogenous material.

Understanding metamaterials was important for improving resolution in guided ultrasonic waves due to their unique properties in controlling wave behavior. Utilizing them allows for the creation of structures with tailored acoustic properties (Ma and Sheng, 2016b; Shen et al., 2019). These materials can control wave propagation to enhance resolution in NDT. By harnessing metamaterials, it becomes possible to design surfaces or structures that can control and manipulate guided ultrasonic waves. This understanding paves the way for the development of innovative materials and devices that can significantly advance the capabilities of guided ultrasonic wave-based inspections in NDT applications.

Metamaterials are used to manipulate waves in various ways such as absorbing, blocking, enhancing, and bending. This kind of manipulation is not attainable in conventional materials. Negative parameter values can be obtained as a result of manipulation of material structure (Kaina et al., 2015; Popa and Cummer, 2015). Some of the parameters of interest in electromagnetism include electric and magnetic field strength, flux density, permittivity, and permeability. In electromagnetism, materials have been developed having negative permeability, permittivity and refractive index. In acoustics, materials have been developed having negative bulk modulus, mass density, and refractive index. Metamaterials find applications in many fields. Some application areas include filters in optics, medical devices, remote sensors, monitoring of infrastructure, smart management of energy, control of crowds, air defense radars, communication in harsh conditions, antennas, ultrasonic sensors, protection of structures against earthquakes, and invisibility cloaking (Kumar et al., 2022; Ma et al., 2020; Muhammad et al., 2019; Yu and Zhou, 2023).

Veselago, (1968) suggested the possibility of the existence of materials with negative permittivity and permeability values. These materials were predicted that they would exhibit characteristics of negative refraction at materials' interface. The properties of these materials would generally be different from those having a positive index. They were called left-handed substances and would have negative group velocities. At the time appropriate technology to develop the proposed type of materials was not available.

Pendry et al., (1999) proposed a method to obtain left-handed materials having negative refractive index. This was achieved by using split rings to build a 3D image by considering two concentric pipes of different diameters such that one can fit into the other with some separation between them. Instead of having full round pipes a slit was then made in each of the pipes but in opposite sides. The slits create a discontinuity thus any applied current does not flow all the way. Having two rings creates a capacitance and thus current can flow from the inner ring to the outer ring and vice versa through the capacitance created. Instead of using long pipes to make the composite a very thin slice was taken. Many of these split ring composites were made. Cube blocks were then made and the composites attached on three of the faces. Several blocks were then stack on top and on all sides to create a 3D structure. This arrangement created a structure that could have negative magnetic permeability, negative electrical permittivity and negative refractive index (Kaina et al., 2015). The term metamaterial was coined around the same period to describe these engineered materials and it remains in use to define any kind of engineered structure fabricated with the intention of obtaining exotic properties not ordinarily existing in natural materials.

Pendry, (2000) demonstrated through simulation that a silver slab of negative index material has power to image features separated by distances smaller than the diffraction limits. These negative index metamaterials were given the name superlenses. A model was then developed which demonstrated how non-propagating evanescent waves could be recovered and amplified rather than allowed to decay in amplitude. Hence both propagating waves and non-propagating evanescent waves could be utilized to aid in improving resolution of an image. It relied on the theories developed by Veselago (1968) coupled with advances in technology.

Following the findings by Pendry (2000), different research groups moved to verify the theory. One area was in the development of negative index material. The other area was the ability to capture, amplify and channel evanescent waves to a detector. Experiments were carried out to verify existence of a negative index of refraction as correctly predicted by Maxwell's equations (Shelby et al., 2001). This was done using microwave frequency and successfully achieved negative refractive index. A variety of repetitive unit cells constructed of copper strips and split ring resonators on interlocking circuit board material were used to create these metamaterials. Garcia and Nieto-Vesperinas, (2002) experimentally demonstrated that evanescent waves are amplified in an ideal lossless and dispersion-less left-handed metamaterials.

The field of metamaterials quickly attracted a huge interest in the scientific community following the verification of the development of left-handed materials (LHM). With the development of metamaterials with negative permeability, negative permittivity or negative refractive index scientists began to explore how these metamaterials could be used to solve day to day problems through the manipulation of electromagnetic waves as desired to obtain specific responses (Fan and Padilla, 2015; Smith et al., 2000). Metamaterials have since been developed to the extent of achieving materials with negative refractive index, materials with perfect absorption, materials used for invisibility cloaking and materials used to achieve superlensing (Ergin et al., 2010;

Fang et al., 2005; Martinez and Maldovan, 2022; Tao et al., 2008; Valentine et al., 2009). Metamaterials made it possible to break the diffraction limit barrier. This was particularly useful in optics whereby there has always been desire to image tiny organisms, viruses, DNAs among many other biological concepts using light and microscopes.

Applications of metamaterial has since expanded beyond optics (Chen et al., 2012; Surjadi et al., 2019; Zhu et al., 2015). The initial developments of metamaterials were for applications in the electromagnetic wave regime, however similar applications have also been developed for applications in the mechanical and other wave regimes. This was possible since electromagnetic properties have equivalent mechanical properties. For example, bulk modulus and density in acoustics are analogs of permittivity and permeability in electromagnetic metamaterials. Hence the solution of the wave equation and the developments of metamaterials have grown in parallel for both electromagnetic and mechanical wave applications (Zhou et al., 2012; Zhou & Hu, 2009).

There are many types of mechanical metamaterials with different properties for specific applications. Coverage of all metamaterials is beyond the scope of this thesis. Suffice here is to highlight some of the key concepts. Mechanical metamaterials can be grouped based on applications, structure and properties manipulated. Mechanical metamaterials with negative Poisson’s ratio are metamaterials which when compressed in the axial direction also get compressed in the transverse direction (Ye et al., 2020). Conventional materials when compressed in one direction would expand in the perpendicular direction. Some metamaterials also when subjected to a tensile force they contract instead of the expected conventional way of expanding in the direction of applied force (Ye et al., 2020). When compressed these types of materials expand instead of contracting. Materials that exhibit negative compressibility or negative Poisson's ratio are exceptional in the sense that they expand in lateral dimensions when compressed longitudinally. This behavior contrasts with most common materials that exhibit positive Poisson's ratio, where compressing the material longitudinally causes it to expand laterally (Xu et al., 1999). Metamaterials or structures engineered with specific architectures at the microscale or nanoscale can exhibit these counterintuitive properties. Traditional materials, when compressed, reduce their lateral dimensions due to the positive Poisson's ratio. In contrast, materials with a negative Poisson's ratio expand in lateral directions when subjected to longitudinal compression. Another category is acoustic or phononic metamaterials, which are intended to have a negative effective mass density and bulk modulus. These materials have found use in transformation acoustics, negative refraction, superlensing, and acoustic subwavelength imaging (Haberman and Norris, 2016).

One of the applications of metamaterials is in subwavelength imaging in mechanical waves. Imaging of objects smaller than the wavelength of the interacting wave is known as subwavelength imaging. This breaks the diffraction limit which was not possible before the concept of metamaterials came along. Based on the successes in subwavelength imaging in electromagnetic waves, the same concepts have been exported to other areas such as acoustics and bulk ultrasonics (Page, 2016). Some progress was demonstrated in bulk ultrasonics super-resolution (Amireddy et al., 2017). A resolution of $\lambda/7$ was achieved with a sub wavelength crack in a plate-like sample using bulk ultrasonic waves. They made use of holey structured resonating metamaterials with longitudinal waves to achieve this level of resolution. Metamaterials achieve subwavelength resolution by recovering evanescent waves. Whenever waves encounter a boundary, be it a defect or a change in material properties, some of the waves are reflected back while others are refracted inside the second material. An additional mode known as evanescent wave is also generated (Grimberg et al., 2012; Park et al., 2011). Evanescent waves decay exponential at the regions where they are formed and generally dissipate within a wavelength distance. Conventionally the information carried by these high frequency evanescent waves is generally lost. When a metamaterial is introduced, it is capable of capturing these evanescent waves in the near-field and propagating them to be imaged in the far field. Since the evanescent waves contain high-frequency components, they contain detailed information on the defect and that is what enables the subwavelength imaging to be achieved. Evanescent waves are typically created when waves are totally internally reflected from an interface due to an incident angle larger than the critical angle. If these evanescent waves are utilized in imaging, it is possible that higher resolution can be achieved (Syed Akbar Ali et al., 2019). Natural materials are diffraction limited hence features smaller than half of the working wavelength cannot be resolved. To be able to image subwavelength features it is necessary to capture evanescent fields and use them to aid in imaging. Unfortunately, evanescent waves are normally non-propagating in natural materials.

Metamaterials can be used to achieve subwavelength resolution in different ways. All designs however rely on harnessing evanescent waves. The positioning of the metamaterial is such that the object end is close enough to the object of interest so as to capture the evanescent waves before they decay off completely. Three such designs of metamaterials are superlenses, hyperlenses and metalenses (Ma et al., 2022). Superlenses are based on metamaterials having negative refractive index (Deng et al., 2009; Kaina et al., 2015; Park et al., 2011). Superlenses are metamaterials engineered to yield negative dynamic density and bulk modulus. These metamaterials have been called superlenses due to their negative parameters. The superlenses have successfully been used to achieve subwavelength imaging (Liang et al., 2012). Magnification of the signal in hyperlenses is achieved monotonically across the lens due to excitation of surface resonance. The image is enhanced while inside the lens but the level drops to original level upon exciting the lens at the imaging side. Superlenses are made of resonant microstructures. Due to local resonance of the microstructures, superlenses experience significant energy losses which affect recovery of evanescent waves and hinder proper resolution in the subwavelength regime (Ma et al., 2022). Hyperlenses are metamaterials with anisotropic parameters (Lu and Liu, 2012). A typical hyperlens consists of channels spreading out radially like from the centre of a circle to the outer circumference. Two features which are located at an inner circle close to the centre of the circle end up expanding as they are projected and imaged at a larger outer circle. The level of amplification is generally equivalent to the ratio of outer circumference to the inner circumference. Metalenses are metamaterials engineered to attain resonance in channels/tunnels (Amireddy et al., 2018; Hur et al., 2022; Lemoult et al., 2010; Su et al., 2014). Resonant tunnelling metamaterials achieve subwavelength resolution through the process of resonance. The loses in metalenses is small compared to superlesnes as the resolution enhancement relies on formation of a standing wave through Fabry-Perot resonance (Lin et al., 2014). Evanescent waves generated at the defects are picked up, tunneled and amplified by the specially designed metamaterials which then is used to image the defect away from its actual location. This can happen both in the near-field and in the far-field. The metamaterial can be positioned very near to the object being evaluated or it can be positioned far. Because metamaterials magnify evanescent fields, the metamaterial can be lifted off from the object of interest within a certain limit. The length of the channels, however is not restricted provided a standing wave can be generated. Thus, imaging can happen several wavelengths away from the object. This is only restricted by the strength of the incident wave and any attenuation losses that lead to a drop in signal amplitude. For effective subwavelength resolution, the displacement of the metamaterial from the object has to be restricted. As the resolution relies upon the recovery of evanescent waves for imaging, the metamaterial should therefore be located within this field before the evanescent waves decay completely. This distance is typically within one wavelength of the working wave.

Fabrication of metalenses is much simpler and straightforward as opposed to superlenses and hyperlenses (Hur et al., 2022; Syed-Akbar-Ali and Rajagopal, 2022; Zhang and Liu, 2008). Metalens structures are also easy to incorporate in existing commercial inspection systems. Typically, metamaterials are made by drilling holes of selected sizes, pattern and periodicity into a block of parent material. The holes can be round, square, rectangle or any other determined shape. Other variable of interest is the spacing between these holes. The materials are arranged in a repeating pattern at scales below the wavelength of interest. The attained geometry, size and shape yields properties that can block, absorb, enhance, bend, or otherwise manipulate waves as desired. These new properties go beyond what is attainable with normal materials. Zhu et al., (2011) demonstrated that the Fabry-Perot resonance phenomena alongside evanescent waves harnessing can be exploited to achieve subwavelength resolution in acoustics. They developed a holey structured metalens which was capable of subwavelength resolution. The metalens achieved its subwavelength capabilities by coupling evanescent waves with Fabry-Perot resonance modes. The metalens developed required access to the near-field of the object being imaged. Cheng et al., (2013) developed a technique for subwavelength imaging subsurface objects using resonant metalens. They achieved subwavelength acoustic imaging using these metamaterials. Anisotropy in holey structured metamaterials was exploited to achieve magnification of evanescent waves thus overcoming the need for close access to object. The magnification of evanescent waves compensated for any decays experienced up to the location of the metamaterial. This demonstrated that subsurface features can be imaged successfully.

A typical metamaterial fabrication consists of taking a metal or plastic block and making periodic holes in it (Hur et al., 2022; Lemoult et al., 2010). The holes are then filled with a different material such as water to create a liquid-solid composite. The choice of the filler material in the metamaterial hole is such that there is maximum impedance mismatch between the two materials. Consider a square block of dimensions $(x,y,z) = (\Lambda,\Lambda,L)$. A square hole is then machined into the block so that the hole is of dimensions $(x,y,z) = (a,a,L)$. This hollow block constitutes a unit cell. The unit cells are then stuck together to form a three dimensional structure of dimensions $(x,y,z) = (m\Lambda,n\Lambda,L)$ where m and n are the number of unit cells in the x and y directions respectively. The periodicity between adjacent holes is Λ. The effective density of this type of metamaterial can be evaluated as follows:

Density in the x and y directions:

The properties in the x and y directions are similar.

Let the subscript A represent the hollow part whereas subscript B represent the solid part of the metamaterial.

Volume of the hollow section is given by,

$$V_A = aL \tag{2.238}$$

Mass of the hollow section is given by,

$$M_A = \rho_A \, aL \tag{2.239}$$

Volume of the solid section is given by,

$$V_B = (\Lambda - a)L \tag{2.240}$$

Mass solid

$$M_B = \rho_B \, (\Lambda - a)L \tag{2.241}$$

Total volume is given by,

$$V = aL + (\Lambda - a)L = \Lambda L \tag{2.242}$$

Total mass is given by,

$$M = \rho_A \, aL + \rho_B \, (\Lambda - a)L \tag{2.243}$$

Effective density (ρ) is given by the ratio between total mass (M) and volume (V).

$$\rho = M/V$$

$$\rho = [\, \rho_A \, aL + \rho_B \, (\Lambda - a)L \,] \, / \, \Lambda L$$

$$\rho = [\, \rho_A \, a + \rho_B \, (\Lambda - a) \,] \, / \, \Lambda$$

$$\rho \;= \frac{\rho_A\, a + \rho_B\, (\Lambda - a)}{\Lambda} \;= \frac{a}{\Lambda}\, \rho_A + \frac{(\Lambda - a)}{\Lambda} \rho_B$$

$$\rho \;= \frac{a}{\Lambda}\, \rho_A + \frac{(\Lambda - a)}{\Lambda} \rho_B \tag{2.244}$$

Let,

$$\eta = \frac{\Lambda - a}{a} \tag{2.245}$$

$$\eta + 1 = \frac{\Lambda - a}{a} + 1 = \frac{\Lambda - a}{a} + \frac{a}{a} = \frac{\Lambda}{a}$$

$$\eta + 1 = \frac{\Lambda}{a} \tag{2.246}$$

thus,

$$\rho \;= \frac{a}{\Lambda}\, \rho_A + \frac{(\Lambda - a)}{\Lambda} \rho_B = \frac{a}{\Lambda}\, \rho_A + \frac{(\Lambda - a)}{a}\frac{a}{\Lambda}\, \rho_B = \frac{1}{\eta+1}\, \rho_A + \frac{\eta}{\eta+1} \rho_B = \frac{1}{\eta+1}\, (\rho_A + \eta \rho_B)$$

$$\rho_x = \frac{\rho_A + \eta \rho_B}{\eta+1} \tag{2.247}$$

$$\rho_y = \frac{\rho_A + \eta \rho_B}{\eta+1} \tag{2.248}$$

Density in the z direction:

The effective mass density in the z direction is obtained as follows (Lee et al., 2009): Volume is the ratio between mass and density. The total volume *(M/ρ)* is obtained by summing the volume of the hollow *(M_A/ρ_A)* and the solid *(M_B/ρ_B)* sections.

$$\frac{M}{\rho} = \frac{M_A}{\rho_A} + \frac{M_B}{\rho_B}$$

$$\frac{1}{\rho} = \frac{1}{M}\left(\frac{M_A}{\rho_A} + \frac{M_B}{\rho_B}\right)$$

$$\frac{1}{\rho} = \frac{1}{\Lambda}\left(\frac{a}{\rho_A} + \frac{\Lambda - a}{\rho_B}\right) = \frac{a}{\Lambda}\frac{1}{\rho_A} + \frac{\Lambda - a}{\Lambda}\frac{1}{\rho_B} = \frac{a}{\Lambda}\frac{1}{\rho_A} + \frac{\Lambda - a}{a}\frac{a}{\Lambda}\frac{1}{\rho_B} = \frac{1}{\eta+1}\frac{1}{\rho_A} + \eta\frac{1}{\eta+1}\frac{1}{\rho_B}$$

$$\frac{1}{\rho_z} \;= \frac{1}{\eta+1}\frac{1}{\rho_A} + \frac{\eta}{\eta+1}\frac{1}{\rho_B} = \frac{1}{\eta+1}\left(\frac{1}{\rho_A} + \frac{\eta}{\rho_B}\right)$$

$$\frac{1}{\rho_z} \;= \frac{1}{\eta+1}\left(\frac{1}{\rho_A} + \frac{\eta}{\rho_B}\right) \tag{2.249}$$

Bulk modulus:

Similarly, the effective bulk modulus is evaluated as follows (Ding et al., 2007):

$$\frac{1}{k} = \frac{1}{\eta+1}\left(\frac{1}{k_A} + \frac{\eta}{k_B}\right) \tag{2.250}$$

The above evaluation of density and modulus demonstrates how properties of a metamaterial can be manipulated. For instance, the size of the unit cell can be increased or decreased, the size of hole can be increased or decreased, the length can be changed, the hole shape can be changed to say rounded, rectangular, star shaped or any other shape imaginable (Nash et al., 2015). Each of these changes creates structured metamaterials with totally different properties. All the manipulations are done to achieve desired outputs.

It is possible to write out the transmission coefficient for a plane wave through a metamaterial channel as follows (Zhu et al., 2011),

$$T(\lambda, m) = \frac{4\left(\frac{a}{\Lambda}\right)^2 Y e^{ikl}}{\left(1+Y\left(\frac{a}{\Lambda}\right)^2\right)^2 - \left(1-Y\left(\frac{a}{\Lambda}\right)^2\right)^2 e^{2ikl}} \tag{2.251}$$

Where,

$$Y = \frac{k}{\sqrt{k^2-m^2}}\,; \tag{2.252}$$

$$m=\sqrt{\left({k_x}^2 + {k_x}^2\right)}\,; \tag{2.253}$$

$$k=\frac{2\pi}{\lambda} \tag{2.254}$$

a = width of a metamaterial channel opening;

l = length of metamaterial;

Λ = periodicity;

k = propagation constant;

m = parallel momentum;

From the equations above, it can be inferred that resonance will occur when $kl = n\pi$, where n is an integer.

Research in metamaterials has demonstrated that it is possible to manipulate evanescent waves using structured materials which can lead to subwavelength imaging which overcome the diffraction limit (Park et al., 2011). The subwavelength resolution may be attained by manipulating the unit cell dimensions width of a metamaterial channel opening, periodicity, and length of the metamaterial such that a state of resonant standing wave is attained which aids in recovery and magnification of evanescent waves. The resolution is primarily affected by the periodicity of the metamaterial (Amireddy and Raj, 2023). Thus, the smaller the unit cell the higher the resolution achievable. Metamaterials have successfully been used to achieve subwavelength resolution in optics, acoustics and bulk ultrasonic waves. The work reported in this thesis focused on using metamaterials to achieve subwavelength resolution in guided ultrasonic waves regime. The method selected was based on resonant tunnelling metalenses. To accomplishing the targeted goal of super resolution imaging, resonating structures were designed, fabricated and used to carry out resolution investigations.

2.6 Summary

In summary this chapter has presented the theoretical background as well as the literature directions with respect to guided waves and the resolution problem under investigation. Guided ultrasonic waves testing is an important nondestructive testing technique due to its long-range capability which allows for inspection to be carried out from a remote location. However, they are diffraction limited meaning that defects separated by gaps smaller than $\lambda/2$ (where λ is the interrogating wavelength) cannot be resolved. This is particularly of concern since defects located close to design features like welds and supports may go undetected due to defect signals getting overshadowed. Attempts have been made in literature to improve the resolution of guided ultrasonic wave testing. Most of these attempts have been based on focusing techniques whereby multiple transducers are deployed to focus on a particular suspect-area. The limitation of the focusing techniques is that they increase the cost of guided wave inspection. Most importantly, these focusing techniques do not overcome the diffraction limit. Thus, guided wave testing is generally used as a screening tool to identify areas of general concern. A high-resolution method such as bulk ultrasonic wave testing is then deployed to further characterize the suspected flaws. The aim of this research was to develop a technique that could overcome diffraction limit allowing for resolution of defects at the subwavelength level. The path chosen for this was by use of metamaterials. Recent research has shown the potential of these metamaterials to achieve subwavelength resolution for applications in optics as well as in acoustics.

However, the literature does not show much work on exploitation of metamaterial properties to solve the resolution challenge in guided ultrasonic waves. Hence this research aimed at addressing that knowledge gap.

CHAPTER 3: METHODOLOGY

3.1 Introduction

This chapter gives a description of the materials that were employed in the research investigation. These are the equipment as well as the hardware and software resources. The chapter is organized in line with the objectives. Each of the sections presented below describes the methodology and equipment used to achieve the objective.

The purpose of this work was to improve defect resolution capability of guided wave testing to overcome the diffraction limit. It was achieved by use of specially designed materials commonly referred to as metamaterials. These metamaterials achieve their special properties purely because of their geometrical characteristics as opposed to their physical and mechanical properties. The work done comprised of numerical simulation and experiments. Simulations were carried out to explore the viability of the proposed technique and to determine appropriate parameters. Upon optimization of the parameters through simulation, experiments were then done to validate the developed simulation model. In this chapter the variables, procedures and methods used are presented.

The activities that were carried out to achieve the set objectives included the selection of excitation wave parameters, determination of metamaterials specifications, design and fabrication of metamaterials, measurement of resolution achievable and optimization of the parameters.

3.2 Wave scattering at defects

Numerical simulations were done using a commercial finite element software *Abaqus* version 6.14 (through IIT Madras high performance computing infrastructure). The manner in which ultrasonic waves interact with defects was studied. This was important because the scattering behaviour informs the options to be exploited in imaging. The component being studied was modelled as two-dimensional (2D) deformable shells. Plane waves were generated on one end of a sample.

Numerical simulation allowed for the investigation of how waves interact with a circular defect in a shell, providing an understanding on the scattering phenomenon. It was used to understand how different parameters, such as defect size, influence the scattering behavior, thereby aiding in the optimization and improvement of defect detection methods that was eventually utilized in this research. Abaqus software was used to simulate and analyze scattering phenomena. A 2D model of a shell with a circular defect was created and the material properties of the shell and the defect were defined. Then a mesh was generated for the model. It was ensured that the mesh was fine enough to accurately capture the behavior of waves interacting with the defect in the shell. Structured meshes were selected for most cases whenever this was practicable. This was followed by applying appropriate boundary conditions to represent the physical scenario that was to be investigated. For the case of defects investigated the edges were given rigid constraints. Loading conditions were then specified in the model and it included applying an incident Hanning pulse to induce wave scattering and eventual scattering at the defects. The defined model was then executed.

The considered sample design had a defect in the center and after the waves were scattered, the vibration fields were recorded at varying distances from the defect surface. The C-scan and radar plots were used to visualize the amplitude variations around the defect. Figure 3.1 is a schematic of the sample that was used to evaluate the interaction of ultrasonic waves with the defects. It shows a rounded defect located in the path of a propagating wave that was excited from the left-hand side. After the wave interacted with the defect it was scattered in different directions. The amplitudes of scattered waves were monitored in two zones namely the region adjacent to the defect and some distance (ranging from fractions of a wavelength to several wavelengths) away from the defects. These regions are indicated in the diagram as monitoring lines/circles.

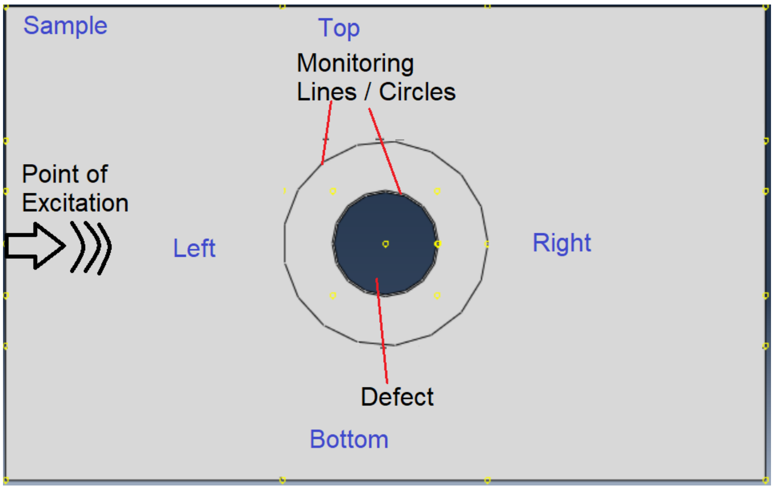

Figure 3. 1. Schematic of wave scattering sample design showing the relative positions of excitation, defect and monitoring

3.3 Wave mode selection

Guided waves are dispersive thus a contrast to conventional ultrasonic bulk waves which usually have constant longitudinal velocity and shear velocity for a given material. Two values are commonly quoted in literature for the two velocities of bulk waves for different materials. The dispersive nature of guided waves is visualized more clearly by disperse curves where the vertical axis is the phase velocity and the horizontal axis is the frequency-thickness. The dispersion relationship was derived by Lamb (Stobbe et al., 2019). For waves travelling in a structure only specific frequency-velocity pairs can propagate. These are the symmetric and antisymmetric modes.

Dispersion curves for guided waves in a plate were generated by examining the relationship between the phase velocity of the waves and their corresponding frequency and mode. These curves depict how the velocity of waves traveling through a plate varies with frequency and mode. They are necessary in understanding the behavior of guided waves in plates, aiding in the identification of specific wave modes and their characteristics, including velocity, attenuation, and mode conversion. These parameters were necessary in this research particularly in identifying propagating wavelength for purpose of metamaterial design. To generate the curves theoretical models were used in which relevant equations were derived to describe the behavior of waves propagating through the plate. The equations account for factors like material properties, plate thickness, and wave modes (such as Lamb waves) and were derived and presented in the theoretical background. Numerical approximation methods were then used to solve the derived equations. Matlab software (https://www.mathworks.com/) was used to solve the equations and to calculate the dispersion relationships and plotting the dispersion curves. The obtained results were analysed to determine the relationship between the wave frequency and wavenumber. The dispersion relationship between frequency and wavenumber is important in understanding how the waves behave in the plate. The data relating frequency and wavenumber was plotted to create dispersion curves that illustrated the phase velocity of waves as a function of frequency and mode. Each curve represented a different mode of wave propagation in the plate. Simulations were then carried out in Abaqus software to measure the actual wave propagation characteristics in a plate vis a viz the generated dispersion curves.

Some of the variables in guided wave experiments included excitation frequency, structure thickness, velocity, and modes. These variables are related since for a given frequency-thickness combination, higher frequency means selecting lower thickness and vice versa. Similarly, for a given frequency-thickness, different modes exist and each mode has specific velocity. In simulation all these parameters were selected based on the desired guided wave mode. However, in experiments the waveguide thickness was fixed which means that appropriate frequency was selected so as to excite the desired wave mode. Plate dispersion curves were plotted and the observed modes were evaluated. For operation, the area with the fewest modes was chosen and a location with a gentle slope (least dispersive) was selected. This was to avoid regions with many wave modes that would create confusing signals. Also, the dispersive regions were avoided so that the velocity of the selected mode remains constant even for any slight changes in thickness and frequency. When a wave mode is least dispersive, any change in thickness or frequency has the smallest effect on the speed of propagation.

3.4 Metamaterial parameters and design

Numerical simulation was used to optimize metamaterial parameters. The metamaterial was modelled as a two-dimensional (2D) deformable shell and was assigned the properties of water. A series of empty channels were built into the water part. This created a water/air composite. Some of the metamaterial variables included channel opening size, periodicity, channel length, pitch, and inclination angle. These variables were varied individually while holding all the other variables constant. A wave was generated from one side of the metamaterial and transmitted through the channels. The amplitudes on the other end were recorded. The dimensions were varied until optimum values were obtained yielding maximum transmitted signal amplitude. The values of the respective variables that yielded maximum transmission were taken to be the optimized metamaterial parameters. Metamaterials were then designed and fabricated based on these optimized dimensions and configuration. Additional correction was done on the designs based on experimental results.

The Figure 3.2 shows a sectional view of the metamaterial. The variables that were manipulated include channel opening size *(a)*, periodicity *(Λ)*, channel length *(L)*, pitch *(p)*, and inclination angle *(θ)*. Both vertical channel *(θ=0°)* and inclined channel *(θ≠0°)* metamaterials were considered.

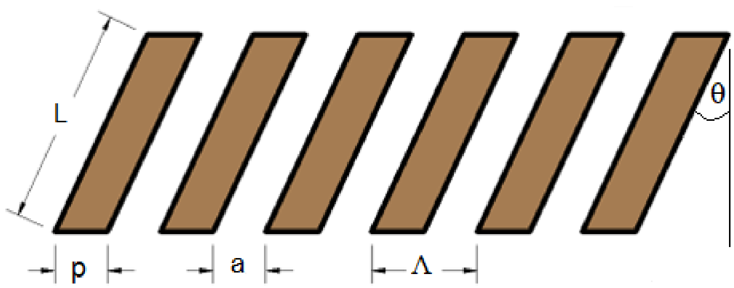

Figure 3. 2. Metamaterial sectional view

3.5 Resolution limits for rounded defects

Both numerical simulations and experiments were used to investigate resolution limits for rounded defects. A defect is considered rounded if the major dimensions are less than or equal to three times the minor dimensions of the defect. This is the general rule in the field of nondestructive testing (ASME, 2021; Kadarno et al., 2019). A side drilled hole is an example of a rounded defect. Metamaterials with straight channels were used in this investigation. The metamaterial used was made from Perspex with channels filled with water.

3.5.1 Numerical simulation for rounded defects

Modeling and numerical simulations were performed using a commercial finite element (FE) package (https://www.3ds.com). Abaqus is a finite element analysis software used to solve many engineering problems both in static and dynamic conditions. The software breaks down partial differential equations into linear equations. The problem at hand was a dynamic linear elasticity problem involving propagation of mechanical vibrations and scattering at defects. The model used in this research had two parts. The first part was a waveguide to be inspected and the second part the metamaterial to aid in subwavelength defect resolution. The two parts were modeled by drawing them separately. Each of the parts was modeled as a planar two dimensional (2D) deformable type. In each model the waveguide was modeled as a solid with defects. The type, size and separation distance between the defects was varied in each model. The metamaterial was modeled as a solid part with an array of hollow channels thus creating a composite structure. The modeling was achieved by drawings using the Abaqus software graphical user interface and that could also have been achieved by importation from any other computer aided design software. Each of the parts was then assigned material properties. The part representing a waveguide was assigned aluminium properties and the metamaterial was assigned water properties. Any other material could have been used. Aluminium was chosen because it does not rust hence stable and can be used for many experiments both in moist environments as well as submerged under water. Aluminium properties assigned were density of 2700 kg m^{-3}, elastic modulus of 70 GPa and Poisson's ratio of 0.33. Water properties assigned were density of 1000 kg m^{-3}, and bulk modulus of 2.2 GPa. The waveguide was a plate of length 1 m and thickness of 10 mm. Two holes were modelled into the waveguide by removing material from the waveguide part. The hole sizes and separation distances were varied in subsequent models. The hole diameters were varied from 1 mm to 9 mm, separation distances from 4λ (288 mm) to $\lambda/72$ (1 mm).

The different parts that were created in different windows were then assembled together to create one continuous model. The parts relative positions were also adjusted to reflect the desired configuration. The metamaterial was positioned above and directly in contact with the waveguide and in different models the relative position of the metamaterial with respect to the defects was adjusted. Since the model comprised several independent parts, an interaction had to be established between the boundaries and a tie constraint was defined between the two parts to establish continuity at the boundary.

The meshing geometry was defined by smaller simpler shapes called finite elements. Finer meshes would lead to more accurate approximations but would be costly in terms of computation; time, disk space, and memory. Coarse mesh would be faster but leads to reduced accuracy of the model. The mesh size was therefore selected to ensure multiple nodes between the features to be resolved. The plate was meshed with 4-nodes bilinear plane-strain quadrilateral elements of size 0.2 mm. The water part was meshed as 4-nodes which were linear 2D acoustic quadrilateral elements of size 0.2 mm. The applied loading boundary conditions included displacement and concentrated force at the transmitter side. The waveguide was then excited on one end with a 3-cycle Hanning windowed tone burst pulse load having a centre frequency of 75 kHz. The pulse was generated using MATLAB software (https://www.mathworks.com/). Hanning window is a type of window function that can be applied to tone bursts in order to improve their spectral properties. When a Hanning window is applied to a tone burst, it tapers the edges of the signal, reducing the abrupt transition at the beginning and end of the burst. This helps to reduce spectral leakage and improves the signal-to-noise ratio (Michaels et al., 2013). Other types of window functions that could have been used to shape tone bursts include Hamming window, Blackman window, and Gaussian window (Hua et al., 2018). Each of these functions has its own unique properties and can be used depending on the specific requirements of the application. Hamming window, for example, has similar properties to the Hanning window, but with a sharper roll-off at the edges. This can be useful when more precise frequency resolution is required (Sun et al., 2020). Blackman window has a more complex shape and provides better spectral resolution than the Hanning and Hamming windows, but can also introduce more spectral leakage (Canale et al., 2012). Gaussian window has a bell-shaped curve and provides very good spectral resolution, but also has a slower decay rate than other windows, which can limit its usefulness in some applications (Beard and Lowe, 2003).

The choice of window function depends on the specific requirements of the application and the trade-offs between spectral properties and other factors such as time-domain characteristics and computational complexity (Reddy et al., 2009). The pulse frequency and sample thickness combination ware selected from the dispersion curve (http://www.disperse.software/) to generate the fundamental symmetric guided wave mode.

The status of the finite elements and nodes in the model were evaluated using Abaqus which converts the developed model with all the defined parameters into an input file to be executed by the solver. The input files for a simplified model of hole defects are given in Appendix D. The solver converts the wave partial differential equations into simple algebraic equations. The equations can then be presented in the form of matrices. Matrices of individual element were assembled to global matrices for the entire geometry which was then solved for the unknown matrices. Due to the dynamic nature of the problem at hand, Abaqus Explicit Solver was selected for the task since it is ideal for extreme non-linear problems with small time increments (dynamic problems). The Abaqus provides for post processing and visualization of the outcome of the analysis. Some of the variables which were animated include the displacement of the finite elements as a function of time in the waveguide and pressure amplitude variations with respect to time in the metamaterial.

The Figure 3.3 shows the overall set-up of the concept under investigation. A displacement load was applied on the left-hand side of the model. The wave generated propagates towards the right and in the process, it interacts with the defects and is scattered in all the directions. The metamaterial lens was positioned directly on top of the defects. The receiver was located on top of the metamaterial and the receiver was in the form of a line of nodes located above the metamaterial. This monitoring line was 1 mm above the metamaterial whereby a thin layer of water was added to ensure readings were taken in a homogeneous medium (water). Pressure amplitudes were recorded on these receiver line of nodes and the readings from the receiver were used to generate scatter plots. Cases were considered when the metamaterial lens was inserted between the defect and the receiver as well as cases without any metamaterial.

(a)

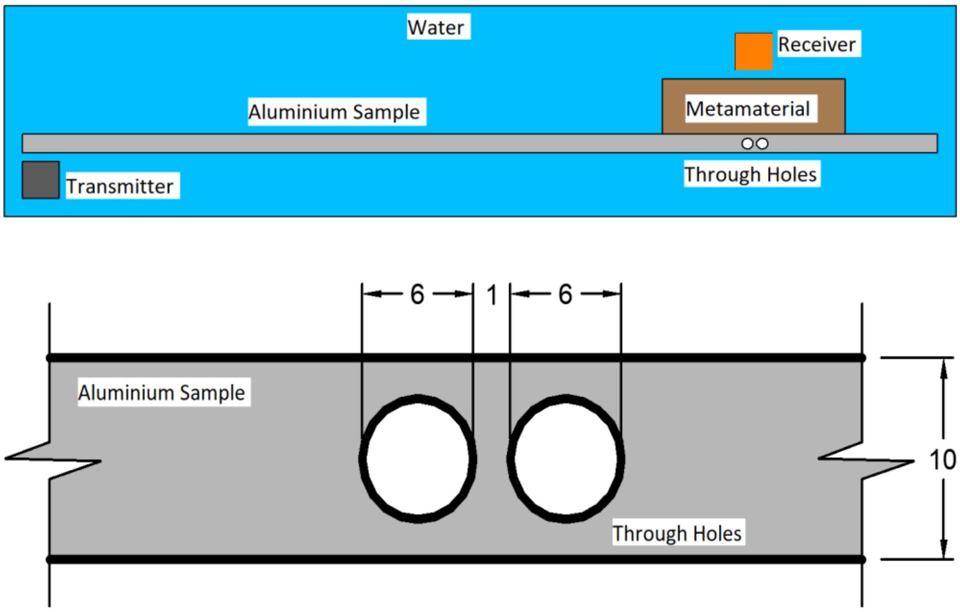

(b)

Figure 3. 3. Schematic of; (a) the concept under investigation, (b) zoom-in on through holes defects

3.5.2 Experimental set-up for rounded defects

Experiments were performed to validate the findings from simulations. A metamaterial was designed and fabricated as per the optimized dimensions and configuration obtained through simulation. The sample was an Aluminium strip of length 1 m, width 50 mm and thickness 10 mm. The length was chosen based on the available experimental set-up while the thickness was selected based on typical thickness expected in industry for plates and pipe structures. The choice of the width was to match the dimensions of the metamaterial designed. Two through holes were drilled on the thickness side of the plate, and were 6 mm in diameter and were separated by 1 mm. A longitudinal bulk ultrasonic piezoelectric probe (Panametrics NDT) of central frequency 100 kHz was used as a transmitter to generate the guided wave on one end of the test sample. The probe frequency was chosen so as to generate the desired fundamental mode in the selected plate. There is an inverse relationship between selected frequency and plate thickness. If it is desired to generate the same wave mode on plates of different thicknesses for instance, a doubling of plate thickness must be accompanied by halving the wave frequency and vice versa.

A metamaterial in the form of a straight channel was positioned directly over the defects. To ensure effective coupling between the transmitter probe and the sample, as well as to provide flexibility in adjusting the probe angle for generating the desired guided wave mode, the sample, metamaterial, and probe were immersed in water. Out-of-plane vibration displacement amplitudes were recorded using a fiber-optic laser Doppler vibrometer (OFV 551, Polytec GmbH, Germany, https://www.polytec.com), which was controlled by a laser controller (OFV 5000, Polytec). The electronic controllers were operated using the Ritec RPR-4000 pulser-receiver (Ritec Inc., http://www.ritecinc.com, Warwick, USA). The transmitter (Piezoelectric probe), receiver (laser vibrometer), and display oscilloscope (National Instruments, USB-5132, 50 MHz bandwidth, 2-channel, 8-bit USB oscilloscope device) were all interconnected via the Ritec system.

Each of the components in the experiment played a unique role. The pulser-receiver controlled all the other components and variables including setting the frequency, number of cycles, amplitude of the transmitted signals, the repetition frequencies, and amplification of signals. The transmitter probe was used to convert electrical signal (voltage) into a mechanical vibration and vibrations back to voltage. The samples guided the generated mechanical wave. The metamaterials picked the scattered signals from the defects and preserved the defect details and channeled them for imaging in the far field. The laser vibrometer picked up the mechanical vibrations on the receiver end and the acquisition box digitized the analog signal that was received.

The controller produced a 3-cycle pulse that drove the transducer at 75 kHz. The choice of the frequencies above was guided by the general frequencies used in guided wave testing as well as by the available experimental equipment. The phase velocity of the guided wave generated in the sample was measured to be 5400 m/s. Using the relationship between velocity, frequency and wavelength, the wavelength was determined to be 72 mm (i.e., λ =72 mm). The Figure 3.4 shows a photograph of the experimental set-up. The experiment was carried out as explained for the concept of investigation with the set-up shown in Figure 3.3. Initial work was done using straight channel metamaterials and later with modified inclination angles of the channels to improve on transmission between the waveguide and the sensor by capitalizing on Snell’s law.

(a) 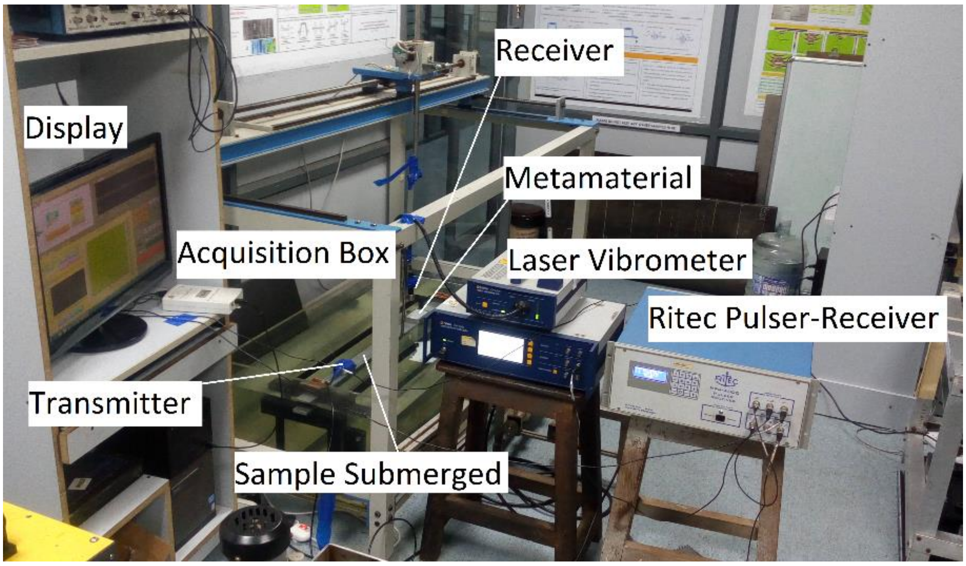

(b) 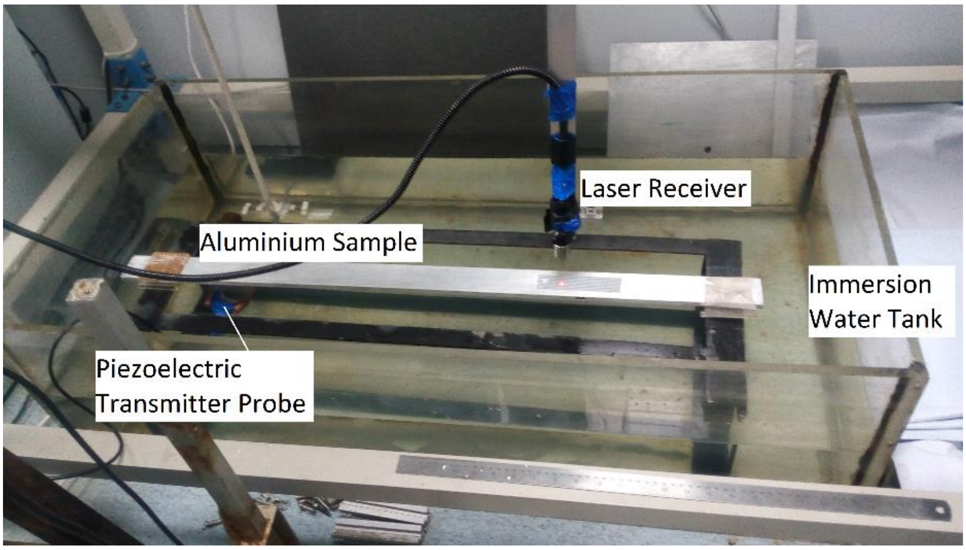

Figure 3. 4. Photograph of; (a) experimental set up, (b) zoom-in on the relative positions of the transmitter, sample, and receiver. These facilities are located at the Indian Institute of Technology Madras (IIT Madras), Chennai, India

3.6 Resolution limits for linear defects

Both numerical simulations and experiments were used to investigate resolution limits for linear defects and a crack is an example. Metamaterials used in this investigation were made from mild steel and had channel inclination angle of 15.9° and were filled with water. The determination of the channel inclination angle is presented in section 4.4 of this thesis.

3.6.1 Numerical simulation for linear defects

Numerical simulations were performed using the same software as for the rounded defect. The model was implemented as described in section 3.5.1. The aluminium waveguide was excited on one end with a 5-cycle Hanning windowed tone burst pulse having a centre frequency of 100 kHz. All other model and simulation parameters are as described in section 3.5.1. The input file for a simplified model of crack defects is given in Appendix E. The waveguide was a plate of length 1 m and thickness 10 mm and two cracks were introduced into the waveguide. The cracks were modelled by 'freezing' displacements on a series of nodes in the waveguide part of the model. The crack sizes and separation distances were varied in subsequent models. The crack depths ranged from 1 mm to 9 mm. The cracks separation distance ranged from 4λ (216 mm) to λ/54 (1 mm).

The Figure 3.5 shows the overall set-up of the concept investigated. The metamaterial lens was positioned at an offset distance from the defect and the offset distance was varied in subsequent models. The receiver was located on top of the metamaterial and the receiver was in the form of a line of nodes located above the metamaterial. Generation of scatter plots and consideration of different cases of metamaterial placed between the defect and receiver were processed as described in in section 3.5.1.

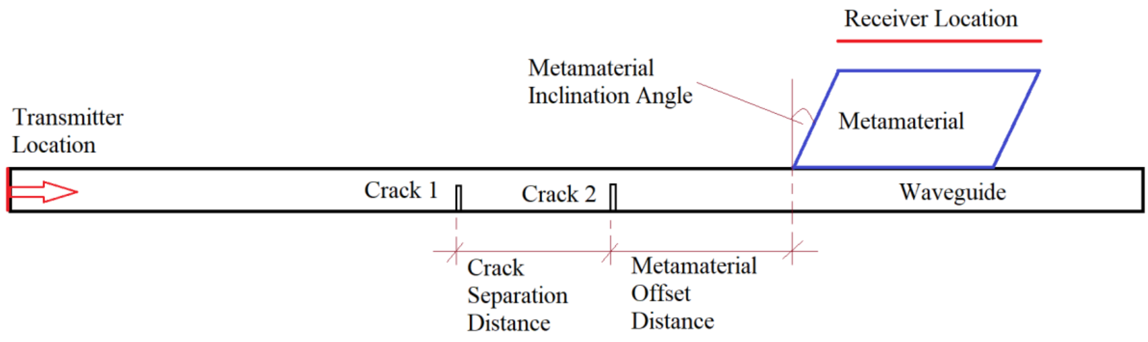

Figure 3. 5. Schematic illustration of the concept under investigation

3.6.2 Experimental set-up for linear defects

Experiments were performed to validate the findings from simulations. A metamaterial was designed and fabricated as per the optimized dimensions and configuration obtained through simulation. The sample was an Aluminium strip of length 1 m, width 50 mm and thickness 10 mm. Two slits were machined into the thickness side of the strip. The direction of the slits was into the thickness and it covered the entire width of the bar. Different samples were made with different slit depths and different slits separation distance. The slits depth of penetration and separation distances were varied. The depth of penetration ranged from 2 mm to 8 mm in the 10 mm thickness. A longitudinal bulk ultrasonic piezoelectric probe was used as a transmitter to generate the guided wave on one end of the test sample. An inclined angle channel metamaterial was positioned at an offset distance from the defects. The metamaterial was filled with water to create a composite and to ensure proper coupling between receiver probe and the metamaterial lens. A shear ultrasonic piezoelectric probe was used as a receiver to record vibration displacement amplitudes. The electronic controls were performed using Ritec RPR-4000 pulser. The transmitter as well as the receiver were connected through the Ritec.

A 5-cycle pulse was generated from the controller, driving the transducer at 100 kHz. The value of the frequency was selected from dispersion curves plotted so as to generate the desired wave mode. The phase velocity of the guided wave generated in the sample was measured to be 5400 m/s. Using the relationship between velocity, frequency and wavelength, the wavelength is determined to be 54 mm (i.e., λ =54 mm).

The Figure 3.6 shows a photograph of the actual experimental set-up, showing the main equipment used and the test plate sample containing defects. The piezoelectric transmitter probe was coupled to the plate waveguide using oil as a couplant. The probe generated fundamental symmetric guided wave mode which propagated through the waveguide. The receiver sensor assembly was positioned beyond the defect location such that the transmitter and the receiver were on opposite sides of the defect. The receiver assembly consisted of a metamaterial with water filled channels, a thin wire waveguide and a shear wave probe. The metamaterial was plastered onto the waveguide such that the water in the channels of the metamaterial could not drain. The edges of the metamaterial were also plastered beyond the channel ends so as to allow a thin (3 mm) pool of water to be contained. This pool acted as a couplant between the receiver waveguide and the metamaterial. The clearance between the wire receiver and the metamaterial channels was about 1 mm which was just small enough to allow uninterrupted receiver movement during the scanning process. The thin wire waveguide was directly coupled to a shear probe with 100 kHz central frequency. This assembly was used as a receiver so as to discretely pick up the displacement amplitudes in fine intervals above the metamaterial. The receiver readings were taken in steps of 0.2 mm along a horizontal line located 1 mm above the metamaterial in the water filled area.

The same operation and information processing were carried out as for the rounded defects experiments. The taken primary readings from the sensor were amplitude variation with time. These were used to generate A-scans for each of the points that readings were taken. The A-scans were then gated with respect to time such that any reflections from the ends of the waveguide were filtered out. The maximum absolute amplitude of the time-filtered A-scans were then recorded for each of the points. These maximum amplitudes were then used to generate the line scan plots.

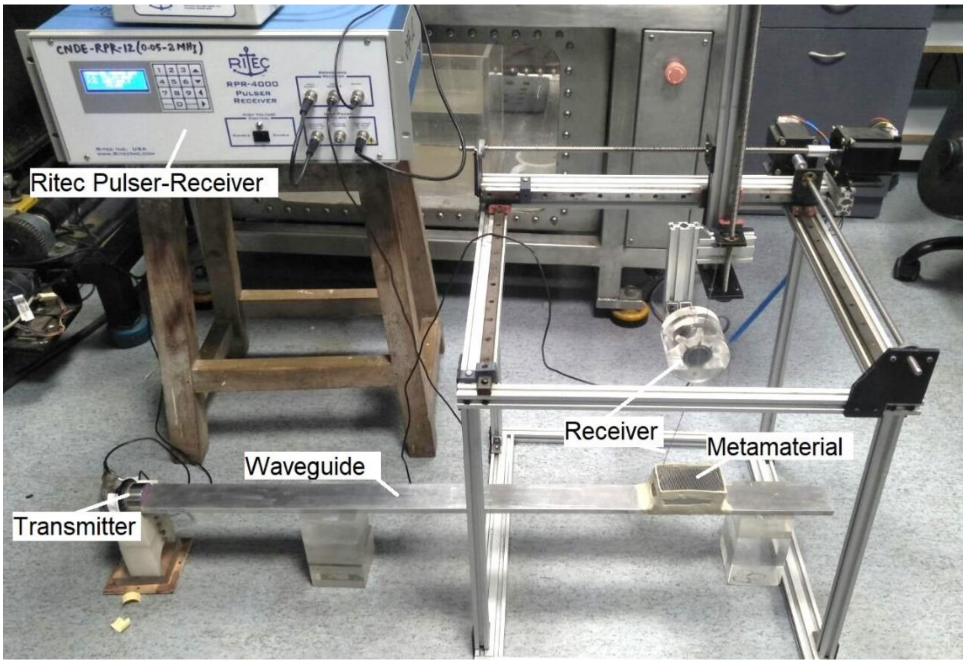

(a)

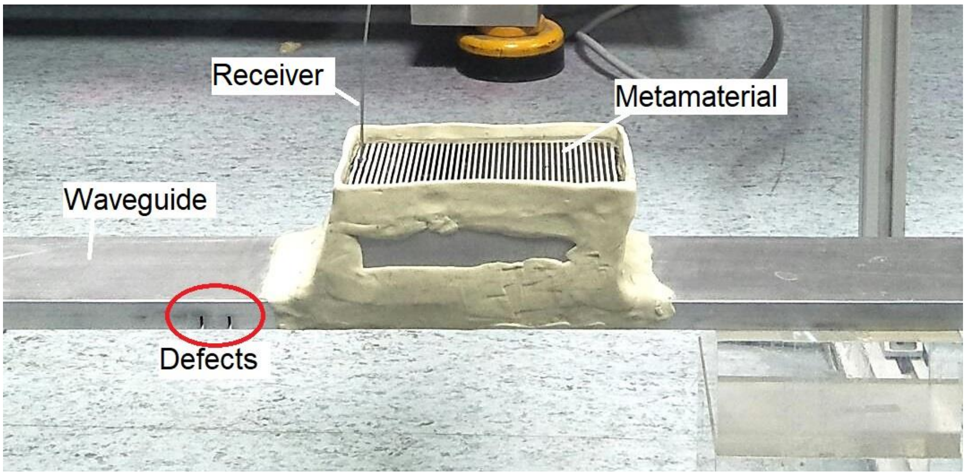

(b)

Figure 3. 6. Experimental setup of crack experiments; (a) entire setup, (b) zoom in on defect and metamaterial. These facilities are located at the Indian Institute of Technology-Madras, Chennai, India.

CHAPTER 4: RESULTS AND DISCUSSION

4.1 Introduction

The purpose of this research was to investigate and develop a technique that improves resolution of defects capability of guided waves. The approach chosen was employment of metamaterials to pick up the non-propagating evanescent waves that were generated at defect boundaries, amplify and use to image the defects. Some of the variables considered included metamaterial dimensions, defect types and defect spacings. Results presented in this chapter focuses on the outcome from these variable manipulations. The most important results are presented whereby cases are compared when the metamaterial was used and when there was no intervention. It was established that when intervention using metamaterials was carried out there was a significant improvement in the resolution. The comparisons are shown using scatter plots.

4.2 Wave scattering at defects

To be able to develop an effective method for defect resolution improvement, it was necessary to first analyze how waves interacted with defects. When a wave encounters a boundary between two materials the wave is interrupted and undergoes reflection, refraction and transmission. This is a result of changes in acoustic impedance between the two materials. It was established that when ultrasonic waves encounter a defect, a part of the energy is reflected back in the direction of incidence whereas another portion is transmitted through. In addition, scattering and diffraction takes place at the defect. The defect edges can be considered to be acting as vibration sources transmitting waves in all directions. Figure 4.1 to Figure 4.4 show the analysed results after the execution of the simulation model. This involved extracting the scattered wave characteristics, such as reflection, transmission, and diffraction patterns resulting from interaction with the circular defect. Abaqus offers various tools for visualizing and interpreting the simulated data. The ultrasonic waves are shown travelling from left to right and interacting with defects of different sizes. The images in the figures 4.1 to 4.4 are screenshots from the finite element package. The colours represent displacement amplitudes in arbitrary units (with red being highest and blue being lowest). In Figure

4.1, the wave is approaching hole defect of diameter 2λ. In Figure 4.2, the wave had just been scattered by the defect. The impedance mismatch between the parent material and defect caused part of the waves to be scattered in all direction. In Figure 4.3, the wave was interacting with a hole defect of diameter λ/4. The defect caused a disturbance in the wave path as part of the wave energy that was reflected back to source. In Figure 4.4, the wave had just been scattered by the defect.

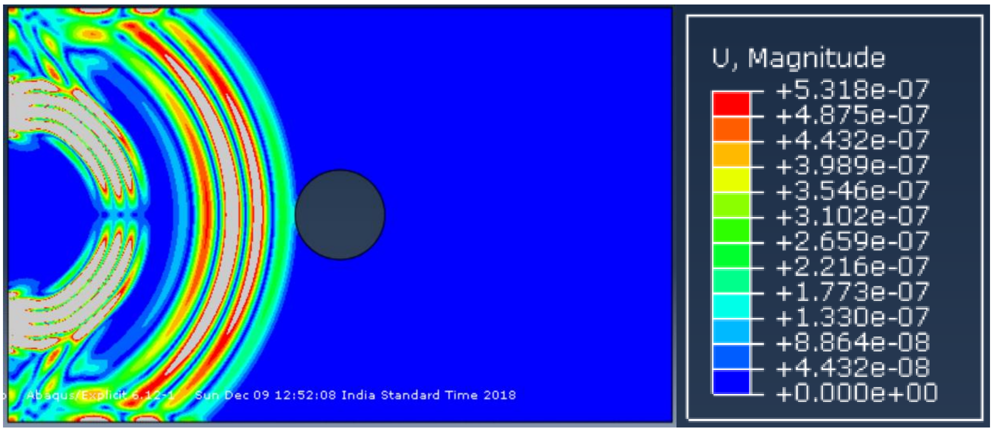

Figure 4. 1. Visualization of ultrasonic waves approaching a rounded defect of size twice the wavelength

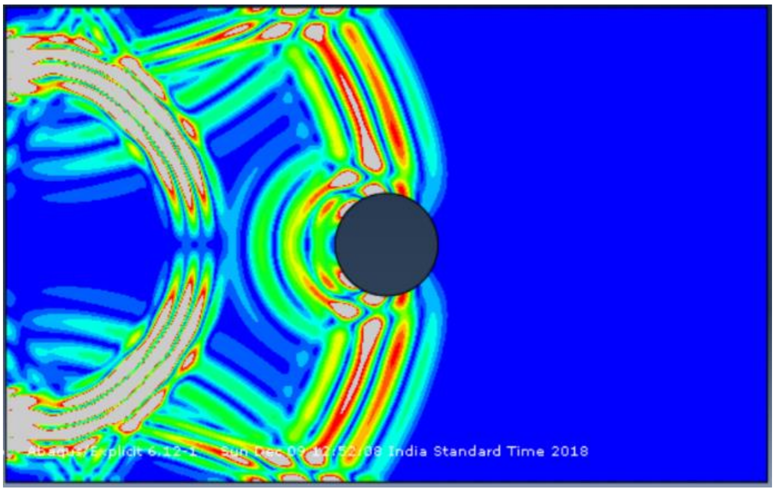

Figure 4. 2. Visualization of ultrasonic waves scattering from a rounded defect of size twice the working wavelength

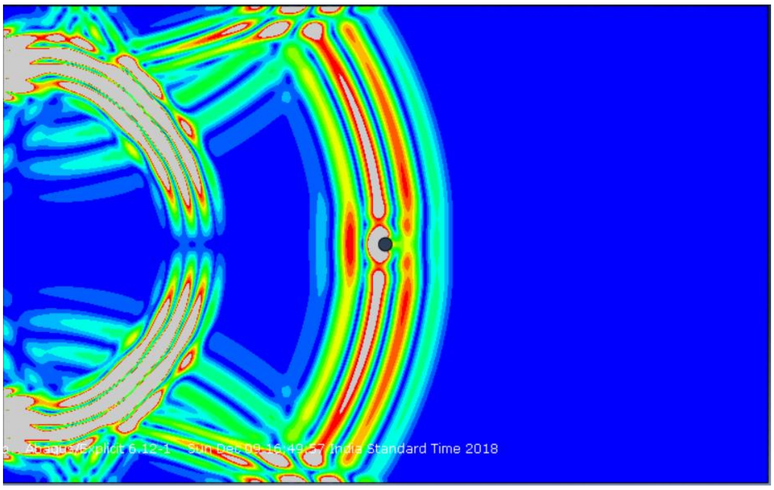

Figure 4. 3. Visualization of ultrasonic waves interacting with a rounded defect of size a quarter of the working wavelength

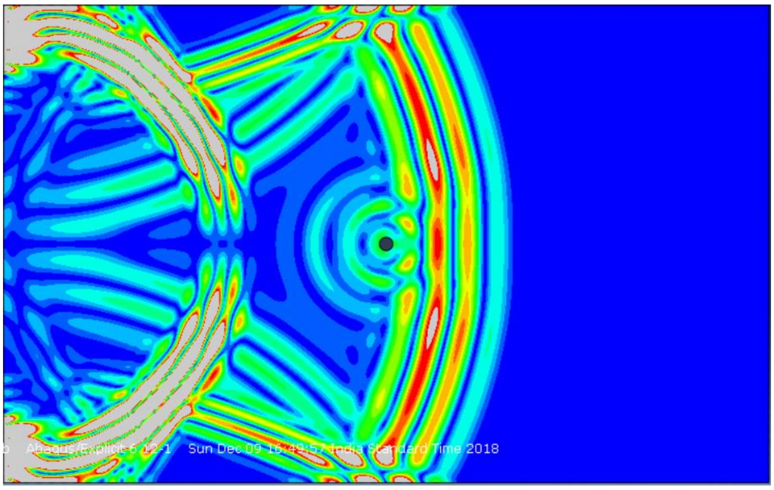

Figure 4. 4. Visualization of ultrasonic waves after interaction with a rounded defect of size quarter of the working wavelength

It was noted that as the defect size changes, so does the magnitude of scattering. The bigger the size of a defect, the more scattering that was taking place. The waves that scatter from the defect are used in ultrasonic testing to determine the location and even the size of a defect. When there are two or more defects which are located close to each other, the reflection from each of the defects starts to interact constructively and destructively. This can be loosely related to the experiments in electromagnetic waves whereby a double-slit is used to demonstrate interference patterns. As the distance of the sensor from the two defects is increased these waves can appear as if they were scattering from just a single perhaps large defect instead of two. Whether the signal appears as one or two it is determined by the ratio of the working wavelength with respect to the size of the separation distance between the two defects. The threshold is referred to as the diffraction limit and is applicable to all types of waves. This threshold value has since been determined to be half of a wavelength (Zhang and Liu, 2008). When the separation between two defects is less than half of a wavelength the two defects will appear as though it is one.

By monitoring the vibrations around the defect, the distribution of energy after scattering was determined. In Figure 4.5 and Figure 4.6 the displacement amplitude distribution around a 6 mm diameter (λ/9) rounded defect are plotted. For an incident plane wave approaching from the left-hand side at the center plane axis of the defect, it was noted that the waves were scattered in all directions. In the case considered here it was seen that the maximum in-plane displacement was in the incident direction. This indicates that most in-plane displacement energy was reflected back to source. The out-of-plane displacement was however maximum in the near-perpendicular direction.

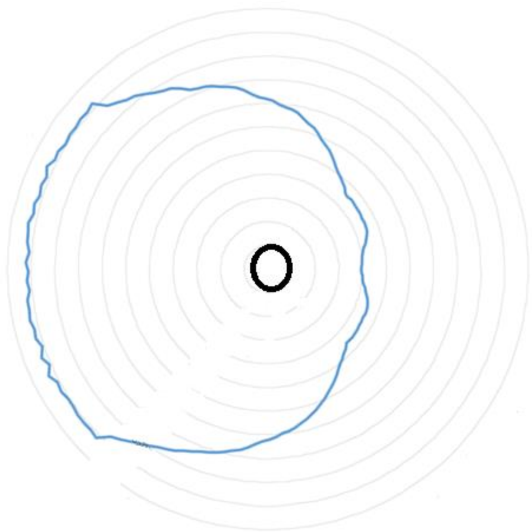

Figure 4. 5. In-plane displacement amplitude in arbitrary units around a 6 mm hole for an incident plane wave approaching from the left-hand side

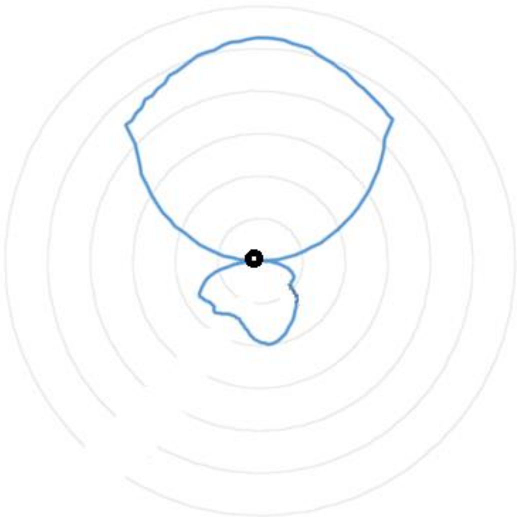

Figure 4. 6. Out-of-plane displacement amplitude in arbitrary units around a 6 mm hole for an incident plane wave approaching from the left-hand-side

Investigations were carried out to evaluate the behaviour of the scattered waves as they propagate away from the defect. Figure 4.7 shows how the displacement amplitude varied as the distance from the defect was increased. The defect was twice the wavelength. The amplitude readings were taken on nodes adjacent to the hole defect and at a distance of one wavelength away from the defect. From the plot it was noted that when readings were taken near the defect there were sharp amplitude variations but as the distance was increased the amplitude smoothened out and the sharp changes disappeared. This was attributed to evanescent fields being present close to the defect but absent further away.

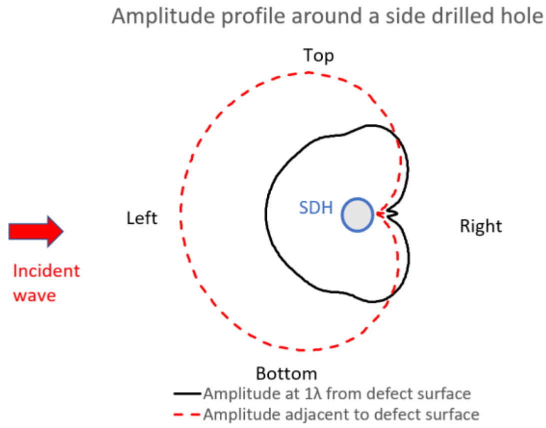

Figure 4. 7. In-plane displacement amplitude in arbitrary units around a 2λ side drilled hole (SDH) for an incident plane wave approaching from the left-hand side

When monitoring was done close to the defect, its profile was almost reproducible. As the distance from the defect was increased the profile of the amplitude begun to change as vibrations from different sources interacted constructively and destructively. When waves interacted with a defect there were evanescent waves generated. When imaging was done for the two defects separated by a gap of less λ/2, and with the sensor located in the near-field, two distinct peaks were observed. Resolution was possible in the near-field. However, the evanescent waves decay exponentially and generally within a wavelength therefore for defects separated by a gap of less than λ/2 and with sensor located in the far-field, only one peak was observed. Resolution was not possible in the far-field. The near-field and far-field here refer to being either within or beyond evanescent field range respectively. Resolution was considered to have been achieved if two distinct signal peaks representing each of the two defects were obtained. It was considered not to have been achieved if only one signal peak coming from two defects was obtained. Since evanescent fields exist close to defect location, the method developed relied on the ability to harness the evanescent fields before they decay off and use them for imaging in the far field. One way that evanescent waves could be recovered was by use of specially engineered metamaterials. Metamaterials were used to achieve subwavelength resolution thus overcoming the diffraction limit.

Scattering of waves by defects is a subject that is well studied in literature (Gupta and Rajagopal, 2023; Rajagopal and Lowe, 2007; Singh et al., 2021). In this work the scattering patterns were investigated with the purpose of optimizing positioning of metamaterial with respect to the defect. The wave scatter directions can be grouped in three namely scatter back to the source (i.e., to the left-side of the defect), scatter in the perpendicular direction (i.e., directly on top of the defect) and scatter in the forward direction (i.e., to the right-side of the defect). The metamaterial can potentially be positioned in any of these three zones. In this work two of the three zones were explored namely the top and the forward components. The rear reflected components were not explored due to lack of appropriate experimental facility. In one case the metamaterial was positioned directly on top of the defect. The advantage of positioning metamaterial directly on top of defect is that the near field of defects spaced in the axial direction can be accessed and the relative positions preserved. In actual inspection it is not always possible to know in advance the position of a defect. In the second case the metamaterial was offset and positioned to the right-side of the defect. This is advantageous in detecting defects even when their position is not known in advance. In the third case the metamaterial can be positioned at an offset to the left-hand side of the defect.

4.3 Wave mode selection

Simulation and experiments were conducted at low frequency-thickness region of the dispersion curve. The area that was selected for operation was the region where basic modes exist. Figure 4.8 shows the dispersion curve of an aluminium plate. The x-axis is frequency-thickness in MHz-mm and the vertical axis is phase velocity in m s^{-1}. Each of the lines represent a wave mode. The A's represent antisymmetric modes and the S's represent symmetric modes. At frequency-thickness below cut-off point which is about 2 MHz-mm on the x-axis, only fundamental modes *A0* and *S0* are present. The region selected was the part of *S0* mode where the curve is flat representing the non-dispersive region. In the non-dispersive regions, the velocity remains fairly constant for any slight changes in excitation frequency and sample thickness. When the frequency is increased the *S0* mode becomes dispersive. This is the sloppy part of the curve where velocity changes rapidly as the frequency is changed slightly. In the highly dispersive regions, a slight change in frequency or thickness leads to a significant change in velocity. This comes with a lot of challenges when it comes to interpretation of signals. The parameters were therefore selected from disperse curves such that only the mode of interest was excited.

At higher frequency-thickness, above 2 MHz-mm, multiple wave modes are generated. This can be seen in the dispersion plots by the many curves present. In theory an infinite number of modes can be generated in guided waves as frequency is increased. When more modes exist in a sample it becomes very difficult to separate the different signals from each of the modes. Additional processing must be carried out to filter the different modes in the region. Hence the motivation to work at low frequencies.

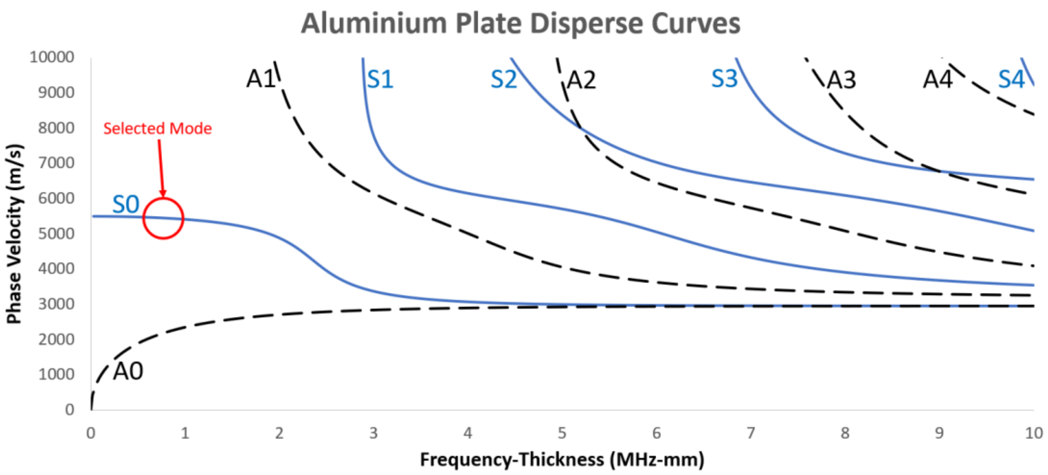

Figure 4. 8. Dispersion curve for an aluminium plate

Frequency and thickness in guided waves are interrelated. In the dispersion plot for the *S0* mode and by selecting 1 MHz-mm as the working region, if a plate of 10 mm is selected then the frequency is fixed at 100 kHz. The thicknesses and frequencies selected for this work was informed by the typical structure thickness in industry and the operational range of commercial equipment.

This work focused on plates due to their geometric simplicity and available experimental facilities. The principles of the method developed can however be extended to geometries that are more complex and implemented accordingly when appropriate equipment is available.

There are many guided wave modes that are generated in a waveguide. The first step in guided wave inspection is to select the wave mode to work with. This is achieved by plotting dispersion curves, selecting the desired region of operation and selectively generating the desired mode. The different regions of the dispersion curve are useful depending on the objectives at hand. For example, the highly dispersive region can be used when the interest is to detect any slight changes in material thickness by noting the change in velocity. The interest in this research was the improvement of resolution. Resolution is a function of wavelength and is limited by the diffraction. By increasing frequency, the wavelength is reduced and therefore to achieve higher resolution the frequency can be increased. From the dispersion curves and to achieve higher resolution, one can opt to operate on the high frequency regions. The problem however is that at high frequencies there are many modes that are generated. This becomes a problem since more sophisticated filtering tools have to be deployed to be able to separate the signals from the different modes. This is the reason why guided waves are generally conducted at low frequencies. Of course, another advantage of low frequencies is that the attenuation is relatively low and the guided wave can travel a greater distance. The low frequency regions were selected for this research. Furthermore, this work required operating at the non-dispersive regions where the velocity remained relatively constant over a range of thicknesses or frequencies. To generate a particular mode, the product of thickness and frequency must remain constant. For a given material thickness, the frequency is fixed by the desired mode. For a smaller thickness the frequency must be increased. In this work a material of thickness 10 mm was selected. From the dispersion curve and to remain on the low frequency zone where only fundamental modes existed and in the non-dispersive section, the frequency of operation needed had to be below 200 kHz. Most of the work reported in this thesis is therefore for frequencies of 75 kHz and 100 kHz propagating in an aluminium sample of thickness 10 mm.

The selection of sample thickness and wave frequency is important in the design of appropriate metamaterials for subwavelength imaging. The sample thickness is generally fixed in real life. In this research the proposed metamaterial for subwavelength resolution work on the principle of resonance tunneling. Each channel of the metamaterial has to attain a state of resonance which is achieved when the channel length equal integer multiples of half the propagating wavelength. For a material of a given thickness, the choice of a given frequency fixes the dimensions of the metamaterial in order to have a state of resonance. Similarly for a metamaterial of a given channel length, the frequency of operating wave has to be selected to achieve a state of resonance.

4.4 Metamaterial parameters and design

Important metamaterial parameters were optimized through simulations. The metamaterials consisted of a liquid/solid composite structure with channels of opening *a*, length *L* and the periodicity of the composite structure was Λ. The channel openings were filled with water. Different materials were explored for the solid part of the metamaterials. These materials included plastics, ceramics and metals. Many investigations were carried out while varying the metamaterial parameters *a*, *L* and Λ. Each of these parameters was varied separately while keeping the other parameters constant. For a working frequency of 100 kHz propagating in an aluminium plate of 10 mm, the phase velocity of the fundamental symmetric mode from the dispersion curve was about 5400 m s^{-1}. Thus, the wavelength in the waveguide at this frequency was 54 mm.

The waves after scattering from defects are transmitted to the water filled metamaterial channels. The wavelength then changes in aluminium to the wavelength in water due to velocity changes in the two medias. For a channel filled with water the velocity of sound in water is about 1500 m s^{-1}. At a frequency of 100 kHz, the wavelength is 15 mm.

The results of the optimization process are presented next. For the metamaterial channel size *a* it was established that subwavelength resolution could only happen when the channel size is much smaller than the working wavelength. In this case working wavelength refer to the wavelength in water. The size of the channel is also related to the smallest separation resolvable. In this work the interest was to achieve subwavelength resolution. To resolve two 6 mm hole defects separated by 1 mm gap in a 10 mm thick plate it was found that the channel size had to be 1 mm or less. Evaluation using metamaterials with channel sizes smaller than 1 mm showed that no additional improvements was gained in terms of resolutions of the defect ranges that were considered. Construction of channels smaller than 1 mm was also a challenge using available research equipment at the time. The challenge of making channels smaller than 1 mm coupled with the lack of additional benefits from smaller sizes in solving the resolution challenge at hand informed the decision to settle for a 1 mm size channel.

The optimum periodicity Λ was established to be twice the channel size, that was 2 mm. The solid part and the hollow part of the channel had the same dimensions.

The metamaterial developed relied on establishment of a resonance status inside of the channels. A standing wave needed to be generated inside the water filled metamaterial channel. This could only happen when the channel length L had dimensions that were multiple integers of half of the working wavelength in water. That is $L = n\lambda/2$ where n=1,2,3, … The resonance phenomenon inside each channel is demonstrated in Figure 4.9. The figure was obtained by analyzing amplitude variation inside a single channel and various frequencies (wavelengths) were considered. Readings were taken at varying time intervals and it was noted that when the channel length were integer multiples of λ/2, then a state of resonance was obtained. At resonance a series of nodes and antinodes were seen thus establishing a standing wave. In the figure, each line represents readings taken at different times. The channel selected in the plot was for a 45 mm (3λ) long metamaterial. The channel was filled with water. Antinodes were observed at 7.5 mm, 15 mm, 22.5 mm, 30 mm, 37.5 mm and 45 mm. These respectively correspond to λ/2, 2λ/2 3λ/2 4λ/2 5λ/2 and 6λ/2. Similar plots can be attained by selecting metamaterial length that corresponds to anti-node locations seen in the image. Only a metamaterial with channel length nλ/2 (where n=1,2,3, … etc.) can be selected for optimum resolution. The length is selected to coincide with the anti-nodes which yields maximum amplitude readings. The image clearly shows that at a state of resonance a situation of standing wave is attained.

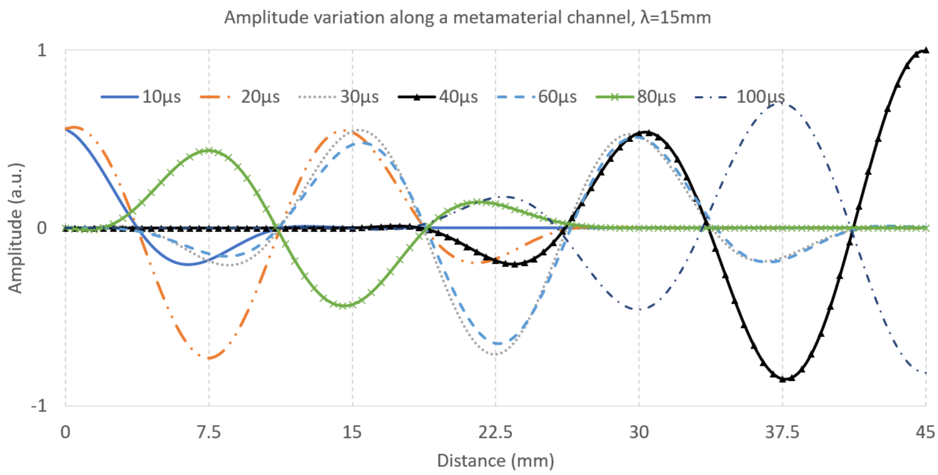

Figure 4. 9. Signal amplitude variation along the length of a single metamaterial channel

In theory any length L of the metamaterial channel can be selected provided it is integer multiple of half wavelength. In simulation this can be achieved. However, in experiment it was possible to achieve wave propagation through the channel up to a few wavelengths in one of the set-ups. The length of the metamaterials was selected to be $L=2\lambda$. By increasing the energy amplitude of the incident wave, the distance of propagation through metamaterial channels could potentially be increased.

The optimized parameters were consistent with what other researchers had established. In acoustics it was determined for similar metamaterial configurations that the size a should be less than a tenth of a wavelength, the spacing between adjacent channels (i.e., pitch) should be even integer multiples of the channel size. Provided that channel dimensions meet the criteria above, propagation of elastic waves can lead to formation of Fabry-Perot resonances within each channel (Askari et al., 2020). Arrangement of such channels side by side lead to metamaterial with novel properties such as subwavelength imaging and signal amplification (Amireddy et al., 2017). The size of the opening was important as it acted as a pixel point preserving the information collected by each channel. The same information was then channeled to a remote location further from the point of generation but confined within each of the metamaterial channels.

The initial metamaterials developed had straight channels with respect to the normal. The channels were perpendicular to the waveguide. As the wave exits the aluminium waveguide and is transmitted to the water filled metamaterial, it was determined that the transmission takes place at an angle. This angle was consistent with Snell's law. The first media was aluminium and the second was water in the metamaterial channels. The angle of scattering was found to be 15.9° degrees obtained as follows: Applying Snell's law,

$(\sin A) / V_A = (\sin B) / V_B$

If $A=90°$, $V_A = 5400$, $V_B=1500$, then $B = 15.9°$

The optimized metamaterial parameters were used to design different types of metamaterials. The metamaterials designed had channel size a = 1 mm, periodicity Λ = 2 mm, pitch p = 1 mm, and channel length L = 30 mm. Two angles were considered namely straight channels (0°) and inclined channels (15.9°). The inclination was with respect to the waveguide normal. The first category of straight channels was used predominantly for resolution of hole defects and were positioned directly above the defect location (Birir et al., 2020). The Figures 4.10 and 4.11 is a metamaterial made from perspex. The metamaterial was made by cutting perspex sheet into desired sizes and assembling by hand. The channels were filled with water. The second category of inclined metamaterials (Figure 4.12) were used predominantly in the detection and resolution of crack defects. The metamaterial was made from mild steel while the channels were fabricated through the process of electrical discharge machining wire cutting. The channels were then filled with water. Inclined metamaterial was an improvement from the straight channel metamaterials and enabled the detection and resolution of defects even when the metamaterial was offset at some distance away from the defect location.

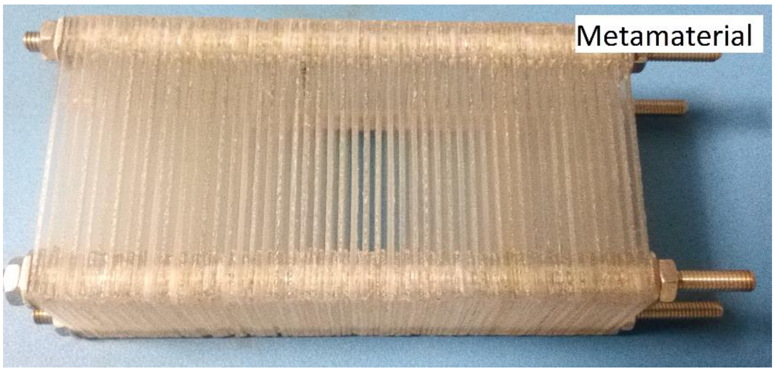

Figure 4. 10. Photograph of straight channel metamaterial

Figure 4. 11. Photograph of straight channel metamaterial positioning on top of defects

Figure 4. 12. Photograph of inclined angle channel metamaterial

The effects of metamaterial inclination angle were also investigated. Figure 4.13 shows the effects of metamaterial channel angles on the resolution. For the case reported in this section it is noted that the signal profile is similar for cases between 0° to 25° of metamaterial channel tilt angles. Above 25° however, the signals profiles change as the peaks location and relative amplitudes appear to shift. This is a subject of further investigation alongside the effects of crack orientation. In the figure, the graphs of 0°, 15°, 30° and 45° inclination angles are presented for comparison.

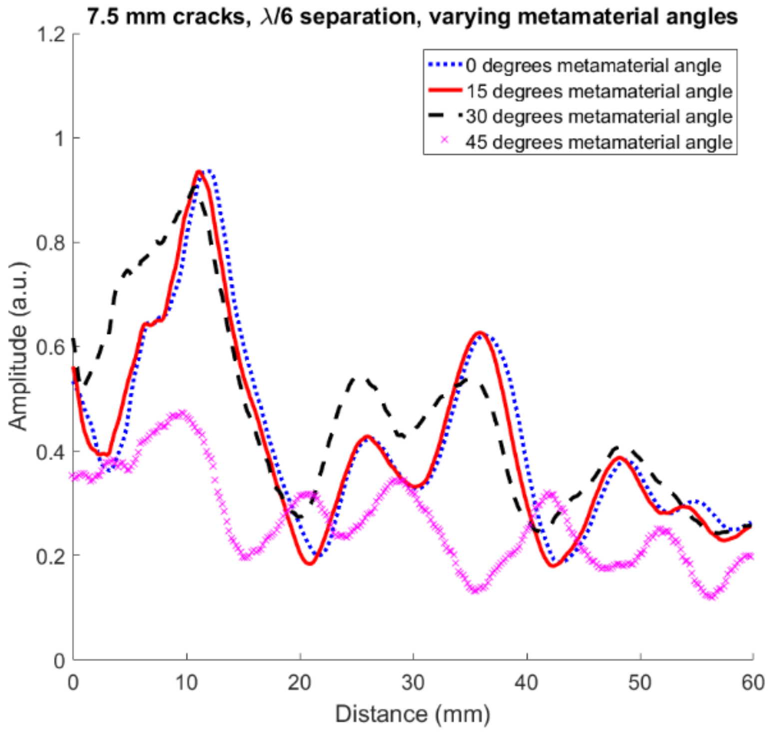

Figure 4. 13. Varying metamaterial channels inclination angle. The signal profiles are similar up to 25° inclination, above which some shift start being noticed

The purpose of the metamaterial was to pick up scattered signals from a defect including evanescent waves in the near field and transmit it to the far field for imaging. Perspex was selected because of the ease of fabrication of the channels from a thin plate. Mild steel was also readily available and machining technology was available to make the desired channels. The choice of water was due to the need of having maximum coupling between the sample and the metamaterial. Ultrasonic waves are totally reflected in the event of an interface with air due to acoustic impedance mismatch.

Water acts as a channel to transmit information as well as acting as the couplant between the test sample and the sensor. When elastic waves interact with a material boundary, part of the wave is transmitted through to the next media while part of the energy is reflected. The boundary is as a result of material property change as the case would be at a defect. The amounts of energy transmitted and reflected is based on impedance mismatch between the two materials. The transmission coefficient in a boundary between two materials, T, is given by $T=(2Z_1Z_2)/(Z_1+Z_2)$, where Z_1 and Z_2 are acoustic impedances of the first and second materials respectively. In addition to the reflected and transmitted waves, an evanescent wave component is also generated at the boundary. These evanescent waves have a higher wave vector (high frequency, short wavelength) than incident wave and they decay exponentially within a distance of approximately one wavelength (O'Hara et al., 2008). Super resolution can be attained by focusing the propagating waves and the enhancement of evanescent waves (Hao et al., 2013; Lewis et al., 2014; Lu and Liu, 2012).

4.5 Resolution limits for rounded defects

In this section results from resolution investigations on rounded defects are reported. Cases were compared with and without metamaterial being incorporated in the inspection system. Different defect sizes and separation distances were considered. Results are presented in the form of scatter plots. Key results are presented in this section. It is demonstrated that by incorporation of metamaterial lens into guided wave inspection system, subwavelength resolution can be achieved.

From theory it is expected that any defects separated by a distance less than half of a 72 mm wavelength cannot be resolved without some form of intervention. Figure 4.14 shows results for the 6 mm diameter holes separated by 1 mm gap. Displacements were measured at a line of nodes positioned above the defect under two conditions: with and without the structured channel metamaterial lens. In simulations, pressure amplitudes were recorded on the water side of the model, as depicted in the conceptual diagram. In experimental trials, the amplitudes of "out-of-plane" displacements were captured using a fiber-optic laser Doppler vibrometer, as detailed in the experimental setup section. Experimental results were overlaid with simulation results. Also overlayed was the case with and without metamaterial. At the selected frequency the wavelength was 72 mm.

As a function of wavelength, the gap between the holes was λ/72 (1 mm) and the holes diameter was λ/12 (6 mm). This translates to a centre-to-centre distance between the holes to be λ/10.3 (7 mm). The holes diameter as well as the separation distances were all smaller than the diffraction limit. From the scatter plots, for the case of no metamaterial, only a single peak was observed. When a metamaterial was used, two peaks were imaged. This demonstrated that the metamaterial had enabled the resolution of subwavelength features. The two peaks coincided exactly with the position of the defects. Results from experiment were in agreement with simulation and therefore a demonstration of the possibility of achieving subwavelength resolution in the guided ultrasonic waves regime using metamaterials.

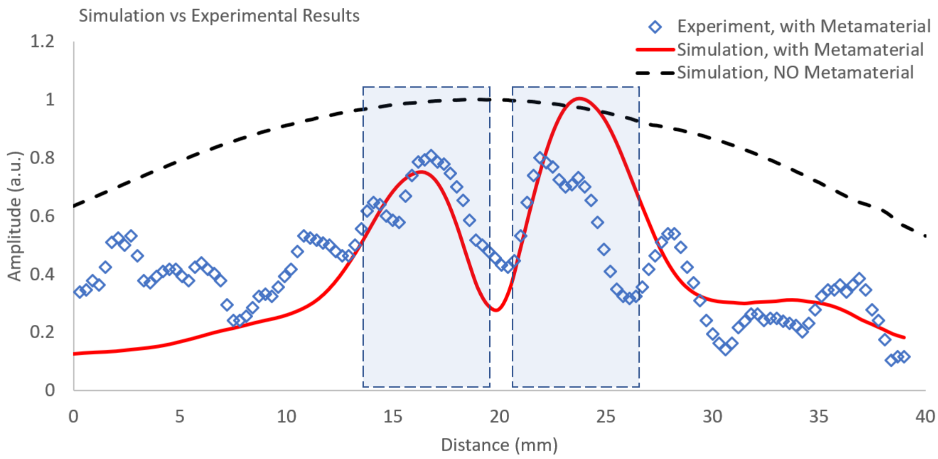

Figure 4. 14. Experimental results for two 6 mm hole defects spaced λ/72 apart imaged with metamaterial, overlaid with simulation results with and without metamaterial

The hole separation distance was varied to verify that the observed peaks actually indicated the position of the defects. As the holes were shifted, the peaks also shifted. This was a confirmation that the peaks observed represented the location of the defects. Figure 4.15 is a scatter plot for 6 mm hole defects with varying separation distances. For clarity only three graphs are presented for 1 mm (λ/72) gap, 8 mm (λ/9) gap, and 36 mm (λ/2) gap. The shaded squares indicate the actual sizes of the defects in the x-axis direction and positions relative to each other. These results are from three different setups and the scatter plots just overlaid in one graph. For the 6 mm holes the smallest resolution was for hole separation of 1 mm (λ/72).

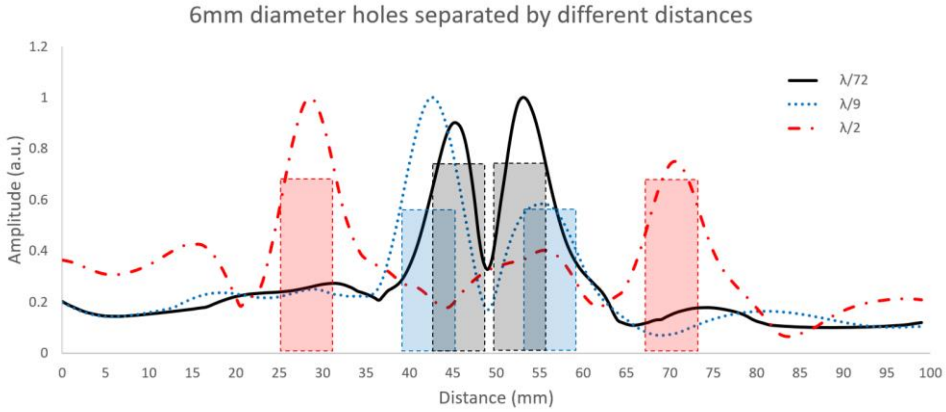

Figure 4. 15. Simulation results for 6 mm holes separated by λ/72 gap, λ/9 gap, and λ/2 gap

The resolution was found to be influenced by the size of the defect. To illustrate this relationship, hole sizes were varied within the range of 3 mm (λ/24) to 9 mm (λ/8) in a 10 mm thick waveguide. Figure 4.16 displays the outcomes for hole sizes of 3 mm, 6 mm, and 9 mm. In each instance, the separation between the holes was consistently maintained at λ/72. The scatter plot reveals that signals from 3 mm holes exhibited only one peak. It was noted that hole diameters less than 6 mm could not be distinguished at the λ/72 separation distance. For holes with diameters equal to or greater than 6 mm, two peaks corresponding to the hole positions were observed.

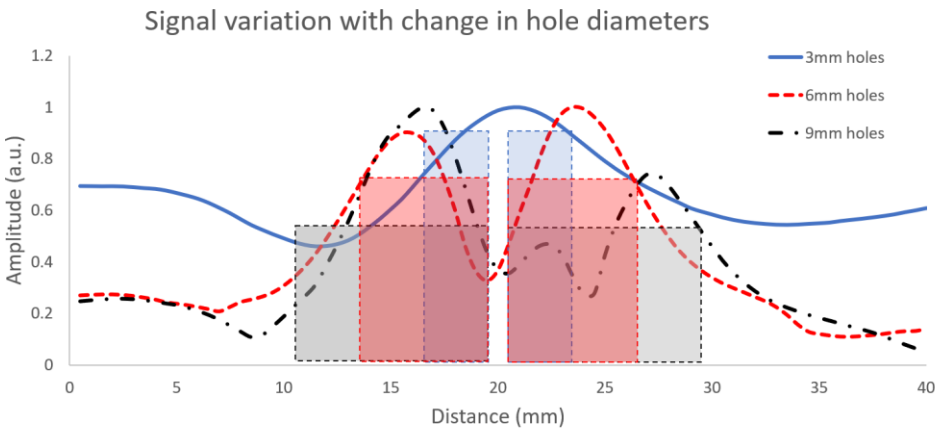

Figure 4. 16. Simulation results for holes of diameter 3 mm, 6 mm and 9 mm for separation gap of λ/72

Investigations were done to evaluate the resolution limits for other defect sizes. In Figure 4.17 results for a 4 mm hole defect is presented. For defects smaller than 6 mm it was noted that resolution was not possible at 1 mm (λ/72) gap. Only one peak was observed. The gap distance between the holes was increased to determine the resolution limit. This is the separation distance at which two peaks start to be observed for the two defects. For clarity the results for hole separation of λ/36, λ/9 and λ/2 are plotted for the case of 4 mm diameter holes. As can be seen from the scatter plot when the separation distance was increased to 2 mm (λ/36) a single peak could still be imaged. However, at a separation of 8 mm (λ/9) two peaks were imaged. Beyond this point the two peaks persist. Thus, for a 4 mm hole defects the resolution limit was found to be λ/9.

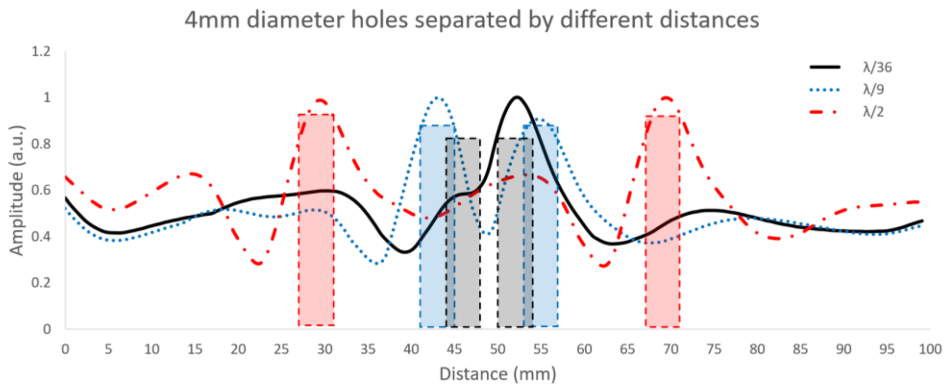

Figure 4. 17. Simulation results for 4 mm diameter holes with separation distances of λ/36, λ/9, and λ/2

Additional simulation results were conducted at 100 kHz central frequency with a metamaterial of channel length 4λ (λ in water channels was 15 mm). As noted earlier it was observed that resolution was a function of hole defect size. Figure 4.18 shows an overlay of 3 mm, 4 mm, 5 mm, and 6 mm diameter holes separated by λ/54. The two defects were resolved with the use of metamaterials for the case of 6 mm diameter holes and could not be resolved for diameters smaller than 6 mm. The Figure 4.19 shows an overlay of 6 mm, 7 mm, 8 mm, and 9 mm diameter holes separated by λ/54. The two defects were resolved with the use of metamaterials in all these cases. Thus, for the case that holes are separated by λ/54, only defects equal to and greater than 6 mm diameter were resolved as demonstrated by the two peaks observed. For smaller defects at the same separation only one peak was observed indicating that the defects were imaged as though it was just one defect.

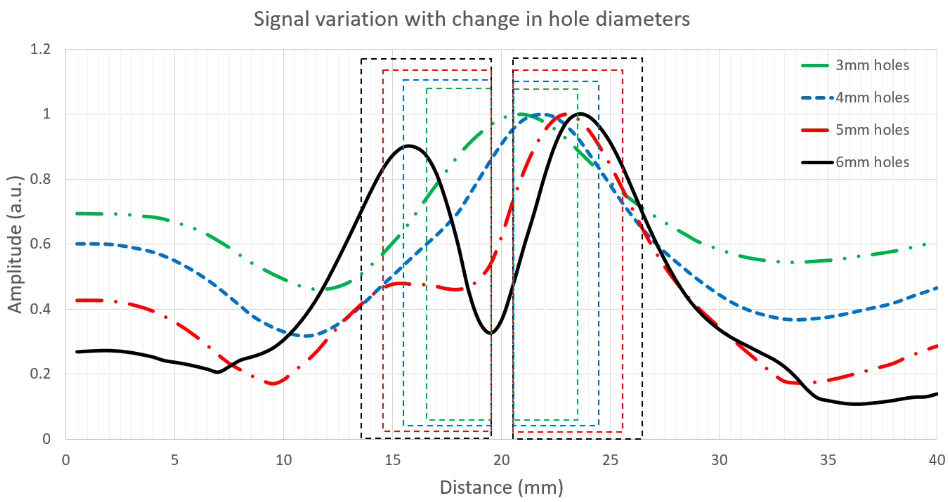

Figure 4. 18. Signal variation with change in hole diameter for separation of λ/54 for hole defects of sizes 3 mm to 6 mm

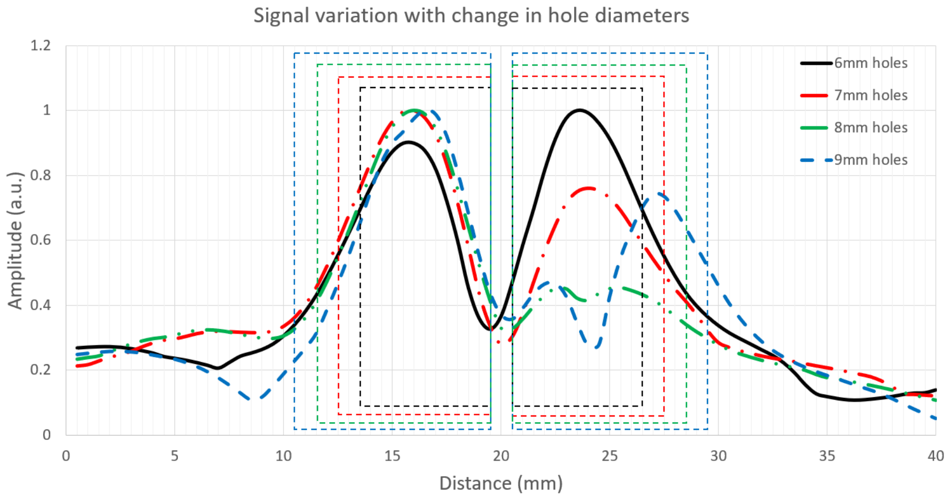

Figure 4. 19. Signal variation with change in hole diameter for separation of λ/54 for hole defects of sizes 6 mm to 9 mm

So far, the results presented are for cases with metamaterials. The results presented next are for both with and without metamaterial. It should be noted that the readings were taken at the same distance from the defect in both cases. For a metamaterial of channel length 4λ (λ in water channels was 15 mm) the readings were taken at a distance of 60 mm from the waveguide surface for when metamaterial was used and when it was not. At a distance of 4λ it was noted that the use of metamaterial not only aided in the resolution but also in the ability to detect the defects. The Figures 4.20 to 4.24 shows results for 6 mm diameter holes. The hole separation distance in each case was λ/27, λ/10, λ/8 λ/4, and λ/2 respectively. The continuous line is for cases with metamaterial and the dashed for cases without. In all these cases it was noted that when a metamaterial was used two peaks were observed at the exact defect locations. When no metamaterial was used no peak was observed. In other words, at the lift-off distance of 4λ the defects could not be detected without the aid of a metamaterial.

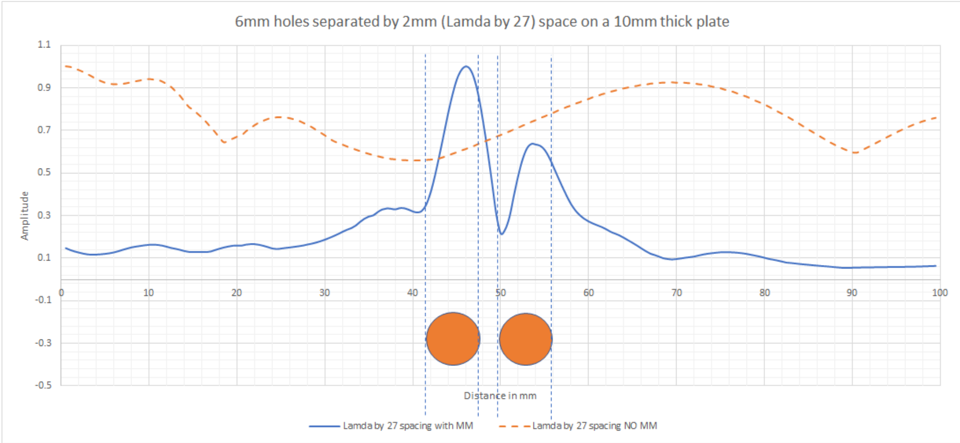

Figure 4. 20. Simulation results for 6 mm holes separated by λ/27 gap, with and without metamaterials (MM)

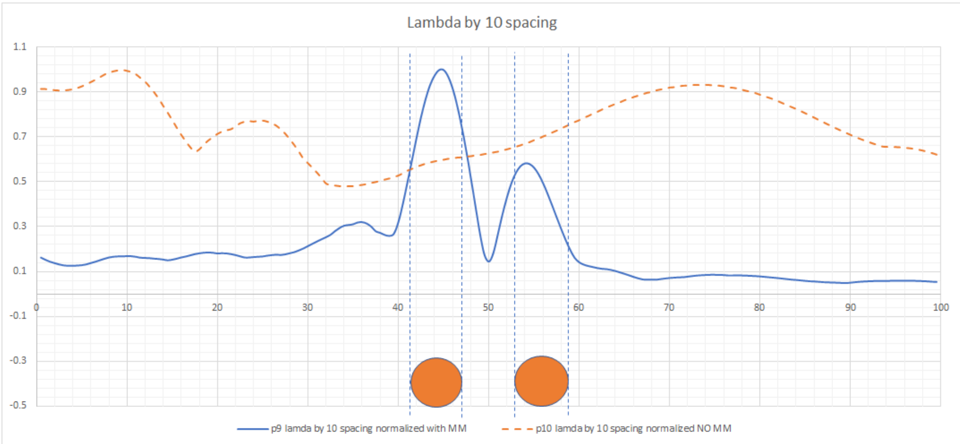

Figure 4. 21. Simulation results for 6 mm holes separated by λ/10 gap, with and without metamaterials (MM)

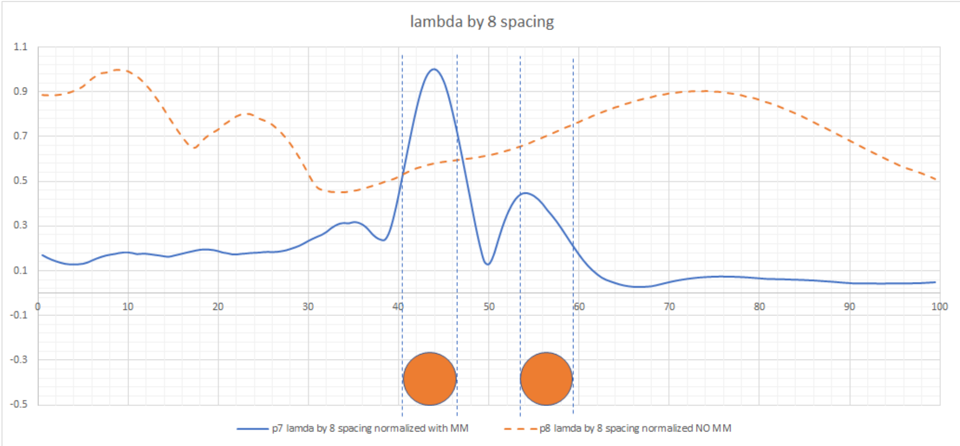

Figure 4. 22. Simulation results for 6 mm holes separated by λ/8 gap, with and without metamaterials (MM)

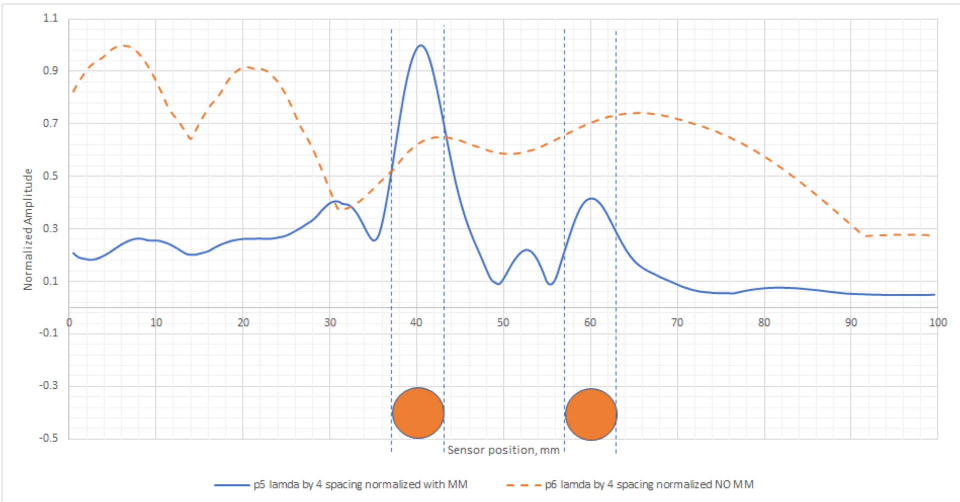

Figure 4. 23. Simulation results for 6 mm holes separated by λ/4 gap, with and without metamaterials (MM)

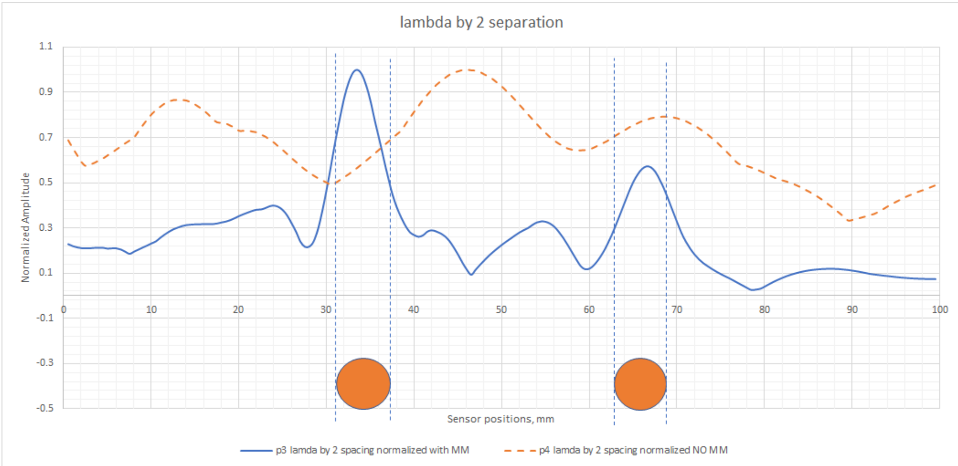

Figure 4. 24. Simulation results for 6 mm holes separated by λ/2 gap, with and without metamaterials (MM)

It was observed that the use of metamaterials made it possible to achieve subwavelength resolution. The peaks observed in the findings were ascribed to diffractions originating from the circular hole defects. A portion of the signal underwent diffraction in the perpendicular direction as the incident wave interacted with the reflecting holes. The sensors placed above the defect detected this diffracted signal. The results from experiments were overlaid with simulation results. There was a good agreement between these results. It was demonstrated that flaws much smaller than the working wavelength can be resolved by the proposed structured channel metamaterial lens.

The level of resolution was dependent on defect size. As the hole diameter was increased, a higher level of resolution was achieved. On the other hand, for smaller defects the resolution was poorer. The holes presented here were centred at the central axis of the bar. The distance from the wall of the defect to the boundary of the structure reduced as the hole diameter increased. Resolution was related to the distance the wave has to travel before arriving at the metamaterial. When distance was smaller more details could be picked by the metamaterial before they could be lost due to interference of signals from adjacent defects. When the defects were further apart however it required a longer travel distance before the signals from the two defects interfere with each other. This explains why as the size of defect got smaller, they needed to be further apart for resolution to happen with the aid of metamaterials. Furthermore, in all these cases when there was no metamaterial used, the defects could not be resolved when they were separated by distances less than the diffraction limit. Given that the flaw is substantially smaller than the diffraction limit, this was to be expected. Therefore, without some sort of intervention, it was impossible to resolve the two flaws that were subwavelength apart. However, due to metamaterial's ability to recover the evanescent components, flaws were resolved with clarity when it was deployed. It was concluded that using metamaterial helped to achieve super resolution imaging of hole defects. In the regime of guided ultrasonic waves, the resolution of $\lambda/72$ was attained. This resolution applies to the particular configuration and size of the above-mentioned metamaterial.

Both simulations and experiments were conducted however simulations were conducted in ideal situations where it was assumed there was no viscosity and losses. In real life experiments, some losses were expected and experienced due to effects such as absorption losses. Simulation also assumed a perfect smooth defect. In practice it was not possible to reproduce a perfect defect due to fabrication limitations and human factors.

4.6 Resolution limits for linear defects

In this section results from resolution investigations on linear defects are reported. Different defect sizes and separation distances were considered. The metamaterial used had an inclination consistent with Snell’s law to maximize energy transfer. As it is not always possible to know the exact position of a defect so as to position the metamaterial lens on top of the defect, cases were considered in which the metamaterial was offset some distance away from the defect. Key results are presented in the form of scatter plots in this section. The results presented are for a working frequency of 100 kHz. For a frequency-thickness of 0.1 MHz-mm and by choosing a bar of 10 mm thick the frequency was fixed at 100 kHz. The wavelength (λ) at this frequency was large (54 mm). From theory any defects separated by a distance less than half of this wavelength (i.e., 27 mm) are unlikely to be resolved without some form of intervention.

It was demonstrated that by incorporation of metamaterial lens into guided wave inspection system, subwavelength resolution was achieved. When the metamaterial lens was offset, it was still possible to determine the exact location of the defects. This was a huge breakthrough in the field of guided waves for remote defect detection and location. The results presented are for guided ultrasonic waves imaging of crack-like defects separated by subwavelength distance. Two key results are presented in this work. First result was that subwavelength defects were resolved and the second was that the defect location with respect to the sensor location was determined. This was achieved with the aid of a channel metamaterial lens in both simulations and experiments. Experiments were carried out to validate the developed simulation model. Various crack sizes were investigated. For the selected mode and a working frequency of 100 kHz, the velocity was 5400 m s^{-1} resulting in a wavelength (λ) of 54 mm in aluminium plate. Variables considered included crack size, crack separation distance and metamaterial offset distance.

The first result presented is for subwavelength imaging. The Figure 4.25 shows results of two cracks separated by $\lambda/6$. The metamaterial was offset by a distance of $\lambda/2$ from the 'far-tip' of the crack. The amplitude has been normalized to the maximum value for each curve. The x-axis is distance measured from the second defect. The leading edge of the metamaterial was offset a distance of 27 mm ($\lambda/2$ in aluminium) and the cracks presented are of depth 9 mm, 7.5 mm and 4 mm. Two main peaks were imaged. In each case there were two cracks separated by a distance of $\lambda/6$ (9 mm). A close evaluation of the results showed that the location of the peaks was consistent with what was expected. On the scatter plot the dashed rectangle shape shows the incident wave peak whereas the dashed elliptic shapes show the peaks from the cracks. The incident peak is at about 42 mm (on the x-axis). The crack peaks are at about 69 mm and 78 mm. By measuring the separation of these peaks on the x-axis it was established that from the first peak (marked as 'Incident' in the plot) to the second peak (marked as 'Crack2') the distance is 27 mm ($\lambda/2$) while from the second peak to the third peak (marked 'Crack1') the distance was 9 mm ($\lambda/6$). The distance between the first peak and the second peak represented the metamaterial offset distance from the second crack. (The relative positions are presented in methodology section). The distance between the second peak and the third peak represented the separation distance between the cracks. The vertical dashed lines in the plot indicate the expected relative positions of the two cracks (marked 'Crack1' and 'Crack2') and the incident wave (marked 'Incident') peaks. These peaks were as a result of represented multiple reflections back and forth between the cracks in which the metamaterial, amplified the latter. Since the metamaterial was close enough to the evanescent fields from the cracks the recovery of the fields aided the subwavelength imaging.

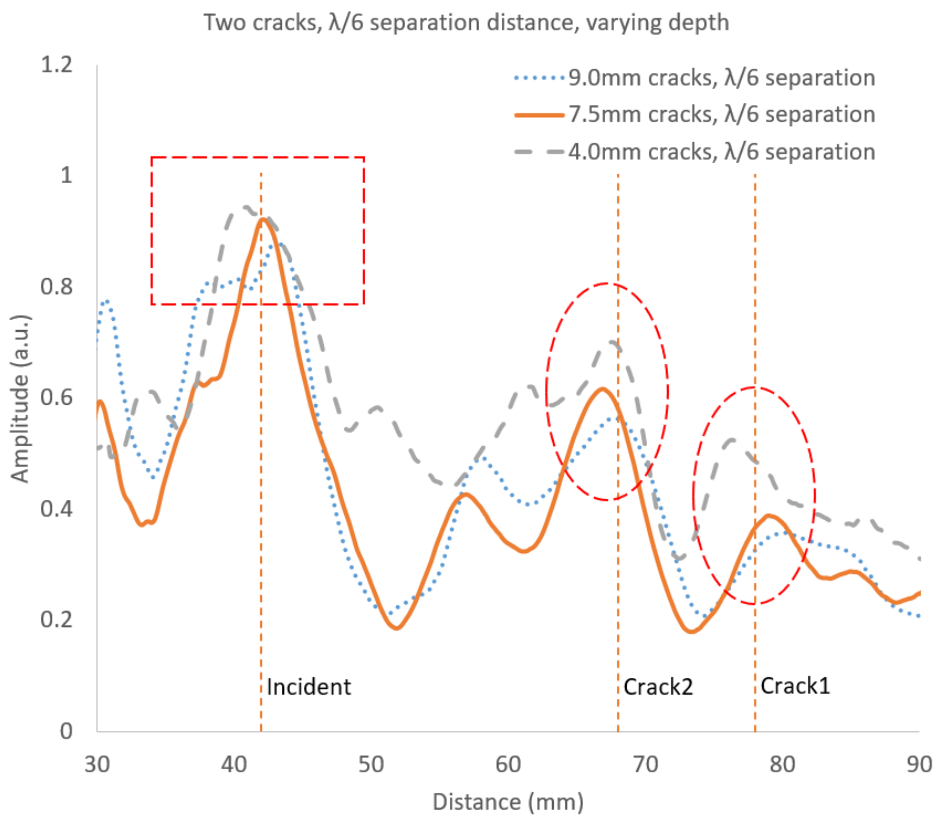

Figure 4. 25. Simulation results for 9 mm, 7.5 mm and 4 mm cracks separated by λ/6 gap, with λ/2 metamaterial offset

Simulation model was validated by experiment. The Figure 4.26 shows the experimental results used to validate the model. Simulation results is overlayed on the experiment results. It was seen that experimental and simulation results were similar in terms of the position of the peaks. The sample used was an aluminium plate of thickness 10 mm. Two cracks of 3 mm depth each and separated by 9 mm (λ/6) are clearly resolved. The metamaterial was located some distance away from the defects at an offset of λ/2. The two peaks observed demonstrate this. The incident peak is at about 37 mm on the x-axis. The two peaks from the cracks are at about 64 mm and 73 mm on the plot. Again, here the distance from the first peak (marked 'Incident') to the second peak (marked 'Crack2') was equivalent to the metamaterial offset distance while the distance between second and third peak (marked 'Crack1') was equivalent to the crack's separation distance. Vertical dashed lines have been used on the scatter plot to mark the relative positions of the incident wave and the reflections from the cracks.

Experiments done with different crack depths were similar with simulation results in terms of position of the peaks.

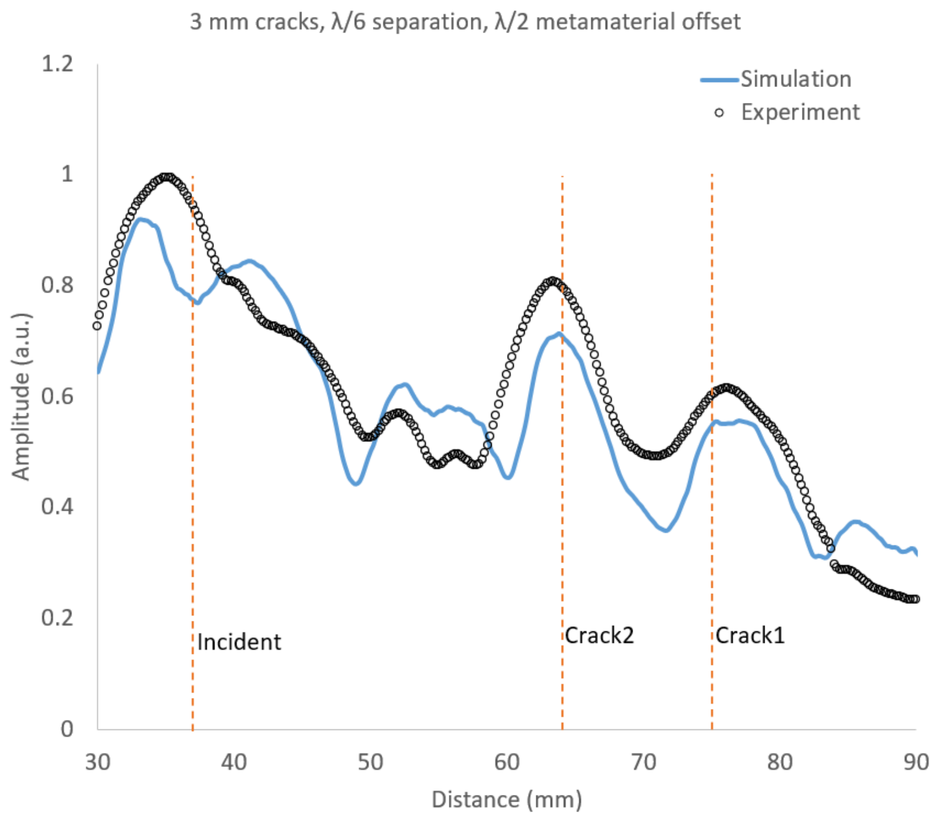

Figure 4. 26. Simulation vs experimental results for 3 mm cracks separated by λ/6 gap, with λ/2 metamaterial offset

So far, crack penetration greater than or less than 5 mm (50 % penetration for a sample of 10 mm thickness) have been considered. When cracks of 5 mm depth separated by λ/6 with metamaterial offset of λ/2 was considered, there was a slight variation in the cracks' peaks positions. Instead of the peaks appearing on the positions of each of the cracks or at least on the position of the crack closest to the metamaterial, the peak appeared in between the two crack positions. The Figure 4.27 is a scatter plot of simulation and experiments conducted for cracks of depth 5 mm. Both simulation and experiments agreed. As can be seen the second peak is appearing midway between where the first and the second crack peaks are expected to be. This was as a result of the signals from the two cracks interfering with each other leading to the two defects appearing and being imaged as though it is one defect.

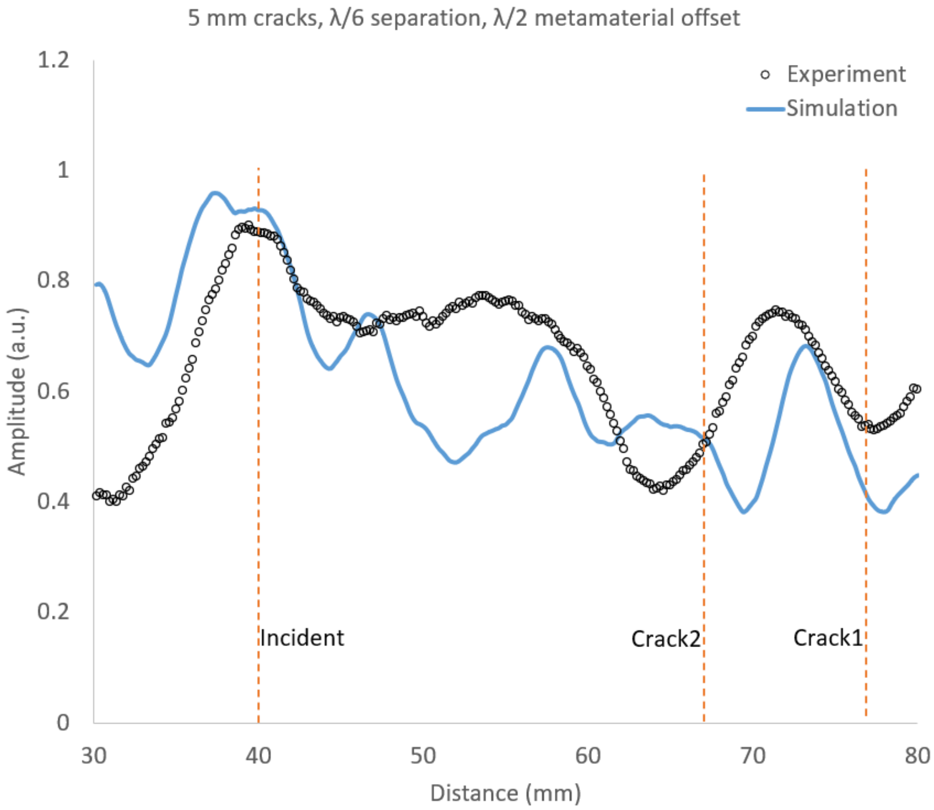

Figure 4. 27. Simulation vs experimental results for 5 mm cracks separated by λ/6 gap, with λ/2 metamaterial offset

The two crack peaks observed in the cases presented so far was as a result of multiple reflections between the defects and the metamaterial as well as the latter's ability to harness evanescent fields originating from the defects. By measuring the separation between the first and second peak the actual position of the defects with respect to the metamaterial position was determined. The peaks separation distance was equivalent to the metamaterial offset distance. To demonstrate this fact the metamaterial offset distance was adjusted back and forth and it was observed that indeed the separation distance between the first and second main peaks changed accordingly. For clarity only two offset distances are presented in Figure 4.28. Here results for two metamaterial offset distances of λ/2 and λ/3 for the case of a 7.5 mm crack are presented. By aligning the position of the first peaks it was noted that as the offset distance was increased so did the relative position of the second peak. For the continuous line in the plot the separation distance between the two peaks was about 27 mm (λ/2) which was consistent with an offset distance of λ/2. Similarly, for the dashed line the separation distance between the two peaks was about 18 mm (λ/3) which is consistent with an offset distance of λ/3.

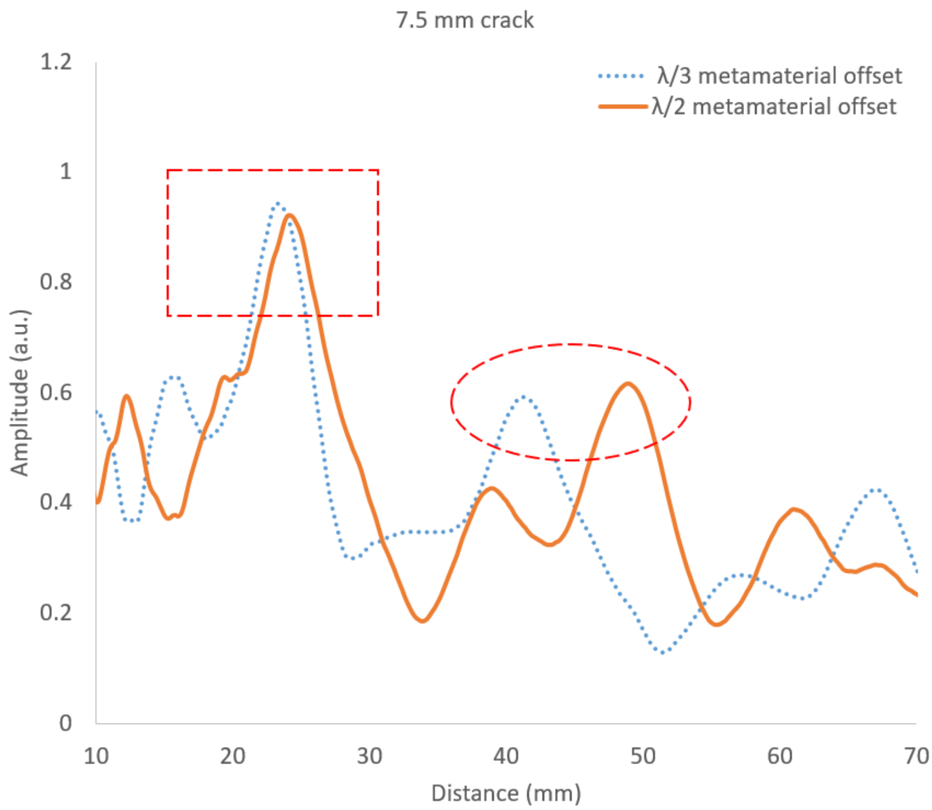

Figure 4. 28. Simulation results for 7.5 mm cracks separated by λ/3 and λ/2 gap, with λ/2 metamaterial offset

This was a novelty since it demonstrated that simply by adjusting the position of the metamaterial the precise location of the defect with respect to the sensor location was determined. The distance between the incident and the second peak indicated the exact distance to the defect from the sensor location.

To evaluate the resolution limits for the selected defects, cracks of different depths and different separation distances were considered. The results obtained indicated that resolution was a function of the distance of each crack from the metamaterial. While holding the metamaterial offset distance constant, by increasing the separation between cracks, the distance of the first crack from the metamaterial was simply increasing. As the distance increased the evanescent fields from the first crack (the crack furthest from the metamaterial) could no longer reach the metamaterial. Hence the resolution was lost at that point. As the separation distance was increased, only the crack closest to the metamaterial could be imaged. This is indicated by a single peak corresponding to the 'Crack2' position. This was because the distance from the first defect to the metamaterial had increased and thus evanescent waves field was not being picked by the metamaterial for imaging. When the metamaterial was offset a distance of λ/2 (where λ=54 mm) from the second crack, it meant that the first crack was even much further from the metamaterial lens. For crack separation of λ/6 and metamaterial offset of λ/2 the first crack was at a distance of λ/1.5 from the metamaterial. As the crack separation distance was increased beyond λ/6 it was no longer possible to image both cracks. Only the crack closer to the metamaterial could be imaged as the separation distance was increased further. For simplicity, three different crack depths with metamaterial offset by λ/2 are plotted. In Figure 4.29 the results for λ/2 (27 mm) defect separation for varying crack depths (9.0 mm, 7.5 mm and 5.0 mm) are presented. For these three cases, it was observed that there were two main peaks appearing. The first peak represents the 'Incident' wave peak. The second peak represent the peak from the crack closest to the metamaterial (marked 'Crack2' in above results). The dashed rectangular shape indicates the incident peak whereas the dashed elliptic shape indicates the peak from the crack. The peaks are separated by approximately 27 mm which is equivalent to the offset distance from the second crack. The Figure 4.30 shows results for two cracks 5 mm deep, separated by λ/3 gap with metamaterial offset λ/2. Again, here the two defects were not resolved. The distance between the incident peak and crack peak was equivalent to the metamaterial offset distance. Thus, the defect closer to the metamaterial side was detected.

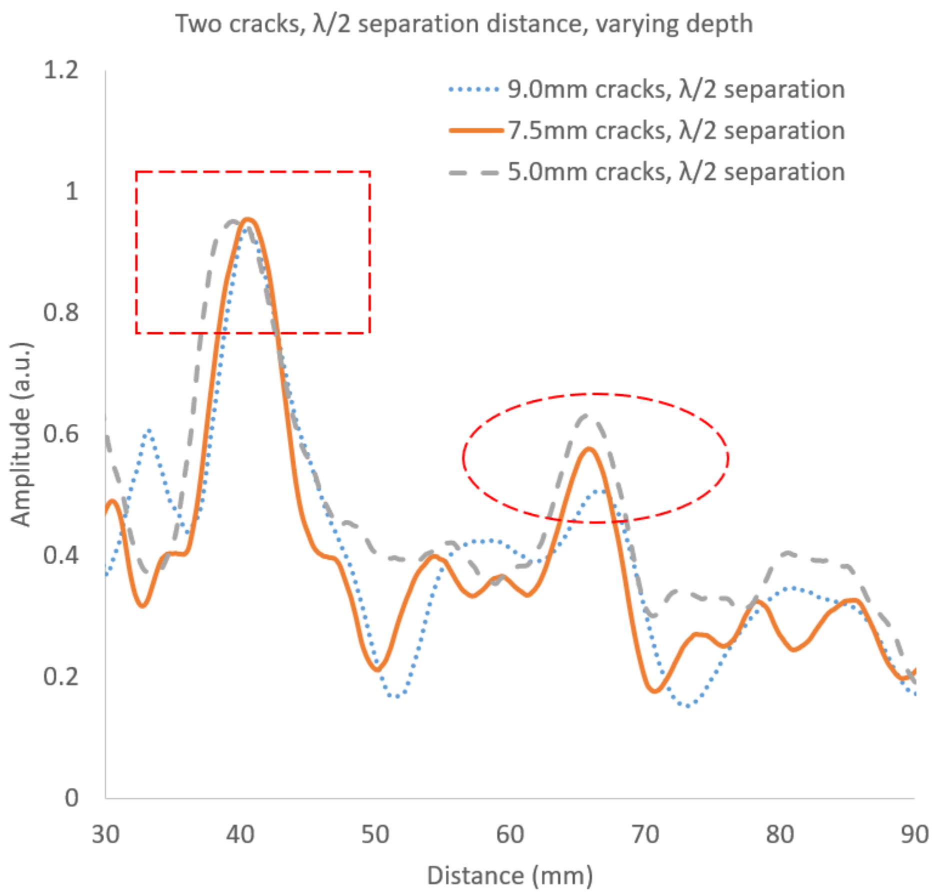

Figure 4. 29. Simulation results for 9 mm, 7.5 mm and 5 mm cracks separated by λ/2 gap, with λ/2 metamaterial offset

To evaluate the resolution limits for linear defects, cracks of different depths and different separation distances were considered. The results obtained indicate that resolution was a function of the offset distance of the metamaterial from the defects. Each of the variables was varied while holding all other variables constant. Various crack depths and separation distance in a 10 mm thick aluminium plate were considered. Notable results here is that by offsetting the metamaterial away from defects, the actual position of the defect was determined simply by evaluating the distance between peaks. For small offset distances cracks separated by subwavelength distance was resolved. Subwavelength resolution was possible when the metamaterial offset distance was equal to or smaller than λ/2 and when the crack separation distance was equal to or smaller than λ/6. As the crack separation distance was increased or as the metamaterial offset distance was increased then resolution was lost. However, despite the loss of resolution the second defect which was located closer to the metamaterial side was detected and actual relative position determined.

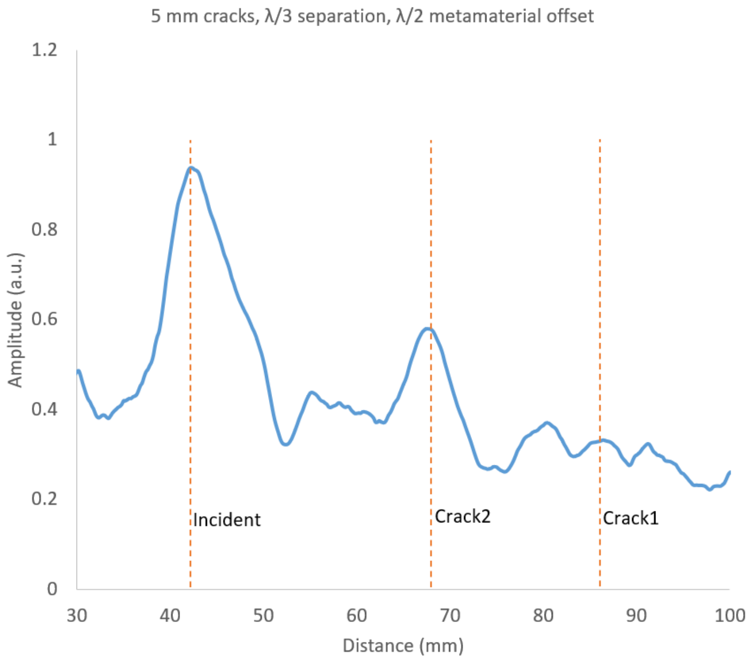

Figure 4. 30. Simulation results for 5 mm cracks separated by λ/3 gap, with λ/2 metamaterial offset

In this thesis the objective was to develop a guided wave inspection system that enabled detection of defects that are usually located at difficult to access areas. The method adopted was the use of metamaterials which have potential of picking evanescent waves to aid in imaging. Both simulation and experimental results were considered. There was a great agreement between both results. The simulation model was used to evaluate many other variables. Few selected results have been presented for purposes of clarity.

In practice the defects that are of great interest are those located on the inaccessible side such as under a storage tank bottom plate or inside of a pipe. Hence the cracks that were considered are the ones that lie on the opposite side to the detector location. The depth of the cracks into the sample plate thickness was varied. The spacing between cracks was also varied. The spacing was less than diffraction limit. Cases were considered with and without metamaterials. It was noted that detection and resolution of cracks was different from the case of holes. It was anticipated, based on reviewed literature, that indeed the detection of cracks is quite a challenging task. This necessitated the variation of metamaterial location relative to the defects. Also, the angle of inclination of metamaterials was changed so as to maximize on the detection and resolution of cracks.

Two key results demonstrated in this work were the subwavelength resolution of crack-like defects and the ability to achieve this while the sensor is positioned some distance from the defects. The guided ultrasonic wave considered was incident from the left-hand side, interacted with two defects in the middle and the metamaterial lens and imaging was done on the right-hand side. There was a state of resonance that was established between the defects and the metamaterial. The angles of the metamaterial channels with respect to the waveguide were optimized by Snell's law to ensure maximum energy transmission between the waveguide and metamaterial as the wave is 'trapped' and bounced back and forth between the defect and the metamaterial sensor. Two concepts were at play here. First concept was related to the evanescent fields at the defects and second concept was the resonance established between defect and metamaterial. Subwavelength resolution was possible because of the recovery of evanescent fields. When a metamaterial was located within this field it was able to recover the evanescent waves. The best resolution that was achieved in the set-up presented in this work was $\lambda/6$. As the offset distance was increased, the evanescent fields get out of range hence could not be imaged. Even though resolution was not possible as the offset distance was increased beyond a wavelength, it was still possible to detect and locate the defects. This in itself was a great breakthrough in the field of guided waves inspection. After locating the defects, the metamaterial had to be brought closer to within a wavelength of both cracks to be able to resolve them.

To summarize this chapter, results have been presented and discussed on a method developed that enabled subwavelength resolution imaging in guided ultrasonic waves. A plate was inspected using the proposed technique. Different types and sizes of defects were fabricated into the plate. An understanding of wave scattering patterns was important in determining the metamaterial positioning with respect to defects. Selection of wave modes dictated the choice of metamaterial dimensions. The metamaterials were used to aid in subwavelength imaging. Simulation and experiments were then carried out to determine the resolution limits of selected defect types using designed metamaterials. Two techniques were developed with the use of metamaterials. The first technique involved the positioning of the metamaterial directly on top of the defect. This was used to image hole defects. A metamaterial was developed and it was able to attain subwavelength resolution in the guided waves regime (Birir et al., 2020). This first technique required that a defect location be known in advance. The second technique involved offsetting of metamaterial some distance away from the defects. This was used to image crack defects. The offset technique was found to be important for purposes of detecting defects that were located in hidden or otherwise inaccessible locations (Bai et al., 2020; Chen et al., 2019; Ducousso and Reverdy, 2020; Trushkevych and Edwards, 2019). Thus, it was possible to obtain subwavelength resolution without the need to position the metamaterial directly on top of the defect. This was of practical significance since in real life cases the location of defects is generally not known in advance. An example of a scenario envisioned here is a pipe going through a concrete wall. Since the pipe section within the wall thickness cannot be accessed to position metamaterial sensor directly on top it is envisioned that a metamaterial positioned away from the wall section will still be able to pick up signals scattered from any defect that might be located within the wall thickness where the pipe is going through. This technique can also be used to detect defects such as corrosion located too close to a weld or structural supports.

This research has demonstrated that it is possible to utilize the long-range capabilities of guided waves to carry out comprehensive high defect-resolution inspections. The need for a secondary technique could no longer be necessary. Previously guided waves were used for screening purposes only to identify areas of interest that required detailed evaluation. With the improved resolution the guided waves can be used not only for screening but also for detailed characterization of flaws. This finding is of great interest to asset management organizations as it provides a cost-effective method that ensures integrity of structures that are difficult to access. These assets include nuclear power plants whereby access to certain areas and components of the plant are usually prohibited by the high radiation levels.

Adoption of this technology is expected to reduce the cost of inspection and to increase the safety of structures, pipelines and nuclear power plants. In addition to the needs of the high-end industries, this technology can also be adopted for use in improving the quality and ensuring the safety of products delivered by the local small and medium enterprises.

CHAPTER 5: CONCLUSION AND RECOMMENDATIONS

5.1 Conclusions

This research work aimed at developing an improved resolution in guided waves testing. This was achieved through simulations and experimental work. Metamaterials were successfully explored for this purpose. Important dimensions such as pattern, periodicity, spacing and length were investigated, determined and optimized by simulation using commercial finite element analysis software. These metamaterials were then fabricated and experimental work carried out to validate the simulation model.

The fundamental guided wave modes at low frequency-thickness regions were evaluated to be convenient for resolution investigations. At these regions only the two fundamental modes exist. In addition, the region that was selected for excitation was identified to be the section in the dispersion plots where the modes had limited dispersion. The choice of low frequency-thickness non dispersive fundamental mode regions ensured that multiple signals that would otherwise have been encountered at higher frequencies with many dispersive modes present was avoided. For optimum transmission and resolution in the configuration considered, it was determined that the metamaterial channel sizes had to be a tenth of a wavelength or less, the periodicity had to be twice the channel, and the length of each channel had to be integer multiple of half wavelength. From experimental results, the metamaterial channel length of two wavelengths was found to be ideal and convenient to fabricate and use.

Two types of discontinuities, namely holes and cracks, were considered. Two cases of metamaterial location relative to defect were considered. In one case metamaterial was positioned directly above the defects. In another scenario the metamaterial was offset at varying distances from the defects. Resolution was improved thus overcoming the diffraction limit in all the cases considered with the aid of a metamaterial. A resolution of $\lambda/72$ and $\lambda/6$ was attained for hole and crack defects respectively. The actual distance of the defects from the sensor was also determined. This is a demonstration in guided ultrasonic wave testing that the location of a defect can be detected even when operating in the through-transmission technique.

The presented findings in this thesis have potential for wide applications. With improved resolution to the levels usually attained only by bulk ultrasonic waves, the guided waves could be used as a final inspection technique rather than being used only as a screening tool. This could lead to reduction in inspection time due to guided waves inspection covering 100% of volume of interest over long ranges as well as reduced intervals of excavation for the case of buried structures. Hazardous areas such as radiation zones, chemical zones and high temperature zones could be inspected without the need to be in close proximity to these areas. This could lead to increased safety of the structures as well as protection of the inspection personnel through reduced risks. The adoption of this technology could also lead to reduced cost due to the reduced time of inspection, reduced excavation requirements, reduced need for a secondary inspection technique for characterization of defects as well as reduced insurance premiums and safety gears for inspection workers.

Employing metamaterials for subwavelength imaging in guided ultrasonic wave testing holds promise in enhancing resolution and it is necessary to consider the challenges related to design, fabrication and practical implementation limitations. As technology advances and more research focuses on overcoming these challenges, the potential for metamaterials in ultrasonic testing for subwavelength imaging may become more feasible and practical in the future. The proposed metamaterials needed to be located in close proximity to the defects. This presented both advantages and limitations hence warranting some critical analysis. The first advantage was that this close proximity ensured evanescent fields were captured enabling subwavelength imaging. This allows for the detection and characterization of defects or structures smaller than the diffraction limit of the probing waves. The second advantage was that the metamaterial could be engineered for specific applications and defect types. This allows for customization of their parameters (hence properties) to optimize imaging for different scenarios. The limitations of the proposed solution must also be considered. First challenge is that there is need for expensive manufacturing techniques to ensure precision because the properties of these metamaterials can be highly sensitive to their structure and composition. Secondly, the metamaterials needed to be in close proximity to the object as well as the defect for optimal performance. This constraint could limit their practicality in some testing scenarios and applications. Thirdly, the metamaterials needed to be designed to work on a specific frequency band (or wavelength). Therefore, if the frequency range of interest in the ultrasonic testing deviates significantly from the operational band of the metamaterial, its effectiveness might be limited.

5.2 Recommendations

This work has demonstrated the concept of using metamaterials to improve on resolution capability for guided wave inspection. The developed technique could for example be applied in structural health monitoring whereby the metamaterial can be embedded with the structure, during the construction stage, at strategic positions and the signals from these sensors monitored over time to determine any variations as a result of defect development and growth. In the design of the metamaterials proposed in this work it is recommended that the channel holes should be smaller than a tenth of the probing wavelength while the channel lengths should be integer multiples of half a wavelength.

Additional work can be done to improve commercial viability of the proposed solution. The resolution achieved in this research was for side drilled holes and cracks in a plate. For holes the maximum resolution achieved was for holes greater than 50% of sample thickness in diameter. More work could be done to bring resolution of smaller diameter holes to the same level. Improvement in cracks' resolution is also recommended to be brought to the same level as for holes. Work can also be done to consider other shapes of defects and ultimately realistic randomly oriented and randomly shaped defects that represent randomness in real life situations. In all cases possibility of even better resolution beyond what is reported in this work should be considered. This can be done by further optimization of wave modes variation, metamaterial design and configuration.

The carried-out investigations were mainly on simple geometry of a plate to prove the concepts. Other shapes of test sample remain to be explored in greater details such as symmetric pipes, bars, rods, asymmetric rails, beams among others. Therefore, the concepts developed for plates can be optimized and applied to other shapes of structures.

The fundamental mode of the low frequency-thickness in the limited dispersion region was used for excitation in this study. Future research could explore higher frequency-thickness region with multiple modes to investigate the implications and viability of operating at these regions. The advantage of operating at higher frequencies is that wavelength is smaller and thus a higher resolution in absolute terms can be achieved.

The study also used the pitch-catch configuration whereby the excitation probe and the receiver sensor are on opposite sides on the defect. Future work could explore the pulse-echo configuration whereby the transmitter and the receiver are in the same position. The advantage of pulse-echo mode is that access to the second side is no longer necessary.

REFERENCES

Achenbach, J. D. (1999). *Wave propagation in elastic solids* (8th ed.). Elsevier B.V.

Alleyne, D. N., Lowe, M. J. S. S., & Cawley, P. (2015). The reflection of guided waves from simple dents in pipes. *Ultrasonics*, *57*(C), 190–197. https://doi.org/10.1016/j.ultras.2014.11.012

Alleyne, D. N., Pavlakovic, B., Lowe, M. J. S., & Cawley, P. (2001). Rapid long-range inspection of chemical plant pipework using guided waves. *Insight: Non-Destructive Testing and Condition Monitoring*, *43*(2), 93–96. https://doi.org/10.1063/1.1373757

Amireddy, K. K., Balasubramaniam, K., & Rajagopal, P. (2016). Holey-structured metamaterial lens for subwavelength resolution in ultrasonic characterization of metallic components. *Applied Physics Letters*, *108*(22), 224101. https://doi.org/10.1063/1.4950967

Amireddy, K. K., Balasubramaniam, K., & Rajagopal, P. (2017). Deep subwavelength ultrasonic imaging using optimized holey structured metamaterials. *Scientific Reports*, *7*(1). https://doi.org/10.1038/s41598-017-08036-4

Amireddy, K. K., Balasubramaniam, K., & Rajagopal, P. (2018). Porous metamaterials for deep sub-wavelength ultrasonic imaging. *Applied Physics Letters*, *113*(12), 124102. https://doi.org/10.1063/1.5045087

Amireddy, K. K., & Raj, S. S. (2023). Metamaterials for Subwavelength Imaging. *Techniques and Innovation in Engineering Research Vol. 5*, 59–69. https://doi.org/10.9734/BPI/TAIER/V5/17959D

Anzan-Uz-Zaman, M., Song, K., Lee, D. G., & Hur, S. (2020). A novel approach to Fabry–Pérot-resonance-based lens and demonstrating deep-subwavelength imaging. *Scientific Reports 2020 10:1*, *10*(1), 1–10. https://doi.org/10.1038/s41598-020-67409-4

Articolo, G. A. (2009). The Wave Equation in Two Spatial Dimensions. *Partial Differential Equations & Boundary Value Problems with Maple*, 409–476. https://doi.org/10.1016/B978-0-12-374732-7.00010-X

Askari, M., Hutchins, D. A., Watson, R. L., Astolfi, L., Nie, L., Freear, S., Thomas, P. J., Laureti, S., Ricci, M., Clark, M., & Clare, A. T. (2020). An ultrasonic metallic Fabry–Pérot metamaterial for use in water. *Additive Manufacturing*, *35*, 101309. https://doi.org/10.1016/j.addma.2020.101309

ASME. (2021). *2021 ASME boiler & pressure vessel code*. https://www.asme.org/codes-standards/find-codes-standards/bpvc-v-bpvc-section-v-nondestructive-examination

Auld, B. A. (1979). General electromechanical reciprocity relations applied to the calculation of elastic wave scattering coefficients. *Wave Motion*, *1*(1), 3–10. https://doi.org/10.1016/0165-2125(79)90020-9

Bai, H., Shah, A. H., Popplewell, N., & Datta, S. K. (2001). Scattering of Guided Waves by Circumferential Cracks in Steel Pipes. *Journal of Applied Mechanics*, *68*(4), 619–631. https://doi.org/10.1115/1.1364493

Bai, L., Velichko, A., Clare, A. T., Dryburgh, P., Pieris, D., & Drinkwater, B. W. (2020). The effect of distortion models on characterisation of real defects using ultrasonic arrays. *NDT and E International*, *113*, 102263. https://doi.org/10.1016/j.ndteint.2020.102263

Beard, M. D. (2002). Guided wave inspection of embedded cylindrical structures. *Imperial College, Department of Mechanical Engineering*, *January*, Doctoral dissertation.

Beard, M. D., & Lowe, M. J. S. (2003). Non-destructive testing of rock bolts using guided ultrasonic waves. *International Journal of Rock Mechanics and Mining Sciences*, *40*(4), 527–536. https://doi.org/10.1016/S1365-1609(03)00027-3

Beard, M. D., Lowe, M. J. S., & Cawley, P. (2003). Ultrasonic Guided Waves for Inspection of Grouted Tendons and Bolts. *Journal of Materials in Civil Engineering*, *15*(3), 212–218. https://doi.org/10.1061/(asce)0899-1561(2003)15:3(212)

Behnamfar, P., Molavi, R., & Mirabbasi, S. (2016). Transceiver Design for CMUT-Based Super-Resolution Ultrasound Imaging. *IEEE Transactions on Biomedical Circuits and Systems*, *10*(2), 383–393. https://doi.org/10.1109/TBCAS.2015.2406777

Beniwal, S., & Ganguli, A. (2015). Defect detection around rebars in concrete using focused ultrasound and reverse time migration. *Ultrasonics*, *62*, 112–125. https://doi.org/10.1016/j.ultras.2015.05.008

Beranek, L. L., & Mellow, T. J. (2012). The wave equation and solutions. *Acoustics: Sound Fields and Transducers*, 21–63. https://doi.org/10.1016/B978-0-12-391421-7.00002-6

Bertoldi, K., Vitelli, V., Christensen, J., & van Hecke, M. (2017). Flexible mechanical metamaterials. In *Nature Reviews Materials* (Vol. 2, Issue 11, pp. 1–11). Nature Publishing Group. https://doi.org/10.1038/natrevmats.2017.66

Birir, J. K., Gatari, M. J., & Rajagopal, P. (2019). Channel structured metamaterials for super resolution imaging. *Review of Progress in Quantitative Nondestructive Evaluation, 0*. https://www.iastatedigitalpress.com/qnde/article/id/8613/

Birir, J. K., Gatari, M. J., & Rajagopal, P. (2020). Structured channel metamaterials for deep sub-wavelength resolution in guided ultrasonics. *AIP Advances*, *10*(6), 065027. https://doi.org/10.1063/1.5143696

Birir, J. K., Kairu, W. M., Gatari, M. J., & Rajagopal, P. (2019). Ultrasonic guided wave scattering. *ISNT Journal of Nondestructive Testing & Evaluation*, *17*(19), 13–16. https://isnt.in/ebook/

Brizuela, J., Camacho, J., Cosarinsky, G., Iriarte, J. M., & Cruza, J. F. (2019). Improving elevation resolution in phased-array inspections for NDT. *NDT and E International*, *101*, 1–16. https://doi.org/10.1016/j.ndteint.2018.09.002

Cagniard, L., Flinn, E. A., Hewitt Dix, C., & Mayer, W. G. (1963). Reflection and Refraction of Progressive Seismic Waves. *Physics Today*, *16*(2), 64–64. https://doi.org/10.1063/1.3050759

Canale, A., Dagna, F., Lacilla, M., Piumetto, E., & Albera, R. (2012). Relationship between pure tone audiometry and tone burst auditory brainstem response at low frequencies gated with Blackman window. *European Archives of Oto-Rhino-Laryngology*, *269*(3), 781–785. https://doi.org/10.1007/S00405-011-1723-7/METRICS

Castaings, M., le Clezio, E., & Hosten, B. (2002). Modal decomposition method for modeling the interaction of Lamb waves with cracks. *The Journal of the Acoustical Society of America*, *112*(6), 2567–2582. https://doi.org/10.1121/1.1500756

Cawley, P. (2003). Practical long range guided wave testing - Applications to pipes and rail. *Materials Evaluation*, *61*(1), 66–74. https://ndtlibrary.asnt.org/publication?p=ME&v=61

Cawley, P., & Alleyne, D. (1996). The use of Lamb waves for the long range inspection of large structures. *Ultrasonics*, *34*(2–5), 287–290. https://doi.org/10.1016/0041-624X(96)00024-8

Chan, H., Masserey, B., & Fromme, P. (2015). High frequency guided ultrasonic waves for hidden fatigue crack growth monitoring in multi-layer model aerospace structures. *Smart Materials and Structures*, *24*(2), 025037. https://doi.org/10.1088/0964-1726/24/2/025037

Chen, C. H., Sheen, Y. N., & Wang, H. Y. (2016). Case analysis of catastrophic underground pipeline gas explosion in Taiwan. *Engineering Failure Analysis*, *65*, 39–47. https://doi.org/10.1016/j.engfailanal.2016.03.013

Chen, G., Katagiri, T., Song, H., Yusa, N., & Hashizume, H. (2019). Detection of cracks with arbitrary orientations in a metal pipe using linearly-polarized circular TE11 mode microwaves. *NDT and E International*, *107*, 102125. https://doi.org/10.1016/j.ndteint.2019.102125

Chen, J. T., Chou, K. S., & Kao, S. K. (2009). One-dimensional wave animation using Mathematica. *Computer Applications in Engineering Education*, *17*(3), 323–339. https://doi.org/10.1002/CAE.20224

Chen, T., Li, S., & Sun, H. (2012). Metamaterials application in sensing. In *Sensors* (Vol. 12, Issue 3, pp. 2742–2765). https://doi.org/10.3390/s120302742

Cheng, Y., Zhou, C., Wei, Q., Wu, D., & Liu, X. (2013). Acoustic subwavelength imaging of subsurface objects with acoustic resonant metalens. *Applied Physics Letters*, *103*(22), 224104. https://doi.org/10.1063/1.4837875

Chimenti, D. E. (1997). Guided wave in plates and their use in materials characterization. *Applied Mechanics Reviews*, *50*(5), 247–284.

Deng, K., Ding, Y., He, Z., Zhao, H., Shi, J., & Liu, Z. (2009). Theoretical study of subwavelength imaging by acoustic metamaterial slabs. *Journal of Applied Physics*, *105*(12), 124909. https://doi.org/10.1063/1.3153976

Diligent, O., & Rose, J. L. (2002). A baseline and vision of ultrasonic guided wave inspection potential. *Journal of Pressure Vessel Technology, Transactions of the ASME*, *124*(3), 273–282. https://doi.org/10.1115/1.1491272

Ding, Y., Liu, Z., Qiu, C., & Shi, J. (2007). Metamaterial with simultaneously negative bulk modulus and mass density. *Physical Review Letters*, *99*(9). https://doi.org/10.1103/PhysRevLett.99.093904

Dobson, J., Cawley, P., Dobson, J., & Cawley, P. (2017). *The scattering of torsional guided waves from Gaussian rough surfaces in pipework The scattering of torsional guided waves from Gaussian rough surfaces in pipework*. *1852*. https://doi.org/10.1121/1.4978244

Dongsheng, L., Tao, R., & Junhui, Y. (2012). Inspection of reinforced concrete interface delamination using ultrasonic guided wave non-destructive test technique. *Science China Technological Sciences 2012 55:10*, *55*(10), 2893–2901. https://doi.org/10.1007/S11431-012-4882-X

Drewry, M. A., & Georgiou, G. A. (2007). A review of NDT techniques for wind turbines. *Insight: Non-Destructive Testing and Condition Monitoring*, *49*(3), 137–141. https://doi.org/10.1784/INSI.2007.49.3.137

Drozdz, M. B. (2008). *Efficient finite element modelling of ultrasound waves in elastic media* (Issue January) [Imperial college of science technology and medicine, University of London]. https://www.imperial.ac.uk/media/imperial-college/research-centres-and-groups/non-destructive-evaluation/Mickael_Drozdz_Thesis.pdf

Duan, W., Kirby, R., & Mudge, P. (2016). On the scattering of elastic waves from a non-axisymmetric defect in a coated pipe. *Ultrasonics*, *65*, 228–241. https://doi.org/10.1016/j.ultras.2015.09.019

Dubois, M., Farhat, M., Bossy, E., Enoch, S., Guenneau, S., & Sebbah, P. (2013). Flat lens for pulse focusing of elastic waves in thin plates. *Applied Physics Letters*, *103*(7). https://doi.org/10.1063/1.4818716

Ducousso, M., & Reverdy, F. (2020). Real-time imaging of microcracks on metallic surface using total focusing method and plane wave imaging with Rayleigh waves. *NDT and E International*, *116*, 102311. https://doi.org/10.1016/j.ndteint.2020.102311

Ergin, T., Stenger, N., Brenner, P., Pendry, J. B., & Wegener, M. (2010). Three-dimensional invisibility cloak at optical wavelengths. *Science*, *328*(5976), 337–339. https://doi.org/10.1126/science.1186351

Fan, G., Zhang, H., Zhang, H., Zhu, W., & Chai, X. (2018). Lamb Wave Local Wavenumber Approach for Characterizing Flat Bottom Defects in an Isotropic Thin Plate. *Applied Sciences 2018, Vol. 8, Page 1600*, *8*(9), 1600. https://doi.org/10.3390/APP8091600

Fan, K., & Padilla, W. J. (2015). Dynamic electromagnetic metamaterials. *Materials Today*, *18*(1), 39–50. https://doi.org/10.1016/j.mattod.2014.07.010

Fan, Z., Zhan, L., Hu, X., & Xia, Y. (n.d.). *Critical process of extraordinary optical transmission through periodic subwavelength hole array: Hole-assisted evanescent-field coupling*. https://doi.org/10.1016/j.optcom.2008.07.077

Fang, J., Wu, C., Rabczuk, T., Wu, C., Ma, C., Sun, G., & Li, Q. (2019). Phase field fracture in elasto-plastic solids: Abaqus implementation and case studies. *Theoretical and Applied Fracture Mechanics*, *103*, 102252. https://doi.org/10.1016/J.TAFMEC.2019.102252

Fang, N., Lee, H., Sun, C., & Zhang, X. (2005). Sub-diffraction-limited optical imaging with a silver superlens. *Science*, *308*(5721), 534–537. https://doi.org/10.1126/science.1108759

Garcia, N., & Nieto-Vesperinas, M. (2002). Left-Handed Materials Do Not Make a Perfect Lens. *Physical Review Letters*, *88*(20). https://doi.org/10.1103/PhysRevLett.88.207403

Gerasimov, V., & Bender, W. (2000). Things that talk: Using sound for device-to-device and device-to-human communication. *IBM Systems Journal*, *39*(3–4), 530–546. https://doi.org/10.1147/SJ.393.0530

Graham, A. (1981). *Kronecker Products and Matrix Calculus with Applications* (E. Horwood, Ed.). Halsted Press. https://books.google.co.ke/books?id=DMBYDwAAQBAJ&printsec=frontcover&source=gbs_ge_summary_r&cad=0#v=onepage&q&f=false

Grahn, T. (2003). Lamb wave scattering from a circular partly through-thickness hole in a plate. *Wave Motion*, *37*(1), 63–80. https://doi.org/10.1016/S0165-2125(02)00051-3

Gresil, M., Poohsai, A., & Chandarana, N. (2017). Guided Wave Propagation and Damage Detection in Composite Pipes Using Piezoelectric Sensors. *Procedia Engineering*, *188*(0), 148–155. https://doi.org/10.1016/j.proeng.2017.04.468

Grimberg, R., Savin, A., & Steigmann, R. (2012). Electromagnetic imaging using evanescent waves. *NDT and E International*, *46*(1), 70–76. https://doi.org/10.1016/j.ndteint.2011.11.004

Gupta, S., & Rajagopal, P. (2023). S0 Lamb mode scattering studies in laminated composite plate structures with surface breaking cracks; insights into crack opening behavior. *Ultrasonics*, *129*, 106901. https://doi.org/10.1016/J.ULTRAS.2022.106901

Haberman, M. R., & Norris, A. N. (2016). Acoustic Metamaterials. *Acoustic Today*, *12*(3), 31–39.

Hao, X., Liu, X., Kuang, C., Li, Y., Ku, Y., Zhang, H., Li, H., & Tong, L. (2013). Far-field super-resolution imaging using near-field illumination by micro-fiber. *Applied Physics Letters*, *102*(1), 013104. https://doi.org/10.1063/1.4773572

Hartman, W., Lecinq, B., Higgs, J., & David, T. (2010). Non destructive integrity testing of rock reinforcement elements in Australian mines. *2010 Underground Coal Operators' Conference*, 161–170.

Hassan, A. M. T., & Jones, S. W. (2012). Non-destructive testing of ultra high performance fibre reinforced concrete (UHPFRC): A feasibility study for using ultrasonic and resonant frequency testing techniques. *Construction and Building Materials*, *35*, 361–367. https://doi.org/10.1016/J.CONBUILDMAT.2012.04.047

Haxha, S., AbdelMalek, F., Ouerghi, F., Charlton, M. D. B., Aggoun, A., & Fang, X. (2018). Metamaterial Superlenses Operating at Visible Wavelength for Imaging Applications. *Scientific Reports*, *8*(1), 1–15. https://doi.org/10.1038/s41598-018-33572-y

Hua, J., Zeng, L., Lin, J., & Huang, L. (2018). Excitation series design and pulse compression synthesis for high-resolution Lamb wave inspection. *Https://Doi.Org/10.1177/1475921718801996*, *18*(5–6), 1464–1478. https://doi.org/10.1177/1475921718801996

Huang, X., Bie, Z., Wang, L., Jin, Y., Liu, X., Su, G., & He, X. (2019). Finite element method of bond-based peridynamics and its ABAQUS implementation. *Engineering Fracture Mechanics*, *206*, 408–426. https://doi.org/10.1016/J.ENGFRACMECH.2018.11.048

Huho, J. M., Mashara, J. N., & Musyimi, P. K. (2016). Profiling disasters in Kenya and their causes. *Academic Research International*, *7*(1). www.savap.org.pk290www.journals.savap.org.pk

Hur, S., Jeon, H., Anzan-Uz-Zaman, M., Kim, Y., Shah, M. A., Kim, J., & Lee, B. C. (2022). Subwavelength ultrasonic imaging via a harmonic resonant tunneling metalens. *International Journal of Mechanical Sciences*, *224*, 107339. https://doi.org/10.1016/J.IJMECSCI.2022.107339

Huszka, G., & Gijs, M. A. M. (2019). Super-resolution optical imaging: A comparison. In *Micro and Nano Engineering* (Vol. 2, pp. 7–28). Elsevier B.V. https://doi.org/10.1016/j.mne.2018.11.005

Idesman, A., & Pham, D. (2014). Finite element modeling of linear elastodynamics problems with explicit time-integration methods and linear elements with the reduced dispersion error. *Computer Methods in Applied Mechanics and Engineering*, *271*, 86–108. https://doi.org/10.1016/J.CMA.2013.12.002

Jarvis, R., Cawley, P., & Nagy, P. B. (2016). *Current deflection NDE for the inspection and monitoring of pipes*. https://doi.org/10.1016/j.ndteint.2016.03.006

Kadarno, P., Park, D. S., Mahardika, N., Irianto, I. D., & Nugroho, A. (2019). Fatigue Evaluation of Pressure Vessel using Finite Element Analysis based on ASME BPVC Sec. VIII Division 2. *Journal of Physics: Conference Series*, *1198*(4), 042015. https://doi.org/10.1088/1742-6596/1198/4/042015

Kaina, N., Lemoult, F., Fink, M., & Lerosey, G. (2015). Negative refractive index and acoustic superlens from multiple scattering in single negative metamaterials. *Nature*, *525*(7567), 77–81. https://doi.org/10.1038/nature14678

Karaiskos, G., Deraemaeker, A., Aggelis, D. G., & Van Hemelrijck, D. (2015). Monitoring of concrete structures using the ultrasonic pulse velocity method. *Smart Materials and Structures*, *24*(11), 113001. https://doi.org/10.1088/0964-1726/24/11/113001

Kelkar, P. U., Kim, H. S., Cho, K.-H., Kwak, J. Y., Kang, C.-Y., & Song, H.-C. (2020). Cellular Auxetic Structures for Mechanical Metamaterials: A Review. *Sensors*, *20*(11), 3132. https://doi.org/10.3390/s20113132

Kim, M., & Rho, J. (2015). Metamaterials and imaging. *Nano Convergence*, *2*(1). https://doi.org/10.1186/s40580-015-0053-7

Kolsky, H. (1964). Stress waves in solids. *Journal of Sound and Vibration*, *1*(1), 88–110. https://doi.org/10.1016/0022-460X(64)90008-2

Kuchibhatla, S. A. R., & Rajagopal, P. (2019). A transformation elasticity based device for wavefront manipulation. *NDT and E International*, *102*, 304–310. https://doi.org/10.1016/j.ndteint.2019.01.006

Kumar, R., Kumar, M., Chohan, J. S., & Kumar, S. (2022). Overview on metamaterial: History, types and applications. *Materials Today: Proceedings*, *56*, 3016–3024. https://doi.org/10.1016/J.MATPR.2021.11.423

Kundu, T. (2014). Ultrasonic and electromagnetic waves for nondestructive evaluation and structural health monitoring. *Procedia Engineering*, *86*, 395–405. https://doi.org/10.1016/j.proeng.2014.11.053

Lais, H., Lowe, P. S., Gan, T. H., Wrobel, L. C., & Kanfoud, J. (2018). Characterization of the Use of Low Frequency Ultrasonic Guided Waves to Detect Fouling Deposition in Pipelines. *Sensors 2018, Vol. 18, Page 2122*, *18*(7), 2122. https://doi.org/10.3390/S18072122

Lauterbach, M. A. (2012). Finding, defining and breaking the diffraction barrier in microscopy – a historical perspective. *Lauterbach Optical Nanoscopy*, *1*(8). http://www.optnano.com/content/1/1/8

Lee, J. H. (2016). Status and prospect of NDT technology for nuclear energy industry in Korea. *AIP Conference Proceedings*, *1706*(1), 020001. https://doi.org/10.1063/1.4940447

Lee, S. H., Park, C. M., Seo, Y. M., Wang, Z. G., & Kim, C. K. (2009). Acoustic metamaterial with negative density. *Physics Letters, Section A: General, Atomic and Solid State Physics*, *373*(48), 4464–4469. https://doi.org/10.1016/j.physleta.2009.10.013

Leinov, E., Lowe, M. J. S., & Cawley, P. (2015). Investigation of guided wave propagation and attenuation in pipe buried in sand. *Journal of Sound and Vibration*, *347*, 96–114. https://doi.org/10.1016/j.jsv.2015.02.036

Leinov, E., Lowe, M. J. S., & Cawley, P. (2016). Investigation of guided wave propagation in pipes fully and partially embedded in concrete. *The Journal of the Acoustical Society of America*, *140*(6), 4528–4539. https://doi.org/10.1121/1.4972118

Lemoult, F., Lerosey, G., De Rosny, J., & Fink, M. (2010). Resonant metalenses for breaking the diffraction barrier. *Physical Review Letters*, *104*(20), 203901. https://doi.org/10.1103/physrevlett.104.203901/figures/3/medium

Leonard, K. R., & Hinders, M. K. (2003). Guided wave helical ultrasonic tomography of pipes. *The Journal of the Acoustical Society of America*, *114*(2), 767–774. https://doi.org/10.1121/1.1593068

Lewis, A., Lev, D., Sebag, D., Hamra, P., Levy, H., Bernstein, Y., Brahami, A., Tal, N., Goldstein, O., & Yeshua, T. (2014). The optical near-field: Super-resolution imaging with structural and phase correlation. *Nanophotonics*, *3*(1–2), 3–18. https://doi.org/10.1515/nanoph-2014-0007

Lewis, B. J., Onder, E. N., & Prudil, A. A. (2022). Partial differential equations. *Advanced Mathematics for Engineering Students*, 131–164. https://doi.org/10.1016/B978-0-12-823681-9.00013-7

Li, S., & Chu, T. P. (2013). Super-Resolution Image Reconstruction for Ultrasonic Nondestructive Evaluation. *IEEE Transactions on Ultrasonics, Ferroelectrics and Frequency Control*, *60*(12), 2575–2585. https://doi.org/papers2://publication/doi/10.1109/TUFFC.2013.2856

Liang, Y. J., McQuien, J. S., & Iarve, E. v. (2020). Implementation of the regularized extended finite element method in Abaqus framework for fracture modeling in laminated composites. *Engineering Fracture Mechanics*, *230*, 106989. https://doi.org/10.1016/J.ENGFRACMECH.2020.106989

Liang, Z., Willatzen, M., Li, J., & Christensen, J. (2012). Tunable acoustic double negativity metamaterial. *Scientific Reports 2012 2:1*, *2*(1), 1–5. https://doi.org/10.1038/srep00859

Lin, Z., Guo, X., Tu, J., Cheng, J., Wu, J., & Zhang, D. (2014). Acoustic focusing of sub-wavelength scale achieved by multiple Fabry-Perot resonance effect. *Journal of Applied Physics*, *115*(10), 104504. https://doi.org/10.1063/1.4868629

Liu, C., Yang, Y., Wang, J. J., Fan, J. S., Tao, M. X., & Mo, Y. L. (2020). Biaxial reinforced concrete constitutive models for implicit and explicit solvers with reduced mesh sensitivity. *Engineering Structures*, *219*, 110880. https://doi.org/10.1016/J.ENGSTRUCT.2020.110880

Lowe, M. J. S., Alleyne, D. N., & Cawley, P. (1998). Defect detection in pipes using guided waves. *Ultrasonics*, *36*(1–5), 147–154. https://doi.org/10.1016/S0041-624X(97)00038-3

Lowe, M. J. S., & Cawley, P. (2006). Long Range Guided Wave Inspection Usage – Current Commercial Capabilities and Research Directions. *Department of*

Mechanical Engineering, Imperial College London. https://doi.org/10.1177/058310240

Lowe, M. J. S., Cawley, P., Kao, J.-Y., & Diligent, O. (2002). The low frequency reflection characteristics of the fundamental antisymmetric Lamb wave a0 from a rectangular notch in a plate. *The Journal of the Acoustical Society of America*, *112*(6), 2612–2622. https://doi.org/10.1121/1.1512702

Lu, D., & Liu, Z. (2012). Hyperlenses and metalenses for far-field super-resolution imaging. *Nature Communications*, *3*(1), 1205. https://doi.org/10.1038/ncomms2176

Luo, Y. (2010). A local multivariate Lagrange interpolation method for constructing shape functions. *International Journal for Numerical Methods in Biomedical Engineering*, *26*(2), 252–261. https://doi.org/10.1002/CNM.1149

Ma, F., Huang, Z., Liu, C., & Wu, J. H. (2022). Acoustic focusing and imaging via phononic crystal and acoustic metamaterials. *Journal of Applied Physics*, *131*(1), 011103. https://doi.org/10.1063/5.0074503

Ma, G., & Sheng, P. (2016a). Acoustic metamaterials: From local resonances to broad horizons. In *Science Advances* (Vol. 2, Issue 2, p. e1501595). American Association for the Advancement of Science. https://doi.org/10.1126/sciadv.1501595

Ma, G., & Sheng, P. (2016b). Acoustic metamaterials: From local resonances to broad horizons. In *Science Advances* (Vol. 2, Issue 2). American Association for the Advancement of Science. https://doi.org/10.1126/sciadv.1501595

Ma, R., Wu, D., Liu, Y., Ye, H., & Sutherland, D. (2020). Copper plasmonic metamaterial glazing for directional thermal energy management. *Materials & Design*, *188*, 108407. https://doi.org/10.1016/J.MATDES.2019.108407

Mahal, H. N., Yang, K., & Nandi, A. K. (2019). Defect Detection using Power Spectrum of Torsional Waves in Guided-Wave Inspection of Pipelines. *Applied Sciences 2019, Vol. 9, Page 1449*, *9*(7), 1449. https://doi.org/10.3390/APP9071449

Marcantonio, V., Monarca, D., Colantoni, A., & Cecchini, M. (2019). Ultrasonic waves for materials evaluation in fatigue, thermal and corrosion damage: A review. *Mechanical Systems and Signal Processing*, *120*, 32–42. https://doi.org/10.1016/J.YMSSP.2018.10.012

Martinez, F., & Maldovan, M. (2022). Metamaterials: Optical, Acoustic, Elastic, Heat, Mass, Electric, Magnetic, and Hydrodynamic Cloaking. *Materials Today Physics*, 100819. https://doi.org/10.1016/J.MTPHYS.2022.100819

Martínez-Oña, R. (2021). NDE in Energy and Nuclear Industry. *Handbook of Nondestructive Evaluation 4.0*, 1–35. https://doi.org/10.1007/978-3-030-48200-8_31-1

Masserey, B., Raemy, C., & Fromme, P. (2014). High-frequency guided ultrasonic waves for hidden defect detection in multi-layered aircraft structures. *Ultrasonics, 54*(7), 1720–1728. https://doi.org/10.1016/J.ULTRAS.2014.04.023

McCann, D. M., & Forde, M. C. (2001). Review of NDT methods in the assessment of concrete and masonry structures. *NDT & E International*, *34*(2), 71–84. https://doi.org/10.1016/S0963-8695(00)00032-3

Michaels, J. E., Lee, S. J., Croxford, A. J., & Wilcox, P. D. (2013). Chirp excitation of ultrasonic guided waves. *Ultrasonics, 53*(1), 265–270. https://doi.org/10.1016/J.ULTRAS.2012.06.010

Michaels, T. E., Michaels, J. E., & Ruzzene, M. (2011). Frequency-wavenumber domain analysis of guided wavefields. *Ultrasonics*, *51*(4), 452–466. https://doi.org/10.1016/j.ultras.2010.11.011

Miklowitz, J. (1984). *The theory of elastic waves and waveguides*. North-Holland.

Milton, G. W., & Cherkaev, A. V. (1995). Which elasticity tensors are realizable? *Journal of Engineering Materials and Technology, Transactions of the ASME, 117*(4), 483–493. https://doi.org/10.1115/1.2804743

Muhammad, Lim, C. W., & Reddy, J. N. (2019). Built-up structural steel sections as seismic metamaterials for surface wave attenuation with low frequency wide bandgap in layered soil medium. *Engineering Structures, 188,* 440–451. https://doi.org/10.1016/J.ENGSTRUCT.2019.03.046

Nagaraj, M., & Maiaru, M. (2023). Progressive damage analysis of steel-reinforced concrete beams using higher-order 1D finite elements. *International Journal* *for Multiscale Computational Engineering*, *21*(4). https://doi.org/10.1615/INTJMULTCOMPENG.2022045649

Nakhli Mahal, H., Yang, K., & Nandi, A. (2019). Defect Detection using Power Spectrum of Torsional Waves in Guided-Wave Inspection of Pipelines. *Applied Sciences*, *9*(7), 1449. https://doi.org/10.3390/app9071449

Nash, L. M., Kleckner, D., Read, A., Vitelli, V., Turner, A. M., & Irvine, W. T. M. (2015). Topological mechanics of gyroscopic metamaterials. *Proceedings of the National Academy of Sciences of the United States of America*, *112*(47), 14495–14500. https://doi.org/10.1073/pnas.1507413112

Nobrega, E. D., Gautier, F., Pelat, A., & dos Santos, J. M. C. (2016). Vibration band gaps for elastic metamaterial rods using wave finite element method. *Mechanical Systems and Signal Processing*, *79*, 192–202. https://doi.org/10.1016/j.ymssp.2016.02.059

O'Hara, J. F., Singh, R., Brener, I., Smirnova, E., Han, J., Taylor, A. J., & Zhang, W. (2008). Thin-film sensing with planar terahertz metamaterials: sensitivity and limitations. *Optics Express*, *16*(3), 1786. https://doi.org/10.1364/oe.16.001786

Okumura, S., Nguyen, V. H., Taki, H., Haïat, G., Naili, S., & Sato, T. (2018). Rapid High-Resolution Wavenumber Extraction from Ultrasonic Guided Waves Using Adaptive Array Signal Processing. *Applied Sciences 2018, Vol. 8, Page 652*, *8*(4), 652. https://doi.org/10.3390/APP8040652

Ou, J.-Y., Plum, E., & Zheludev, N. I. (2018). Optical addressing of nanomechanical metamaterials with subwavelength resolution. *Applied Physics Letters*, *113*(8), 081104. https://doi.org/10.1063/1.5036966

Page, J. H. (2016). Focusing of ultrasonic waves by negative refraction in phononic crystals. *AIP Advances*, *6*. https://doi.org/10.1063/1.4972204

Pao, Y. H., & Mow, C. C. (1973). *Diffraction of elastic waves and dynamic stress concentrations*. New York: Crane Russak.

Park, C. M., Park, J. J., Lee, S. H., Seo, Y. M., Kim, C. K., & Lee, S. H. (2011). Amplification of acoustic evanescent waves using metamaterial slabs. *Physical*

Review Letters, *107*(19), 194301. https://doi.org/10.1103/physrevlett.107.194301/figures/4/medium

Park, H. W., Sohn, H., Law, K. H., & Farrar, C. R. (2007). Time reversal active sensing for health monitoring of a composite plate. *Journal of Sound and Vibration*, *302*(1–2), 50–66. https://doi.org/10.1016/j.jsv.2006.10.044

Pavlakovic, B., & Calwley, P. (1999). The inspection of tendons in post-tensioned concrete using guided ultrasonic waves. *Insight*, *41*(7), 101373.

Pavlopoulou, S., Staszewski, W. J., & Soutis, C. (2013). Evaluation of instantaneous characteristics of guided ultrasonic waves for structural quality and health monitoring. *Structural Control and Health Monitoring*, *20*(6), 937–955. https://doi.org/10.1002/STC.1506

Pech, S., Lukacevic, M., & Füssl, J. (2021). A robust multisurface return-mapping algorithm and its implementation in Abaqus. *Finite Elements in Analysis and Design*, *190*, 103531. https://doi.org/10.1016/J.FINEL.2021.103531

Pendry, J. B. (2000). Negative Refraction Makes a Perfect Lens. *Physical Review Letters*, *85*(18), 3966–3969. https://doi.org/10.1103/PhysRevLett.85.3966

Pendry, J. B., Holden, A. J., Robbins, D. J., & Stewart, W. J. (1999). Magnetism from conductors and enhanced nonlinear phenomena. *IEEE Transactions on Microwave Theory and Techniques*, *47*(11), 2075–2084. https://doi.org/10.1109/22.798002

Periyannan, S., & Balasubramaniam, K. (2016). *Elastic Moduli Measurements at Elevated Temperatures using Ultrasonic Waveguide Embodiments*. 1–8.

Periyannan, S., Rajagopal, P., & Balasubramaniam, K. (2016). Re-configurable multi-level temperature sensing by ultrasonic "spring-like" helical waveguide. *Journal of Applied Physics*, *119*(14). https://doi.org/10.1063/1.4945322

Popa, B.-I., & Cummer, S. A. (2015). Negative refraction of sound. *Nature Materials*, *14*(4), 363–364. https://doi.org/10.1038/nmat4253

Qi, M. X., Zhang, P. G., Ni, J., & Zhou, S. P. (2015). Experiment and Numerical Simulation of Ultrasonic Guided Wave Propagation in Bent Pipe. *Procedia Engineering*, *130*, 1603–1611. https://doi.org/10.1016/j.proeng.2015.12.338

Rajagopal, P., Drozdz, M., Skelton, E. A., Lowe, M. J. S., & Craster, R. v. (2012). NDT & E International On the use of absorbing layers to simulate the propagation of elastic waves in unbounded isotropic media using commercially available Finite Element packages. *NDT and E International*, *51*, 30–40. https://doi.org/10.1016/j.ndteint.2012.04.001

Rajagopal, P., & Lowe, M. J. S. (2007). Short range scattering of the fundamental shear horizontal guided wave mode normally incident at a through-thickness crack in an isotropic plate. *The Journal of the Acoustical Society of America*, *122*(3), 1527. https://doi.org/10.1121/1.2764472

Rajagopal, P., & Lowe, M. J. S. (2008). Angular influence on the scattering of fundamental shear horizontal guided waves by a through-thickness crack in an isotropic plate. *The Journal of the Acoustical Society of America*, *124*(4), 2021. https://doi.org/10.1121/1.2968697

Ramdhas, A., Pattanayak, R. K., Balasubramaniam, K., & Rajagopal, P. (2015). Symmetric low-frequency feature-guided ultrasonic waves in thin plates with transverse bends. *Ultrasonics*, *56*, 232–242. https://doi.org/10.1016/J.ULTRAS.2014.07.014

Ray, P., Rajagopal, P., Srinivasan, B., & Balasubramaniam, K. (2017). Feature-guided wave-based health monitoring of bent plates using fiber Bragg gratings. *Journal of Intelligent Material Systems and Structures*, *28*(9), 1211–1220. https://doi.org/10.1177/1045389X16667554

Razdan, A. K., & Ravichandran, V. (2022). Laplace Transform. *Fundamentals of Partial Differential Equations*, 479–521. https://doi.org/10.1007/978-981-16-9865-1_11

Reddy, J. N. (2006). *An introduction to the finite element method* (3rd ed.). McGraw-Hill.

Reddy, R. K., Ramachandra, V., Kumar, N., & Singh, N. C. (2009). Categorization of environmental sounds. *Biological Cybernetics*, *100*(4), 299–306. https://doi.org/10.1007/S00422-009-0299-4/METRICS

Repän, T., Lavrinenko, A. v., & Zhukovsky, S. v. (2015). Dark-field hyperlens: Super-resolution imaging of weakly scattering objects. *Optics Express*, *23*(19), 25350. https://doi.org/10.1364/OE.23.025350

Rose, J. L. (1995). Recent advances in guided wave NDE. *1995 IEEE Ultrasonics Symposium. Proceedings. An International Symposium*, *1*(1995), 761–770. https://doi.org/10.1109/ULTSYM.1995.495679

Rose, J. L. (2007). *An Introduction to Ultrasonic Guided Waves*.

Rose, J. L. (2014). *Ultrasonic Guided Waves in Solid Media*. https://doi.org/10.1017/CBO9781107273610

Shah, H., Balasubramaniam, K., & Rajagopal, P. (2017). In-situ process- and online structural health-monitoring of composites using embedded acoustic waveguide sensors. *Journal of Physics Communications*, *1*(5), 055004. https://doi.org/10.1088/2399-6528/aa8bfa

Sharma, S., & Mukherjee, A. (2011). Monitoring Corrosion in Oxide and Chloride Environments Using Ultrasonic Guided Waves. *Journal of Materials in Civil Engineering*, *23*(2), 207–211. https://doi.org/10.1061/(asce)mt.1943-5533.0000144

Shelby, R. A., Smith, D. R., & Schultz, S. (2001). Experimental verification of a negative index of refraction. *Science (New York, N.Y.)*, *292*(5514), 77–79. https://doi.org/10.1126/science.1058847

Shen, Y. X., Peng, Y. G., Cai, F., Huang, K., Zhao, D. G., Qiu, C. W., Zheng, H., & Zhu, X. F. (2019). Ultrasonic super-oscillation wave-packets with an acoustic meta-lens. *Nature Communications*, *10*(1), 1–7. https://doi.org/10.1038/s41467-019-11430-3

Sikundalapuram Ramesh, S. K., Chitnaduku Thippeswamy, M., Rajagopal, P., & Balasubramaniam, K. (2020). Elastic metamaterial rod for mode filtering in ultrasonic applications. *Electronics Letters*, *56*(19), 1024–1027. https://doi.org/10.1049/el.2020.1576

Silk, M. G. (1984). The use of diffraction-based time-of-flight measurements to locate and size defects. *British Journal of Nondestructive Testing*, *26*, 208–213.

Silk, M. G. (1987). Changes in ultrasonic defect location and sizing. *NDT International*, *20*(1), 9–14. https://doi.org/10.1016/0308-9126(87)90367-1

Singh, D., Bentahar, M., Mechri, C., & Guerjouma, R. el. (2021). 3D Modelling of the Scattering of the Fundamental Anti-Symmetric Lamb Mode (A0) Propagating within a Point-Impacted Transverse-Isotropic Composite Plate. *Applied Sciences 2021, Vol. 11, Page 7276*, *11*(16), 7276. https://doi.org/10.3390/APP11167276

Smith, D. R., Padilla, W. J., Vier, D. C., Nemat-Nasser, S. C., & Schultz, S. (2000). *Composite Medium with Simultaneously Negative Permeability and Permittivity*. https://journals.aps.org/prl/pdf/10.1103/PhysRevLett.84.4184

Snieder, R. (2002). *General theory of elastic wave scattering* (R. Pike & P. Sabatier, Eds.). Academic press.

Solodov, I., Bernhardt, Y., & Kreutzbruck, M. (2021). Resonant Airborne Acoustic Emission for Nondestructive Testing and Defect Imaging in Composites. *Applied Sciences 2021, Vol. 11, Page 10141*, *11*(21), 10141. https://doi.org/10.3390/APP112110141

Spytek, J., Mrowka, J., Pieczonka, L., & Ambrozinski, L. (2020). Multi-resolution non-contact damage detection in complex-shaped composite laminates using ultrasound. *NDT and E International*, *116*, 102366. https://doi.org/10.1016/j.ndteint.2020.102366

Staszewski, W. J., Mahzan, S., & Traynor, R. (2009). Health monitoring of aerospace composite structures - Active and passive approach. *Composites Science and Technology*, *69*(11–12), 1678–1685. https://doi.org/10.1016/j.compscitech.2008.09.034

Stobbe, D. M., Grünsteidl, C. M., & Murray, T. W. (2019). Propagation and Scattering of Lamb Waves at Conical Points in Plates. *Scientific Reports 2019 9:1*, *9*(1), 1–10. https://doi.org/10.1038/s41598-019-51187-9

Su, H., Zhou, X., Xu, X., & Hu, G. (2014). Experimental study on acoustic subwavelength imaging of holey-structured metamaterials by resonant tunneling. *The Journal of the Acoustical Society of America*, *135*(4), 1686. https://doi.org/10.1121/1.4868395

Sun, X., Shui, G., Zhao, Y., Liu, W., Hu, N., & Deng, M. (2020). Evaluation of early stage local plastic damage induced by bending using quasi-static component of Lamb waves. *NDT & E International*, *116*, 102332. https://doi.org/10.1016/J.NDTEINT.2020.102332

Surjadi, J. U., Gao, L., Du, H., Li, X., Xiong, X., Fang, N. X., & Lu, Y. (2019). Mechanical Metamaterials and Their Engineering Applications. *Advanced Engineering Materials*, *21*(3), 1800864. https://doi.org/10.1002/adem.201800864

Syed Akbar Ali, M. S., Amireddy, K. K., Balasubramaniam, K., & Rajagopal, P. (2019). Characterization of Deep Sub-wavelength Sized Horizontal Cracks Using Holey-Structured Metamaterials. *Transactions of the Indian Institute of Metals*, *72*(11), 2917–2921. https://doi.org/10.1007/s12666-019-01684-2

Syed Akbar Ali, M. S., & Rajagopal, P. (2022). Far-field ultrasonic imaging using hyperlenses. *Scientific Reports 2022 12:1*, *12*(1), 1–10. https://doi.org/10.1038/s41598-022-23046-7

Tan, M., & Auld, B. A. (1980). Normal mode variational method for two- and three-dimensional acoustic scattering in an isotropic plate. *Ultrasonics*, 857–861.

Tang, Y., Ren, S., Meng, H., Xin, F., Huang, L., Chen, T., Zhang, C., & Lu, T. J. (2017). Hybrid acoustic metamaterial as super absorber for broadband low-frequency sound. *Scientific Reports*, *7*(1), 1–11. https://doi.org/10.1038/srep43340

Tao, H., Bingham, C. M., Strikwerda, A. C., Pilon, D., Shrekenhamer, D., Landy, N. I., Fan, K., Zhang, X., Padilla, W. J., & Averitt, R. D. (2008). Highly flexible wide angle of incidence terahertz metamaterial absorber: Design, fabrication, and characterization. *Physical Review B - Condensed Matter and Materials Physics*, *78*(24), 241103. https://doi.org/10.1103/PhysRevB.78.241103

Thakare, D. R., Abid, A., Pereira, D., Fernandes, J., Belanger, P., & Rajagopal, P. (2017). Semi-analytical finite-element modeling approach for guided wave assessment of mechanical degradation in bones. *International Biomechanics*, *4*(1), 17–27. https://doi.org/10.1080/23335432.2017.1319295

Thiyagarajan, J. S. (2020). Non-Destructive Testing Mechanism for Pre-Stressed Steel Wire Using Acoustic Emission Monitoring. *Materials 2020, Vol. 13, Page 5029*, *13*(21), 5029. https://doi.org/10.3390/MA13215029

Tian, H., Li, S., & Cui, X. (2020). Development of element model subroutines for implicit and explicit analysis considering large deformations. *Advances in Engineering Software*, *148*, 102805. https://doi.org/10.1016/J.ADVENGSOFT.2020.102805

Trushkevych, O., & Edwards, R. S. (2019). Characterisation of small defects using miniaturised EMAT system. *NDT and E International*, *107*, 102140. https://doi.org/10.1016/j.ndteint.2019.102140

Valentine, J., Li, J., Zentgraf, T., Bartal, G., & Zhang, X. (2009). An optical cloak made of dielectrics. *Nature Materials*, *8*(7), 568–571. https://doi.org/10.1038/nmat2461

Van Pamel, A., Nagy, P. B., & Lowe, M. J. S. (2016). On the dimensionality of elastic wave scattering within heterogeneous media. *The Journal of the Acoustical Society of America*, *140*(6), 4360–4366. https://doi.org/10.1121/1.4971383

Velichko, A., & Wilcox, P. D. (2008). Guided wave arrays for high resolution inspection. *The Journal of the Acoustical Society of America*, *123*(1), 186–196. https://doi.org/10.1121/1.2804699

Verma, B., Mishra, T. K., Balasubramaniam, K., & Rajagopal, P. (2014). Interaction of low-frequency axisymmetric ultrasonic guided waves with bends in pipes of arbitrary bend angle and general bend radius. *Ultrasonics*, *54*(3), 801–808. https://doi.org/10.1016/j.ultras.2013.10.007

Veselago, V. G. (1968). The electrodynamics of substances with simultaneously negative values of ε and μ. *Soviet Physics Uspekhi*, *10*(4), 509–514. https://doi.org/10.1070/PU1968v010n04ABEH003699

Wang, X.-M., & Ying, C. F. (2001). Scattering of Lamb waves by a circular cylinder. *The Journal of the Acoustical Society of America*, *110*(4), 1752–1763. https://doi.org/10.1121/1.1396330

Wang, X.-M., Ying, C. F., & Li, M.-X. (2000). Scattering of antiplane shear waves by a circular cylinder in a traction-free plate. *The Journal of the Acoustical Society of America*, *108*(3), 913. https://doi.org/10.1121/1.1287028

Waterman, N., Styles, I., Thomas, S., & Zhang, S. (2015). Super-resolution imaging with metamaterials for cardiovascular disease. *Novel Techniques in Microscopy, NTM 2015*, JT3A.10. https://doi.org/10.1364/boda.2015.jt3a.10

Wilcox, P., Evans, M., Pavlakovic, B., Alleyne, D., Vine, K., Cawley, P., & Lowe, M. (2003). Guided wave testing of rail. *Insight: Non-Destructive Testing and Condition Monitoring*, *45*(6), 413–420. https://doi.org/10.1784/insi.45.6.413.52892

Wright, R. F., Lu, P., Devkota, J., Lu, F., Ziomek-Moroz, M., & Ohodnicki, P. R. (2019). Corrosion sensors for structural health monitoring of oil and natural gas infrastructure: A review. In *Sensors (Switzerland)* (Vol. 19, Issue 18, p. 3964). MDPI AG. https://doi.org/10.3390/s19183964

Wronkowicz, A., Dragan, K., & Lis, K. (2018). Assessment of uncertainty in damage evaluation by ultrasonic testing of composite structures. *Composite Structures*, *203*, 71–84. https://doi.org/10.1016/j.compstruct.2018.06.109

Xing, B., Yu, Z., Xu, X., Zhu, L., & Shi, H. (2019). Research on a Rail Defect Location Method Based on a Single Mode Extraction Algorithm. *Applied Sciences 2019, Vol. 9, Page 1107*, *9*(6), 1107. https://doi.org/10.3390/APP9061107

Xu, B., Arias, F., Brittain, S. T., Zhao, X.-M., Grzybowski, B., Torquato, S., & Whitesides, G. M. (1999). Making Negative Poisson's Ratio Microstructures by Soft Lithography. *Advanced Materials*, *11*(14), 1186–1189. https://doi.org/10.1002/(sici)1521-4095(199910)11:14<1186::aid-adma1186>3.0.co;2-k

Yang, K., Rongong, J. A., & Worden, K. (2018). Damage detection in a laboratory wind turbine blade using techniques of ultrasonic NDT and SHM. *Strain*, *54*(6), e12290. https://doi.org/10.1111/STR.12290

Yang, T., JIN, Y., Choi, T., Dahotre, N. B., & Neogi, A. (2020). Mechanically tunable ultrasonic metamaterial lens with a subwavelength resolution at long working distances for bioimaging. *Smart Materials and Structures*, *30*(1), 015022. https://doi.org/10.1088/1361-665x/abcab0

Ye, M., Gao, L., & Li, H. (2020). A design framework for gradually stiffer mechanical metamaterial induced by negative Poisson's ratio property. *Materials & Design*, *192*, 108751. https://doi.org/10.1016/J.MATDES.2020.108751

Yu, W., & Zhou, L. (2023). Seismic metamaterial surface for broadband Rayleigh waves attenuation. *Materials & Design*, *225*, 111509. https://doi.org/10.1016/J.MATDES.2022.111509

Yu, X., Zhou, J., Liang, H., Jiang, Z., & Wu, L. (2018). Mechanical metamaterials associated with stiffness, rigidity and compressibility: A brief review. In *Progress in Materials Science* (Vol. 94, pp. 114–173). Elsevier Ltd. https://doi.org/10.1016/j.pmatsci.2017.12.003

Yu, X., Zuo, P., Xiao, J., & Fan, Z. (2019). Detection of damage in welded joints using high order feature guided ultrasonic waves. *Mechanical Systems and Signal Processing*, *126*, 176–192. https://doi.org/10.1016/J.YMSSP.2019.02.026

Yuan, W. H., Wang, H. C., Zhang, W., Dai, B. B., Liu, K., & Wang, Y. (2021). Particle finite element method implementation for large deformation analysis using Abaqus. *Acta Geotechnica*, *16*(8), 2449–2462. https://doi.org/10.1007/S11440-020-01124-2/METRICS

Zangeneh-Nejad, F., & Fleury, R. (2019). Active times for acoustic metamaterials. In *Reviews in Physics* (Vol. 4, p. 100031). Elsevier B.V. https://doi.org/10.1016/j.revip.2019.100031

Zhang, L., Yang, Y., Wei, X., & Yao, W. (2018). The Study of Non-Detection Zones in Conventional Long-Distance Ultrasonic Guided Wave Inspection on Square Steel Bars. *Applied Sciences 2018, Vol. 8, Page 129*, *8*(1), 129. https://doi.org/10.3390/APP8010129

Zhang, P., Tang, Z., Lv, F., & Yang, K. (2019). Numerical and Experimental Investigation of Guided Wave Propagation in a Multi-Wire Cable. *Applied*

Sciences 2019, Vol. 9, Page 1028, *9*(5), 1028. https://doi.org/10.3390/APP9051028

Zhang, X., & Liu, Z. (2008). Superlenses to overcome the diffraction limit. *Nature Materials*, *7*(6), 435–441. https://doi.org/10.1038/nmat2141

Zhao, L., Laredo, E., Ryan, O., Yazdkhasti, A., Kim, H. T., Ganye, R., Horiuchi, T., & Yu, M. (2020). Ultrasound beam steering with flattened acoustic metamaterial Luneburg lens. *Applied Physics Letters*, *116*(7), 071902. https://doi.org/10.1063/1.5140467

Zhao, X., & Rose, J. L. (2016). Ultrasonic guided wave tomography for ice detection. *Ultrasonics*, *67*, 212–219. https://doi.org/10.1016/j.ultras.2015.12.005

Zheng, H., Cai, R. C., & Pan, L. S. (2013). A modified Galerkin FEM for 1D Helmholtz equations. *Applied Acoustics*, *74*(1), 211–216. https://doi.org/10.1016/J.APACOUST.2012.06.014

Zheng, M., Lu, C., Chen, G., & Men, P. (2011). Modeling Three-dimensional Ultrasonic Guided Wave Propagation and Scattering in Circular Cylindrical Structures using Finite Element Approach. *Physics Procedia*, *22*, 112–118. https://doi.org/10.1016/J.PHPRO.2011.11.018

Zhou, X., & Hu, G. (2009). Analytic model of elastic metamaterials with local resonances. *Physical Review B - Condensed Matter and Materials Physics*, *79*(19), 195109. https://doi.org/10.1103/PhysRevB.79.195109

Zhou, X., Liu, X., & Hu, G. (2012). Elastic metamaterials with local resonances: an overview. *Theoretical and Applied Mechanics Letters*, *2*(4), 041001. https://doi.org/10.1063/2.1204101

Zhu, H., & Semperlotti, F. (2014). A passively tunable acoustic metamaterial lens for selective ultrasonic excitation. *Journal of Applied Physics*, *116*(9), 094901. https://doi.org/10.1063/1.4894279

Zhu, J., Christensen, J., Jung, J., Martin-Moreno, L., Yin, X., Fok, L., Zhang, X., & Garcia-Vidal, F. J. (2011). A holey-structured metamaterial for acoustic deep-subwavelength imaging. *Nature Physics*, *7*(1), 52–55. https://doi.org/10.1038/nphys1804

Zhu, R., Liu, X. N., Hu, G. K., Sun, C. T., & Huang, G. L. (2014). Negative refraction of elastic waves at the deep-subwavelength scale in a single-phase metamaterial. *Nature Communications, 5*. https://doi.org/10.1038/ncomms6510

Zhu, R., Liu, X. N., Hu, G. K., Yuan, F. G., & Huang, G. L. (2015). Microstructural designs of plate-type elastic metamaterial and their potential applications: A review. *International Journal of Smart and Nano Materials*, *6*(1), 14–40. https://doi.org/10.1080/19475411.2015.1025249

Appendix A: First publication

BACK TO BASICS | 13

Ultrasonic Guided Wave Scattering

John K. Birir[1], Wilson Macharia Kairu[1], Michael J. Gatari[1], Prabhu Rajagopal[2]
[1]Institute of Nuclear Science and Technology, University of Nairobi, Kenya
[2]Center for Nondestructive Evaluation and Department of Mechanical Engineering, Indian Institute of Technology Madras, Chennai 600036, Tamil Nadu, India
Email: jbirir@uonbi.ac.ke

BACK TO

Abstract

Ultrasonic waves are widely used in medical and industrial diagnostics. This is made possible due to the scattering phenomena that results from acoustic impedance variations in a media. Whenever sound waves encounter such a discontinuity, it will be partially transmitted, reflected, diffracted, and mode converted. This paper presents the fundamental theory of guided ultrasonic waves interaction with obstacles. It is these scattered wave signals are then processed to yield obstacle characteristics such as size, shape and depth, which are important for nondestructive testing.

Key words: *Guided waves, ultrasonic testing, exact solutions, approximate solutions, hybrid methods*

https://isnt.in/ebook

AIP Advances ARTICLE scitation.org/journal/adv

Structured channel metamaterials for deep sub-wavelength resolution in guided ultrasonics

Cite as: AIP Advances 10, 065027 (2020); doi: 10.1063/1.5143696
Submitted: 25 January 2020 • Accepted: 25 May 2020 •
Published Online: 19 June 2020

View Online Export Citation CrossMark

John K. Birir,[1] Michael J. Gatari,[1] and Prabhu Rajagopal[2,a)]

AFFILIATIONS

[1]Institute of Nuclear Science and Technology, College of Architecture and Engineering, University of Nairobi, P.O Box 30197, 00100 Nairobi, Kenya

[2]Center for Nondestructive Evaluation and Department of Mechanical Engineering, Indian Institute of Technology Madras, Chennai, 600036 Tamil Nadu, India

[a)]Author to whom correspondence should be addressed: prajagopal@iitm.ac.in

ABSTRACT

Experimental results on deep subwavelength resolution of defects are presented for the first time in the context of guided ultrasonic wave inspection of defects, using novel "structured channel" metamaterials. An Aluminum bar with side-drilled holes is used as a test sample, interrogated by the fundamental bar-guided symmetric mode. Simulations were conducted to optimize dimensional parameters of the metamaterial structure. Experiments using metamaterials fabricated accordingly demonstrate a resolution down to 1/72 of the operating wavelength, potentially bringing the resolution of guided wave inspection to the same range as that of bulk ultrasonics. This work has much promise for remote inspection in industry and biomedicine.

© 2020 Author(s). All article content, except where otherwise noted, is licensed under a Creative Commons Attribution (CC BY) license (http://creativecommons.org/licenses/by/4.0/). https://doi.org/10.1063/1.5143696

Appendix C: Third publication

46th Annual Review of Progress
in Quantitative Nondestructive Evaluation
QNDE2019
July 14-19, 2019, Portland, OR, USA

QNDE2019-6901

CHANNEL STRUCTURED METAMATERIALS FOR SUPER RESOLUTION IMAGING

John Birir[1], Michael J. Gatari
Institute of Nuclear Science and Technology,
University of Nairobi, Kenya

Prabhu Rajagopal
Center for Nondestructive Evaluation and Department of Mechanical Engineering,
Indian Institute of Technology Madras, Chennai 600036, Tamil Nadu, India

ABSTRACT

Ultrasonic testing is one of the NDT methods that is critical for ensuring integrity of critical assets such as in the nuclear and aerospace industries. The traditional bulk ultrasonic waves have been proven very useful in finding defects over a narrow span and short ranges of distance. The short range is attributed to the fact that high frequency waves with short wavelengths are used hence subjected to greater attenuation. When inspection is required to be conducted from a remote distance, due for example to safety concerns, guided ultrasonic wave testing technique is the preferred choice. Guided waves are usually low frequency hence are not subjected to much attenuation relative to the bulk waves. As a result, guided waves can travel a longer distance. One of the limitations of guided waves however, is that the low frequency (longer wavelength) used lead to lower resolution capabilities due to the inherent diffraction limits of $\lambda/2$ (where λ is wavelength). Guided waves are therefore generally used as screening tools to locate areas of interest. A higher resolution technique is then employed to further investigate and characterize the features of defects in the identified areas.

To overcome this challenge of resolution, a technique is proposed that increases the resolution capability of guided waves beyond the diffraction limit. Simulation using commercial finite element software is used to optimize variables involved in the proposed method. The simulation is then validated with experiments. In the present work a resolution of $\lambda/72$ is demonstrated experimentally.

Keywords: guided waves, super resolution, metamaterials

https://www.iastatedigitalpress.com/qnde/article/id/8613/

Appendix D: Model input file code for hole defects

```
%{
-----------------------------------------------------------------------------------------------------------
%Purpose: Input file generated by Abaqus from the hole defects model developed in Abaqus
%graphical user interface. This input file is then executed by the Abaqus solver.
%Author: John Birir
%Research Work: Super resolution imaging in guided ultrasonic waves (for PhD in NS at EIE-
%UoN)
-----------------------------------------------------------------------------------------------------------
%}

*Heading
** Job name: Job-1 Model name: Model-1
*Preprint, echo=NO, model=NO, history=NO, contact=NO
**
** PARTS
**
*Part, name=Part-1-aluminium
*End Part
**
*Part, name=Part-2-water
*End Part
**
**
** ASSEMBLY
**
*Assembly, name=Assembly
**
*Instance, name=Part-1-aluminium-1, part=Part-1-aluminium
*Node
      1,  0.100000001,           0.
      2,  0.100000001, 0.00999999978
      3,           0., 0.00999999978
      4,           0.,           0.
      5,  0.118000001, 0.00499999989
      6,  0.128000006, 0.00499999989
      7,  0.140000001,           0.
      8,  0.140000001, 0.00999999978
      9,  0.159999996,           0.
     10,  0.159999996, 0.00999999978
     11,  0.100000001, 0.00200000009
     12,  0.100000001, 0.00400000019
     13,  0.100000001, 0.00600000005
     14,  0.100000001, 0.00800000038
     15, 0.0979999974, 0.00999999978
     16, 0.0960000008, 0.00999999978
     17, 0.0939999968, 0.00999999978
     18, 0.0920000002, 0.00999999978
     19, 0.0900000036, 0.00999999978
     20, 0.0879999995, 0.00999999978
     21, 0.0860000029, 0.00999999978
     22, 0.0839999989, 0.00999999978
     23, 0.0820000023, 0.00999999978
     24, 0.0799999982, 0.00999999978
     25, 0.0780000016, 0.00999999978
     26, 0.0759999976, 0.00999999978
     27,  0.074000001, 0.00999999978
     28, 0.0719999969, 0.00999999978
     29, 0.0700000003, 0.00999999978
     30, 0.0680000037, 0.00999999978
     31, 0.0659999996, 0.00999999978
     32,  0.064000003, 0.00999999978
     33,  0.061999999, 0.00999999978
     34, 0.0599999987, 0.00999999978
     35, 0.0579999983, 0.00999999978
     36, 0.0560000017, 0.00999999978
     37, 0.0540000014, 0.00999999978
     38, 0.0520000011, 0.00999999978
     39, 0.0500000007, 0.00999999978
     40, 0.0480000004, 0.00999999978
     41, 0.0460000001, 0.00999999978
     42, 0.0439999998, 0.00999999978
     43, 0.0419999994, 0.00999999978
     44, 0.0399999991, 0.00999999978
     45, 0.0379999988, 0.00999999978
     46, 0.0359999985, 0.00999999978
```

47, 0.0340000018, 0.00999999978
48, 0.0320000015, 0.00999999978
49, 0.0299999993, 0.00999999978
50, 0.0280000009, 0.00999999978
51, 0.0260000005, 0.00999999978
52, 0.0240000002, 0.00999999978
53, 0.0219999999, 0.00999999978
54, 0.0199999996, 0.00999999978
55, 0.0179999992, 0.00999999978
56, 0.0160000008, 0.00999999978
57, 0.0140000004, 0.00999999978
58, 0.0120000001, 0.00999999978
59, 0.00999999978, 0.00999999978
60, 0.00800000038, 0.00999999978
61, 0.00600000005, 0.00999999978
62, 0.00400000019, 0.00999999978
63, 0.00200000009, 0.00999999978
64, 0., 0.00800000038
65, 0., 0.00600000005
66, 0., 0.00400000019
67, 0., 0.00200000009
68, 0.00200000009, 0.
69, 0.00400000019, 0.
70, 0.00600000005, 0.
71, 0.00800000038, 0.
72, 0.00999999978, 0.
73, 0.0120000001, 0.
74, 0.0140000004, 0.
75, 0.0160000008, 0.
76, 0.0179999992, 0.
77, 0.0199999996, 0.
78, 0.0219999999, 0.
79, 0.0240000002, 0.
80, 0.0260000005, 0.
81, 0.0280000009, 0.
82, 0.0299999993, 0.
83, 0.0320000015, 0.
84, 0.0340000018, 0.
85, 0.0359999985, 0.
86, 0.0379999988, 0.
87, 0.0399999991, 0.
88, 0.0419999994, 0.
89, 0.0439999998, 0.
90, 0.0460000001, 0.
91, 0.0480000004, 0.
92, 0.0500000007, 0.
93, 0.0520000011, 0.
94, 0.0540000014, 0.
95, 0.0560000017, 0.
96, 0.0579999983, 0.
97, 0.0599999987, 0.
98, 0.061999999, 0.
99, 0.064000003, 0.
100, 0.0659999996, 0.
101, 0.0680000037, 0.
102, 0.0700000003, 0.
103, 0.0719999969, 0.
104, 0.074000001, 0.
105, 0.0759999976, 0.
106, 0.0780000016, 0.
107, 0.0799999982, 0.
108, 0.0820000023, 0.
109, 0.0839999989, 0.
110, 0.0860000029, 0.
111, 0.0879999995, 0.
112, 0.0900000036, 0.
113, 0.0920000002, 0.
114, 0.0939999968, 0.
115, 0.0960000008, 0.
116, 0.0979999974, 0.
117, 0.117298134, 0.00692836288
118, 0.115520947, 0.00795442332
119, 0.113499999, 0.00759807602
120, 0.112180918, 0.00602606032
121, 0.112180918, 0.00397393946
122, 0.113499999, 0.00240192376
123, 0.115520947, 0.00204557669
124, 0.117298134, 0.00307163713
125, 0.127298132, 0.00692836288
126, 0.125520945, 0.00795442332
127, 0.123499997, 0.00759807602
128, 0.122180924, 0.00602606032
129, 0.122180924, 0.00397393946
130, 0.123499997, 0.00240192376
131, 0.125520945, 0.00204557669
132, 0.127298132, 0.00307163713
133, 0.140000001, 0.00200000009
134, 0.140000001, 0.00400000019
135, 0.140000001, 0.00600000005
136, 0.140000001, 0.00800000038
137, 0.137999997, 0.00999999978
138, 0.136000007, 0.00999999978
139, 0.134000003, 0.00999999978
140, 0.131999999, 0.00999999978
141, 0.129999995, 0.00999999978
142, 0.128000006, 0.00999999978
143, 0.126000002, 0.00999999978
144, 0.123999998, 0.00999999978
145, 0.122000001, 0.00999999978
146, 0.119999997, 0.00999999978
147, 0.118000001, 0.00999999978
148, 0.115999997, 0.00999999978
149, 0.114, 0.00999999978
150, 0.112000003, 0.00999999978
151, 0.109999999, 0.00999999978
152, 0.108000003, 0.00999999978
153, 0.105999999, 0.00999999978
154, 0.104000002, 0.00999999978
155, 0.101999998, 0.00999999978
156, 0.101999998, 0.

157, 0.104000002, 0.
158, 0.105999999, 0.
159, 0.108000003, 0.
160, 0.109999999, 0.
161, 0.112000003, 0.
162, 0.114, 0.
163, 0.115999997, 0.
164, 0.118000001, 0.
165, 0.119999997, 0.
166, 0.122000001, 0.
167, 0.123999998, 0.
168, 0.126000002, 0.
169, 0.128000006, 0.
170, 0.129999995, 0.
171, 0.131999999, 0.
172, 0.134000003, 0.
173, 0.136000007, 0.
174, 0.137999997, 0.
175, 0.142000005, 0.
176, 0.143999994, 0.
177, 0.145999998, 0.
178, 0.148000002, 0.
179, 0.150000006, 0.
180, 0.151999995, 0.
181, 0.153999999, 0.
182, 0.156000003, 0.
183, 0.158000007, 0.
184, 0.159999996, 0.00200000009
185, 0.159999996, 0.00400000019
186, 0.159999996, 0.00600000005
187, 0.159999996, 0.00800000038
188, 0.158000007, 0.00999999978
189, 0.156000003, 0.00999999978
190, 0.153999999, 0.00999999978
191, 0.151999995, 0.00999999978
192, 0.150000006, 0.00999999978
193, 0.148000002, 0.00999999978
194, 0.145999998, 0.00999999978
195, 0.143999994, 0.00999999978
196, 0.142000005, 0.00999999978
197, 0.0979999974, 0.00200000009
198, 0.0979999974, 0.00400000019
199, 0.0979999974, 0.00600000005
200, 0.0979999974, 0.00800000038
201, 0.0960000008, 0.00200000009
202, 0.0960000008, 0.00400000019
203, 0.0960000008, 0.00600000005
204, 0.0960000008, 0.00800000038
205, 0.0939999968, 0.00200000009
206, 0.0939999968, 0.00400000019
207, 0.0939999968, 0.00600000005
208, 0.0939999968, 0.00800000038
209, 0.0920000002, 0.00200000009
210, 0.0920000002, 0.00400000019
211, 0.0920000002, 0.00600000005
212, 0.0920000002, 0.00800000038
213, 0.0900000036, 0.00200000009
214, 0.0900000036, 0.00400000019
215, 0.0900000036, 0.00600000005
216, 0.0900000036, 0.00800000038
217, 0.0879999995, 0.00200000009
218, 0.0879999995, 0.00400000019
219, 0.0879999995, 0.00600000005
220, 0.0879999995, 0.00800000038
221, 0.0860000029, 0.00200000009
222, 0.0860000029, 0.00400000019
223, 0.0860000029, 0.00600000005
224, 0.0860000029, 0.00800000038
225, 0.0839999989, 0.00200000009
226, 0.0839999989, 0.00400000019
227, 0.0839999989, 0.00600000005
228, 0.0839999989, 0.00800000038
229, 0.0820000023, 0.00200000009
230, 0.0820000023, 0.00400000019
231, 0.0820000023, 0.00600000005
232, 0.0820000023, 0.00800000038
233, 0.0799999982, 0.00200000009
234, 0.0799999982, 0.00400000019
235, 0.0799999982, 0.00600000005
236, 0.0799999982, 0.00800000038
237, 0.0780000016, 0.00200000009
238, 0.0780000016, 0.00400000019
239, 0.0780000016, 0.00600000005
240, 0.0780000016, 0.00800000038
241, 0.0759999976, 0.00200000009
242, 0.0759999976, 0.00400000019
243, 0.0759999976, 0.00600000005
244, 0.0759999976, 0.00800000038
245, 0.074000001, 0.00200000009
246, 0.074000001, 0.00400000019
247, 0.074000001, 0.00600000005
248, 0.074000001, 0.00800000038
249, 0.0719999969, 0.00200000009
250, 0.0719999969, 0.00400000019
251, 0.0719999969, 0.00600000005
252, 0.0719999969, 0.00800000038
253, 0.0700000003, 0.00200000009
254, 0.0700000003, 0.00400000019
255, 0.0700000003, 0.00600000005
256, 0.0700000003, 0.00800000038
257, 0.0680000037, 0.00200000009
258, 0.0680000037, 0.00400000019
259, 0.0680000037, 0.00600000005
260, 0.0680000037, 0.00800000038
261, 0.0659999996, 0.00200000009
262, 0.0659999996, 0.00400000019
263, 0.0659999996, 0.00600000005
264, 0.0659999996, 0.00800000038
265, 0.064000003, 0.00200000009
266, 0.064000003, 0.00400000019

267, 0.064000003, 0.00600000005
268, 0.064000003, 0.00800000038
269, 0.061999999, 0.00200000009
270, 0.061999999, 0.00400000019
271, 0.061999999, 0.00600000005
272, 0.061999999, 0.00800000038
273, 0.0599999987, 0.00200000009
274, 0.0599999987, 0.00400000019
275, 0.0599999987, 0.00600000005
276, 0.0599999987, 0.00800000038
277, 0.0579999983, 0.00200000009
278, 0.0579999983, 0.00400000019
279, 0.0579999983, 0.00600000005
280, 0.0579999983, 0.00800000038
281, 0.0560000017, 0.00200000009
282, 0.0560000017, 0.00400000019
283, 0.0560000017, 0.00600000005
284, 0.0560000017, 0.00800000038
285, 0.0540000014, 0.00200000009
286, 0.0540000014, 0.00400000019
287, 0.0540000014, 0.00600000005
288, 0.0540000014, 0.00800000038
289, 0.0520000011, 0.00200000009
290, 0.0520000011, 0.00400000019
291, 0.0520000011, 0.00600000005
292, 0.0520000011, 0.00800000038
293, 0.0500000007, 0.00200000009
294, 0.0500000007, 0.00400000019
295, 0.0500000007, 0.00600000005
296, 0.0500000007, 0.00800000038
297, 0.0480000004, 0.00200000009
298, 0.0480000004, 0.00400000019
299, 0.0480000004, 0.00600000005
300, 0.0480000004, 0.00800000038
301, 0.0460000001, 0.00200000009
302, 0.0460000001, 0.00400000019
303, 0.0460000001, 0.00600000005
304, 0.0460000001, 0.00800000038
305, 0.0439999998, 0.00200000009
306, 0.0439999998, 0.00400000019
307, 0.0439999998, 0.00600000005
308, 0.0439999998, 0.00800000038
309, 0.0419999994, 0.00200000009
310, 0.0419999994, 0.00400000019
311, 0.0419999994, 0.00600000005
312, 0.0419999994, 0.00800000038
313, 0.0399999991, 0.00200000009
314, 0.0399999991, 0.00400000019
315, 0.0399999991, 0.00600000005
316, 0.0399999991, 0.00800000038
317, 0.0379999988, 0.00200000009
318, 0.0379999988, 0.00400000019
319, 0.0379999988, 0.00600000005
320, 0.0379999988, 0.00800000038
321, 0.0359999985, 0.00200000009
322, 0.0359999985, 0.00400000019
323, 0.0359999985, 0.00600000005
324, 0.0359999985, 0.00800000038
325, 0.0340000018, 0.00200000009
326, 0.0340000018, 0.00400000019
327, 0.0340000018, 0.00600000005
328, 0.0340000018, 0.00800000038
329, 0.0320000015, 0.00200000009
330, 0.0320000015, 0.00400000019
331, 0.0320000015, 0.00600000005
332, 0.0320000015, 0.00800000038
333, 0.0299999993, 0.00200000009
334, 0.0299999993, 0.00400000019
335, 0.0299999993, 0.00600000005
336, 0.0299999993, 0.00800000038
337, 0.0280000009, 0.00200000009
338, 0.0280000009, 0.00400000019
339, 0.0280000009, 0.00600000005
340, 0.0280000009, 0.00800000038
341, 0.0260000005, 0.00200000009
342, 0.0260000005, 0.00400000019
343, 0.0260000005, 0.00600000005
344, 0.0260000005, 0.00800000038
345, 0.0240000002, 0.00200000009
346, 0.0240000002, 0.00400000019
347, 0.0240000002, 0.00600000005
348, 0.0240000002, 0.00800000038
349, 0.0219999999, 0.00200000009
350, 0.0219999999, 0.00400000019
351, 0.0219999999, 0.00600000005
352, 0.0219999999, 0.00800000038
353, 0.0199999996, 0.00200000009
354, 0.0199999996, 0.00400000019
355, 0.0199999996, 0.00600000005
356, 0.0199999996, 0.00800000038
357, 0.0179999992, 0.00200000009
358, 0.0179999992, 0.00400000019
359, 0.0179999992, 0.00600000005
360, 0.0179999992, 0.00800000038
361, 0.0160000008, 0.00200000009
362, 0.0160000008, 0.00400000019
363, 0.0160000008, 0.00600000005
364, 0.0160000008, 0.00800000038
365, 0.0140000004, 0.00200000009
366, 0.0140000004, 0.00400000019
367, 0.0140000004, 0.00600000005
368, 0.0140000004, 0.00800000038
369, 0.0120000001, 0.00200000009
370, 0.0120000001, 0.00400000019
371, 0.0120000001, 0.00600000005
372, 0.0120000001, 0.00800000038
373, 0.00999999978, 0.00200000009
374, 0.00999999978, 0.00400000019
375, 0.00999999978, 0.00600000005
376, 0.00999999978, 0.00800000038

377, 0.00800000038, 0.00200000009
378, 0.00800000038, 0.00400000019
379, 0.00800000038, 0.00600000005
380, 0.00800000038, 0.00800000038
381, 0.00600000005, 0.00200000009
382, 0.00600000005, 0.00400000019
383, 0.00600000005, 0.00600000005
384, 0.00600000005, 0.00800000038
385, 0.00400000019, 0.00200000009
386, 0.00400000019, 0.00400000019
387, 0.00400000019, 0.00600000005
388, 0.00400000019, 0.00800000038
389, 0.00200000009, 0.00200000009
390, 0.00200000009, 0.00400000019
391, 0.00200000009, 0.00600000005
392, 0.00200000009, 0.00800000038
393, 0.102547526, 0.00605859514
394, 0.137914509, 0.00393700274
395, 0.102047719, 0.00815935433
396, 0.102208197, 0.00394722354
397, 0.107661963, 0.00830960926
398, 0.105775408, 0.00844638888
399, 0.109546579, 0.00815661438
400, 0.111466102, 0.00800957531
401, 0.118099079, 0.00775563158
402, 0.120713606, 0.00730458135
403, 0.127787352, 0.00853915606
404, 0.129888415, 0.00843826216
405, 0.133930579, 0.00827091094
406, 0.13585791, 0.00804228988
407, 0.137915283, 0.00797032565
408, 0.106182702, 0.00182955561
409, 0.135997683, 0.00183719967
410, 0.134037182, 0.00166486844
411, 0.132091492, 0.001493769
412, 0.130138695, 0.00139374542
413, 0.128135085, 0.00143976044
414, 0.121446833, 0.00187402323
415, 0.119288661, 0.0019758807
416, 0.110858269, 0.00164250529
417, 0.108268633, 0.00188413006
418, 0.104109719, 0.00187864853
419, 0.120596766, 0.00529405056
420, 0.120321706, 0.00361538539
421, 0.128912762, 0.00396345509
422, 0.129776359, 0.00695766369
423, 0.117753223, 0.00124701182
424, 0.131943733, 0.00839937665
425, 0.137987405, 0.00194679725
426, 0.102065839, 0.00197174912
427, 0.103889845, 0.00846692827
428, 0.137832895, 0.00594571885
429, 0.104297377, 0.00366008165
430, 0.105394021, 0.00682118535
431, 0.107181996, 0.00653926283
432, 0.133660153, 0.0066376077
433, 0.108251773, 0.00396377733
434, 0.106273957, 0.00346756028
435, 0.135845065, 0.00376042351
436, 0.110811636, 0.00613428652
437, 0.133891657, 0.0033561876
438, 0.110561989, 0.00377889699
439, 0.108983047, 0.00621867692
440, 0.129926637, 0.00549766421
441, 0.132044956, 0.00296243979
442, 0.135455817, 0.00588790234
443, 0.133430898, 0.00501297927
444, 0.131836027, 0.00689972751
445, 0.106570989, 0.004867977
446, 0.131734103, 0.00554696145
447, 0.125772536, 0.00886108447
448, 0.123822063, 0.00890307687
449, 0.128566027, 0.00273268553
450, 0.119224764, 0.00843046419
451, 0.120259807, 0.00906111207
452, 0.121970296, 0.00858761836
453, 0.119396329, 0.00627948204
454, 0.130206332, 0.0041493834
455, 0.130232662, 0.00274875341
456, 0.10396558, 0.00717428513
457, 0.131824374, 0.00432382571
458, 0.10472066, 0.00527334912
459, 0.142000005, 0.00800000038
460, 0.142000005, 0.00600000005
461, 0.142000005, 0.00400000019
462, 0.142000005, 0.00200000009
463, 0.143999994, 0.00800000038
464, 0.143999994, 0.00600000005
465, 0.143999994, 0.00400000019
466, 0.143999994, 0.00200000009
467, 0.145999998, 0.00800000038
468, 0.145999998, 0.00600000005
469, 0.145999998, 0.00400000019
470, 0.145999998, 0.00200000009
471, 0.148000002, 0.00800000038
472, 0.148000002, 0.00600000005
473, 0.148000002, 0.00400000019
474, 0.148000002, 0.00200000009
475, 0.150000006, 0.00800000038
476, 0.150000006, 0.00600000005
477, 0.150000006, 0.00400000019
478, 0.150000006, 0.00200000009
479, 0.151999995, 0.00800000038
480, 0.151999995, 0.00600000005
481, 0.151999995, 0.00400000019
482, 0.151999995, 0.00200000009
483, 0.153999999, 0.00800000038
484, 0.153999999, 0.00600000005
485, 0.153999999, 0.00400000019
486, 0.153999999, 0.00200000009

```
   487,  0.156000003, 0.00800000038
   488,  0.156000003, 0.00600000005
   489,  0.156000003, 0.00400000019
   490,  0.156000003, 0.00200000009
*Element, type=CPE4R
  1,   1,  11, 197, 116
  2,  11,  12, 198, 197
  3,  12,  13, 199, 198
  4,  13,  14, 200, 199
  5,  14,   2,  15, 200
  6, 116, 197, 201, 115
  7, 197, 198, 202, 201
  8, 198, 199, 203, 202
  9, 199, 200, 204, 203
 10, 200,  15,  16, 204
 11, 115, 201, 205, 114
 12, 201, 202, 206, 205
 13, 202, 203, 207, 206
 14, 203, 204, 208, 207
 15, 204,  16,  17, 208
 16, 114, 205, 209, 113
 17, 205, 206, 210, 209
 18, 206, 207, 211, 210
 19, 207, 208, 212, 211
 20, 208,  17,  18, 212
 21, 113, 209, 213, 112
 22, 209, 210, 214, 213
 23, 210, 211, 215, 214
 24, 211, 212, 216, 215
 25, 212,  18,  19, 216
 26, 112, 213, 217, 111
 27, 213, 214, 218, 217
 28, 214, 215, 219, 218
 29, 215, 216, 220, 219
 30, 216,  19,  20, 220
 31, 111, 217, 221, 110
 32, 217, 218, 222, 221
 33, 218, 219, 223, 222
 34, 219, 220, 224, 223
 35, 220,  20,  21, 224
 36, 110, 221, 225, 109
 37, 221, 222, 226, 225
 38, 222, 223, 227, 226
 39, 223, 224, 228, 227
 40, 224,  21,  22, 228
 41, 109, 225, 229, 108
 42, 225, 226, 230, 229
 43, 226, 227, 231, 230
 44, 227, 228, 232, 231
 45, 228,  22,  23, 232
 46, 108, 229, 233, 107
 47, 229, 230, 234, 233
 48, 230, 231, 235, 234
 49, 231, 232, 236, 235
 50, 232,  23,  24, 236
```

```
   491,  0.158000007, 0.00800000038
   492,  0.158000007, 0.00600000005
   493,  0.158000007, 0.00400000019
   494,  0.158000007, 0.00200000009
 51, 107, 233, 237, 106
 52, 233, 234, 238, 237
 53, 234, 235, 239, 238
 54, 235, 236, 240, 239
 55, 236,  24,  25, 240
 56, 106, 237, 241, 105
 57, 237, 238, 242, 241
 58, 238, 239, 243, 242
 59, 239, 240, 244, 243
 60, 240,  25,  26, 244
 61, 105, 241, 245, 104
 62, 241, 242, 246, 245
 63, 242, 243, 247, 246
 64, 243, 244, 248, 247
 65, 244,  26,  27, 248
 66, 104, 245, 249, 103
 67, 245, 246, 250, 249
 68, 246, 247, 251, 250
 69, 247, 248, 252, 251
 70, 248,  27,  28, 252
 71, 103, 249, 253, 102
 72, 249, 250, 254, 253
 73, 250, 251, 255, 254
 74, 251, 252, 256, 255
 75, 252,  28,  29, 256
 76, 102, 253, 257, 101
 77, 253, 254, 258, 257
 78, 254, 255, 259, 258
 79, 255, 256, 260, 259
 80, 256,  29,  30, 260
 81, 101, 257, 261, 100
 82, 257, 258, 262, 261
 83, 258, 259, 263, 262
 84, 259, 260, 264, 263
 85, 260,  30,  31, 264
 86, 100, 261, 265,  99
 87, 261, 262, 266, 265
 88, 262, 263, 267, 266
 89, 263, 264, 268, 267
 90, 264,  31,  32, 268
 91,  99, 265, 269,  98
 92, 265, 266, 270, 269
 93, 266, 267, 271, 270
 94, 267, 268, 272, 271
 95, 268,  32,  33, 272
 96,  98, 269, 273,  97
 97, 269, 270, 274, 273
 98, 270, 271, 275, 274
 99, 271, 272, 276, 275
100, 272,  33,  34, 276
101,  97, 273, 277,  96
```

102, 273, 274, 278, 277
103, 274, 275, 279, 278
104, 275, 276, 280, 279
105, 276, 34, 35, 280
106, 96, 277, 281, 95
107, 277, 278, 282, 281
108, 278, 279, 283, 282
109, 279, 280, 284, 283
110, 280, 35, 36, 284
111, 95, 281, 285, 94
112, 281, 282, 286, 285
113, 282, 283, 287, 286
114, 283, 284, 288, 287
115, 284, 36, 37, 288
116, 94, 285, 289, 93
117, 285, 286, 290, 289
118, 286, 287, 291, 290
119, 287, 288, 292, 291
120, 288, 37, 38, 292
121, 93, 289, 293, 92
122, 289, 290, 294, 293
123, 290, 291, 295, 294
124, 291, 292, 296, 295
125, 292, 38, 39, 296
126, 92, 293, 297, 91
127, 293, 294, 298, 297
128, 294, 295, 299, 298
129, 295, 296, 300, 299
130, 296, 39, 40, 300
131, 91, 297, 301, 90
132, 297, 298, 302, 301
133, 298, 299, 303, 302
134, 299, 300, 304, 303
135, 300, 40, 41, 304
136, 90, 301, 305, 89
137, 301, 302, 306, 305
138, 302, 303, 307, 306
139, 303, 304, 308, 307
140, 304, 41, 42, 308
141, 89, 305, 309, 88
142, 305, 306, 310, 309
143, 306, 307, 311, 310
144, 307, 308, 312, 311
145, 308, 42, 43, 312
146, 88, 309, 313, 87
147, 309, 310, 314, 313
148, 310, 311, 315, 314
149, 311, 312, 316, 315
150, 312, 43, 44, 316
151, 87, 313, 317, 86
152, 313, 314, 318, 317
153, 314, 315, 319, 318
154, 315, 316, 320, 319
155, 316, 44, 45, 320
156, 86, 317, 321, 85
157, 317, 318, 322, 321
158, 318, 319, 323, 322
159, 319, 320, 324, 323
160, 320, 45, 46, 324
161, 85, 321, 325, 84
162, 321, 322, 326, 325
163, 322, 323, 327, 326
164, 323, 324, 328, 327
165, 324, 46, 47, 328
166, 84, 325, 329, 83
167, 325, 326, 330, 329
168, 326, 327, 331, 330
169, 327, 328, 332, 331
170, 328, 47, 48, 332
171, 83, 329, 333, 82
172, 329, 330, 334, 333
173, 330, 331, 335, 334
174, 331, 332, 336, 335
175, 332, 48, 49, 336
176, 82, 333, 337, 81
177, 333, 334, 338, 337
178, 334, 335, 339, 338
179, 335, 336, 340, 339
180, 336, 49, 50, 340
181, 81, 337, 341, 80
182, 337, 338, 342, 341
183, 338, 339, 343, 342
184, 339, 340, 344, 343
185, 340, 50, 51, 344
186, 80, 341, 345, 79
187, 341, 342, 346, 345
188, 342, 343, 347, 346
189, 343, 344, 348, 347
190, 344, 51, 52, 348
191, 79, 345, 349, 78
192, 345, 346, 350, 349
193, 346, 347, 351, 350
194, 347, 348, 352, 351
195, 348, 52, 53, 352
196, 78, 349, 353, 77
197, 349, 350, 354, 353
198, 350, 351, 355, 354
199, 351, 352, 356, 355
200, 352, 53, 54, 356
201, 77, 353, 357, 76
202, 353, 354, 358, 357
203, 354, 355, 359, 358
204, 355, 356, 360, 359
205, 356, 54, 55, 360
206, 76, 357, 361, 75
207, 357, 358, 362, 361
208, 358, 359, 363, 362
209, 359, 360, 364, 363
210, 360, 55, 56, 364
211, 75, 361, 365, 74

212, 361, 362, 366, 365
213, 362, 363, 367, 366
214, 363, 364, 368, 367
215, 364, 56, 57, 368
216, 74, 365, 369, 73
217, 365, 366, 370, 369
218, 366, 367, 371, 370
219, 367, 368, 372, 371
220, 368, 57, 58, 372
221, 73, 369, 373, 72
222, 369, 370, 374, 373
223, 370, 371, 375, 374
224, 371, 372, 376, 375
225, 372, 58, 59, 376
226, 72, 373, 377, 71
227, 373, 374, 378, 377
228, 374, 375, 379, 378
229, 375, 376, 380, 379
230, 376, 59, 60, 380
231, 71, 377, 381, 70
232, 377, 378, 382, 381
233, 378, 379, 383, 382
234, 379, 380, 384, 383
235, 380, 60, 61, 384
236, 70, 381, 385, 69
237, 381, 382, 386, 385
238, 382, 383, 387, 386
239, 383, 384, 388, 387
240, 384, 61, 62, 388
241, 69, 385, 389, 68
242, 385, 386, 390, 389
243, 386, 387, 391, 390
244, 387, 388, 392, 391
245, 388, 62, 63, 392
246, 68, 389, 67, 4
247, 389, 390, 66, 67
248, 390, 391, 65, 66
249, 391, 392, 64, 65
250, 392, 63, 3, 64
257, 128, 402, 453, 419
258, 129, 128, 419, 420
259, 450, 401, 453, 402
260, 448, 127, 126, 447
261, 149, 119, 118, 148
262, 150, 400, 119, 149
263, 398, 430, 431, 397
264, 13, 12, 396, 393
265, 434, 408, 417, 433
266, 416, 122, 121, 438
267, 123, 122, 162, 163
268, 131, 130, 167, 168
269, 124, 123, 423, 415
270, 414, 130, 129, 420
271, 124, 415, 420, 5
272, 394, 435, 409, 425
273, 444, 422, 440, 446
274, 403, 142, 143, 447
275, 404, 141, 142, 403
276, 410, 409, 435, 437
277, 136, 8, 137, 407
278, 136, 407, 428, 135
279, 173, 409, 410, 172
280, 155, 2, 14, 395
281, 396, 426, 418, 429
282, 155, 395, 427, 154
283, 433, 439, 431, 445
284, 152, 397, 399, 151
285, 151, 399, 400, 150
286, 401, 148, 118, 117
287, 147, 148, 401, 450
288, 451, 450, 402, 452
289, 144, 145, 452, 448
290, 144, 448, 447, 143
291, 141, 404, 424, 140
292, 139, 405, 406, 138
293, 138, 406, 407, 137
294, 13, 393, 395, 14
295, 438, 433, 417, 416
296, 156, 426, 11, 1
297, 133, 425, 174, 7
298, 174, 425, 409, 173
299, 172, 410, 411, 171
300, 171, 411, 412, 170
301, 170, 412, 413, 169
302, 166, 167, 130, 414
303, 165, 166, 414, 415
304, 164, 423, 123, 163
305, 161, 162, 122, 416
306, 436, 438, 121, 120
307, 400, 436, 120, 119
308, 158, 408, 418, 157
309, 153, 398, 397, 152
310, 396, 12, 11, 426
311, 134, 135, 428, 394
312, 398, 153, 154, 427
313, 458, 393, 396, 429
314, 402, 128, 127, 452
315, 451, 452, 145, 146
316, 126, 125, 403, 447
317, 403, 125, 422, 404
318, 422, 125, 6, 440
319, 440, 6, 421, 454
320, 405, 139, 140, 424
321, 435, 442, 443, 437
322, 432, 442, 406, 405
323, 428, 407, 406, 442
324, 408, 158, 159, 417
325, 417, 159, 160, 416
326, 455, 454, 421, 449
327, 413, 449, 132, 131

```
328, 132, 449, 421,   6
329, 164, 165, 415, 423
330, 397, 431, 439, 399
331, 420, 419, 453,   5
332, 453, 401, 117,   5
333, 441, 411, 410, 437
334, 446, 440, 454, 457
335, 413, 131, 168, 169
336, 424, 404, 422, 444
337, 425, 133, 134, 394
338, 426, 156, 157, 418
339, 456, 430, 398, 427
340, 430, 458, 445, 431
341, 456, 427, 395, 393
342, 405, 424, 444, 432
343, 438, 436, 439, 433
344, 434, 429, 418, 408
345, 442, 435, 394, 428
346, 436, 400, 399, 439
347, 454, 455, 441, 457
348, 411, 441, 455, 412
349, 432, 444, 446, 443
350, 434, 445, 458, 429
351, 437, 443, 457, 441
352, 449, 413, 412, 455
353, 146, 147, 450, 451
354, 456, 393, 458, 430
355,   8, 136, 459, 196
356, 136, 135, 460, 459
357, 135, 134, 461, 460
358, 134, 133, 462, 461
359, 133,   7, 175, 462
360, 196, 459, 463, 195
361, 459, 460, 464, 463
362, 460, 461, 465, 464
363, 461, 462, 466, 465
364, 462, 175, 176, 466
365, 195, 463, 467, 194
366, 463, 464, 468, 467
*Element, type=CPE3
251, 452, 127, 448
252, 443, 442, 432
253, 416, 160, 161
254, 420, 415, 414
255, 433, 445, 434
256, 457, 443, 446
*Nset, nset=Set-1-transmitter
  3,  4, 64, 65, 66, 67
*Elset, elset=Set-1-transmitter, generate
 246,  250,    1
*Nset, nset=_PickedSet13, internal, generate
   1,  494,    1
*Elset, elset=_PickedSet13, internal, generate
   1,  404,    1
*Elset, elset=_Surf-1-AluminiumInterface_S2, internal
367, 464, 465, 469, 468
368, 465, 466, 470, 469
369, 466, 176, 177, 470
370, 194, 467, 471, 193
371, 467, 468, 472, 471
372, 468, 469, 473, 472
373, 469, 470, 474, 473
374, 470, 177, 178, 474
375, 193, 471, 475, 192
376, 471, 472, 476, 475
377, 472, 473, 477, 476
378, 473, 474, 478, 477
379, 474, 178, 179, 478
380, 192, 475, 479, 191
381, 475, 476, 480, 479
382, 476, 477, 481, 480
383, 477, 478, 482, 481
384, 478, 179, 180, 482
385, 191, 479, 483, 190
386, 479, 480, 484, 483
387, 480, 481, 485, 484
388, 481, 482, 486, 485
389, 482, 180, 181, 486
390, 190, 483, 487, 189
391, 483, 484, 488, 487
392, 484, 485, 489, 488
393, 485, 486, 490, 489
394, 486, 181, 182, 490
395, 189, 487, 491, 188
396, 487, 488, 492, 491
397, 488, 489, 493, 492
398, 489, 490, 494, 493
399, 490, 182, 183, 494
400, 188, 491, 187,  10
401, 491, 492, 186, 187
402, 492, 493, 185, 186
403, 493, 494, 184, 185
404, 494, 183,   9, 184
```

```
 5,  10,  15,  20,  25,  30,  35,  40,  45,  50,  55,  60,  65,  70,  75,  80
 85,  90,  95, 100, 105, 110, 115, 120, 125, 130, 135, 140, 145, 150, 155, 160
 165, 170, 175, 180, 185, 190, 195, 200, 205, 210, 215, 220, 225, 230, 235, 240
 245, 250, 274, 275, 277, 312, 320
*Elset, elset=_Surf-1-AluminiumInterface_S4, internal
 261, 262, 282, 284, 285, 290, 291, 292, 293, 309, 355, 360, 365, 370, 375, 380
 385, 390, 395, 400
*Elset, elset=_Surf-1-AluminiumInterface_S1, internal
 280, 287, 289, 353
*Elset, elset=_Surf-1-AluminiumInterface_S3, internal
 315,
*Surface, type=ELEMENT, name=Surf-1-AluminiumInterface
_Surf-1-AluminiumInterface_S2, S2
_Surf-1-AluminiumInterface_S4, S4
_Surf-1-AluminiumInterface_S1, S1
_Surf-1-AluminiumInterface_S3, S3
** Section: Section-1-aluminium
*Solid Section, elset=_PickedSet13, material=Material-1-aluminium
,
*End Instance
**
*Instance, name=Part-2-water-1, part=Part-2-water
        0.1,        0.01,           0.
*Node

1, 0.0179999992, 0.0189999994
      2, 0.0160000008, 0.0189999994
      3, 0.0160000008, 0.00100000005
      4, 0.0179999992, 0.00100000005
      5, 0.0140000004, 0.0189999994
      6, 0.0120000001, 0.0189999994
      7, 0.0120000001, 0.00100000005
      8, 0.0140000004, 0.00100000005
      9, 0.00999999978, 0.0189999994
     10, 0.00800000038, 0.0189999994
     11, 0.00800000038, 0.00100000005
     12, 0.00999999978, 0.00100000005
     13, 0.00600000005, 0.0189999994
     14, 0.00400000019, 0.0189999994
     15, 0.00400000019, 0.00100000005
     16, 0.00600000005, 0.00100000005
     17, 0.00200000009, 0.0189999994
     18,           0., 0.0189999994
     19,           0., 0.00100000005
     20, 0.00200000009, 0.00100000005
     21, 0.0419999994, 0.0189999994
     22, 0.0399999991, 0.0189999994
     23, 0.0399999991, 0.00100000005
     24, 0.0419999994, 0.00100000005
     25, 0.0379999988, 0.0189999994
     26, 0.0359999985, 0.0189999994
     27, 0.0359999985, 0.00100000005
     28, 0.0379999988, 0.00100000005
     29, 0.0340000018, 0.0189999994
     30, 0.0320000015, 0.0189999994
     31, 0.0320000015, 0.00100000005
     32, 0.0340000018, 0.00100000005
     33, 0.0299999993, 0.0189999994
     34, 0.0280000009, 0.0189999994
     35, 0.0280000009, 0.00100000005
     36, 0.0299999993, 0.00100000005
     37, 0.0260000005, 0.0189999994
     38, 0.0240000002, 0.0189999994
     39, 0.0240000002, 0.00100000005
     40, 0.0260000005, 0.00100000005
     41,           0.,           0.
     42, 0.0419999994,           0.
     43, 0.0199999996, 0.00100000005
     44, 0.0219999999, 0.00100000005
     45, 0.0419999994, 0.0199999996
     46,           0., 0.0199999996
     47, 0.0219999999, 0.0189999994
     48, 0.0199999996, 0.0189999994
     49, 0.0160000008, 0.0170000009
     50, 0.0160000008, 0.0149999997
     51, 0.0160000008, 0.0130000003
     52, 0.0160000008, 0.0109999999
     53, 0.0160000008, 0.00899999961
     54, 0.0160000008, 0.00700000022
     55, 0.0160000008, 0.00499999989
     56, 0.0160000008, 0.00300000003
     57, 0.0179999992, 0.00300000003
     58, 0.0179999992, 0.00499999989
     59, 0.0179999992, 0.00700000022
     60, 0.0179999992, 0.00899999961
```

61, 0.0179999992, 0.0109999999
62, 0.0179999992, 0.0130000003
63, 0.0179999992, 0.0149999997
64, 0.0179999992, 0.0170000009
65, 0.0120000001, 0.0170000009
66, 0.0120000001, 0.0149999997
67, 0.0120000001, 0.0130000003
68, 0.0120000001, 0.0109999999
69, 0.0120000001, 0.00899999961
70, 0.0120000001, 0.00700000022
71, 0.0120000001, 0.00499999989
72, 0.0120000001, 0.00300000003
73, 0.0140000004, 0.00300000003
74, 0.0140000004, 0.00499999989
75, 0.0140000004, 0.00700000022
76, 0.0140000004, 0.00899999961
77, 0.0140000004, 0.0109999999
78, 0.0140000004, 0.0130000003
79, 0.0140000004, 0.0149999997
80, 0.0140000004, 0.0170000009
81, 0.00800000038, 0.0170000009
82, 0.00800000038, 0.0149999997
83, 0.00800000038, 0.0130000003
84, 0.00800000038, 0.0109999999
85, 0.00800000038, 0.00899999961
86, 0.00800000038, 0.00700000022
87, 0.00800000038, 0.00499999989
88, 0.00800000038, 0.00300000003
89, 0.00999999978, 0.00300000003
90, 0.00999999978, 0.00499999989
91, 0.00999999978, 0.00700000022
92, 0.00999999978, 0.00899999961
93, 0.00999999978, 0.0109999999
94, 0.00999999978, 0.0130000003
95, 0.00999999978, 0.0149999997
96, 0.00999999978, 0.0170000009
97, 0.00400000019, 0.0170000009
98, 0.00400000019, 0.0149999997
99, 0.00400000019, 0.0130000003
100, 0.00400000019, 0.0109999999
101, 0.00400000019, 0.00899999961
102, 0.00400000019, 0.00700000022
103, 0.00400000019, 0.00499999989
104, 0.00400000019, 0.00300000003
105, 0.00600000005, 0.00300000003
106, 0.00600000005, 0.00499999989
107, 0.00600000005, 0.00700000022
108, 0.00600000005, 0.00899999961
109, 0.00600000005, 0.0109999999
110, 0.00600000005, 0.0130000003
111, 0.00600000005, 0.0149999997
112, 0.00600000005, 0.0170000009
113, 0., 0.0170000009
114, 0., 0.0149999997
115, 0., 0.0130000003
116, 0., 0.0109999999
117, 0., 0.00899999961
118, 0., 0.00700000022
119, 0., 0.00499999989
120, 0., 0.00300000003
121, 0.00200000009, 0.00300000003
122, 0.00200000009, 0.00499999989
123, 0.00200000009, 0.00700000022
124, 0.00200000009, 0.00899999961
125, 0.00200000009, 0.0109999999
126, 0.00200000009, 0.0130000003
127, 0.00200000009, 0.0149999997
128, 0.00200000009, 0.0170000009
129, 0.0399999991, 0.0170000009
130, 0.0399999991, 0.0149999997
131, 0.0399999991, 0.0130000003
132, 0.0399999991, 0.0109999999
133, 0.0399999991, 0.00899999961
134, 0.0399999991, 0.00700000022
135, 0.0399999991, 0.00499999989
136, 0.0399999991, 0.00300000003
137, 0.0419999994, 0.00300000003
138, 0.0419999994, 0.00499999989
139, 0.0419999994, 0.00700000022
140, 0.0419999994, 0.00899999961
141, 0.0419999994, 0.0109999999
142, 0.0419999994, 0.0130000003
143, 0.0419999994, 0.0149999997
144, 0.0419999994, 0.0170000009
145, 0.0359999985, 0.0170000009
146, 0.0359999985, 0.0149999997
147, 0.0359999985, 0.0130000003
148, 0.0359999985, 0.0109999999
149, 0.0359999985, 0.00899999961
150, 0.0359999985, 0.00700000022
151, 0.0359999985, 0.00499999989
152, 0.0359999985, 0.00300000003
153, 0.0379999988, 0.00300000003
154, 0.0379999988, 0.00499999989
155, 0.0379999988, 0.00700000022
156, 0.0379999988, 0.00899999961
157, 0.0379999988, 0.0109999999
158, 0.0379999988, 0.0130000003
159, 0.0379999988, 0.0149999997
160, 0.0379999988, 0.0170000009
161, 0.0320000015, 0.0170000009
162, 0.0320000015, 0.0149999997
163, 0.0320000015, 0.0130000003
164, 0.0320000015, 0.0109999999
165, 0.0320000015, 0.00899999961
166, 0.0320000015, 0.00700000022
167, 0.0320000015, 0.00499999989
168, 0.0320000015, 0.00300000003
169, 0.0340000018, 0.00300000003
170, 0.0340000018, 0.00499999989

171, 0.0340000018, 0.00700000022
172, 0.0340000018, 0.00899999961
173, 0.0340000018, 0.0109999999
174, 0.0340000018, 0.0130000003
175, 0.0340000018, 0.0149999997
176, 0.0340000018, 0.0170000009
177, 0.0280000009, 0.0170000009
178, 0.0280000009, 0.0149999997
179, 0.0280000009, 0.0130000003
180, 0.0280000009, 0.0109999999
181, 0.0280000009, 0.00899999961
182, 0.0280000009, 0.00700000022
183, 0.0280000009, 0.00499999989
184, 0.0280000009, 0.00300000003
185, 0.0299999993, 0.00300000003
186, 0.0299999993, 0.00499999989
187, 0.0299999993, 0.00700000022
188, 0.0299999993, 0.00899999961
189, 0.0299999993, 0.0109999999
190, 0.0299999993, 0.0130000003
191, 0.0299999993, 0.0149999997
192, 0.0299999993, 0.0170000009
193, 0.0240000002, 0.0170000009
194, 0.0240000002, 0.0149999997
195, 0.0240000002, 0.0130000003
196, 0.0240000002, 0.0109999999
197, 0.0240000002, 0.00899999961
198, 0.0240000002, 0.00700000022
199, 0.0240000002, 0.00499999989
200, 0.0240000002, 0.00300000003
201, 0.0260000005, 0.00300000003
202, 0.0260000005, 0.00499999989
203, 0.0260000005, 0.00700000022
204, 0.0260000005, 0.00899999961
205, 0.0260000005, 0.0109999999
206, 0.0260000005, 0.0130000003
207, 0.0260000005, 0.0149999997
208, 0.0260000005, 0.0170000009
209, 0.00200000009, 0.
210, 0.00400000019, 0.
211, 0.00600000005, 0.
212, 0.00800000038, 0.
213, 0.00999999978, 0.
214, 0.0120000001, 0.
215, 0.0140000004, 0.
216, 0.0160000008, 0.
217, 0.0179999992, 0.
218, 0.0199999996, 0.
219, 0.0219999999, 0.
220, 0.0240000002, 0.
221, 0.0260000005, 0.
222, 0.0280000009, 0.
223, 0.0299999993, 0.
224, 0.0320000015, 0.
225, 0.0340000018, 0.
226, 0.0359999985, 0.
227, 0.0379999988, 0.
228, 0.0399999991, 0.
229, 0.0399999991, 0.0199999996
230, 0.0379999988, 0.0199999996
231, 0.0359999985, 0.0199999996
232, 0.0340000018, 0.0199999996
233, 0.0320000015, 0.0199999996
234, 0.0299999993, 0.0199999996
235, 0.0280000009, 0.0199999996
236, 0.0260000005, 0.0199999996
237, 0.0240000002, 0.0199999996
238, 0.0219999999, 0.0199999996
239, 0.0199999996, 0.0199999996
240, 0.0179999992, 0.0199999996
241, 0.0160000008, 0.0199999996
242, 0.0140000004, 0.0199999996
243, 0.0120000001, 0.0199999996
244, 0.00999999978, 0.0199999996
245, 0.00800000038, 0.0199999996
246, 0.00600000005, 0.0199999996
247, 0.00400000019, 0.0199999996
248, 0.00200000009, 0.0199999996
249, 0.0199999996, 0.0170000009
250, 0.0199999996, 0.0149999997
251, 0.0199999996, 0.0130000003
252, 0.0199999996, 0.0109999999
253, 0.0199999996, 0.00899999961
254, 0.0199999996, 0.00700000022
255, 0.0199999996, 0.00499999989
256, 0.0199999996, 0.00300000003
257, 0.0219999999, 0.00300000003
258, 0.0219999999, 0.00499999989
259, 0.0219999999, 0.00700000022
260, 0.0219999999, 0.00899999961
261, 0.0219999999, 0.0109999999
262, 0.0219999999, 0.0130000003
263, 0.0219999999, 0.0149999997
264, 0.0219999999, 0.0170000009
*Element, type=AC2D4R

1, 1, 2, 49, 64
2, 64, 49, 50, 63
3, 63, 50, 51, 62
4, 62, 51, 52, 61
5, 61, 52, 53, 60
6, 60, 53, 54, 59
7, 59, 54, 55, 58
8, 58, 55, 56, 57
9, 57, 56, 3, 4
10, 5, 6, 65, 80
11, 80, 65, 66, 79
12, 79, 66, 67, 78

13, 78, 67, 68, 77
14, 77, 68, 69, 76
15, 76, 69, 70, 75
16, 75, 70, 71, 74
17, 74, 71, 72, 73
18, 73, 72, 7, 8
19, 9, 10, 81, 96
20, 96, 81, 82, 95
21, 95, 82, 83, 94
22, 94, 83, 84, 93
23, 93, 84, 85, 92
24, 92, 85, 86, 91
25, 91, 86, 87, 90
26, 90, 87, 88, 89
27, 89, 88, 11, 12
28, 13, 14, 97, 112
29, 112, 97, 98, 111
30, 111, 98, 99, 110
31, 110, 99, 100, 109
32, 109, 100, 101, 108
33, 108, 101, 102, 107
34, 107, 102, 103, 106
35, 106, 103, 104, 105
36, 105, 104, 15, 16
37, 17, 18, 113, 128
38, 128, 113, 114, 127
39, 127, 114, 115, 126
40, 126, 115, 116, 125
41, 125, 116, 117, 124
42, 124, 117, 118, 123
43, 123, 118, 119, 122
44, 122, 119, 120, 121
45, 121, 120, 19, 20
46, 21, 22, 129, 144
47, 144, 129, 130, 143
48, 143, 130, 131, 142
49, 142, 131, 132, 141
50, 141, 132, 133, 140
51, 140, 133, 134, 139
52, 139, 134, 135, 138
53, 138, 135, 136, 137
54, 137, 136, 23, 24
55, 25, 26, 145, 160
56, 160, 145, 146, 159
57, 159, 146, 147, 158
58, 158, 147, 148, 157
59, 157, 148, 149, 156
60, 156, 149, 150, 155
61, 155, 150, 151, 154
62, 154, 151, 152, 153
63, 153, 152, 27, 28
64, 29, 30, 161, 176
65, 176, 161, 162, 175
66, 175, 162, 163, 174
67, 174, 163, 164, 173
68, 173, 164, 165, 172
69, 172, 165, 166, 171
70, 171, 166, 167, 170
71, 170, 167, 168, 169
72, 169, 168, 31, 32
73, 33, 34, 177, 192
74, 192, 177, 178, 191
75, 191, 178, 179, 190
76, 190, 179, 180, 189
77, 189, 180, 181, 188
78, 188, 181, 182, 187
79, 187, 182, 183, 186
80, 186, 183, 184, 185
81, 185, 184, 35, 36
82, 37, 38, 193, 208
83, 208, 193, 194, 207
84, 207, 194, 195, 206
85, 206, 195, 196, 205
86, 205, 196, 197, 204
87, 204, 197, 198, 203
88, 203, 198, 199, 202
89, 202, 199, 200, 201
90, 201, 200, 39, 40
91, 19, 41, 209, 20
92, 20, 209, 210, 15
93, 15, 210, 211, 16
94, 16, 211, 212, 11
95, 11, 212, 213, 12
96, 12, 213, 214, 7
97, 7, 214, 215, 8
98, 8, 215, 216, 3
99, 3, 216, 217, 4
100, 4, 217, 218, 43
101, 43, 218, 219, 44
102, 44, 219, 220, 39
103, 39, 220, 221, 40
104, 40, 221, 222, 35
105, 35, 222, 223, 36
106, 36, 223, 224, 31
107, 31, 224, 225, 32
108, 32, 225, 226, 27
109, 27, 226, 227, 28
110, 28, 227, 228, 23
111, 23, 228, 42, 24
112, 21, 45, 229, 22
113, 22, 229, 230, 25
114, 25, 230, 231, 26
115, 26, 231, 232, 29
116, 29, 232, 233, 30
117, 30, 233, 234, 33
118, 33, 234, 235, 34
119, 34, 235, 236, 37
120, 37, 236, 237, 38
121, 38, 237, 238, 47
122, 47, 238, 239, 48

```
123,  48, 239, 240,   1
124,   1, 240, 241,   2
125,   2, 241, 242,   5
126,   5, 242, 243,   6
127,   6, 243, 244,   9
128,   9, 244, 245,  10
129,  10, 245, 246,  13
130,  13, 246, 247,  14
131,  14, 247, 248,  17
132,  17, 248,  46,  18
133,  47,  48, 249, 264
134, 264, 249, 250, 263
135, 263, 250, 251, 262
136, 262, 251, 252, 261
137, 261, 252, 253, 260
138, 260, 253, 254, 259
139, 259, 254, 255, 258
140, 258, 255, 256, 257
141, 257, 256,  43,  44

*Nset, nset=Set-1-receiver
  45,  46, 229, 230, 231, 232, 233, 234, 235, 236, 237, 238, 239, 240, 241, 242
 243, 244, 245, 246, 247, 248
*Elset, elset=Set-1-receiver, generate
 112,  132,    1
*Nset, nset=_PickedSet15, internal, generate
   1,  264,    1
*Elset, elset=_PickedSet15, internal, generate
   1,  141,    1
*Elset, elset=_Surf-1-WaterInterface_S2, internal, generate
  91,  111,    1
*Surface, type=ELEMENT, name=Surf-1-WaterInterface
_Surf-1-WaterInterface_S2, S2
** Section: Section-2-water
*Solid Section, elset=_PickedSet15, material=Material-2-water
,
*End Instance
**
** Constraint: Constraint-1
*Tie, name=Constraint-1, adjust=yes
Part-2-water-1.Surf-1-WaterInterface, Part-1-aluminium-1.Surf-1-AluminiumInterface
*End Assembly
*Amplitude, name=Amp-1
             0.,              0.,           1e-06, 0.0176789623742178,           2e-06, 0.0267159228293451,
3e-06, -0.0590169943749474
          4e-06, -0.267678962374218,           5e-06,            -0.5,           6e-06, -0.559016994374948,
7e-06, -0.276715922829345
          8e-06, 0.341318065920549,           9e-06, 1.05901699437495,           1e-05,              1.5,
1.1e-05, 1.35035502637568
        1.2e-05,  0.559016994374948,           1.3e-05,  -0.591318065920546,           1.4e-05,  -
1.60035502637568,         1.5e-05,             -2.
        1.6e-05,  -1.60035502637568,           1.7e-05,  -0.591318065920551,           1.8e-05,
0.559016994374947,         1.9e-05, 1.35035502637568
          2e-05,             1.5,         2.1e-05, 1.05901699437495,         2.2e-05, 0.341318065920552,
2.3e-05, -0.276715922829343
        2.4e-05, -0.559016994374947,       2.5e-05,         -0.5,       2.6e-05, -0.267678962374218,
2.7e-05, -0.0590169943749484
        2.8e-05, 0.026715922829345,         2.9e-05, 0.0176789623742179
**
** MATERIALS
**
*Material, name=Material-1-aluminium
*Density
2700.,
```

```
*Elastic
 7e+10, 0.33
*Material, name=Material-2-water
*Acoustic Medium
 2.2e+09,
*Density
1000.,
** ----------------------------------------------------------------
**
** STEP: Step-1
**
*Step, name=Step-1, nlgeom=YES
*Dynamic, Explicit, direct user control
1e-06, 0.0002
*Bulk Viscosity
0.06, 1.2
**
** OUTPUT REQUESTS
**
*Restart, write, number interval=1, time marks=NO
**
** FIELD OUTPUT: F-Output-1
**
*Output, field
*Node Output
PABS, POR, U
**
** HISTORY OUTPUT: H-Output-1
**
*Output, history, frequency=20
*Node Output, nset=Part-2-water-1.Set-1-receiver
PABS, POR
*End Step
```

Appendix E: Model input file code for crack defects

```
%{
 --------------------------------------------------------------------------------------------------------------
%Purpose: Input file generated by Abaqus from the crack defects model developed in Abaqus
%graphical user interface. This input file is then executed by the Abaqus solver.
%Author: John Birir
%Research Work: Super resolution imaging in guided ultrasonic waves (for PhD in NS at EIE-
%UoN)
--------------------------------------------------------------------------------------------------------------
%}

*Heading
** Job name: Job-1 Model name: Model-1
*Preprint, echo=NO, model=NO, history=NO, contact=NO
**
** PARTS
**
*Part, name=Part-1-aluminium
*End Part
**
*Part, name=Part-2-water
*End Part
**
**
** ASSEMBLY
**
*Assembly, name=Assembly
**
*Instance, name=Part-1-aluminium-1, part=Part-1-aluminium
*Node
      1,           0.,           0.
      2, 0.00200000009,           0.
      3, 0.00400000019,           0.
      4, 0.00600000005,           0.
      5, 0.00800000038,           0.
      6, 0.00999999978,           0.
      7, 0.0120000001,           0.
      8, 0.0140000004,           0.
      9, 0.0160000008,           0.
     10, 0.0179999992,           0.
     11, 0.0199999996,           0.
     12, 0.0219999999,           0.
     13, 0.0240000002,           0.
     14, 0.0260000005,           0.
     15, 0.0280000009,           0.
     16, 0.0299999993,           0.
     17, 0.0320000015,           0.
     18, 0.0340000018,           0.
     19, 0.0359999985,           0.
     20, 0.0379999988,           0.
     21, 0.0399999991,           0.
     22, 0.0419999994,           0.
     23, 0.0439999998,           0.
     24, 0.0460000001,           0.
     25, 0.0480000004,           0.
     26, 0.0500000007,           0.
     27, 0.0520000011,           0.
     28, 0.0540000014,           0.
     29, 0.0560000017,           0.
     30, 0.0579999983,           0.
     31, 0.0599999987,           0.
     32,  0.061999999,           0.
     33,  0.064000003,           0.
     34, 0.0659999996,           0.
     35, 0.0680000037,           0.
     36, 0.0700000003,           0.
     37, 0.0719999969,           0.
     38,  0.074000001,           0.
     39, 0.0759999976,           0.
     40, 0.0780000016,           0.
     41, 0.0799999982,           0.
     42, 0.0820000023,           0.
     43, 0.0839999989,           0.
     44, 0.0860000029,           0.
     45, 0.0879999995,           0.
     46, 0.0900000036,           0.
```

47,	0.0920000002,	0.
48,	0.0939999968,	0.
49,	0.0960000008,	0.
50,	0.0979999974,	0.
51,	0.100000001,	0.
52,	0.101999998,	0.
53,	0.104000002,	0.
54,	0.105999999,	0.
55,	0.108000003,	0.
56,	0.109999999,	0.
57,	0.112000003,	0.
58,	0.114,	0.
59,	0.115999997,	0.
60,	0.118000001,	0.
61,	0.119999997,	0.
62,	0.122000001,	0.
63,	0.123999998,	0.
64,	0.126000002,	0.
65,	0.128000006,	0.
66,	0.129999995,	0.
67,	0.131999999,	0.
68,	0.134000003,	0.
69,	0.136000007,	0.
70,	0.137999997,	0.
71,	0.140000001,	0.
72,	0.142000005,	0.
73,	0.143999994,	0.
74,	0.145999998,	0.
75,	0.148000002,	0.
76,	0.150000006,	0.
77,	0.151999995,	0.
78,	0.153999999,	0.
79,	0.156000003,	0.
80,	0.158000007,	0.
81,	0.159999996,	0.
82,	0.,	0.00200000009
83,	0.00200000009,	0.00200000009
84,	0.00400000019,	0.00200000009
85,	0.00600000005,	0.00200000009
86,	0.00800000038,	0.00200000009
87,	0.00999999978,	0.00200000009
88,	0.0120000001,	0.00200000009
89,	0.0140000004,	0.00200000009
90,	0.0160000008,	0.00200000009
91,	0.0179999992,	0.00200000009
92,	0.0199999996,	0.00200000009
93,	0.0219999999,	0.00200000009
94,	0.0240000002,	0.00200000009
95,	0.0260000005,	0.00200000009
96,	0.0280000009,	0.00200000009
97,	0.0299999993,	0.00200000009
98,	0.0320000015,	0.00200000009
99,	0.0340000018,	0.00200000009
100,	0.0359999985,	0.00200000009
101,	0.0379999988,	0.00200000009
102,	0.0399999991,	0.00200000009
103,	0.0419999994,	0.00200000009
104,	0.0439999998,	0.00200000009
105,	0.0460000001,	0.00200000009
106,	0.0480000004,	0.00200000009
107,	0.0500000007,	0.00200000009
108,	0.0520000011,	0.00200000009
109,	0.0540000014,	0.00200000009
110,	0.0560000017,	0.00200000009
111,	0.0579999983,	0.00200000009
112,	0.0599999987,	0.00200000009
113,	0.061999999,	0.00200000009
114,	0.064000003,	0.00200000009
115,	0.0659999996,	0.00200000009
116,	0.0680000037,	0.00200000009
117,	0.0700000003,	0.00200000009
118,	0.0719999969,	0.00200000009
119,	0.074000001,	0.00200000009
120,	0.0759999976,	0.00200000009
121,	0.0780000016,	0.00200000009
122,	0.0799999982,	0.00200000009
123,	0.0820000023,	0.00200000009
124,	0.0839999989,	0.00200000009
125,	0.0860000029,	0.00200000009
126,	0.0879999995,	0.00200000009
127,	0.0900000036,	0.00200000009
128,	0.0920000002,	0.00200000009
129,	0.0939999968,	0.00200000009
130,	0.0960000008,	0.00200000009
131,	0.0979999974,	0.00200000009
132,	0.100000001,	0.00200000009
133,	0.101999998,	0.00200000009
134,	0.104000002,	0.00200000009
135,	0.105999999,	0.00200000009
136,	0.108000003,	0.00200000009
137,	0.109999999,	0.00200000009
138,	0.112000003,	0.00200000009
139,	0.114,	0.00200000009
140,	0.115999997,	0.00200000009
141,	0.118000001,	0.00200000009
142,	0.119999997,	0.00200000009
143,	0.122000001,	0.00200000009
144,	0.123999998,	0.00200000009
145,	0.126000002,	0.00200000009
146,	0.128000006,	0.00200000009
147,	0.129999995,	0.00200000009
148,	0.131999999,	0.00200000009
149,	0.134000003,	0.00200000009
150,	0.136000007,	0.00200000009
151,	0.137999997,	0.00200000009
152,	0.140000001,	0.00200000009
153,	0.142000005,	0.00200000009
154,	0.143999994,	0.00200000009
155,	0.145999998,	0.00200000009
156,	0.148000002,	0.00200000009

157, 0.150000006, 0.00200000009
158, 0.151999995, 0.00200000009
159, 0.153999999, 0.00200000009
160, 0.156000003, 0.00200000009
161, 0.158000007, 0.00200000009
162, 0.159999996, 0.00200000009
163, 0., 0.00400000019
164, 0.00200000009, 0.00400000019
165, 0.00400000019, 0.00400000019
166, 0.00600000005, 0.00400000019
167, 0.00800000038, 0.00400000019
168, 0.00999999978, 0.00400000019
169, 0.0120000001, 0.00400000019
170, 0.0140000004, 0.00400000019
171, 0.0160000008, 0.00400000019
172, 0.0179999992, 0.00400000019
173, 0.0199999996, 0.00400000019
174, 0.0219999999, 0.00400000019
175, 0.0240000002, 0.00400000019
176, 0.0260000005, 0.00400000019
177, 0.0280000009, 0.00400000019
178, 0.0299999993, 0.00400000019
179, 0.0320000015, 0.00400000019
180, 0.0340000018, 0.00400000019
181, 0.0359999985, 0.00400000019
182, 0.0379999988, 0.00400000019
183, 0.0399999991, 0.00400000019
184, 0.0419999994, 0.00400000019
185, 0.0439999998, 0.00400000019
186, 0.0460000001, 0.00400000019
187, 0.0480000004, 0.00400000019
188, 0.0500000007, 0.00400000019
189, 0.0520000011, 0.00400000019
190, 0.0540000014, 0.00400000019
191, 0.0560000017, 0.00400000019
192, 0.0579999983, 0.00400000019
193, 0.0599999987, 0.00400000019
194, 0.061999999, 0.00400000019
195, 0.064000003, 0.00400000019
196, 0.0659999996, 0.00400000019
197, 0.0680000037, 0.00400000019
198, 0.0700000003, 0.00400000019
199, 0.0719999969, 0.00400000019
200, 0.074000001, 0.00400000019
201, 0.0759999976, 0.00400000019
202, 0.0780000016, 0.00400000019
203, 0.0799999982, 0.00400000019
204, 0.0820000023, 0.00400000019
205, 0.0839999989, 0.00400000019
206, 0.0860000029, 0.00400000019
207, 0.0879999995, 0.00400000019
208, 0.0900000036, 0.00400000019
209, 0.0920000002, 0.00400000019
210, 0.0939999968, 0.00400000019
211, 0.0960000008, 0.00400000019
212, 0.0979999974, 0.00400000019
213, 0.100000001, 0.00400000019
214, 0.101999998, 0.00400000019
215, 0.104000002, 0.00400000019
216, 0.105999999, 0.00400000019
217, 0.108000003, 0.00400000019
218, 0.109999999, 0.00400000019
219, 0.112000003, 0.00400000019
220, 0.114, 0.00400000019
221, 0.115999997, 0.00400000019
222, 0.118000001, 0.00400000019
223, 0.119999997, 0.00400000019
224, 0.122000001, 0.00400000019
225, 0.123999998, 0.00400000019
226, 0.126000002, 0.00400000019
227, 0.128000006, 0.00400000019
228, 0.129999995, 0.00400000019
229, 0.131999999, 0.00400000019
230, 0.134000003, 0.00400000019
231, 0.136000007, 0.00400000019
232, 0.137999997, 0.00400000019
233, 0.140000001, 0.00400000019
234, 0.142000005, 0.00400000019
235, 0.143999994, 0.00400000019
236, 0.145999998, 0.00400000019
237, 0.148000002, 0.00400000019
238, 0.150000006, 0.00400000019
239, 0.151999995, 0.00400000019
240, 0.153999999, 0.00400000019
241, 0.156000003, 0.00400000019
242, 0.158000007, 0.00400000019
243, 0.159999996, 0.00400000019
244, 0., 0.00600000005
245, 0.00200000009, 0.00600000005
246, 0.00400000019, 0.00600000005
247, 0.00600000005, 0.00600000005
248, 0.00800000038, 0.00600000005
249, 0.00999999978, 0.00600000005
250, 0.0120000001, 0.00600000005
251, 0.0140000004, 0.00600000005
252, 0.0160000008, 0.00600000005
253, 0.0179999992, 0.00600000005
254, 0.0199999996, 0.00600000005
255, 0.0219999999, 0.00600000005
256, 0.0240000002, 0.00600000005
257, 0.0260000005, 0.00600000005
258, 0.0280000009, 0.00600000005
259, 0.0299999993, 0.00600000005
260, 0.0320000015, 0.00600000005
261, 0.0340000018, 0.00600000005
262, 0.0359999985, 0.00600000005
263, 0.0379999988, 0.00600000005
264, 0.0399999991, 0.00600000005
265, 0.0419999994, 0.00600000005
266, 0.0439999998, 0.00600000005

267, 0.0460000001, 0.00600000005
268, 0.0480000004, 0.00600000005
269, 0.0500000007, 0.00600000005
270, 0.0520000011, 0.00600000005
271, 0.0540000014, 0.00600000005
272, 0.0560000017, 0.00600000005
273, 0.0579999983, 0.00600000005
274, 0.0599999987, 0.00600000005
275, 0.061999999, 0.00600000005
276, 0.064000003, 0.00600000005
277, 0.0659999996, 0.00600000005
278, 0.0680000037, 0.00600000005
279, 0.0700000003, 0.00600000005
280, 0.0719999969, 0.00600000005
281, 0.074000001, 0.00600000005
282, 0.0759999976, 0.00600000005
283, 0.0780000016, 0.00600000005
284, 0.0799999982, 0.00600000005
285, 0.0820000023, 0.00600000005
286, 0.0839999989, 0.00600000005
287, 0.0860000029, 0.00600000005
288, 0.0879999995, 0.00600000005
289, 0.0900000036, 0.00600000005
290, 0.0920000002, 0.00600000005
291, 0.0939999968, 0.00600000005
292, 0.0960000008, 0.00600000005
293, 0.0979999974, 0.00600000005
294, 0.100000001, 0.00600000005
295, 0.101999998, 0.00600000005
296, 0.104000002, 0.00600000005
297, 0.105999999, 0.00600000005
298, 0.108000003, 0.00600000005
299, 0.109999999, 0.00600000005
300, 0.112000003, 0.00600000005
301, 0.114, 0.00600000005
302, 0.115999997, 0.00600000005
303, 0.118000001, 0.00600000005
304, 0.119999997, 0.00600000005
305, 0.122000001, 0.00600000005
306, 0.123999998, 0.00600000005
307, 0.126000002, 0.00600000005
308, 0.128000006, 0.00600000005
309, 0.129999995, 0.00600000005
310, 0.131999999, 0.00600000005
311, 0.134000003, 0.00600000005
312, 0.136000007, 0.00600000005
313, 0.137999997, 0.00600000005
314, 0.140000001, 0.00600000005
315, 0.142000005, 0.00600000005
316, 0.143999994, 0.00600000005
317, 0.145999998, 0.00600000005
318, 0.148000002, 0.00600000005
319, 0.150000006, 0.00600000005
320, 0.151999995, 0.00600000005
321, 0.153999999, 0.00600000005
322, 0.156000003, 0.00600000005
323, 0.158000007, 0.00600000005
324, 0.159999996, 0.00600000005
325, 0., 0.00800000038
326, 0.00200000009, 0.00800000038
327, 0.00400000019, 0.00800000038
328, 0.00600000005, 0.00800000038
329, 0.00800000038, 0.00800000038
330, 0.00999999978, 0.00800000038
331, 0.0120000001, 0.00800000038
332, 0.0140000004, 0.00800000038
333, 0.0160000008, 0.00800000038
334, 0.0179999992, 0.00800000038
335, 0.0199999996, 0.00800000038
336, 0.0219999999, 0.00800000038
337, 0.0240000002, 0.00800000038
338, 0.0260000005, 0.00800000038
339, 0.0280000009, 0.00800000038
340, 0.0299999993, 0.00800000038
341, 0.0320000015, 0.00800000038
342, 0.0340000018, 0.00800000038
343, 0.0359999985, 0.00800000038
344, 0.0379999988, 0.00800000038
345, 0.0399999991, 0.00800000038
346, 0.0419999994, 0.00800000038
347, 0.0439999998, 0.00800000038
348, 0.0460000001, 0.00800000038
349, 0.0480000004, 0.00800000038
350, 0.0500000007, 0.00800000038
351, 0.0520000011, 0.00800000038
352, 0.0540000014, 0.00800000038
353, 0.0560000017, 0.00800000038
354, 0.0579999983, 0.00800000038
355, 0.0599999987, 0.00800000038
356, 0.061999999, 0.00800000038
357, 0.064000003, 0.00800000038
358, 0.0659999996, 0.00800000038
359, 0.0680000037, 0.00800000038
360, 0.0700000003, 0.00800000038
361, 0.0719999969, 0.00800000038
362, 0.074000001, 0.00800000038
363, 0.0759999976, 0.00800000038
364, 0.0780000016, 0.00800000038
365, 0.0799999982, 0.00800000038
366, 0.0820000023, 0.00800000038
367, 0.0839999989, 0.00800000038
368, 0.0860000029, 0.00800000038
369, 0.0879999995, 0.00800000038
370, 0.0900000036, 0.00800000038
371, 0.0920000002, 0.00800000038
372, 0.0939999968, 0.00800000038
373, 0.0960000008, 0.00800000038
374, 0.0979999974, 0.00800000038
375, 0.100000001, 0.00800000038
376, 0.101999998, 0.00800000038

377, 0.104000002, 0.00800000038
378, 0.105999999, 0.00800000038
379, 0.108000003, 0.00800000038
380, 0.109999999, 0.00800000038
381, 0.112000003, 0.00800000038
382, 0.114, 0.00800000038
383, 0.115999997, 0.00800000038
384, 0.118000001, 0.00800000038
385, 0.119999997, 0.00800000038
386, 0.122000001, 0.00800000038
387, 0.123999998, 0.00800000038
388, 0.126000002, 0.00800000038
389, 0.128000006, 0.00800000038
390, 0.129999995, 0.00800000038
391, 0.131999999, 0.00800000038
392, 0.134000003, 0.00800000038
393, 0.136000007, 0.00800000038
394, 0.137999997, 0.00800000038
395, 0.140000001, 0.00800000038
396, 0.142000005, 0.00800000038
397, 0.143999994, 0.00800000038
398, 0.145999998, 0.00800000038
399, 0.148000002, 0.00800000038
400, 0.150000006, 0.00800000038
401, 0.151999995, 0.00800000038
402, 0.153999999, 0.00800000038
403, 0.156000003, 0.00800000038
404, 0.158000007, 0.00800000038
405, 0.159999996, 0.00800000038
406, 0., 0.00999999978
407, 0.00200000009, 0.00999999978
408, 0.00400000019, 0.00999999978
409, 0.00600000005, 0.00999999978
410, 0.00800000038, 0.00999999978
411, 0.00999999978, 0.00999999978
412, 0.0120000001, 0.00999999978
413, 0.0140000004, 0.00999999978
414, 0.0160000008, 0.00999999978
415, 0.0179999992, 0.00999999978
416, 0.0199999996, 0.00999999978
417, 0.0219999999, 0.00999999978
418, 0.0240000002, 0.00999999978
419, 0.0260000005, 0.00999999978
420, 0.0280000009, 0.00999999978
421, 0.0299999993, 0.00999999978
422, 0.0320000015, 0.00999999978
423, 0.0340000018, 0.00999999978
424, 0.0359999985, 0.00999999978
425, 0.0379999988, 0.00999999978
426, 0.0399999991, 0.00999999978
427, 0.0419999994, 0.00999999978
428, 0.0439999998, 0.00999999978
429, 0.0460000001, 0.00999999978
430, 0.0480000004, 0.00999999978
431, 0.0500000007, 0.00999999978
432, 0.0520000011, 0.00999999978
433, 0.0540000014, 0.00999999978
434, 0.0560000017, 0.00999999978
435, 0.0579999983, 0.00999999978
436, 0.0599999987, 0.00999999978
437, 0.061999999, 0.00999999978
438, 0.064000003, 0.00999999978
439, 0.0659999996, 0.00999999978
440, 0.0680000037, 0.00999999978
441, 0.0700000003, 0.00999999978
442, 0.0719999969, 0.00999999978
443, 0.074000001, 0.00999999978
444, 0.0759999976, 0.00999999978
445, 0.0780000016, 0.00999999978
446, 0.0799999982, 0.00999999978
447, 0.0820000023, 0.00999999978
448, 0.0839999989, 0.00999999978
449, 0.0860000029, 0.00999999978
450, 0.0879999995, 0.00999999978
451, 0.0900000036, 0.00999999978
452, 0.0920000002, 0.00999999978
453, 0.0939999968, 0.00999999978
454, 0.0960000008, 0.00999999978
455, 0.0979999974, 0.00999999978
456, 0.100000001, 0.00999999978
457, 0.101999998, 0.00999999978
458, 0.104000002, 0.00999999978
459, 0.105999999, 0.00999999978
460, 0.108000003, 0.00999999978
461, 0.109999999, 0.00999999978
462, 0.112000003, 0.00999999978
463, 0.114, 0.00999999978
464, 0.115999997, 0.00999999978
465, 0.118000001, 0.00999999978
466, 0.119999997, 0.00999999978
467, 0.122000001, 0.00999999978
468, 0.123999998, 0.00999999978
469, 0.126000002, 0.00999999978
470, 0.128000006, 0.00999999978
471, 0.129999995, 0.00999999978
472, 0.131999999, 0.00999999978
473, 0.134000003, 0.00999999978
474, 0.136000007, 0.00999999978
475, 0.137999997, 0.00999999978
476, 0.140000001, 0.00999999978
477, 0.142000005, 0.00999999978
478, 0.143999994, 0.00999999978
479, 0.145999998, 0.00999999978
480, 0.148000002, 0.00999999978
481, 0.150000006, 0.00999999978
482, 0.151999995, 0.00999999978
483, 0.153999999, 0.00999999978
484, 0.156000003, 0.00999999978
485, 0.158000007, 0.00999999978
486, 0.159999996, 0.00999999978

```
*Element, type=CPE4R
  1,   1,   2,  83,  82
  2,   2,   3,  84,  83
  3,   3,   4,  85,  84
  4,   4,   5,  86,  85
  5,   5,   6,  87,  86
  6,   6,   7,  88,  87
  7,   7,   8,  89,  88
  8,   8,   9,  90,  89
  9,   9,  10,  91,  90
 10,  10,  11,  92,  91
 11,  11,  12,  93,  92
 12,  12,  13,  94,  93
 13,  13,  14,  95,  94
 14,  14,  15,  96,  95
 15,  15,  16,  97,  96
 16,  16,  17,  98,  97
 17,  17,  18,  99,  98
 18,  18,  19, 100,  99
 19,  19,  20, 101, 100
 20,  20,  21, 102, 101
 21,  21,  22, 103, 102
 22,  22,  23, 104, 103
 23,  23,  24, 105, 104
 24,  24,  25, 106, 105
 25,  25,  26, 107, 106
 26,  26,  27, 108, 107
 27,  27,  28, 109, 108
 28,  28,  29, 110, 109
 29,  29,  30, 111, 110
 30,  30,  31, 112, 111
 31,  31,  32, 113, 112
 32,  32,  33, 114, 113
 33,  33,  34, 115, 114
 34,  34,  35, 116, 115
 35,  35,  36, 117, 116
 36,  36,  37, 118, 117
 37,  37,  38, 119, 118
 38,  38,  39, 120, 119
 39,  39,  40, 121, 120
 40,  40,  41, 122, 121
 41,  41,  42, 123, 122
 42,  42,  43, 124, 123
 43,  43,  44, 125, 124
 44,  44,  45, 126, 125
 45,  45,  46, 127, 126
 46,  46,  47, 128, 127
 47,  47,  48, 129, 128
 48,  48,  49, 130, 129
 49,  49,  50, 131, 130
 50,  50,  51, 132, 131
 51,  51,  52, 133, 132
 52,  52,  53, 134, 133
 53,  53,  54, 135, 134
 54,  54,  55, 136, 135
 55,  55,  56, 137, 136
 56,  56,  57, 138, 137
 57,  57,  58, 139, 138
 58,  58,  59, 140, 139
 59,  59,  60, 141, 140
 60,  60,  61, 142, 141
 61,  61,  62, 143, 142
 62,  62,  63, 144, 143
 63,  63,  64, 145, 144
 64,  64,  65, 146, 145
 65,  65,  66, 147, 146
 66,  66,  67, 148, 147
 67,  67,  68, 149, 148
 68,  68,  69, 150, 149
 69,  69,  70, 151, 150
 70,  70,  71, 152, 151
 71,  71,  72, 153, 152
 72,  72,  73, 154, 153
 73,  73,  74, 155, 154
 74,  74,  75, 156, 155
 75,  75,  76, 157, 156
 76,  76,  77, 158, 157
 77,  77,  78, 159, 158
 78,  78,  79, 160, 159
 79,  79,  80, 161, 160
 80,  80,  81, 162, 161
 81,  82,  83, 164, 163
 82,  83,  84, 165, 164
 83,  84,  85, 166, 165
 84,  85,  86, 167, 166
 85,  86,  87, 168, 167
 86,  87,  88, 169, 168
 87,  88,  89, 170, 169
 88,  89,  90, 171, 170
 89,  90,  91, 172, 171
 90,  91,  92, 173, 172
 91,  92,  93, 174, 173
 92,  93,  94, 175, 174
 93,  94,  95, 176, 175
 94,  95,  96, 177, 176
 95,  96,  97, 178, 177
 96,  97,  98, 179, 178
 97,  98,  99, 180, 179
 98,  99, 100, 181, 180
 99, 100, 101, 182, 181
100, 101, 102, 183, 182
101, 102, 103, 184, 183
102, 103, 104, 185, 184
103, 104, 105, 186, 185
104, 105, 106, 187, 186
105, 106, 107, 188, 187
106, 107, 108, 189, 188
107, 108, 109, 190, 189
108, 109, 110, 191, 190
```

109, 110, 111, 192, 191
110, 111, 112, 193, 192
111, 112, 113, 194, 193
112, 113, 114, 195, 194
113, 114, 115, 196, 195
114, 115, 116, 197, 196
115, 116, 117, 198, 197
116, 117, 118, 199, 198
117, 118, 119, 200, 199
118, 119, 120, 201, 200
119, 120, 121, 202, 201
120, 121, 122, 203, 202
121, 122, 123, 204, 203
122, 123, 124, 205, 204
123, 124, 125, 206, 205
124, 125, 126, 207, 206
125, 126, 127, 208, 207
126, 127, 128, 209, 208
127, 128, 129, 210, 209
128, 129, 130, 211, 210
129, 130, 131, 212, 211
130, 131, 132, 213, 212
131, 132, 133, 214, 213
132, 133, 134, 215, 214
133, 134, 135, 216, 215
134, 135, 136, 217, 216
135, 136, 137, 218, 217
136, 137, 138, 219, 218
137, 138, 139, 220, 219
138, 139, 140, 221, 220
139, 140, 141, 222, 221
140, 141, 142, 223, 222
141, 142, 143, 224, 223
142, 143, 144, 225, 224
143, 144, 145, 226, 225
144, 145, 146, 227, 226
145, 146, 147, 228, 227
146, 147, 148, 229, 228
147, 148, 149, 230, 229
148, 149, 150, 231, 230
149, 150, 151, 232, 231
150, 151, 152, 233, 232
151, 152, 153, 234, 233
152, 153, 154, 235, 234
153, 154, 155, 236, 235
154, 155, 156, 237, 236
155, 156, 157, 238, 237
156, 157, 158, 239, 238
157, 158, 159, 240, 239
158, 159, 160, 241, 240
159, 160, 161, 242, 241
160, 161, 162, 243, 242
161, 163, 164, 245, 244
162, 164, 165, 246, 245
163, 165, 166, 247, 246
164, 166, 167, 248, 247
165, 167, 168, 249, 248
166, 168, 169, 250, 249
167, 169, 170, 251, 250
168, 170, 171, 252, 251
169, 171, 172, 253, 252
170, 172, 173, 254, 253
171, 173, 174, 255, 254
172, 174, 175, 256, 255
173, 175, 176, 257, 256
174, 176, 177, 258, 257
175, 177, 178, 259, 258
176, 178, 179, 260, 259
177, 179, 180, 261, 260
178, 180, 181, 262, 261
179, 181, 182, 263, 262
180, 182, 183, 264, 263
181, 183, 184, 265, 264
182, 184, 185, 266, 265
183, 185, 186, 267, 266
184, 186, 187, 268, 267
185, 187, 188, 269, 268
186, 188, 189, 270, 269
187, 189, 190, 271, 270
188, 190, 191, 272, 271
189, 191, 192, 273, 272
190, 192, 193, 274, 273
191, 193, 194, 275, 274
192, 194, 195, 276, 275
193, 195, 196, 277, 276
194, 196, 197, 278, 277
195, 197, 198, 279, 278
196, 198, 199, 280, 279
197, 199, 200, 281, 280
198, 200, 201, 282, 281
199, 201, 202, 283, 282
200, 202, 203, 284, 283
201, 203, 204, 285, 284
202, 204, 205, 286, 285
203, 205, 206, 287, 286
204, 206, 207, 288, 287
205, 207, 208, 289, 288
206, 208, 209, 290, 289
207, 209, 210, 291, 290
208, 210, 211, 292, 291
209, 211, 212, 293, 292
210, 212, 213, 294, 293
211, 213, 214, 295, 294
212, 214, 215, 296, 295
213, 215, 216, 297, 296
214, 216, 217, 298, 297
215, 217, 218, 299, 298
216, 218, 219, 300, 299
217, 219, 220, 301, 300
218, 220, 221, 302, 301

219, 221, 222, 303, 302
220, 222, 223, 304, 303
221, 223, 224, 305, 304
222, 224, 225, 306, 305
223, 225, 226, 307, 306
224, 226, 227, 308, 307
225, 227, 228, 309, 308
226, 228, 229, 310, 309
227, 229, 230, 311, 310
228, 230, 231, 312, 311
229, 231, 232, 313, 312
230, 232, 233, 314, 313
231, 233, 234, 315, 314
232, 234, 235, 316, 315
233, 235, 236, 317, 316
234, 236, 237, 318, 317
235, 237, 238, 319, 318
236, 238, 239, 320, 319
237, 239, 240, 321, 320
238, 240, 241, 322, 321
239, 241, 242, 323, 322
240, 242, 243, 324, 323
241, 244, 245, 326, 325
242, 245, 246, 327, 326
243, 246, 247, 328, 327
244, 247, 248, 329, 328
245, 248, 249, 330, 329
246, 249, 250, 331, 330
247, 250, 251, 332, 331
248, 251, 252, 333, 332
249, 252, 253, 334, 333
250, 253, 254, 335, 334
251, 254, 255, 336, 335
252, 255, 256, 337, 336
253, 256, 257, 338, 337
254, 257, 258, 339, 338
255, 258, 259, 340, 339
256, 259, 260, 341, 340
257, 260, 261, 342, 341
258, 261, 262, 343, 342
259, 262, 263, 344, 343
260, 263, 264, 345, 344
261, 264, 265, 346, 345
262, 265, 266, 347, 346
263, 266, 267, 348, 347
264, 267, 268, 349, 348
265, 268, 269, 350, 349
266, 269, 270, 351, 350
267, 270, 271, 352, 351
268, 271, 272, 353, 352
269, 272, 273, 354, 353
270, 273, 274, 355, 354
271, 274, 275, 356, 355
272, 275, 276, 357, 356
273, 276, 277, 358, 357
274, 277, 278, 359, 358
275, 278, 279, 360, 359
276, 279, 280, 361, 360
277, 280, 281, 362, 361
278, 281, 282, 363, 362
279, 282, 283, 364, 363
280, 283, 284, 365, 364
281, 284, 285, 366, 365
282, 285, 286, 367, 366
283, 286, 287, 368, 367
284, 287, 288, 369, 368
285, 288, 289, 370, 369
286, 289, 290, 371, 370
287, 290, 291, 372, 371
288, 291, 292, 373, 372
289, 292, 293, 374, 373
290, 293, 294, 375, 374
291, 294, 295, 376, 375
292, 295, 296, 377, 376
293, 296, 297, 378, 377
294, 297, 298, 379, 378
295, 298, 299, 380, 379
296, 299, 300, 381, 380
297, 300, 301, 382, 381
298, 301, 302, 383, 382
299, 302, 303, 384, 383
300, 303, 304, 385, 384
301, 304, 305, 386, 385
302, 305, 306, 387, 386
303, 306, 307, 388, 387
304, 307, 308, 389, 388
305, 308, 309, 390, 389
306, 309, 310, 391, 390
307, 310, 311, 392, 391
308, 311, 312, 393, 392
309, 312, 313, 394, 393
310, 313, 314, 395, 394
311, 314, 315, 396, 395
312, 315, 316, 397, 396
313, 316, 317, 398, 397
314, 317, 318, 399, 398
315, 318, 319, 400, 399
316, 319, 320, 401, 400
317, 320, 321, 402, 401
318, 321, 322, 403, 402
319, 322, 323, 404, 403
320, 323, 324, 405, 404
321, 325, 326, 407, 406
322, 326, 327, 408, 407
323, 327, 328, 409, 408
324, 328, 329, 410, 409
325, 329, 330, 411, 410
326, 330, 331, 412, 411
327, 331, 332, 413, 412
328, 332, 333, 414, 413

```
329, 333, 334, 415, 414
330, 334, 335, 416, 415
331, 335, 336, 417, 416
332, 336, 337, 418, 417
333, 337, 338, 419, 418
334, 338, 339, 420, 419
335, 339, 340, 421, 420
336, 340, 341, 422, 421
337, 341, 342, 423, 422
338, 342, 343, 424, 423
339, 343, 344, 425, 424
340, 344, 345, 426, 425
341, 345, 346, 427, 426
342, 346, 347, 428, 427
343, 347, 348, 429, 428
344, 348, 349, 430, 429
345, 349, 350, 431, 430
346, 350, 351, 432, 431
347, 351, 352, 433, 432
348, 352, 353, 434, 433
349, 353, 354, 435, 434
350, 354, 355, 436, 435
351, 355, 356, 437, 436
352, 356, 357, 438, 437
353, 357, 358, 439, 438
354, 358, 359, 440, 439
355, 359, 360, 441, 440
356, 360, 361, 442, 441
357, 361, 362, 443, 442
358, 362, 363, 444, 443
359, 363, 364, 445, 444
360, 364, 365, 446, 445
361, 365, 366, 447, 446
362, 366, 367, 448, 447
363, 367, 368, 449, 448
364, 368, 369, 450, 449
365, 369, 370, 451, 450
366, 370, 371, 452, 451
367, 371, 372, 453, 452
368, 372, 373, 454, 453
369, 373, 374, 455, 454
370, 374, 375, 456, 455
371, 375, 376, 457, 456
372, 376, 377, 458, 457
373, 377, 378, 459, 458
374, 378, 379, 460, 459
375, 379, 380, 461, 460
376, 380, 381, 462, 461
377, 381, 382, 463, 462
378, 382, 383, 464, 463
379, 383, 384, 465, 464
380, 384, 385, 466, 465
381, 385, 386, 467, 466
382, 386, 387, 468, 467
383, 387, 388, 469, 468
384, 388, 389, 470, 469
385, 389, 390, 471, 470
386, 390, 391, 472, 471
387, 391, 392, 473, 472
388, 392, 393, 474, 473
389, 393, 394, 475, 474
390, 394, 395, 476, 475
391, 395, 396, 477, 476
392, 396, 397, 478, 477
393, 397, 398, 479, 478
394, 398, 399, 480, 479
395, 399, 400, 481, 480
396, 400, 401, 482, 481
397, 401, 402, 483, 482
398, 402, 403, 484, 483
399, 403, 404, 485, 484
400, 404, 405, 486, 485

*Nset, nset=_PickedSet6, internal, generate
   1,  486,    1
*Elset, elset=_PickedSet6, internal, generate
   1,  400,    1
*Elset, elset=_Surf-1-AluminiumInterface_S3, internal, generate
 321,  400,    1
*Surface, type=ELEMENT, name=Surf-1-AluminiumInterface
_Surf-1-AluminiumInterface_S3, S3
** Section: Section-1-aluminium
*Solid Section, elset=_PickedSet6, material=Material-1-aluminium
,
*End Instance
**
*Instance, name=Part-2-water-1, part=Part-2-water
         0.1,         0.01,           0.
*Node

1, 0.0179999992, 0.0189999994
2, 0.0160000008, 0.0189999994
```

3, 0.0160000008, 0.00100000005
4, 0.0179999992, 0.00100000005
5, 0.0140000004, 0.0189999994
6, 0.0120000001, 0.0189999994
7, 0.0120000001, 0.00100000005
8, 0.0140000004, 0.00100000005
9, 0.00999999978, 0.0189999994
10, 0.00800000038, 0.0189999994
11, 0.00800000038, 0.00100000005
12, 0.00999999978, 0.00100000005
13, 0.00600000005, 0.0189999994
14, 0.00400000019, 0.0189999994
15, 0.00400000019, 0.00100000005
16, 0.00600000005, 0.00100000005
17, 0.00200000009, 0.0189999994
18, 0., 0.0189999994
19, 0., 0.00100000005
20, 0.00200000009, 0.00100000005
21, 0.0419999994, 0.0189999994
22, 0.0399999991, 0.0189999994
23, 0.0399999991, 0.00100000005
24, 0.0419999994, 0.00100000005
25, 0.0379999988, 0.0189999994
26, 0.0359999985, 0.0189999994
27, 0.0359999985, 0.00100000005
28, 0.0379999988, 0.00100000005
29, 0.0340000018, 0.0189999994
30, 0.0320000015, 0.0189999994
31, 0.0320000015, 0.00100000005
32, 0.0340000018, 0.00100000005
33, 0.0299999993, 0.0189999994
34, 0.0280000009, 0.0189999994
35, 0.0280000009, 0.00100000005
36, 0.0299999993, 0.00100000005
37, 0.0260000005, 0.0189999994
38, 0.0240000002, 0.0189999994
39, 0.0240000002, 0.00100000005
40, 0.0260000005, 0.00100000005
41, 0., 0.
42, 0.0419999994, 0.
43, 0.0199999996, 0.00100000005
44, 0.0219999999, 0.00100000005
45, 0.0419999994, 0.0199999996
46, 0., 0.0199999996
47, 0.0219999999, 0.0189999994
48, 0.0199999996, 0.0189999994
49, 0.0160000008, 0.0170000009
50, 0.0160000008, 0.0149999997
51, 0.0160000008, 0.0130000003
52, 0.0160000008, 0.0109999999
53, 0.0160000008, 0.00899999961
54, 0.0160000008, 0.00700000022
55, 0.0160000008, 0.00499999989
56, 0.0160000008, 0.00300000003
57, 0.0179999992, 0.00300000003
58, 0.0179999992, 0.00499999989
59, 0.0179999992, 0.00700000022
60, 0.0179999992, 0.00899999961
61, 0.0179999992, 0.0109999999
62, 0.0179999992, 0.0130000003
63, 0.0179999992, 0.0149999997
64, 0.0179999992, 0.0170000009
65, 0.0120000001, 0.0170000009
66, 0.0120000001, 0.0149999997
67, 0.0120000001, 0.0130000003
68, 0.0120000001, 0.0109999999
69, 0.0120000001, 0.00899999961
70, 0.0120000001, 0.00700000022
71, 0.0120000001, 0.00499999989
72, 0.0120000001, 0.00300000003
73, 0.0140000004, 0.00300000003
74, 0.0140000004, 0.00499999989
75, 0.0140000004, 0.00700000022
76, 0.0140000004, 0.00899999961
77, 0.0140000004, 0.0109999999
78, 0.0140000004, 0.0130000003
79, 0.0140000004, 0.0149999997
80, 0.0140000004, 0.0170000009
81, 0.00800000038, 0.0170000009
82, 0.00800000038, 0.0149999997
83, 0.00800000038, 0.0130000003
84, 0.00800000038, 0.0109999999
85, 0.00800000038, 0.00899999961
86, 0.00800000038, 0.00700000022
87, 0.00800000038, 0.00499999989
88, 0.00800000038, 0.00300000003
89, 0.00999999978, 0.00300000003
90, 0.00999999978, 0.00499999989
91, 0.00999999978, 0.00700000022
92, 0.00999999978, 0.00899999961
93, 0.00999999978, 0.0109999999
94, 0.00999999978, 0.0130000003
95, 0.00999999978, 0.0149999997
96, 0.00999999978, 0.0170000009
97, 0.00400000019, 0.0170000009
98, 0.00400000019, 0.0149999997
99, 0.00400000019, 0.0130000003
100, 0.00400000019, 0.0109999999
101, 0.00400000019, 0.00899999961
102, 0.00400000019, 0.00700000022
103, 0.00400000019, 0.00499999989
104, 0.00400000019, 0.00300000003
105, 0.00600000005, 0.00300000003
106, 0.00600000005, 0.00499999989
107, 0.00600000005, 0.00700000022
108, 0.00600000005, 0.00899999961
109, 0.00600000005, 0.0109999999
110, 0.00600000005, 0.0130000003
111, 0.00600000005, 0.0149999997
112, 0.00600000005, 0.0170000009

113, 0., 0.0170000009
114, 0., 0.0149999997
115, 0., 0.0130000003
116, 0., 0.0109999999
117, 0., 0.00899999961
118, 0., 0.00700000022
119, 0., 0.00499999989
120, 0., 0.00300000003
121, 0.00200000009, 0.00300000003
122, 0.00200000009, 0.00499999989
123, 0.00200000009, 0.00700000022
124, 0.00200000009, 0.00899999961
125, 0.00200000009, 0.0109999999
126, 0.00200000009, 0.0130000003
127, 0.00200000009, 0.0149999997
128, 0.00200000009, 0.0170000009
129, 0.0399999991, 0.0170000009
130, 0.0399999991, 0.0149999997
131, 0.0399999991, 0.0130000003
132, 0.0399999991, 0.0109999999
133, 0.0399999991, 0.00899999961
134, 0.0399999991, 0.00700000022
135, 0.0399999991, 0.00499999989
136, 0.0399999991, 0.00300000003
137, 0.0419999994, 0.00300000003
138, 0.0419999994, 0.00499999989
139, 0.0419999994, 0.00700000022
140, 0.0419999994, 0.00899999961
141, 0.0419999994, 0.0109999999
142, 0.0419999994, 0.0130000003
143, 0.0419999994, 0.0149999997
144, 0.0419999994, 0.0170000009
145, 0.0359999985, 0.0170000009
146, 0.0359999985, 0.0149999997
147, 0.0359999985, 0.0130000003
148, 0.0359999985, 0.0109999999
149, 0.0359999985, 0.00899999961
150, 0.0359999985, 0.00700000022
151, 0.0359999985, 0.00499999989
152, 0.0359999985, 0.00300000003
153, 0.0379999988, 0.00300000003
154, 0.0379999988, 0.00499999989
155, 0.0379999988, 0.00700000022
156, 0.0379999988, 0.00899999961
157, 0.0379999988, 0.0109999999
158, 0.0379999988, 0.0130000003
159, 0.0379999988, 0.0149999997
160, 0.0379999988, 0.0170000009
161, 0.0320000015, 0.0170000009
162, 0.0320000015, 0.0149999997
163, 0.0320000015, 0.0130000003
164, 0.0320000015, 0.0109999999
165, 0.0320000015, 0.00899999961
166, 0.0320000015, 0.00700000022
167, 0.0320000015, 0.00499999989
168, 0.0320000015, 0.00300000003
169, 0.0340000018, 0.00300000003
170, 0.0340000018, 0.00499999989
171, 0.0340000018, 0.00700000022
172, 0.0340000018, 0.00899999961
173, 0.0340000018, 0.0109999999
174, 0.0340000018, 0.0130000003
175, 0.0340000018, 0.0149999997
176, 0.0340000018, 0.0170000009
177, 0.0280000009, 0.0170000009
178, 0.0280000009, 0.0149999997
179, 0.0280000009, 0.0130000003
180, 0.0280000009, 0.0109999999
181, 0.0280000009, 0.00899999961
182, 0.0280000009, 0.00700000022
183, 0.0280000009, 0.00499999989
184, 0.0280000009, 0.00300000003
185, 0.0299999993, 0.00300000003
186, 0.0299999993, 0.00499999989
187, 0.0299999993, 0.00700000022
188, 0.0299999993, 0.00899999961
189, 0.0299999993, 0.0109999999
190, 0.0299999993, 0.0130000003
191, 0.0299999993, 0.0149999997
192, 0.0299999993, 0.0170000009
193, 0.0240000002, 0.0170000009
194, 0.0240000002, 0.0149999997
195, 0.0240000002, 0.0130000003
196, 0.0240000002, 0.0109999999
197, 0.0240000002, 0.00899999961
198, 0.0240000002, 0.00700000022
199, 0.0240000002, 0.00499999989
200, 0.0240000002, 0.00300000003
201, 0.0260000005, 0.00300000003
202, 0.0260000005, 0.00499999989
203, 0.0260000005, 0.00700000022
204, 0.0260000005, 0.00899999961
205, 0.0260000005, 0.0109999999
206, 0.0260000005, 0.0130000003
207, 0.0260000005, 0.0149999997
208, 0.0260000005, 0.0170000009
209, 0.00200000009, 0.
210, 0.00400000019, 0.
211, 0.00600000005, 0.
212, 0.00800000038, 0.
213, 0.00999999978, 0.
214, 0.0120000001, 0.
215, 0.0140000004, 0.
216, 0.0160000008, 0.
217, 0.0179999992, 0.
218, 0.0199999996, 0.
219, 0.0219999999, 0.
220, 0.0240000002, 0.
221, 0.0260000005, 0.
222, 0.0280000009, 0.

223, 0.0299999993,   0.
224, 0.0320000015,   0.
225, 0.0340000018,   0.
226, 0.0359999985,   0.
227, 0.0379999988,   0.
228, 0.0399999991,   0.
229, 0.0399999991, 0.0199999996
230, 0.0379999988, 0.0199999996
231, 0.0359999985, 0.0199999996
232, 0.0340000018, 0.0199999996
233, 0.0320000015, 0.0199999996
234, 0.0299999993, 0.0199999996
235, 0.0280000009, 0.0199999996
236, 0.0260000005, 0.0199999996
237, 0.0240000002, 0.0199999996
238, 0.0219999999, 0.0199999996
239, 0.0199999996, 0.0199999996
240, 0.0179999992, 0.0199999996
241, 0.0160000008, 0.0199999996
242, 0.0140000004, 0.0199999996
243, 0.0120000001, 0.0199999996
244, 0.00999999978, 0.0199999996
245, 0.00800000038, 0.0199999996
246, 0.00600000005, 0.0199999996
247, 0.00400000019, 0.0199999996
248, 0.00200000009, 0.0199999996
249, 0.0199999996, 0.0170000009
250, 0.0199999996, 0.0149999997
251, 0.0199999996, 0.0130000003
252, 0.0199999996, 0.0109999999
253, 0.0199999996, 0.00899999961
254, 0.0199999996, 0.00700000022
255, 0.0199999996, 0.00499999989
256, 0.0199999996, 0.00300000003
257, 0.0219999999, 0.00300000003
258, 0.0219999999, 0.00499999989
259, 0.0219999999, 0.00700000022
260, 0.0219999999, 0.00899999961
261, 0.0219999999, 0.0109999999
262, 0.0219999999, 0.0130000003
263, 0.0219999999, 0.0149999997
264, 0.0219999999, 0.0170000009
*Element, type=AC2D4R
1, 1, 2, 49, 64
2, 64, 49, 50, 63
3, 63, 50, 51, 62
4, 62, 51, 52, 61
5, 61, 52, 53, 60
6, 60, 53, 54, 59
7, 59, 54, 55, 58
8, 58, 55, 56, 57
9, 57, 56, 3, 4
10, 5, 6, 65, 80
11, 80, 65, 66, 79
12, 79, 66, 67, 78
13, 78, 67, 68, 77
14, 77, 68, 69, 76
15, 76, 69, 70, 75
16, 75, 70, 71, 74
17, 74, 71, 72, 73
18, 73, 72, 7, 8
19, 9, 10, 81, 96
20, 96, 81, 82, 95
21, 95, 82, 83, 94
22, 94, 83, 84, 93
23, 93, 84, 85, 92
24, 92, 85, 86, 91
25, 91, 86, 87, 90
26, 90, 87, 88, 89
27, 89, 88, 11, 12
28, 13, 14, 97, 112
29, 112, 97, 98, 111
30, 111, 98, 99, 110
31, 110, 99, 100, 109
32, 109, 100, 101, 108
33, 108, 101, 102, 107
34, 107, 102, 103, 106
35, 106, 103, 104, 105
36, 105, 104, 15, 16
37, 17, 18, 113, 128
38, 128, 113, 114, 127
39, 127, 114, 115, 126
40, 126, 115, 116, 125
41, 125, 116, 117, 124
42, 124, 117, 118, 123
43, 123, 118, 119, 122
44, 122, 119, 120, 121
45, 121, 120, 19, 20
46, 21, 22, 129, 144
47, 144, 129, 130, 143
48, 143, 130, 131, 142
49, 142, 131, 132, 141
50, 141, 132, 133, 140
51, 140, 133, 134, 139
52, 139, 134, 135, 138
53, 138, 135, 136, 137
54, 137, 136, 23, 24
55, 25, 26, 145, 160
56, 160, 145, 146, 159
57, 159, 146, 147, 158
58, 158, 147, 148, 157
59, 157, 148, 149, 156
60, 156, 149, 150, 155
61, 155, 150, 151, 154
62, 154, 151, 152, 153
63, 153, 152, 27, 28
64, 29, 30, 161, 176
65, 176, 161, 162, 175
66, 175, 162, 163, 174

```
67, 174, 163, 164, 173
68, 173, 164, 165, 172
69, 172, 165, 166, 171
70, 171, 166, 167, 170
71, 170, 167, 168, 169
72, 169, 168,  31,  32
73,  33,  34, 177, 192
74, 192, 177, 178, 191
75, 191, 178, 179, 190
76, 190, 179, 180, 189
77, 189, 180, 181, 188
78, 188, 181, 182, 187
79, 187, 182, 183, 186
80, 186, 183, 184, 185
81, 185, 184,  35,  36
82,  37,  38, 193, 208
83, 208, 193, 194, 207
84, 207, 194, 195, 206
85, 206, 195, 196, 205
86, 205, 196, 197, 204
87, 204, 197, 198, 203
88, 203, 198, 199, 202
89, 202, 199, 200, 201
90, 201, 200,  39,  40
 91,  19,  41, 209,  20
 92,  20, 209, 210,  15
 93,  15, 210, 211,  16
 94,  16, 211, 212,  11
 95,  11, 212, 213,  12
 96,  12, 213, 214,   7
 97,   7, 214, 215,   8
 98,   8, 215, 216,   3
 99,   3, 216, 217,   4
100,   4, 217, 218,  43
101,  43, 218, 219,  44
102,  44, 219, 220,  39
103,  39, 220, 221,  40
104,  40, 221, 222,  35
105,  35, 222, 223,  36
106,  36, 223, 224,  31
107,  31, 224, 225,  32
108,  32, 225, 226,  27
109,  27, 226, 227,  28
110,  28, 227, 228,  23
111,  23, 228,  42,  24
112,  21,  45, 229,  22
113,  22, 229, 230,  25
114,  25, 230, 231,  26
115,  26, 231, 232,  29
116,  29, 232, 233,  30
117,  30, 233, 234,  33
118,  33, 234, 235,  34
119,  34, 235, 236,  37
120,  37, 236, 237,  38
121,  38, 237, 238,  47
122,  47, 238, 239,  48
123,  48, 239, 240,   1
124,   1, 240, 241,   2
125,   2, 241, 242,   5
126,   5, 242, 243,   6
127,   6, 243, 244,   9
128,   9, 244, 245,  10
129,  10, 245, 246,  13
130,  13, 246, 247,  14
131,  14, 247, 248,  17
132,  17, 248,  46,  18
133,  47,  48, 249, 264
134, 264, 249, 250, 263
135, 263, 250, 251, 262
136, 262, 251, 252, 261
137, 261, 252, 253, 260
138, 260, 253, 254, 259
139, 259, 254, 255, 258
140, 258, 255, 256, 257
141, 257, 256,  43,  44
*Nset, nset=Set-1-receiver
  45,  46, 229, 230, 231, 232, 233, 234, 235, 236, 237, 238, 239, 240, 241, 242
 243, 244, 245, 246, 247, 248
*Elset, elset=Set-1-receiver, generate
 112,  132,    1
*Nset, nset=_PickedSet13, internal, generate
   1,  264,    1
*Elset, elset=_PickedSet13, internal, generate
   1,  141,    1
*Elset, elset=_Surf-1-WaterInterface_S2, internal, generate
  91,  111,    1
*Surface, type=ELEMENT, name=Surf-1-WaterInterface
_Surf-1-WaterInterface_S2, S2
** Section: Section-2-water
*Solid Section, elset=_PickedSet13, material=Material-2-water
,
*End Instance
```

```
**
*Nset, nset=Set-1-transmitter, instance=Part-1-aluminium-1, generate
  1,  406,   81
*Nset, nset=Set-2-crack1, instance=Part-1-aluminium-1, generate
 59,  221,   81
*Nset, nset=Set-3-crack2, instance=Part-1-aluminium-1, generate
 64,  226,   81
** Constraint: Constraint-1
*Tie, name=Constraint-1, adjust=yes
Part-2-water-1.Surf-1-WaterInterface, Part-1-aluminium-1.Surf-1-AluminiumInterface
*End Assembly
*Amplitude, name=Amp-1
            0.,              0.,           1e-06, 0.0176789623742178,           2e-06, 0.0267159228293451,
3e-06, -0.0590169943749474
          4e-06, -0.267678962374218,           5e-06,            -0.5,           6e-06, -0.559016994374948,
7e-06, -0.276715922829345
          8e-06, 0.341318065920549,           9e-06, 1.05901699437495,           1e-05,             1.5,
1.1e-05, 1.35035502637568
        1.2e-05,  0.559016994374948,             1.3e-05,  -0.591318065920546,             1.4e-05,  -
1.60035502637568,          1.5e-05,             -2.
        1.6e-05,  -1.60035502637568,              1.7e-05,  -0.591318065920551,              1.8e-05,
0.559016994374947,         1.9e-05, 1.35035502637568
          2e-05,             1.5,         2.1e-05, 1.05901699437495,        2.2e-05, 0.341318065920552,
2.3e-05, -0.276715922829343
        2.4e-05, -0.559016994374947,       2.5e-05,           -0.5,       2.6e-05, -0.267678962374218,
2.7e-05, -0.0590169943749484
        2.8e-05, 0.026715922829345,        2.9e-05, 0.0176789623742179
**
** MATERIALS
**
*Material, name=Material-1-aluminium
*Density
2700.,
*Elastic
 7e+10, 0.33
*Material, name=Material-2-water
*Acoustic Medium
 2.2e+09,
*Density
1000.,
** ----------------------------------------------------------------
**
** STEP: Step-1
**
*Step, name=Step-1, nlgeom=YES
*Dynamic, Explicit, direct user control
1e-06, 0.0002
*Bulk Viscosity
0.06, 1.2
**
** BOUNDARY CONDITIONS
**
** Name: BC-1-transmiter Type: Displacement/Rotation
*Boundary, amplitude=Amp-1
Set-1-transmitter, 1, 1, 0.001
```

```
** Name: BC-2-crack1 Type: Displacement/Rotation
*Boundary
Set-2-crack1, 1, 1
Set-2-crack1, 2, 2
** Name: BC-3-crack2 Type: Displacement/Rotation
*Boundary
Set-3-crack2, 1, 1
Set-3-crack2, 2, 2
**
** OUTPUT REQUESTS
**
*Restart, write, number interval=1, time marks=NO
**
** FIELD OUTPUT: F-Output-1
**
*Output, field
*Node Output
PABS, POR, U
**
** HISTORY OUTPUT: H-Output-1
**
*Output, history, frequency=20
*Node Output, nset=Part-2-water-1.Set-1-receiver
PABS, POR
*End Step
```